

Brave blue world

Human spaceflight is no excuse for ignoring the home planet, which needs constant monitoring from space.

It is commonplace to dismiss NASA's human spaceflight efforts as a waste of money and expertise. For a country with an alarming budget deficit to devote tens of billions of dollars to a project with so little prospect of palpable returns is hard to justify. Certainly, science does not come close to offering a justification.

But arguments against this peculiarly pricey form of showing off, however strong, will not prevail in the foreseeable future. Space exploration resonates with the expectations many Americans have of their country as a home to the exceptional, a conqueror of frontiers and a leader of the world.

Furthermore, the inspiring, potentially transcendent impact of human spaceflight on the imagination should not be lightly dismissed. In the words of one uplifted pioneer: "In that instant I could feel no doubt of man's oneness with the universe... It was a feeling that transcended reason; that went to the heart of man's despair and found it groundless. The universe was a cosmos, not a chaos; man was rightfully a part of that cosmos as were the day and night."

The pioneer quoted above was not an astronaut, although he got as close to the alien isolation of space as any man could at the time. He was the US Antarctic explorer Richard Byrd. As NASA administrator Michael Griffin has argued, there are some interesting parallels to be drawn between the history of Antarctic exploration and the possible future for American spaceflight. But there are differences, too, to which NASA, the Bush administration and Congress should pay careful attention.

Griffin points out that after the South Pole was first explored, it was largely ignored for decades before an eventual return in the 1957 International Geophysical Year led to a continuous presence. Similarly, NASA's plans now call for ending the post-Apollo hiatus by setting up a permanent lunar base — probably at the south pole. But there the comparisons end. For one thing, the renewal of Antarctic exploration was empowered by new technologies, notably reliable diesel engines, capable aircraft and portable radios. But the technologies that NASA plans to implement on its return to the Moon look

remarkably similar to those it used the first time (see page 474).

Another difference is that ever since humanity's return to the South Pole, Antarctic science has been central to the great project of understanding the changes that humans are inflicting on the Earth. An Antarctic component to the nascent global carbon dioxide monitoring effort was established in 1957. Since then the contributions have been legion: discovery of the Antarctic ozone hole; the extraction of greenhouse-gas records and climate data reaching back more than half-a-million years from ice cores; the study of the anomalous warming of the Antarctic peninsula; and so on.

Although lunar research may illuminate some far deeper recesses of Earth's history, the Moon is no Antarctica: the only input that lunar activity will provide for the study of Earth is the iconic and inspiring sight of a blue planet in a black sky over a grey desert.

The human exploration of new worlds may well be important, as inspiration and even, eventually, as something more. But it is not urgent in the same way as understanding and monitoring the Earth system. This is why, as the amount NASA spends on its new vision of exploration increases, it is vital that the resources needed to monitor and study Earth are brought up to the levels required, from which funding currently falls short. As a report by the National Academy of Science recently pointed out, some of this remediation needs to take place at the National Oceanic and Atmospheric Administration, where various instruments need to be placed on future weather satellites or flown on other platforms. But there are also challenges for NASA, notably in studying land-use change and global precipitation, that need to be seen as high priorities for the immediate future.

Mapping the march of global change and exploring possible futures have an urgency that the study of eternal verities and ancient deserts cannot match. The Moon is not going anywhere; Earth is. ■

"The only input that lunar activity will provide for the study of Earth is the iconic sight of a blue planet in a black sky over a grey desert."

Defence deficit

A public debate about renewing Britain's nuclear weaponry is undermined by excessive secrecy.

The RS21007 document could have featured in a John le Carré spy novel. The author of its six drily written pages discusses a plan to turn nuclear submarines into cruise-missile carriers. It is a detailed analysis, probing issues such as exactly which firing tubes would need to be modified. In Britain, it is unlikely that such matters would be discussed outside classified government meetings or clandestine get-togethers between le Carré's fictional spies.

Yet the origins of RS21007 are mundane: its authors are a group of uncontroversial public officials working at the US Congressional Research Service (CRS). The level of detail is not unusual for such a report. In the United States, RS21007 is seen as a useful contribution to the debate about the country's military capabilities. Had the document been written in Britain, it might never have seen the light of day. And that's a problem — without such documents it is impossible to properly scrutinize government proposals.

The proposal that matters right now, and which is currently being studied under conditions of information poverty (see page 464), is an important one. Britain's Trident submarines carry the country's nuclear weapons. The end of their design life is around 15 years away. What comes next? The government favours building a new fleet, at

a cost of up to £20 billion (US\$40 billion), and a parliamentary vote is expected next month.

Submarine builders and the military say that replacing the fleet will ensure that Britain can deter nuclear attacks and avoid the expensive repair costs associated with old vessels. Lining up against them are various weapons experts and think-tanks who argue that the submarines' working lives could be extended by up to 20 years. That would give the government time to better assess whether a system designed for the cold war is really the right defence for a world where rogue nuclear states and terrorists are the biggest threats.

Which side is correct? Unhappily, *Nature* has to admit ignorance on this point. Just a few pages of the relevant White Paper were devoted to the issue of replacement versus repair. Attempts by think-tanks to prise information from the Ministry of Defence have failed. A document like RS21007 would have gone a long way towards helping assess the options. Yet no such document exists and there are no plans for one to be published before the vote takes place.

The debate would be more robust if Britain took the US approach, of which the CRS is a relatively minor component. More important are

the scientific experts who are given security clearance. Congressional committees have access to information, can interrogate officials and pass judgements, in public and in private, on classified programmes. Non-profit groups such as the Natural Resources Defense Council have accumulated considerable knowledge on nuclear matters and frequently engage the federal government in lively and informed public debate. The National Academy of Sciences is also used by the government as a sounding board for security issues, and many reports are published in unclassified form.

In Britain, the gulf between the Ministry of Defence and academia is far wider, partly because of the over-secretive culture of the civil service. But there is little reason why this should be so. If Britain is to properly evaluate the threat it faces, outside experts need to join the debate. Groups such as the Royal Society and the Royal Academy of Engineering would be obvious first points of contact, and both organizations could do more to make the case for their being involved.

The United States has shown that public scrutiny of critical defence expenditures needn't hand its enemies critical secrets. Britain can learn to do the same. ■

A changing drug supply

Research cuts by the world's largest drug company reflect a challenging outlook for the industry.

Pfizer's announcement last week that it will cut its research marks a watershed for the pharmaceutical industry (see page 466).

Until now Pfizer, the leading drug company in terms of both sales and research spending, and an important industry bellwether, has refrained from cutting its efforts to discover new drugs. Yet its \$7 billion in annual R&D expenditures has failed to generate anything near the number of discoveries needed to cover those costs.

The problems facing Pfizer also affect the rest of the industry. A November report by the US Government Accountability Office found that while the industry's US R&D spending rose by 147% from 1993 to 2004, applications for drug approvals to the US Food and Drug Administration rose by only 38%. Applications for drugs with ingredients never before marketed in the United States grew by just 7%.

Former Pfizer chief executive Hank McKinnell found a fix by buying blockbusters instead of discovering them. The acquisition in 2000 of Warner-Lambert gave Pfizer the cholesterol-lowering drug Lipitor, with almost \$13 billion in 2006 sales. In 2003, Pfizer bought Pharmacia and with it the arthritis drug Celebrex, which brought in around \$2 billion last year.

But last summer, Pfizer's board ousted McKinnell in a clear signal of its impatience with that strategy's lack of longer-term delivery, compounded by its concern about the spectre of expiring patents. Five Pfizer drugs worth nearly \$9 billion a year will lose patent protection before Lipitor goes off-patent four years from now. The board wants a change in the firm's R&D strategy and allocation of resources. With new chief executive Jeffrey Kindler — a lawyer who has been at the company for five years — it is getting one.

However, it is not clear whether Kindler is inaugurating a bold era

in drug discovery or a period of creeping retrenchment. He is cutting several layers of middle management and bringing together scientists working on each of ten disease areas, from cancer to cardiovascular disease. In so doing, Kindler is not only seeking simplified logistics but also giving Pfizer's researchers a sense of collaborative ownership of the drug-discovery process. By dropping some discovery efforts entirely, he is acknowledging that the company can no longer afford to play every slot machine in the room. In the best of worlds, this will lead to greater focus and productivity, with the company doing better work in fewer disease areas.

But pessimists see an axe at work rather than a surgical scalpel — with more blows to follow at both Pfizer and its big competitors. These could well include sending a significant amount of early drug discovery to India, China or Eastern Europe, following the route that many clinical trials are already taking.

Observers also predict that big companies will increasingly rely on partnerships with small and mid-sized drug and biotechnology firms to generate drug candidates. If the research labs of Pfizer and its competitors cannot match the productivity of smaller, more flexible firms, it is not hard to imagine the bulk of discoveries being driven by such alliances. Then the big drug firms would be able to focus on what they do best: the heavy lifting of late-stage development and marketing.

Even then, sustaining profits won't be easy. With most, if not all, of the low-hanging fruit having been picked in the past quarter-century, even successful drugs are likely to generate revenues in the hundreds of millions, rather than billions, of dollars.

The industry must acknowledge this if it is to prepare for what is rapidly becoming the post-blockbuster era. All the signs say that companies need to shift their research sights to tailored drugs with smaller, targeted populations. These are cheaper to develop and, importantly, would face less market competition than the mega-blockbuster. Reading between the lines, Pfizer's announcement last week may have opened a door that leads in that direction. ■

RESEARCH HIGHLIGHTS

DRUG DEVELOPMENT

Drift off quickly

Nature Med. doi:10.1038/nm1544 (2007)

A novel sleep-inducing agent has been developed that acts by blocking the actions of brain peptides called orexins.

Orexins promote wakefulness, and people with narcolepsy — a condition causing daytime sleepiness and sudden loss of muscle tone — have low orexin levels.

François Jenck of Actelion Pharmaceuticals in Allschwil, Switzerland, and his colleagues report that their new compound, code-named ACT-078573, reduced alertness in rats, dogs and humans. Human subjects receiving the drug fell asleep more quickly than those receiving the placebo, but none of them experienced loss of muscle tone.

THEORETICAL CHEMISTRY

Sextuple bondage

Angew. Chem. Int. Edn doi:10.1002/anie.200603600 (2007)

In a covalent bond, two atoms share a pair of electrons, knitting together the respective electron orbitals. Two electron pairs are shared in a double bond.

But no-one knew for sure how high a bond could go. Björn Roos of the University of Lund in Sweden and his colleagues have now computed that the maximum number of electron pairs that two atoms can share is actually six.

The best example of such a sextuple bond is that between two tungsten atoms, which bond each other in a complex embrace involving six pairs of electrons.

BIOCHEMISTRY

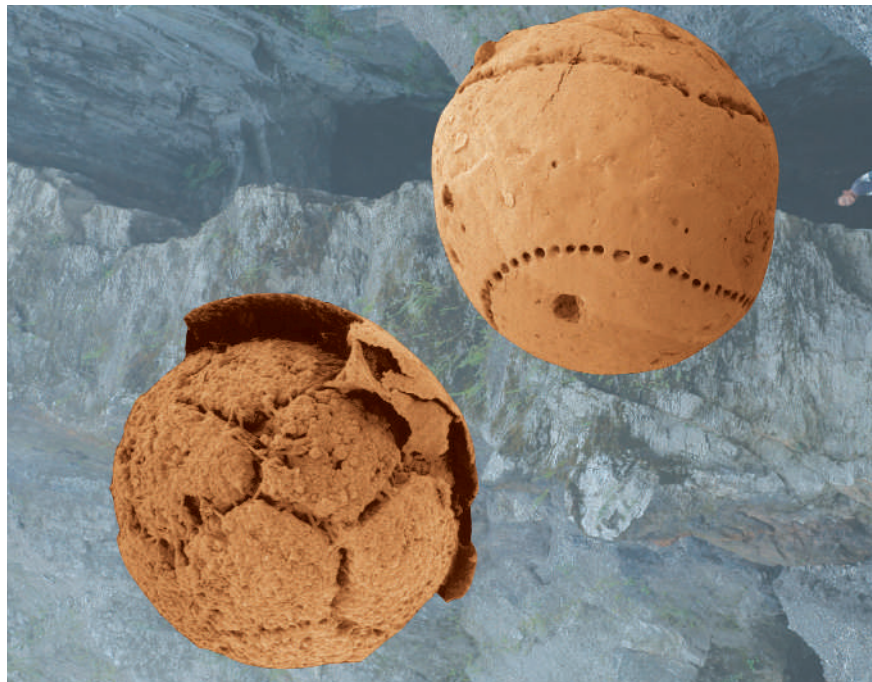
Receptor finally bagged

Science doi:10.1126/science.1136244 (2007)

The elusive receptor that allows cells to take up vitamin A has finally been identified, after a 30-year hunt.

Vitamin A is required for many biological functions, such as vision and immunity. It is carried through the blood bound to retinol-binding protein, RBP.

Hui Sun and his colleagues at the University



Ancient embryos

Geology 35, 115–118 (2007)

Palaeobiologists in China and the United States have identified what may be fossilized embryos (pictured) captured, 600 million years ago, in an early stage of development.

The microfossils, candidate embryos of an as-yet unidentified species, were discovered in southern China. Shuhai Xiao of Virginia

Polytechnic Institute in Blacksburg and his colleagues used microfocus X-ray computer tomography imaging to virtually peel back the outer envelope surrounding the embryos, thus exposing them. The embryos comprised several hundred cells or more arranged in three clockwise coils.

This arrangement suggests that the parent might be a tubular coral-like animal, the authors say.

of California, Los Angeles, devised a strategy to stabilize the binding of RBP to its cell-membrane receptor, and purify the complex. Using mass spectrometry, they identified the receptor as STRA6 (pictured below in retinal cells; green), a widely expressed protein of previously unknown function.

ASTROPHYSICS

Timed burst

Astrophys. J. 655, L25–L28 (2007)

Gamma-ray bursts (GRBs) — explosions of powerful radiation from deep space — are typically classified as being 'short' or 'long'.

But that may be a bad way of doing things.

Bing Zhang of the University of Nevada, Las Vegas, and his colleagues based that conclusion on an analysis of an unusual GRB. The spectral features of the burst, sighted on 14 June 2006 by the Swift satellite, were typical of a short GRB, but lasted for around 100 seconds. Short bursts normally last less than 5 seconds.

Based on the GRB's origin and spectral features, the team concluded that it, like most short GRBs, came from the collision of two compact stars. The team suggests reclassifying GRBs into Type I and Type II.

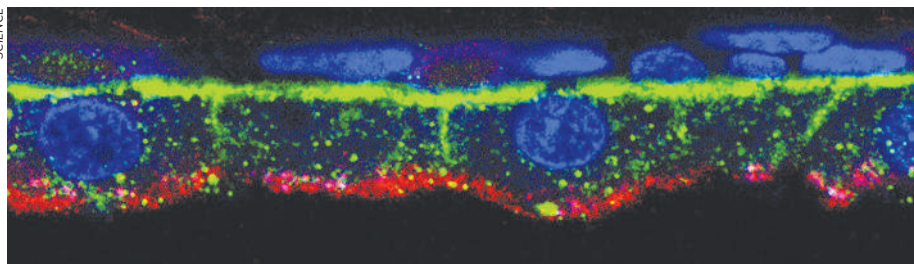
ATMOSPHERIC SCIENCE

Corn monitor

Geophys. Res. Lett. doi:10.1029/2006GL027 (2006)

Trails of carbon dioxide from fossil fuels can be tracked by analysing the leaves and husks of corn.

Fossil fuels contain no carbon-14, so CO₂ from burning coal, gas and oil dilutes levels of this radioisotope in the atmosphere.



SCIENCE

S. XIAO

Diana Hsueh of the University of California, Irvine, and her colleagues reasoned that because carbon in corn is derived from atmospheric CO₂ during photosynthesis in a single growing season, the level of carbon-14 in the plants could be a useful marker of CO₂ release by fossil fuels.

They surveyed samples of corn across North America, unexpectedly finding that levels of fossil-fuel-derived CO₂ were lowest in the western mountain states — perhaps because emissions get blown away from the mountains, or are lifted too high for the corn to incorporate.

IMMUNOLOGY

Sunny response

Nature Immunol. doi:10.1038/ni1433 (2007)

The Sun warms the skin — and may help to protect us from getting sick, report Hekla Sigmundsdottir and Junliang Pan of Stanford University, California, and their co-workers.

The group exposed dendritic cells — a type of immune cell — to a form of vitamin D that is made in the skin after exposure to sunlight. The vitamin stimulated dendritic cells, as well as T cells (another type of immune cell), to convert the vitamin D into a chemically active form. This active form then spurred T cells to stud their surfaces with a specialized homing molecule that guides T cells towards the skin.

The authors suggest that through this mechanism, sunlight triggers the immune system to protect the skin with T cells, which may help to block pathogens and repair damage caused by the Sun.

NANOMECHANICS

Good vibrations

Nature Nanotechnol. advance online publication doi:10.1038/nnano.2006.208 (2007)

Nanoscale vibration sensors sensitive enough to detect their own thermal quivers have been built by scientists at the California Institute of Technology in Pasadena.

Microscopic cantilevers, like miniature springboards, are commonly used to sense motion and mass. But bouncing light off the cantilever to detect its displacement won't work for devices far smaller than the wavelength of light.

One alternative is to detect bending via piezoresistance — a change in electrical conductivity caused by a shape change — in a thin coating. Michael Roukes and his colleagues show that for nanoscale cantilevers, semiconductors are no longer the best piezoresistive materials.

They use gold films instead, giving sensors

that work for very high frequency vibrations and that can detect mass changes of less than 10⁻¹⁸ grams.

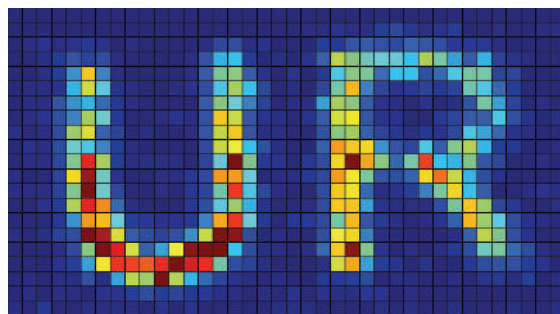
OPTICS

Hold that photon

Phys. Rev. Lett. **98**, 043902 (2007)

Information imprinted in a light beam is easy to transmit but harder to process or store. So today's telecommunications involve the cumbersome interconversion of data encoded optically and electronically.

But Ryan Camacho and his colleagues at the University of Rochester in New York have shown that an image — such as the



'UR' pictured above — recorded in light pulses can indeed be 'stored' after a fashion. Light passing through caesium gas is slowed down massively, delaying a pulse by up to 10 nanoseconds and thus allowing it to be 'held onto' for longer than normal.

The trick works even for beams so dim that a single 2-nanosecond pulse may contain less than one photon, while still encoding an image of several hundred pixels. The technique might enable huge amounts of information to be stored within just a few photons.

CELL BIOLOGY

GATA keep it in check

Cell **127**, 1041-1055 (2006) and *Nature Cell Biol.* **9**, 201-209 (2007)

The transcription factor GATA-3 may underlie the development of a type of breast cancer that is hard to treat, researchers suggest.

Two groups have independently shown that GATA-3 is required for the formation and maintenance of mammary glands.

When the GATA-3 gene was suppressed during development, the mammary gland failed to mature, leading to a build-up of immature cells less likely to express receptors for the hormone oestrogen.

The scientists suggest that GATA-3 loss may perhaps be the cause of some cases of oestrogen-receptor-negative breast tumours, which have notoriously poor prognoses.

JOURNAL CLUB

Andrew Watson

University of East Anglia, UK

An oceanographer describes a missing piece of the climate puzzle.

Most school students know that increasing atmospheric carbon dioxide raises global temperatures. But I've always been fascinated by the other half of the climate-CO₂ connection: why, in the past, have increasing temperatures driven up atmospheric CO₂?

That CO₂ and temperature are locked in a powerful, positive-feedback embrace is obvious from ice-core evidence. But if we add up all the mechanisms that we know about, we fall short of explaining the rise in CO₂ levels seen at the end of glaciations.

Upwelling in the Southern Ocean may be the missing piece. Today, this process brings deep CO₂-rich water rapidly to the surface, where it vents carbon to the atmosphere. If upwelling was shut down during glaciations, we could fit the data better.

It has been suggested that sea ice might have blocked the air-sea transfer of CO₂ during times of glacial maxima (B. B. Stephens & R. F. Keeling *Nature* **404**, 171-174; 2000).

There is good evidence that sea ice was extensive in the region, but any upwelling would have melted that ice, because the rising water has a temperature above freezing point. So the sea ice is evidence that the upwelling itself was absent. What stopped it?

One recent paper (J. R. Toggweiler et al. *Paleoceanography* **21**, PA2005; 2006) argues that the critical factor was a shift to the north of the westerly wind belts that drive the upwelling. I and a colleague propose a subtler connection, a change in the balance of surface heat flux, that would also reduce the upwelling to near-zero (A. J. Watson & A. C. N. Garabato *Tellus B* **58**, 73-87; 2006).

The theories are convergent in many respects, but make distinct predictions that we can test against new proxy evidence. This problem will be solved pretty soon, I think.

AMERICAN PHYSICAL SOCIETY

NEWS

Blair under fire over Trident 'secrecy'

Leading weapons experts and security think-tanks have accused the British government of withholding information needed for proper evaluation of a multibillion-pound proposal to renew the country's fleet of nuclear submarines.

Crucial data on whether the life of the fleet can be extended have not been made public in the run-up to next month's expected parliamentary debate, say the critics. Not releasing the information, they add, fuels fears that the decision will be driven by party politics and industry lobbying rather than by security needs.

Britain's four nuclear submarines, each of which carries up to 16 ballistic Trident missiles and 48 nuclear warheads, will reach the end of their design life in the early 2020s. In a report released last December, the government argued that it would not be prudent to extend the vessels' lives — and that work on replacements should start this year, at a probable cost of between £15 billion and £20 billion (US\$30 billion to \$40 billion). Some critics say that the decision is being rushed so that Prime Minister Tony Blair can secure the replacement of the submarines before he steps down this summer.

But the decision to renew the fleet rests on broad engineering arguments, such as references to past submarine programmes, rather than on a detailed cost analysis. The Ministry of Defence says that releasing the specifics of its plan would amount to telling the world how its submarines work. Others say that this is an exaggeration and that withholding the information prevents a fair comparison with the

main alternative: renovating the fleet to extend its life by 10 to 20 years.

"There is absolutely not enough information out there to make a decision", says Richard Garwin, a physicist and senior adviser on nuclear weapons and other security questions to the US government. Garwin was one of several witnesses who gave evidence on proposed replacements for the submarines to the House of Commons Defence Committee on 23 January.

But attempts to gather such information have been rebuffed. A London-based think-tank, the British American Security Information Council (BASIC), says that it has submitted around eight questions under freedom of information legislation to the Ministry of Defence. Answers to all technical questions, such as whether the submarine hull or the reactor would need to be renovated first, were declared classified. The environmental

group Greenpeace has had similar requests and subsequent appeals turned down.

"They are not going to let people discuss the technical details, even if the information is not particularly sensitive," says Paul Ingram, a senior analyst at BASIC. The ministry says that it answered many of the questions submitted, but that it has to balance public debate with the need to avoid helping nations that might want to undermine Britain's defences. A ministry spokesman said that no state currently had the capability and intent to do so, but that such a threat could potentially arise in coming decades.

Attempts by Britain's top scientific organizations to join the debate have also been rejected.

"There is absolutely not enough information out there to make a decision."



The Royal Society wrote to Roy Anderson, the Ministry of Defence's chief scientific adviser, last April and offered to suggest experts who could assist in the ministry's deliberations. The society was told a month later that the ministry had the matter covered. "We've been running the submarines safely for 40 years," explains Matthew Willey, a ministry spokesman. "There's a huge wealth of expertise here."

But that attitude, says Garwin, contrasts starkly with that in the United States, where outside specialists are often granted the security clearance needed to assess scientific and engineering aspects of military decisions.

California institute woos NIH stem-cell chief

The California Institute for Regenerative Medicine (CIRM) is courting the top stem-cell official at the US National Institutes of Health (NIH) to take over as its president.

James Battey, who since 2002 has coordinated stem-cell research at the NIH as chair of its Stem Cell Task Force, was approached by a member of the CIRM's governing committee in December after its current

president, Zach Hall, announced his resignation (see *Nature* 444, 803; 2006).

Since then, Battey has been excused from all stem-cell-related work at the NIH, agency spokeswoman Marin Allen has confirmed. He remains in his position as director of the National Institute on Deafness and Other Communication Disorders in Bethesda, Maryland. "NIH is grateful for

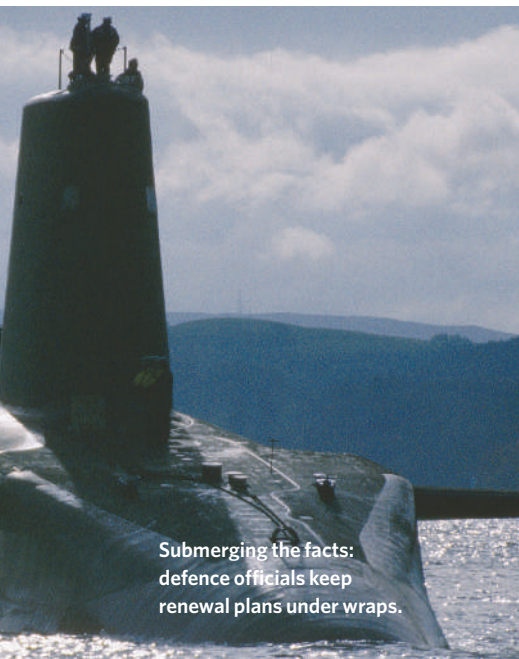
the leadership he has provided and is honouring his privacy," Allen wrote in an e-mail.

Battey was considered as a candidate last time the CIRM was looking for a president, in early 2005 when the \$3-billion institute was newly minted. It ended up hiring Hall.

The 14-member search committee charged with finding the institute's next president was scheduled to hold its first

meeting by teleconference on 31 January. Two days earlier, CIRM spokesman Dale Carlson called any discussion of Battey's candidacy premature. "The search committee hasn't met. They've not retained an [executive search] firm. They haven't posted a job description," he said.

The search committee hasn't discussed a shortlist "with any real seriousness", member Joan



Submerging the facts: defence officials keep renewal plans under wraps.

R. ADSHEAD, THE MILITARY PICTURE LIBRARY/CORBIS

Bodies such as the National Academy of Sciences are also commissioned by the federal government to report on security issues.

Critics assert that the British approach skews decision making. John Finney, a physicist at University College London and a member of Pugwash, which campaigns to reduce armed conflict, says: "Without the technical information and costings of the different options, the agenda can be driven by industrial interests rather than those of national security."

Jim Giles

See Editorial, page 459.

A group of the United States' top ocean specialists this week issued a 'report card' on how the government is treating the sea. And if President George W. Bush had brought home in his school days the grades he received from that exercise, his mother would not have been impressed. The worst grade of all — an F for 'fail' — was for new funding of ocean programmes.

But just before the report was released on 30 January, Bush officials declared that the president will request \$143 million more for the oceans in his 2008 budget than in 2007. Of this, \$80 million will be for research, with focuses on an ocean monitoring network, comparative analysis of marine ecosystems, and research on the water circulation in the Atlantic.

The Bush administration's announcement also listed some legislative goals for the year. These included acceding to the United Nations Law of the Sea and passing specific authorizing legislation for the National Oceanic and Atmospheric Administration (NOAA), the main ocean-research agency, to increase its political heft.

Carlos Gutierrez, head of

the commerce department of which NOAA is part, says the plan will "sharpen our focus and expand our knowledge of our oceans, which is incredibly important for everything we do in the future".

But most years, NOAA gets far more money from Congress than the president requests. So critics of Bush were quick to dismiss the announcement's significance.

"The president's 2007 request provided \$300 million less for ocean, coastal and Great Lakes programmes in research and resource management at NOAA than Congress gave the agency in 2006," says Bart Gordon (Democrat, Tennessee), chair of the House Committee on Science and Technology. "While this year's budget request is an improvement, I suspect this is still disappointing news to

those who want to see more attention paid to ocean and coastal issues."

James Watkins, chair of the congressionally mandated Commission on Ocean Policy, which in 2004 recommended a far-reaching effort to bolster US ocean research, is also unconvinced. "I have been around this town for 50 years and I have always been a bit leery of rhetoric versus reality when it comes to the budget," he says of Bush's plan for ocean research. "We need \$750 million to get this kick-started — that's one day in Iraq."

Gerald Leape, vice-president for marine conservation at the National Environmental Trust in Washington DC, says he is "sceptical" about the Bush plan, but is generally hopeful about the budgetary outlook for ocean research this year. ■
Emma Marris



Commerce secretary Carlos Gutierrez introduces Bush's plan to investigate the deep.

DEPT OF COMMERCE

Samuelson, founder of the Parkinson's Action Network, told *Nature* on 29 January. "We need to think about what talents and what skill set we need in the new president. And we should be clear about that before we write a job description," she said.

The search committee's agenda for this week's meeting includes considering the president's job summary, application criteria and a 'potential timetable' for hiring.

Batthey is highly respected within the NIH as an able

administrator who rarely makes trouble, but who will speak frankly when necessary. During the controversy over tightened

"We need to think about what talents and what skill set we need in the new president."

conflict-of-interest rules at the agency, Batthey said bluntly that if it adopted the stringent set of rules that was first proposed, he would resign (see *Nature* 435, 397; 2005). The rules were loosened

before they were finalized.

Batthey's absence from his NIH stem-cell duties became publicly apparent at a 19 January Senate committee hearing on human embryonic stem-cell research. There, Story Landis, director of the National Institute of Neurological Disorders and Stroke, testified on behalf of the agency. She is now acting chair of the Stem Cell Task Force. It has also emerged that Batthey will not be attending a meeting of stem-cell funding agencies being held in Singapore this week.

The CIRM was created by California voters in a November 2004 ballot initiative as a state agency dedicated to making grants and loans for human embryonic stem-cell research and facilities. But its work has so far been held up by litigation challenging the ballot. With an end to that litigation now on the horizon, "it's a crucial moment in our history," says Samuelson. "The choice of a president can have a lot to do with how much we move ahead and how fast." ■
Meredith Wadman

Bush splashes out on ocean research



UNDERSEA VENT BLOWS BLUE

Coloured hotspot could reveal odd chemistry.

www.nature.com/news

JAMSTEC

Infertility researchers target uterus transplant

Giuseppe Del Priore has the appearance and the soft-spoken, compassionate manner of a well-paid New York doctor. Just the type, in fact, that a woman might trust to stitch a new uterus into her barren abdomen.

And that is exactly what Del Priore, an obstetrician and gynaecologist at New York Downtown Hospital, hopes to do, along with Jeanetta Stega and other colleagues. A spate of recent media reports has highlighted their plans to provide an infertile woman with a transplanted uterus so that she might bear a child — an operation that, if performed, would be only the second such attempt in the world.

A transplant could potentially help some of the most intractable cases of infertility, such as women born without a uterus, those who underwent a hysterectomy at a young age because of cancer or fibroids, or those in whom an infection has closed up the organ. Many such women are desperate to have their own biological children, and the only way for them to do so at present is by having one of their embryos implanted in a surrogate mother — which is illegal in many countries.

But some researchers and bioethicists are voicing concern about the prospect of uterus transplants. They argue that the risks are unknown and that the technique may be

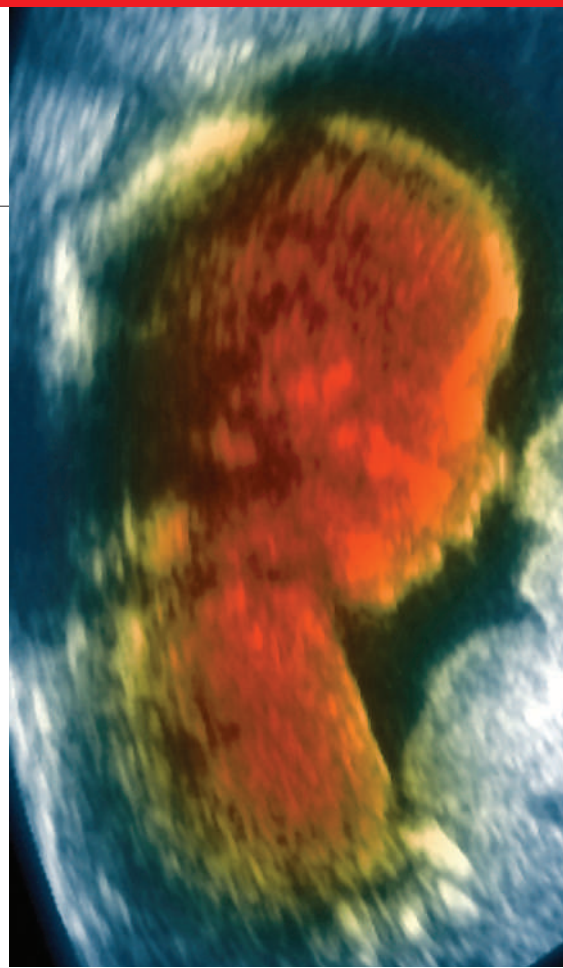
moving too fast into the clinic. “It’s hard to think of another way [of bringing a child into a family] that would be more physically risky or expensive,” says Thomas Murray, director of the Hastings Center, a bioethics research institute in Garrison, New York. If a member of his own family was considering it, he adds, “I’d do everything in my power to talk her out of it.”

In a uterus transplant, the organ would be removed from a living or recently deceased donor and transferred to a recipient. Embryos previously created by *in vitro* fertilization would be transferred to the uterus and, after a child was born, the uterus would be removed to avoid a lifetime of taking powerful immunosuppressant drugs to prevent rejection.

Del Priore says he realized that the operation was feasible after helping to pioneer a surgical technique for cervical cancer that preserves the uterus. In this process, he explains, the uterus is virtually removed from the body, as it would be during a transplant, but is then reconnected. Many women who have had such a procedure have gone on to have healthy babies.

A human uterus transplant has already been done, in Saudi Arabia in 2000, but it had to be removed after 99 days because of a dangerous blood clot¹. Most researchers, including Del Priore, say that before attempting the

“I think technically it can be done, but I say that with a great deal of caution, because it’s a huge undertaking.”



procedure in humans they want to gather more evidence that they can perform three crucial steps in animals: obtain a uterus, transplant it, and show that it can bear healthy offspring. “Yes, I think technically it can be done, but I say that with the greatest deal of caution, because it’s a huge undertaking,” Del Priore says.

Another leading researcher in this small field, Mats Brännström of Gothenburg University in Sweden, showed more than three years ago that mice could bear babies from a transplanted uterus. However, the donor and recipient were virtually genetically identical, so

Michigan lab axed as Pfizer cuts costs

Pfizer’s Ann Arbor laboratory is the largest private-sector employer in the Michigan college town. It is also the birthplace of Lipitor, a cholesterol treatment whose annual sales of \$13 billion make it the biggest-selling drug on the planet. So the lab’s 2,100 staff were stunned when Pfizer announced on 22 January that it will close the lab by the end of next year.

The closure is part of a move by the world’s largest drug company to cut between \$1.5 billion and \$2 billion from its annual costs,

eliminating some 10,000 positions, or about 10% of its workforce. That will include trimming its research and development staff from around 14,000 to 12,500, according to Pfizer’s global research chief John LaMattina, and consolidating researchers at four key sites.

The changes will make Pfizer’s research operation more flexible and cost-effective, says LaMattina. “The simplification will add a lot to our efficiencies as well as the speed of our decision-making.”

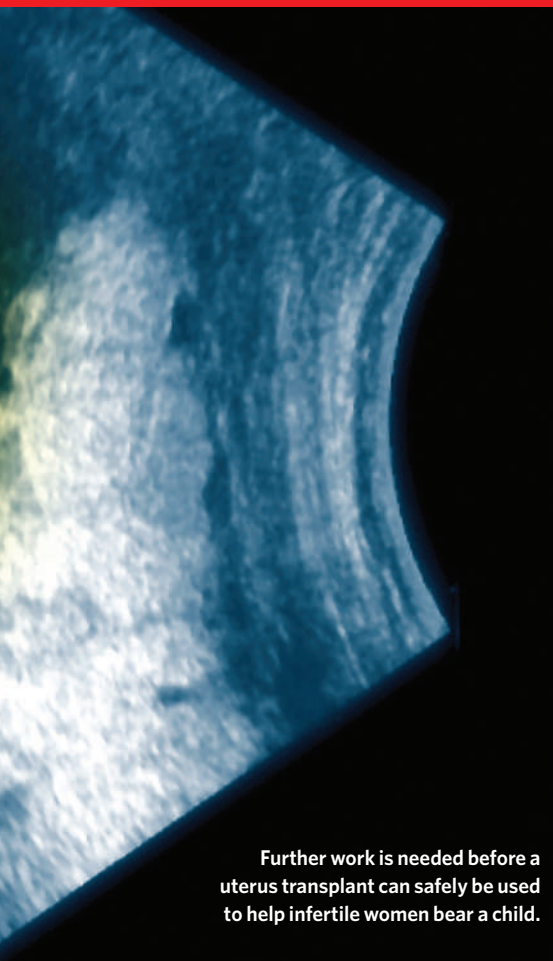
But Michigan academics were left reeling by the announcement’s local impact. “It takes decades to build something like that but, evidently, only 18 months to dismantle it,” says Stephen Forrest, vice-president for research at the University of Michigan.

Pfizer is facing shrinking profits, expiring patents and a pipeline that is looking short of obvious blockbuster drugs. Late last year, it was forced to withdraw torcetrapib — a cholesterol drug that had been touted as a successor to Lipitor

— from clinical trials (see *Nature* 445, 13; 2007).

LaMattina claims the move is needed because the company has so many drug candidates at the expensive, late stages of development all at once, yet needs to control costs. “We’re a little bit a victim of our own success,” he says.

Pfizer will stop some early-stage work, including efforts to find new skin and digestive-tract drugs, and will cut several layers of middle management.



Further work is needed before a uterus transplant can safely be used to help infertile women bear a child.

rejection was not an issue². Since then, his team has successfully removed the uterus of a sheep, then replaced it in the same animal, he says. He believes she is now pregnant.

But animal experiments such as these are not ideal models for a human transplant because the uteri have a different anatomy and, in the case of mice, rabbits and pigs, they support multiple fetuses whereas a woman's uterus typically holds only one or two. So Brännström and others say they want to trial the operation in primates before starting in humans.

Stefan Schlatt of the University of Pittsburgh

in Pennsylvania, who is collaborating with the New York team, says he has tried and failed to perform the transplants in macaques. He adds that he has just received approval for a further two attempts. If primate experiments succeed, human ones are likely to follow quickly. "Once we show the first monkey baby, people will step up and say they want to do it," Schlatt says. "People are so desperate to have children, they wouldn't wait for ten babies to be born to show it's safe." Researchers interviewed by *Nature* estimate that a human operation could take place within two to five years.

Del Priore says he wants to accumulate animal data and gain more experience with human surgery before trying a human transplant: "Somehow we hope we'll know when it's right." But there is no consensus on what experimental data are required before a human operation is considered an acceptable risk.

The group is already laying the groundwork with donors and recipients. Earlier this year, they showed that it was possible to remove a healthy human uterus from a brain-dead organ donor whose heart was still beating³. The researchers are now compiling a list of interested recipients who are being sent information and consent forms to say they are willing to be evaluated for the procedure. The team says the evaluation process will include a psychological assessment and an explanation of alternatives such as adoption.

Del Priore and his colleagues say they are motivated by the number of infertile women who are keen to undergo the operation and who understand the risks. But some bioethicists question how much of the work is really fuelled by doctors' ambition and ego — particularly in the fields of transplant surgery and reproductive medicine, both renowned for aggressively



TRACKING FAKE DRUGS
Chemists develop method for spotting counterfeit pharmaceuticals.
www.nature.com/news

pursuing new methods. "It's a heady cocktail; it brings together two of the more adventurous branches of medicine," says Murray.

Most transplants performed today — such as heart, lung and kidney transplants — are to cure life-threatening or critical conditions. There have been a few exceptions, such as the first face transplant last year, but these are controversial because it is difficult to judge whether the benefits of such transplants are outweighed by the risks.

In the case of uterus transplants, the risk-benefit calculation is even more complex as it must also factor in unknown threats to the future child. Although many thousands of children have been born worldwide to women who have received other transplants, some transplant recipients seem to be at increased risk of pregnancy complications such as high blood pressure and premature birth. It is also not known whether the immunosuppressant drugs might cause subtle effects that become apparent only when the children grow up⁴.

Murray suggests that bodies such as the American College of Obstetricians and Gynecologists should investigate the procedure in order to guide future research. An international symposium on uterine transplantation is to be held in Gothenburg in April. "I'm enthusiastic about the possibility of treatment," says Per-Olof Janson, a gynaecologist at Gothenburg University who is co-chairing the meeting, "but I'm hesitant about rushing."

Helen Pearson

1. Fageeh, W. *et al. Int. J. Gynaecol. Obstet.* **76**, 245–251 (2002).
2. Racho EI-Akouri, R. *et al. Hum. Reprod.* **18**, 2018–2023 (2003).
3. Del Priore, G. *et al. Obstet. Gynecol.* **109**, 101–104 (2007).
4. McKay, D. B. & Josephson, M. A. *New Engl. J. Med.* **354**, 1281–1293 (2006).

Afterwards, LaMattina adds, its laboratories will work at 95% of capacity instead of 65%. Research overhead costs will fall by one-fifth, he says, freeing up hundreds of millions of dollars from bricks and mortar to be spent on science.

The four research sites after the reorganization will be at Groton, Connecticut; Sandwich, UK; St Louis, Missouri; and La Jolla, California. Consolidation into disease-specific groups at these sites will result in "fewer frequent-flier miles and more time at the bench doing science", LaMattina says. The company

is planning a new emphasis on biotherapeutics at St Louis, on cardiovascular work at Groton, and on vaccines at Sandwich and La Jolla.

"It takes decades to build something like that but, evidently, only 18 months to dismantle it."

But Alan Saltiel, director of the Life Sciences Institute at the University of Michigan and a former cell biologist at the Ann Arbor laboratory when it belonged

to Warner-Lambert, before it was acquired by Pfizer in 2000, thinks the separation by disease area has a downside. "What they lose are the opportunities and synergies across therapeutic areas," he points out. "A lot of drug discovery is serendipity."

As well as closing the Ann Arbor site and two smaller Michigan research groups, the company will shut its research facilities in Nagoya in Japan and Amboise in France.

LaMattina says that the company is hoping to transfer, rather than dismiss, up to 70% of workers at targeted facilities. But Tony Butler,

a pharmaceuticals analyst with Lehman Brothers in New York, doubts whether as many as that will move.

And Peter Rost, a former vice-president of marketing and strident critic of Pfizer's current management — now in litigation with the company over the circumstances of his departure in 2005 — predicts that there is worse to come. "This is just the beginning," he says. "It is not the bottom. Two years from now, Pfizer will make another announcement, and cut another \$2 billion. Just watch." **See Editorial, page 460.**

ON THE RECORD

“Isolating stem cells from the placenta is not more difficult than making a steak.”

The editors of online ‘how-to’ guide makezine.com, in a blog entry on the joys of isolating your own amniotic stem cells at home.

SCORECARD

**Ray guns**

US military researchers have turned science fiction into reality with their ‘harmless’ electromagnetic weapon that makes victims feel as if they are about to catch fire. This non-lethal way to disarm people could help save the lives of civilians and army personnel

in battle zones such as Iraq, Pentagon officials claim.

**Space tourism**

‘Lucky’ competition winner Brian Emmett has reluctantly given up his seat on a flight into space with cosmic tour operator Space Adventures after realizing that the prize, offered by software company Oracle, would come with a \$25,000 tax bill.

NUMBER CRUNCH

110% is how much the price of US home heating oil rose between 2000 and 2007.

82% is how much petrol prices rose during the same period.

357% is how much ExxonMobil’s profits grew between 2000 and 2006.

ZOO NEWS

The owners of a Malaysian fruit orchard have discovered why their guard dogs kept disappearing — a 7.1-metre python had eaten 11 of them before being captured by villagers.

Sources: Makezine.com, CNN, Los Angeles Times, Campaign for America’s Future, Reuters

Physicists plan search for the known unknowns

Gravity feels like a force you can trust. Every day, unwavering, it keeps your feet planted firmly on the ground.

But for many physicists, gravity is unsettling. It’s the one force that doesn’t fit into their quantum picture of the world. The best theory to describe it — Einstein’s general theory of relativity — doesn’t mesh with quantum mechanics.

What’s more, general relativity breaks down in the singularities thought to lurk at the centre of black holes, suggesting to physicists that the theory is incomplete. So last week at the University of Arizona in Tucson, around 50 physicists met at a workshop called ‘rethinking gravity’, to confront these problems.

Over three days, participants debated what experiments they could use to hunt for flaws in the general theory of relativity, and asked whether dark matter or dark energy — the unknown stuff that cosmologists now reckon makes up 96% of the Universe — are clues to whatever deeper theory lies beneath.

Their proposals stretch from a table-top experiment so delicate that it can be sent off-kilter by a single piece of dust, to ambitious space missions to measure the gravitational ripples created when two black holes coalesce into one.

Theoretical progress in combining gravity and quantum mechanics has produced ideas such as string theory and loop quantum gravity. And although no theory has yet been proposed that physicists accept as compelling, efforts to develop alternatives have been bolstered by recent discoveries in cosmology.

Maps of the temperature of the cosmic microwave background, for example — the radiation left over from the birth of the Universe — have revealed two opposing influences on the Universe’s structure. One helps matter to clump together, the other accelerates the expansion of the Universe. Taken with other evidence, these observations suggest the existence of dark matter and dark energy, respectively.

A modified theory of gravity might account for the effects — although not everyone is convinced that it will do so. “It’s very easy to sit around in the coffee breaks and say, maybe there is no dark stuff and gravity is different,” warns Sean Carroll of the California Institute of Technology in Pasadena, who works on alternative theories to produce expansion like that seen with dark energy. “But if you sit down to actually do something, there are rules you have to follow. It’s harder than you might think.”

On the launch pad

Five astrophysics projects are competing to be the first mission from NASA’s ‘Beyond Einstein’ programme to fly. Conceived in 2002, the programme aims to address fundamental questions in cosmology (see *Nature* **420**, 593–594; 2002), and could help physicists in their understanding of gravity.

The five ideas are being reviewed by a panel convened by the US National Academies at the request of NASA and the Department of Energy. Mission teams presented their cases at a meeting in Newport Beach, California, this week, in their second meeting with the panel.

Of the two major missions under consideration, one will be built and operated jointly with the European Space Agency. Called the Laser Interferometer Space Antenna, or LISA, the project will search for gravitational waves.

The other large-scale proposal is Constellation-X, a powerful X-ray telescope to study the processes around black holes.

The three smaller proposals are the Joint Dark Energy Mission, being developed jointly by NASA and the Department of Energy; an inflation probe that will try to determine how the Universe

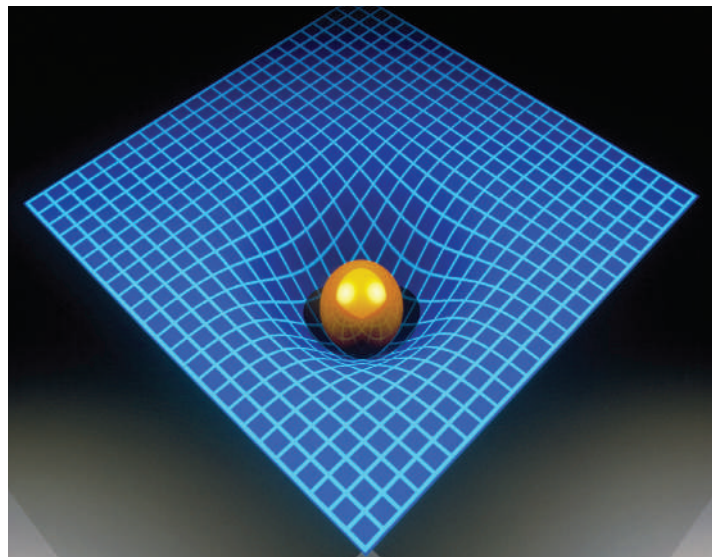
expanded after its birth; and a probe to detect black holes.

The panel will consider the technical and management challenges as well as the missions’ scientific merit. It is expected to report in September, to assist with NASA’s funding plans for 2009.

Some worry that the missions face an uncertain future if they miss the top spot. But Michael Salamon, programme manager for Beyond Einstein, says that all of them will eventually go ahead. “NASA is committed to the entire Beyond Einstein programme”, he says. “There is no ‘winner takes all’ scenario here.”

J.H.

LAGUNA DESIGN/SPL



Curves in space: the theory that matter warps the shape of space and time doesn't mesh with quantum physics.

The hope now is that future experiments will detect some deviation from the predictions of general relativity, or some property of dark matter or dark energy, that will give theorists purchase on the problem. Daniel Holz of the Los Alamos National Laboratory in New Mexico says that, over the past decade, the balance of the field has shifted. "It's definitely experimentally driven at this point," he says.

For instance, Eric Adelberger presented work from his group at the University of Washington in Seattle that checked for anomalies in how the strength of gravity changes with distance. In most circumstances, general relativity gives a dependence that is the same as that familiar from Newton's law: gravity varies with the inverse square of the separation. But new physics, such as the existence of extra dimensions, could modify this behaviour at short range, where these dimensions are thought to operate.

Adelberger's group measured the gravitational attraction between two parallel discs as they were brought to 55 micrometres apart, finding no significant deviation from Newton's law (D. J. Kapner *et al. Phys. Rev. Lett.* **98**, 021101; 2007). This set a new limit on the size of any extra dimension of 44 micrometres, some four times smaller than the previous best estimate.

Other experiments will probe different facets of the theory. In particular, researchers are interested in tests of general relativity that involve strong gravitational fields, such as those around black holes. "It's a regime where we haven't tested gravity," explains Dimitrios Psaltis, one of the conference organizers.

General relativity supposes that matter distorts the shape of space and time, similar to the

way that a ball would sink into a rubber sheet. So far, experiments have mostly probed the gentle curvature around the Sun and planets.

The shape of space and time around a black hole is expected to depend on just two of the black hole's properties: its mass and spin. The Tucson workshop heard that it might be possible to check that a black hole's spin is the same at all radii by tracking hot blobs of infalling matter, or by observing X-rays reflected from the object's surrounding disk of dust.

However, Avery Broderick of the Harvard-Smithsonian Center for Astrophysics in Cambridge, Massachusetts, who presented the results about infalling matter, cautions that processes in the vicinity of a black hole could affect the observations, making it a challenge to confirm whether any deviation is due to differences in gravity or the result of some overlooked astrophysics.

Physicists also hope to test general relativity's predictions about unusual cosmological events, such as mergers of black holes, by detecting gravitational waves. So far, the existence of such waves has only been inferred by measuring changes in the orbit of a binary system containing a radio-emitting pulsar, and ground-based detectors have yet to pick any up. The probable launch date of a proposed space-based detector remains uncertain (see 'On the launch pad').

But whether or not the next round of experiments helps to reconcile general relativity with quantum mechanics, the quest for such a glorious union will continue. "We know there's something we don't know, but we don't what it is," says Adelberger. "We just have to look as hard as we can."

Jenny Hogan

"Processes in the vicinity of a black hole could affect the observations."

Volcano gets choke chains to slow mud

Indonesian geophysicists hope to stem the flow of a destructive mud volcano on East Java by dropping chains of concrete balls into its mouth.

The mud eruption began on 29 May last year in the middle of a rice paddy in the village of Porong, 30 kilometres south of Surabaya, the provincial capital. Since then, the volcano has spewed out up to 126,000 cubic metres of mud a day, flooding an area of more than 4 square kilometres.

Some 10,000 people have been left homeless and 20 factories have closed. Another 200,000 homes could be at risk if the mudflow combines with the rainy season — which has just begun — and weakening dams to flood more land. Attempts to alleviate the problem by drilling relief wells or channelling the mud into a nearby river have so far failed.

Last week, the government team tackling the disaster approved a plan that will use 1,000 steel chains to try to slow the flow of mud. Each chain is 1.5 metres long and links together four concrete balls — two that are 40 centimetres across and two that are 20 centimetres across. Each ball and chain set will weigh about 300 kilograms. The balls themselves will be modified to maximize their friction with the mud.

The team will start off slowly, dropping five chains into the volcano's mouth on the first day — possibly as early as this week — and ten on the second, before hitting a high of up to 50 per day until all of them are used.

The scheme was dreamt up by three geophysicists at the Bandung Institute of Technology: Bagus Nurhandoko, Satria Bijaksana and Umar Fauzi. According to Basuki Hadimuljono, head of the national team managing the disaster, the project will have a budget of 4 billion rupiah (US\$440,000) paid for by PT Lapindo Brantas, the oil drilling company that some locals blame for the disaster.

Bijaksana says that the mudflow calls for an unprecedented solution. "At first we thought it was a common problem in oil exploration, but after a few months we realized this was not a standard situation," he notes.

On 22 January, in a smoky room at the disaster management team's Surabaya headquarters, the geophysicists met with scientists and engineers from the government and the oil company to work out the details of the plan. The next day, Bijaksana and Fauzi were crawling up the side of the volcano to map out plans for



E. WRAY/AP

Can geophysicists calm the mud volcano that has been erupting for eight months in East Java?

the foundations of a bridge that will span the crater and, with the help of a pulley system, will be used for dropping in the chains.

The chains will sink into the conduit that has been feeding the hot mud to the surface, Fauzi explains. "We are aiming to get them to go 100 metres down, but the deeper the better," he says. The goal is to make the channel smaller — not plugging it altogether but, according to a model built by the team, narrowing it enough to slow the mud's rise and so decrease its flow rate by up to three-quarters. Forced to go around the chains and balls, the mud will give up some of its energy to friction, vibration and rotation, says Nurhandoko. "It will make the mud tired. We're killing the mud softly."

But other physicists say they have never heard of such an approach, and question its likely effectiveness. Richard Swarbrick, managing director of consultancy firm GeoPressure Technology in Durham, UK, says that cutting the size of the channel could very well reduce the mud flow. And forcing the mud to take a 'tortuous' path around the balls would also slow it down, he says.

But he points out that reducing the size of the channel is likely to increase the pressure, just like squeezing the end of a hose. "I would

predict that the mud would probably exit at the other holes, or farther along," says Swarbrick. This would just transfer the problem to somewhere else. "The mud will find another way out," he says.

Confident in the face of such criticism, Bijaksana and his colleagues admit that their plan might sound improbable at first. "It took a few months to settle down and make peace with ourselves," he says. But the trio used a simple analogy to sell the project to the government. They cut two holes in the bottom of a plastic bottle and filled it with water. Covering one hole, they showed that the flow rate from the other is unaffected — but the overall rate at which the water leaves the bottle decreases. Likewise, with the volcano, they believe that the volume coming out is directly proportional to the size of the neck of the conduit bringing the mud to the surface.

Bijaksana says there are still uncertainties — the exact flow rate of the mud, for example, and the shape of the crater — that could affect the project's success. He hopes that instruments now being laid over the crater will provide some more information, and adds that he isn't worried about the uncertainty. "People all around here are living in uncertainty," he points out.

David Cyranoski

Terror fears prompt tighter controls for UK labs

In the wake of security concerns about terrorist attacks, the UK Home Office boosted its list of 'controlled substances' used in the lab from 47 to 103 on 25 January.

University, hospital and commercial labs will have to give the government details of their exact stocks of all of these substances, which now include the virus that causes African swine fever and the strain of enterohaemorrhagic *Escherichia coli* that recently caused havoc by contaminating US spinach. If asked, they will also have to inform the police of the names of everyone handling them. The updated list also sees two new categories introduced — 18 animal pathogens and 2 fungi are now included as substances that might be of use to terrorists.

Tony McNulty, minister for police and security, says the measures are to stop terrorist groups using chemical or biological materials as terrorist weapons — a chief threat anticipated by the UK security service MI5. But some scientists say the extended list is overkill, and the increased burden of paperwork will hamper research.

Russia woos India in deal on nuclear fuel

With the much debated Indo-US nuclear deal still facing roadblocks, Russian President Vladimir Putin has offered to build four more nuclear reactors in India, in addition to the two 1,000-megawatt reactors it is already building at Kudankulam in the south of the country.

Indian officials say Russia has offered them a lifetime fuel supply and will not stop them from reprocessing the spent fuel — two crucial issues that have clouded India's deal with Washington. Russian officials say that they are still bound by the guidelines of the Nuclear Suppliers Group; but these may change and, as this regime is voluntary, it may not significantly restrict their actions.

The Indo-Russian accord, signed in New Delhi on 25 January, is seen as a signal that Russia will step in if the US deal falls through.



Vladimir Putin and Manmohan Singh discuss Russia's nuclear deal with India.

Fisheries lay plans to save tuna stocks from extinction

On 26 January, after a five-day meeting in Kobe, Japan, representatives from the world's tuna fisheries issued an 'action plan' on how to save the beleaguered fish. The group agreed that urgent action was needed and decided on broad strategies, from developing catch documentation and tagging systems, to improving trade-tracking programmes and enforcing strict penalties.

But as yet the plan lacks details such as numerical targets or timelines. "Their only agreement was to gather more data and talk more often," said conservation group the WWF in a press release.

Overfishing of tuna is endangering wild stocks — with some now listed as critically endangered. The number of spawning Atlantic bluefin tuna in the western Atlantic is estimated to be at 13% of 1975 levels, for example, according to a WWF report. Japan is widely blamed for the decline, as it consumes more than a quarter of the 2-million-tonne global tuna production.

The group plans to meet next in 2009 to work out more specific plans.



R. HERRMANN/PHOTOLIBRARY

US set to embrace law on genetic discrimination

The US Congress looks likely to ban the use of genetic information in job-hiring and insurance-coverage decisions, after a 12-year effort by lawmakers.

The Genetic Information Nondiscrimination Act would make it illegal for health insurers to deny coverage or increase premium prices for healthy people solely on the basis of a genetic predisposition to a specific disease. It would also stop employers from using such information in making decisions about hiring, firing or promotion.

In the past, Republican House leaders have not brought the bill to a vote. But with Democrats now in charge in both houses, where the bill has bipartisan support, it looks bound for passage into law after its introduction this January. President Bush put his voice behind a ban on genetic discrimination during a visit to the National Institutes of Health earlier in the month.

Britain calls time on plan to advance clocks

A plan to bring Britain's clocks into line with those in Europe failed to gather the necessary political support and so will be dropped.

The potential change, championed by supporters as a way to save lives and energy, would have given Britain an extra hour of evening daylight all year round, by advancing the clocks by an hour from their current times. Preliminary calculations suggest that the move could have saved around 100 lives a year through reducing traffic accidents in the evenings, and about £485 million (US\$950 million) in energy

costs (see *Nature* 445, 344–345; 2007).

The private member's bill got marginal support in the 26 January vote, but failed to draw the necessary 100 Members of Parliament needed for the measure to proceed. Only 52 members voted, with 32 backing the bill.

Bush offers words but no action on climate change

President George W. Bush received some plaudits for referring to "the serious challenge of global climate change" in his State of the Union address last week. He called for a 20% drop in petrol use by 2017, proposed raising fuel-efficiency standards for cars, and called for more research into alternative fuels — specifically boosting investment in finding new ways to produce ethanol as a biofuel. But he did not propose any limits on carbon emissions, leading many experts to say the speech was very light on actual commitments.

In the same week, researchers at the Massachusetts Institute of Technology in Cambridge called for a renewed focus on geothermal energy as part of the country's solution to weaning itself off oil. An investment of up to \$1 billion over 15 years, they said, could allow the United States to harness 10% of its electricity-generating capacity from the hot bowels of Earth by 2050. Geothermal energy currently accounts for less than 1% of US electricity use.

Correction

In our News story "PR's 'pit bull' takes on open access" (*Nature* 445, 347; 2007), we incorrectly quoted Wiley's director of corporate communications, Susan Spilka, as writing in an e-mail: "Media massaging is not the same as intellectual debate." She actually wrote "messaging", not "massaging".

BUSINESS

Display of flexibility

Physicists at the University of Cambridge are leading a revolution in how data can best be displayed. **Katharine Sanderson** reports.

The Cavendish Laboratory in Cambridge, UK, has a storied academic history, with the likes of Ernest Rutherford and James Clerk Maxwell among its alumni. Now in the digital era, the famous laboratory is proving itself no slouch.

Its latest breakthrough came last month, when Plastic Logic — a young company founded by two physicists from the laboratory — said that it had raised about £50 million (US\$100 million) to build a factory that will make flexible displays with organic circuitry laid out on bendable plastic.

The factory will be built in Dresden, Germany, and by 2008 it expects to be producing displays that use flexible plastic semiconductors, instead of glass backing and silicon chips.

Silicon circuitry can't be readily fabricated on plastic because it can be sprayed only when it is hot. But Plastic Logic's tiny, organic polymer circuitry is deposited onto substrates of common plastics such as polyethylene terephthalate (PET) from a solution, keeping process temperatures and costs low. A typical display contains around half a million transistors.

These displays won't displace existing computer screens, most of which are based on liquid-crystal technology and amorphous silicon, any time soon. "It would be madness for a company like Plastic Logic to think that it would compete head-to-head with standard electronics companies," says Henning Sirringhaus, an optoelectronics specialist who was one of the company's co-founders and is now its chief scientist. Instead, it will seek niche applications, hoping to create an entirely new market for flexible, lightweight screens that you can carry about and read on the bus or train.

Plastic Logic was formed in 2000 to exploit research results in organic transistor technology from a team led by Sirringhaus and Richard Friend at the Cavendish. Friend already had one reasonably successful company under his belt — Cambridge Display Technologies (CDT), which has been making organic polymer light-emitting diodes since 1992, and employs around 130 people.



Take it anywhere: plastic displays will provide words where they are needed.

"We believe it is breakthrough-enabling technology."
— Bandel Carano

CDT used organic polymers as the semiconductors in its light-emitting diodes. At the time, these organic semiconductors were not promising candidates to make transistor-based devices. But research into their fabrication continued and by 1999, materials science had progressed to a stage that the organic transistor's mobility — or speed at which electric charge is carried — rivalled that of silicon (H. Sirringhaus *et al. Nature* **401**, 685–688; 1999).

Plastic Logic was then established to exploit this promise commercially. The young company brought in an outside chief executive from the start, Stuart Evans, who already had experience of founding start-up companies such as Cotag International, an early innovator in electronic tagging based in Cambridge.

The company initially raised £1.8 million after persuading Hermann Hauser, co-founder of Cambridge-based venture-capital company Amadeus, that its technology was ripe for commercial development. Other partners at this stage included local venture-capital company Cambridge Research and Innovation and the chemicals giant Dow Chemical. Three funding rounds between 2002 and 2005 raised another £20 million.

But the company's biggest break came when a group of US investors, led by Palo Alto venture-capital firm Oak Investment Partners in California and Tudor Investment of Greenwich, Connecticut, agreed late last year to back the ambitious factory construction plan. "We

closely monitored the company's progress for several years," says Bandel Carano, a partner at Oak. "We believe it is breakthrough-enabling technology."

Barry Young, vice president of DisplaySearch, a market-research firm based in Austin, Texas, says that investors are right to be confident that the flexible displays will find buyers. Newspaper publishers and the book industry are among those with a strong incentive to make sure that handy, lightweight devices soon become available for displaying the printed page.

But he cautions that the success of the company will depend on it being able to create new devices that people actually want to buy. "They are going after a market that doesn't exist," he says, adding that the \$100-million investment is "a giant amount for a company with no defined market and no revenues."

Plastic Logic is keeping details of its first product secret for now. It will probably have to team up with consumer-goods manufacturers to find the 'killer application' that will make it succeed, analysts say.

As it continues on that quest, managers at Plastic Logic are hoping to benefit from a robust infrastructure that has been built at Cambridge to help young companies along. For example, the university's new Integrated Knowledge Centre, which has received £2.3 million from the UK Engineering and Physical Sciences Research Council, will house engineers and scientists to investigate and manufacture new approaches to photonics and electronics. In their roles as academics, Sirringhaus and Friend are both part of the project, and Plastic Logic is one of the five commercial partners involved with the centre.

The Dresden factory will be a scaled-up version of Plastic Logic's prototype production line in Cambridge, and will employ 140 people. Because of the high cost of land and labour, Cambridge was never in contention as a location for the factory, Sirringhaus says. Dresden was chosen because it is an emerging hub for the electronics industry in Europe (see *Nature* **441**, 931; 2006) and because the state government of Saxony will provide an undisclosed cash incentive.

Plastic Logic is unlikely to find that established manufacturers of liquid-crystal displays give up ground easily, however. To compete against them, Plastic Logic's products will have to be cheap, as well as flexible and robust. "Nobody underestimates the challenge ahead," says Sirringhaus.

PLASTIC LOGIC/E INK® IMAGING FILM



WHERE 24 MEN HAVE GONE BEFORE

Three years ago, President George W. Bush told NASA to return American astronauts to the Moon.

Geoff Brumfiel reports on how far they have got.

It's a drizzly afternoon in the middle of January, and a trickle of tourists is visiting the Smithsonian's Air and Space Museum in downtown Washington DC. Ambling around the museum's glass-and-steel atrium, the sightseers gravitate slowly towards the vintage space capsule at its centre.

Nine-year-old John Kalman and his great-aunt Janet peer into the open door of the Apollo 11 command module *Columbia*, the craft in which the first men to walk on the Moon made their epic journey there and back. "That's awesome," exclaims the tow-headed boy as he gazes at panels from another age, jammed with hundreds of switches and indicator lights. "Look at how small it is," his aunt tells him. "It's not like the ones we use today, that's for sure."

True: today's astronauts fly in shuttles that were designed in the 1970s, rather than capsules from the 1960s. But for tomorrow's astronauts, *Columbia* is a glimpse of the future as well as the past. Under the agency's new Vision for Space Exploration, a somewhat larger craft, very similar to the Apollo capsule — 'Apollo on steroids', as it has been dubbed — will have replaced the shuttle in the role of carrying astronauts into orbit as early as 2014. By around 2020, the agency plans to use these new capsules, along with other spacecraft, to return to the Moon and establish an outpost there. That sustained operation, officials hope, will provide a technical basis for a future mission to Mars.

'The vision', as it is often referred to within the agency, was first outlined by President George W. Bush on 14 January 2004. It marks a radical

new direction for America's human spaceflight programme. For the past two decades, NASA has been preoccupied with shuttling people to and from a low Earth orbit, mostly to visit the International Space Station. But the vision "is fundamentally different", says Shana Dale, second in command at NASA. "It's about extending human presence on another world."

This extension, however, can't be built on the cheap; NASA's early estimates put the cost of the programme through to 2018 at around \$104 billion. To meet this bill, the agency is committed to grounding the space shuttle fleet in 2010 and cutting back its spending on the space station, which should be completed by then (see chart, page 477). It is also delaying and cancelling space-based science missions in astronomy, planetary science and Earth observation, as well

NASA/J. FRASSANITO AND ASSOCIATES

as aeronautics programmes. Louis Friedman, executive director of the Planetary Society, a Pasadena-based educational organization in California that regularly criticizes this reallocation of resources, complains: "This is attacking exploration to supposedly pay for exploration."

NASA is thus under pressure from many fronts to make the vision more affordable. At the same time, it needs to be exciting enough to enthuse a population half of which was not born when a man last walked on the Moon. Yet the budgetary constraints mean that things need to be done in a way that seems less than fresh, using spacecraft that look like throwbacks, and making progress in seemingly undramatic, incremental steps. The vision requires NASA to provide an inspiring future frontier while keeping things sustainable, sensible and safe.

On a wing and a prayer

To understand the vision, you have to understand its origin. Business-as-usual at NASA did not come to a close with President Bush's speech in January 2004. It ended a year before. At 08:54 on 1 February 2003, engineers at mission control in Houston, Texas, were guiding another spacecraft called *Columbia* home from a routine, 16-day trip into low Earth orbit. Moving at 24 times the speed of sound, the shuttle had just begun a pre-programmed braking manoeuvre high over California, its wings sheathed in air heated to 1,300 °C. Suddenly, four temperature sensors on the left wing cut out. "You're telling me you lost them all at exactly the same time?" flight director LeRoy Cain asked his team. "No, not exactly," came the reply. "They were within probably four or five seconds of each other." The wing had been damaged, and now the superheated air had found its way inside; within minutes, *Columbia* and its crew of seven were a trail of debris falling out of the morning sky.

The damage was down to a flaw fundamental to the shuttle's design. During the launch, the leading edge of the wings was below the external fuel tank, so anything — in this case, insulating foam — that came off the tank stood a chance of damaging the surfaces most exposed during re-entry. The resultant accident investigation board chided NASA for not coming to grips with the problem earlier.

But the possibility of such engineering lapses was not the only problem with the

shuttle programme, according to John Logsdon, a space-policy expert at George Washington University in Washington DC, who sat on the investigation board. Just as disturbing was the banality for which the astronauts had died. *Columbia* had been on a mission to conduct some small experiments in microgravity, including a promotional test for a fragrance company. Until it ended in tragedy, the mission barely made local headlines in Houston. "We believed this was not an adequate vision to justify the risk of putting astronauts into space," Logsdon says. The board recommended a re-examination of NASA's entire rationale for human spaceflight.

In the late summer of 2003, NASA and the White House began to speak in earnest about the future. The administrator at the time, Sean O'Keefe, was promoting an ambitious programme that would have kept the space shuttle flying until they were ready to go to the Moon, according to Glen Asner, a historian at NASA. But John Marburger, the president's science adviser, and the White House Office of Management and Budget wanted a more conservative programme that focused on robotic

missions to the Moon and Mars and on human missions to the Moon. The debate ended in compromise: an aspirational nod towards Mars in the unspecified future, a near-term focus on the Moon in the 2010s, no more shuttle by the end of this decade. "I don't think anybody got everything they were looking for," Asner says.

A giant leap

When finally given voice, though, the vision's call to "extend human presence across the Solar System" certainly sounded satisfactorily sweeping in scope. "In the past 30 years, no human being has set foot on another world," Bush told a crowd at NASA's headquarters in Washington DC. "It is time for America to take the next steps." The crowd and almost everyone else familiar with NASA greeted the announcement enthusiastically, if only because the status quo had grown increasingly intolerable. "NASA has been lacking a compelling vision for decades," says Keith Cowing, a former employee of NASA and co-author of *New Moon Rising*, a book about NASA's renewed plans for exploration. Before the vision, he says, "You could ask ten people what the goal of the agency was and you would get twelve answers." Now, NASA once again had a single purpose.

NASA: M. GARCIA/REUTERS/CORBIS

"The key word in the current vision has to be sustainability."

— Jeffrey Hoffman



Two Columbias: the iconic Apollo moonship (below) and the ill-fated shuttle.



So far, so Apollo. But Bush made it clear that the vision was not going to involve an Apollo-era surge in NASA's budgets. The billions needed to complete the vision, it is claimed, will be the billions 'saved' by not flying the shuttle and not spending on the space station. The budget for the vision will thus increase slowly, in synch with the decline of the existing programmes. The agency hopes to have its new 'crew exploration vehicle', the capsule called Orion, and the Ares-I rocket on which it will ride to orbit ready by 2014. By 2020, it hopes to have built a lunar lander, and another, larger rocket, allowing missions to the surface of the Moon.

Keeping up appearances

The slow pace of the programme was, at the time, reflected in the president's budget, which initially recommended a modest 7% increase over five years for the US\$15-billion agency, but which didn't envisage an actual landing for 15 years or so. By contrast, Project Apollo went from a standing start to the Moon's Sea of Tranquillity in under a decade, but ramped up the NASA budget by 300% in the process.

This modest approach is the new way to do business at NASA. "The key word in the current vision has to be sustainability," says

Jeffrey Hoffman, professor of engineering at Massachusetts Institute of Technology (MIT) in Cambridge, and a former astronaut. Unlike Apollo, which spent enormous sums on a short-term programme to reach the Moon, the vision is supposed to be a sustained effort that will guide NASA well into the twenty-first century while not breaking the bank.

Perhaps no one element of the vision illustrates NASA's change in strategy better than its replacement for the space shuttle. In the 1980s and 1990s, the agency toyed with various ideas for follow-on crafts that might fly into orbit unaided by booster rockets. Billions were spent, only to demonstrate that many more billions would be needed to build something that actually worked: a single-stage-to-orbit spacecraft is a very difficult proposition.

This time, says Scott Horowitz, who is in charge of developing Orion, "We're not depending on any technological miracles. It is a much more reasonable programme." The Orion capsule eschews wings and advanced propulsion, and depends entirely on disposable booster rockets. The result is not just

operationally similar to Apollo's conical capsule on a cylindrical service module: it is essentially an enlarged carbon-copy that uses specific similarities to cut down the need for expensive novelty. The Ares-I rocket on which it will sit uses a solid-rocket booster just like the shuttle's as its first stage and an Apollo-era J-2 engine to power its second. The crew-escape system, which is also based on an Apollo-era system, can rapidly lift the capsule from the rocket if something goes wrong, making this a safer vehicle than the shuttle, at least during the launch.

Prudence is also guiding the agency's strategic planning, which now operates under what Dale describes as a "go-as-you-can-afford-to-pay approach", taking exploration forward in modest increments. After developing the Orion, which will cut its teeth taking crews to and from the space station, the programme will construct a lunar lander and a new heavy rocket — called Ares V — which will combine solid rockets and J-2 engines to deliver 130 tonnes of payload to Earth orbit, as opposed to Ares I's 25 tonnes. That's enough to launch both the lunar lander and the engine needed to take Orion and its

"I would give Bush an 'A' for vision and a 'C-' for follow-through."
— Keith Cowing

Along for the ride?

NASA officials say that they don't want to go back to the Moon alone; they hope to get some help from international partners.

The space agency has already decided to take the lead in building the rockets, capsules and landers needed to get to the Moon's surface. But NASA hopes that it can get other contributions from foreign powers — perhaps a lunar rover or a module for the planned Moon base. "We're working with our international partners to figure out where they want to play in terms of exploration," says Shana Dale, the agency's deputy administrator.

Although NASA has started consulting with allies from around the world as part of its Global Exploration Strategy, not everyone is convinced by its overtures. "I personally feel a little bit disappointed," says Jean-Michel Desobeau of Arianespace, based in Paris. As an executive at Europe's largest commercial launch company, Desobeau thinks that NASA's decision to exclude foreign powers from its

high-profile rocket- and capsule-development programmes may lead to resentment among these countries. "Europe, Russia and China want to be more than just a subcontractor," he says.

An even greater political obstacle orbits high above Earth. The International Space Station — the centrepiece of European, Russian and Japanese human spaceflight programmes — is still waiting for key modules to be delivered. NASA has committed to finishing the space station by 2010, but intends to bring its involvement to an end after 2016, allowing it to focus its resources on the Moon. Keeping the space station supplied and ferrying crews back and forth will be a significant challenge to the remaining partners, of which only Russia has the capacity to fly humans into space.

The prospective American withdrawal has led to some wringing their hands, and could make other countries hesitant to join yet another NASA-led project.

It will take a little diplomacy to move the vision, says Roger



Approaching from afar: how long will Orion visit the space station?

LOCKHEED MARTIN CORP.

Blandford of Stanford University in California. Blandford believes that, just like modern particle accelerators and fusion machines, a programme as ambitious as

the vision requires collaboration. "Everybody has to band together," he says. "The only way that any of this makes sense economically is as a global enterprise." **G.B.**



Eyes up: will telescopes on the Moon live out the legacy of the Hubble telescope (inset)?

accompanying lander from orbit round the Earth to orbit round the Moon. The difference from the 1960's approach is that Apollo launched its lander and command modules on a single Saturn V rocket; by launching Orion on one rocket and the lunar lander and transfer stage on a second, then having them dock in Earth orbit, the vision architecture allows larger crews and payloads.

Short breaks

At first, astronauts will use the lander/Orion combo for week-long trips to the Moon of the sort undertaken by the later Apollo missions. Gradually, the agency will build up resources for a permanently occupied base at one of the Moon's poles that will be visited by mission after mission. It is hoped that the outpost will give engineers experience in supporting humans on other worlds, eventually paving the way for a much more ambitious expedition to the surface of Mars. Rather than setting hard dates for completing each stage of the vision, NASA will adjust its plans to match each year's budget.

The vision's fiscal conservatism helped it win the imprimatur of Congress, which passed legislation to support it in 2005. But not all of its money-saving strategies have been popular with lawmakers. In August, NASA administrator Michael Griffin, who replaced O'Keefe in 2005, awarded the crew capsule contract to Lockheed Martin in Bethesda, Maryland, before the design had been reviewed fully. The move, says Horowitz, helped to cut costs by allowing NASA to fund one development team, rather than working with a pair of competing designs. But awarding a contract

before the final design and cost had been fully assessed drew criticism. "Congress has to keep a keen and constant eye on the project," warned Sherwood Boehlert, the former Republican chair of the House of Representatives Science and Technology Committee in a hearing last September. "Neither the agency nor the nation can afford another space station — a project that, for all its technical magnificence, has seen its costs balloon while its capabilities shrank to near the vanishing point."

Already the agency is facing some tough financial choices. The 7% over five years that President Bush spoke of did not end up in his budgets; in the White House's budget request for fiscal year 2007, produced last January, NASA's budget was kept essentially flat. "I would give Bush an 'A' for vision and a 'C-' for follow-through," Cowing says. And Congress, which has the final say, has allowed the agency less than the president asked for every year since the vision was first proposed. Adding to its woes have been the unexpected hundreds of millions of dollars

spent on returning the shuttle to flight and repairs to facilities damaged by 2005's Hurricane Katrina. NASA also has a service mission to the Hubble Space Telescope back on the books, with all its attendant costs. And this year, a breakdown in the congressional budget process is likely to leave the agency about half-a-billion dollars short of where it wanted to be (see *Nature* 445, 130; 2007).

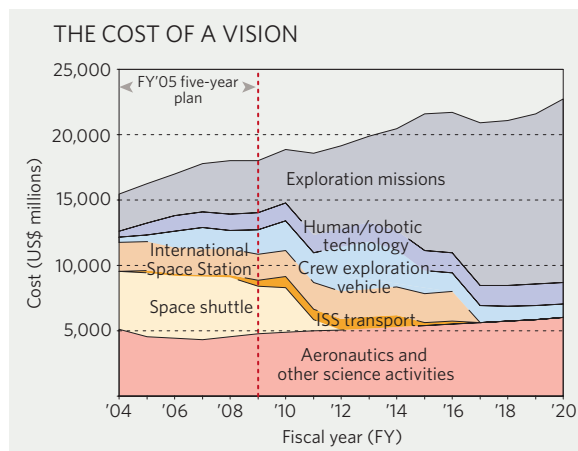
Chopping and changing

To offset a lack of overall growth in NASA's funding, the president's budget for 2007 called for its astrobiology programmes to be slashed by 50% and for an 18% cut in its \$854-million aeronautics budget. Several Earth-observing satellites, notably the Global Precipitation Mission, have been delayed. Longed-for science flagships such as missions to obtain samples from the surface of Mars and to study Earth-like planets around nearby stars have been deferred indefinitely. Friedman argues that similarly inspiring science missions, such as the Hubble telescope and the Mars Exploration Rovers, have been the bedrock of public support for NASA. Cancelling their natural heirs, he says, will erode enthusiasm for space: "You can't maintain public support on just a rocket programme."

Horowitz counters that the exploration programme will open up new areas of research to scientists, especially on the surface of the Moon. Plans call for astronauts to be able to access to any part of the Moon that scientists might want to visit, and NASA is holding workshops to find out the sorts of projects they might want to do there. The bottom line, he says, is that the exploration will fund science "even though you don't see it in dollars in the science budget line".

And some scientists are enthused about the prospect of getting to work on the lunar surface. "There's a lot that we didn't learn about the Moon from the Apollo missions," says Paul Spudis, a geologist at Johns Hopkins University's Applied Physics Laboratory in Laurel, Maryland. Although models show that the Moon was probably formed by Earth's collision with another body the size of Mars, many details about this originating cataclysm remain unknown. Studying materials near the base of the Moon and comparing that information with remote sensing data from all around it will teach scientists a great deal about the specific circumstances surrounding the Moon's creation and evolution.

But most researchers, including some who are enthused by lunar exploration,



SOURCE: NASA



Rocket science: the Ares-I rocket (left) evokes designs from the Apollo era (right).

NASA/NASD/MSC

are deeply sceptical of claims that it offers a worthwhile scientific return. They think that science is being used to lend more legitimacy to a vision that has little chance of producing scientific breakthroughs. These fears are based in part on past experience with the space station, according to Roger Blandford, director of the Kavli Institute for Particle Astrophysics and Cosmology at Stanford University in California. During the planning of the station, scientists were asked to suggest a research agenda. Even if it had been carried out, that agenda could hardly have justified the \$25.7-billion programme (a sum that doesn't take into account the related shuttle flights). As it turned out, only a fraction of that science got done. Now many wonder whether signing on to a mission to the Moon will produce similar results. "There are obviously things one can do," says Blandford, referring to plans for Moon-based telescopes and other instruments, "But as a practical matter, an awful lot of space science is better off not on the Moon."

So far, the vision has been relatively impervious to the scepticism of scientists. A contract for the first stage of Ares I is expected to be awarded in February, following on from the \$3.9-billion contract to design and build Orion signed with Lockheed Martin last August. And the agency

is also eyeing up contracts for a heavy-lift vehicle and a next-generation lunar lander. "I think things are going great," Dale says.

It is possible, though, that the new Democratic Congress will be less sanguine than NASA, or its Republican predecessor. The vision should not "simply shuffle money from NASA's other core missions", says Tennessee Democrat Bart Gordon, who chairs the House Committee on Science and Technology. He and his colleagues are also sceptical of the pay-as-you-go philosophy, which avoids making long-term budget projections of the total cost of the future missions. "I don't think Congress is going to be very tolerant of avoidable overruns," Gordon says.

Congress and observers elsewhere agree that, in the short term, there is no real alternative to the vision, inasmuch as grounding the shuttle for good means that another system has to be developed that is relatively cheap to put people into space. "I don't think this country will ever turn its back on having a human spaceflight capability," says Dale. But the need to develop Orion to keep America aloft will not necessarily translate into the ambitious Moon-base strategy, let alone a renewed push

to Mars. As Gordon says, "If it's not a priority — and the president has made very few statements about it since he announced it three years ago — it's going to be difficult to convince future administrations and congresses to sustain it in its current form."

Public eye

For the vision to become a priority — rather than just a new and safer way of keeping NASA and its contractors ticking over — it needs to excite people. And it is here that some observers feel that NASA has erred too far on the side of practicality, producing a near-pedestrian plan that looks no further than the already-explored Moon. "In order to sustain the vision, you have to think big-picture, long-haul sorts of things," he says, his mind's eye clearly on Mars. "NASA isn't doing that, and until they do, they run the risk of having the vision taken away from them."

Cowing sees a real possibility that the vision could be truncated to simply create a space capsule that can travel to and from the space station.

Dale, however, thinks that the vision is powerful enough to capture the public imagination. NASA is now working out a strategy to communicate it more effectively to the public. "I think when we start to talk about it a little more with the American public and Congress, they will feel the same kind of excitement about it that we feel," she says. Why the agency has seen fit to wait three years before starting to talk the

public into excitement is not clear; maybe they are reluctant to drum up support when everything is still on paper.

Standing beneath the original Apollo 11 capsule, it seems as if Dale might be right. When John Kalman learns of NASA's new plans, his nine-year-old

face lights up. "I want to be an astronaut!" he declares excitedly.

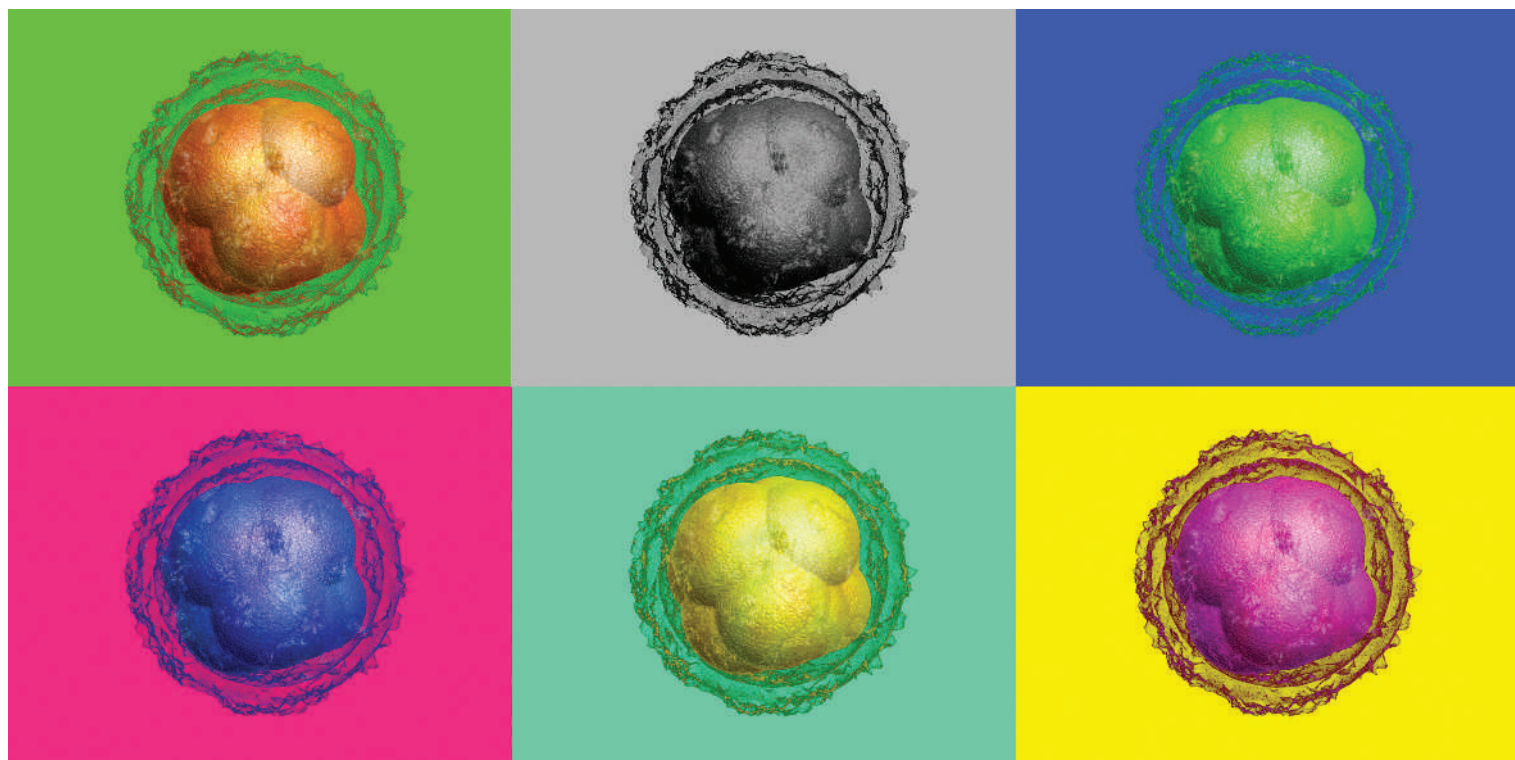
But Aunt Janet, who was just a year older than John when Neil Armstrong first set foot on the Moon, seems more perplexed than impressed. "So they're recreating that whole mission?" she asks while staring thoughtfully at the old command module. Then she shakes her head. "We need to explore other places," she says. "We've already done that."

Geoff Brumfiel is *Nature's* physical sciences correspondent in Washington DC.

See Editorial, page 459.

"In order to sustain the vision, you have to think big-picture, long-haul sorts of things."

— Bart Gordon



THE FIRST CUT

Extracting a cell from a budding human embryo can expose genetic defects, but does it actually help generate more healthy babies? **Bruce Goldman** investigates.

Suppose that one-eighth of you suddenly disappeared — but that within a few hours, your missing parts grew back and life carried on with no obvious sign of harm. Apart from wondering why it happened, you might worry whether your new body parts are proper replacements for the old. Is there something indefinable missing?

This year, more than 1,000 human embryos will begin their lives with just such a loss — and exactly the same nagging doubts will surround them. During a procedure called preimplantation genetic diagnosis (PGD), one cell is teased from the eight or so that comprise a three-day-old embryo. It is analysed for genetic abnormalities as an adjunct to *in vitro* fertilization (IVF). The results are meant to help doctors decide which embryos are free of genetic defects and should be placed in the mother's uterus.

PGD was first reported in 1990 for identifying and screening out male embryos that might carry a sex-linked disorder¹. Since then, its popularity has risen on the coat-tails of IVF. An informal reporting system in Europe, which represents some two-thirds of all PGD activity in the continent, shows a jump from PGD tests in 131 IVF cycles in 1999 to 2,984 in 2003 (ref. 2).

The goal of PGD is to foster life not interfere with it — but a number of researchers and clinicians find its soaring popularity unset-

ling. Many are concerned that a lot of PGD is being done for little benefit, because it may not boost the number of healthy babies. And some question whether removing a single cell — once assumed to be a harmless procedure — might subtly impair an embryo or the long-term health of the resulting children.

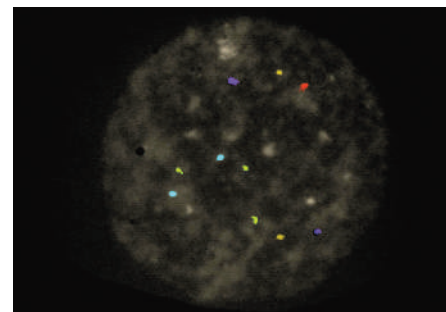
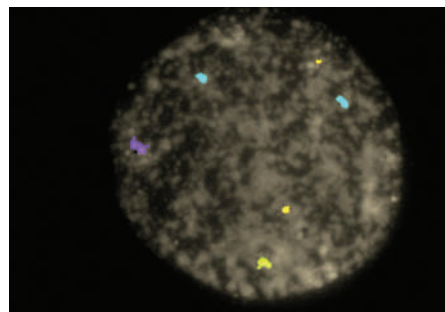
Health check

For prospective parents who could pass on a genetic condition such as cystic fibrosis, PGD has proved priceless. The only alternative to PGD would be to test several weeks into a pregnancy and, if positive, make the difficult choice of whether or not to abort the fetus.

But PGD has another, more controversial use: screening embryos for abnormal chromosome

counts, or aneuploidy. The number of a woman's eggs carrying such defects rises rapidly with advancing age, and embryos with these faulty chromosomes are thought to be more likely to miscarry or produce babies with birth defects. Using aneuploidy screening in IVF should reduce the miscarriage rate and enable doctors to transfer fewer and healthier embryos into the uterus, improving pregnancy rates and cutting multiple births. Roughly two-thirds of more than several thousand PGD procedures in the United States are for aneuploidy screening³, as are well over half in Europe².

There is good evidence that such screening can reduce the proportion of pregnancies lost in women who suffer from recurrent miscarriage — one study⁴ showed a drop from 87%



Normal (left) versus abnormal: PGD can identify extra chromosomes (green) in embryonic cells.

C. DARKIN

R. SCOTT

to 17% using the technique. But there is now intense debate about whether it helps increase the number of IVF attempts that go on to produce a 'take-home' baby.

One of the strongest advocates for routine aneuploidy screening is Yuri Verlinsky, director of the Reproductive Genetics Institute in Chicago. "In the near future I hope all IVF will be done with PGD," he says. Verlinsky points to one of his own studies, in which his team compared what happened to hundreds of IVF recipients before and after undergoing aneuploidy screening. He found that with PGD the miscarriage rate fell from 68% to 28%, and the number who ended up with babies increased⁵.

But other experts are critical of this and similar studies because the women were not randomly assigned to screening. And as there is no ongoing system for collecting PGD outcomes across the United States, "all the reporting is by individual laboratories publishing their own results", says Susannah Baruch, director of reproductive genetics at the Genetics and Public Policy Center (GPPC) in Washington DC. "They're really picking and choosing who they're looking at and what they're writing about."

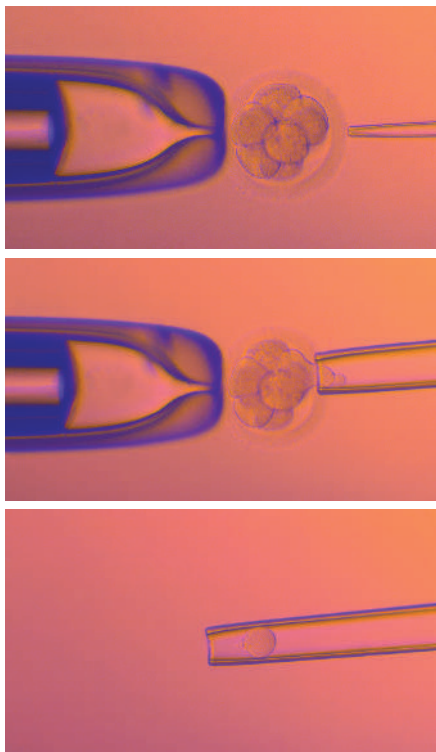
Babes in arms

In one Belgian study done with rigorous controls, women aged 37 or older were randomly assigned to receive aneuploidy screening during IVF. The women who had PGD gave birth to slightly fewer babies than the control group⁶, a similar finding to many other studies. "There's a lot of controversy in the field as to how PGD should be appropriately applied," says Catherine Racowsky, director of the IVF lab at Brigham and Women's Hospital, Boston, Massachusetts. "It doesn't seem to be very helpful in improving overall pregnancy rates."

One reason is that older women produce only a limited number of eggs during IVF. Many of these generate the chromosomally faulty embryos that are identified and discarded after PGD, so there are few embryos left for use in each IVF cycle. The embryos that remain after PGD may be more likely to implant and produce a pregnancy, but this does not seem to compensate for the reduced number of embryos transferred.

Another problem is that some perfectly good embryos may be getting thrown out. In the past few years, embryologists have realized that as many as half of all human embryos exhibit 'mosaicism', in which the embryo is a patchwork of chromosomally normal and abnormal cells. The cell selected for PGD may have a different chromosome tally from the rest.

Recent studies have also suggested that these mosaic embryos tend to self-correct, or eliminate cells with aberrant chromosomes, notes Richard Scott of Reproductive Medicine Associates in West Orange, New Jersey. When Scott's lab took embryos that were abnormal on the third day of development and tested them



On test: a single cell is extracted from an eight-cell embryo for PGD.

again on day five, the researchers could no longer identify the abnormality in one-third of the embryos. So many embryos identified and eliminated using PGD would, quite possibly, develop as normal, another reason why PGD does not dramatically boost pregnancy rates.

"We're probably overcalling the number of faulty embryos," says Robert Jansen, managing and medical director of Sydney IVF, which does close to half of all the PGD in Australia. "The risk, in an older woman, is that so many of her embryos are likely to screen as abnormal that all will be rejected, when one or more of them, if transferred, might have produced a healthy baby." Jansen and the directors of other fertility clinics have been cutting back on aneuploidy screening, and both the American Society for Reproductive Medicine and the European Society of Human Reproduction and Embryology (ESHRE) are debating the technique's validity.

There is another concern clouding the use of PGD — the question of whether it is truly harmless. The traditional view among embryologists is that the first few cells of mammalian embryos are essentially equivalent: remove one or two, and the rest can ably fill the gap. But some recent studies have challenged that idea, and many now believe that even these early cells are predisposed to contribute in different ways to future tissues.

Earlier this year, Magdalena Zernicka-Goetz of the University of Cambridge, UK, and her colleagues established how four genetically identical embryonic cells acquire their own character⁷. Working with mouse embryos, she

showed that the DNA packaging proteins called histones, which help control gene expression, have different levels of specific chemical tags in each cell — and that changing these tags changes the type of embryonic tissues to which that cell contributes.

Studies such as this raise questions about whether removing a cell during PGD leaves a molecular mark on the embryo that somehow affects its ability to develop, or affects the child's long-term health. "I would be very, very surprised if implantation rates overall were not compromised by the removal of a cell from the embryo," Racowsky says, perhaps because the removal has a metabolic cost that compromises its development.

A question of balance

And there the matter sits. Thousands of PGD babies have already been born without any obvious problems. But the oldest of these babies are just teenagers — and rare or subtle effects of the procedure, if they exist, may not become apparent until researchers collect together many more cases and until these children reach middle age or beyond.

Many PGD experts acknowledge the need for a large effort to collect data on the number and health of children born after PGD. In 2005, the GPPC convened a working group of reproductive endocrinologists, IVF doctors and PGD providers in the United States to discuss a voluntary data-collection system. "We're optimistic that it will be up and running within the next year or so," says Baruch. ESHRE already collects information on babies born after PGD and is in the process of setting up a study to follow these babies in more detail.

Meanwhile, patients are left in a quandary about whether the small, unproven risks are worth taking. To avoid having a child with a severe genetic disease, it is probably well worth undergoing PGD; but for aneuploidy screening the decision is less clear. At the very least, experts say, practitioners should spell out the risks and benefits of the procedure to would-be parents (and many already do just that).

Some researchers are seeking ways round the problem by trying to identify genetically abnormal embryos in less invasive ways, such as detecting secreted molecules or testing cells destined to become part of the placenta. "My view is that the less one perturbs an embryo, the better," says Racowsky. "We really do not know yet whether we're doing any harm in removing cells from early embryos."

Bruce Goldman is a science writer based in San Francisco.

- Handyside, A. H., Kontogianni, E. H., Hardy, K. & Winston, R. M. L. *Nature* **344**, 768–770 (1990).
- Sermon, K. D. et al. *Hum. Reprod.* **22**, 323–336 (2007).
- Baruch, S., Kaufman, D. & Hudson, K. L. *Fertil. Steril.* doi:10.1016/j.fertnstert.2006.09.003 (2006).
- Munné, S. et al. *Fertil. Steril.* **84**, 331–335 (2005).
- Verlinsky, Y. et al. *Reprod. BioMed. Online* **11**, 219–225 (2005).
- Staessen, C. et al. *Hum. Reprod.* **19**, 2849–2858 (2004).
- Torres-Padilla, M.-E., Parfitt, D.-E., Kouzarides, T. & Zernicka-Goetz, M. *Nature* **445**, 214–218 (2007).

P. GOETZ-HELICK/SPL

Ground force

Is parachuting into the Amazonian jungle any way to save an ecosystem? One team of biologists thinks so. **Thomas Hayden** joined them on a trip to Peru to find out what they do.

It's dark on the forest floor, the air humid and still. Various birds startle at an intruder's passing — plump brown tinamous and large bush turkeys or curassows, squawking in protest. Further along the trail, prehistoric-looking hoatzins flap and yodel above an oxbow lake, the blue patches on their cheeks bright in the late-afternoon sun. Suddenly, the air is alive with activity — a small band of Goeldi's marmosets, among the rarest of the New World primates, is alarmed by approaching visitors and unsure which way to flee. The tiny, jet-black monkeys leap from tree to tree, almost buzzing with fluffy, comical charm as they swarm to safety. "Perfect," Peruvian ornithologist Christian Albuja exhales into the silence they leave behind.

The upper Amazonian region of Sierra del Divisor — almost 1.5 million hectares of highland forest along Peru's border with Brazil — is full of similar delights. But decades of aggressive economic development throughout the Amazon basin have made such vast stretches of contiguous forest increasingly rare — and increasingly threatened. Although Divisor also faces pressure from development, it is still substantially pristine, protected thus far by its remoteness and elevation.

Albuja is here to help survey the area's flora and fauna in an expedition organized by the Field Museum of Natural History in Chicago, Illinois. It would take years of meticulous fieldwork to fully document the region's rich biodiversity, but the group of 13 Peruvian, Brazilian and American scientists will spend just three weeks on the ground. This is a rapid biological inventory (RBI), the Field Museum's version of an increasingly popular tool in conservation science — a quick, intensive taxonomic expedition designed to identify areas of particular biological, geological and cultural significance before development and exploitation take hold.

Fast and furious

The idea is simple. With funds, expertise and time too limited to conduct thorough species surveys of every unknown region, experts instead target the most promising areas and quickly assess whether they are worthy of conservation. Proponents admit that the resulting data are incomplete, but say the compromise is



Christian Albuja gathers data on biodiversity to help build a case for preserving areas of Peru's jungles.

justified because rough estimates of biodiversity can help inform preservation decisions. And even a quick survey by scientists with decades of broad experience in the field and in museum collections can lead to qualitative estimates of an area's relative conservation value. "We would all love to spend more time," says Debra Moskovits, a tropical biologist at the museum and founder of its RBI initiative. "But the time pressure is intense. If we can protect some of these areas, then maybe people will be able to do the more extensive studies the areas deserve."

The protected areas on a list maintained by the United Nations have grown to some 11.5% of the planet's land surface in recent years¹, but 'gap analysis' studies show that large numbers of species are not represented in the existing network². Conservationists have argued for decades about how best to prioritize areas for future conservation: whether by geographical

location and political expediency, or through some measure of species numbers, degrees of species interconnectedness, or the presence of rare, threatened or keystone organisms.

The Field Museum team has focused its attention on the high-biodiversity upper Amazon and Andean foothills regions of Ecuador, Peru and Bolivia. Working with local, regional and international scientists and conservation groups, members of the core group of five museum biologists have conducted 12 rapid inventories in these regions since 1999, representing 9.2 million hectares of surveyed land — an area about the size of the US state of Maine. Preliminary results are shared immediately with local communities, organizations and political leaders; formal reports are usually published in a matter of months. "People are making land-use decisions all the time, and they can't protect places if they don't know any-

T. HAYDEN

thing about them,” says Corine Vriesendorp, a conservation ecologist and the Field Museum’s director for rapid inventories. “If you bring in a crack team of biologists, you can very quickly tell decision makers whether a place is special or not.” And it can be done relatively inexpensively — a typical, foundation-funded RBI costs about US\$300,000 from initial planning through to the final published report.

Six new protected areas have already been established, comprising about half of the territory the team has surveyed. Most of the remaining land is also on the road to legal protection.

Preservation order

The survey information can also help local communities and governments prioritize specific zones within a surveyed area, identifying those that most urgently need full protection, and those that might be allocated for uses such as tourism and sustainable harvesting. “People overlook the impact that these kinds of survey can have on building local capacity for conservation,” notes tropical land use specialist Arturo Sanchez-Azofeifa of the University of Alberta in Canada, who is not involved in the programme. “You can get local participation and a broader perspective, and that really helps build expertise and interest in the local communities.”

For the Field Museum team, that means working with local scientists and graduate students to compile the inventories, and forming links with indigenous groups, regional and national governments, and local conservation organizations. The biological work is paralleled by ‘social inventories’ — surveys of the organizational structure and natural resource use of local villages. That social aspect, says Vriesendorp, sets RBIs apart from other rapid conservation



assessments and is crucial to their success. “The dream is to protect these areas indefinitely,” she says, “and that can only happen if the local people and their leaders are fully engaged.”

The core of the RBI approach is the rapid inventory itself. The surveys have their roots in a 1987 birding trip, when physicist and avid birder Murray Gell-Mann and ornithologist Ted Parker first started talking about using quick-time biological surveys to spur conservation. By 1990, environmental group Conservation International, based in Washington DC, had put their ideas into practise; Moskovits and other Field Museum team members, including botanist Robin Foster and ornithologists Doug Stotz and Tom Schulenberg, were all early participants. The idea caught on with other groups, and by 1995 the Field Museum had initiated its own rapid inventory programme, spearheaded by Moskovits.

Each inventory starts with satellite images, geological maps and, if possible, video footage taken from the air. Experience has taught that the taxonomists’ time is better spent walking trails than wielding machetes to create them. The RBI scientists identify areas they think will give them a broad cross-section of the available habitats, and advance teams of local workers prepare bush camps and cut trails to their specifications.

In Sierra del Divisor, that means three separate campsites: two at higher elevations, one along a lowland riverbank, and each with a network of trails stretching for dozens of kilometres along streams, through swamps and up mountains. The museum biologists are joined by nine scientists and students from Peru and Brazil. “We try to balance the teams to get broad experience across the region, as well as local expertise,” Vriesendorp says. The inventory focuses on limited taxa — trees, shrubs, mammals, birds, fish, reptiles and amphibians — to keep the workload manageable, and seeks to determine “what’s common, what’s rare, what’s dominant and what’s really weird”, says Vriesendorp. The scientists tabulate individual species of plant and animal, and draw on experience to gauge the relative health, uniqueness and diversity of each ecosystem. The social inventory team, meanwhile, conducts its own surveys to map out the location and structure of local human populations, including the potential for and threats to long-term conservation.

Jungle manoeuvres

The survey site is spectacular. Sierra del Divisor contains the only mountain range in the Peruvian Amazon, a series of low sandstone ridges and weathered volcanic cones with peaks of up to 800 metres high. The resulting series of ‘elevation islands’ supports a stunted forest ecosystem and, combined with a cool wind from the south, provides the unexpected experience of shivering from cold in the middle of the Amazon. Even close to the Equator, seasonal variations in temperature and rainfall affect the forest’s plants and animals, presenting challenges to conducting a survey in a single season.

The dry August conditions are ideal for the fish team — lakes and wetlands have shrunk, leaving their quarry restricted to small ponds. But many trees are without the flowers and fruit that botanists often need to make species-level identifications. Seasonal variations make work even harder for the group studying amphibians. “In the wet season, the trees would be screaming with frogs,” says Moisés Barbosa da Souza of the Federal University of Acre, in Brazil. It’s the middle of the night, and the former jungle warfare specialist is halfway up a tree, working hard to retrieve an Amazon milk frog from a high-up bromeliad. But, he adds, “at this time of year just look what I have to do.”

The Sierra del Divisor RBI results³, published in December, include up to three dozen new species of plant, fish and amphibian, and many more species that are endemic to the area. The forests are also home to many endangered plants and animals, including valuable lumber trees and 20 threatened species of



“Jungle, lungs of the planet”, reads this sign in Pucallpa against a backdrop of wood-smoke smog from slash-and-burn fields.



Out on a limb: numerous species, such as this monkey frog, are threatened by economic development.

mammal, several of which are hunted for bush meat. Schulenberg lured the Acre antshrike — a species of bird previously known from a single ridge on the Brazilian side of the border — out from the stunted ridge-top forests by playing its call on an iPod. And, on one occasion, Moskovits returned to the riverside camp energized, despite hours tramping through an aguajal palm swamp, by the sight of some 30 red uakaris. These monkeys are large, with bald red faces and orange fur, and extremely rare. A total of 12 species of monkey and marmoset was observed at the camp, one of the highest primate diversities documented at a single site in the New World.

Sierra del Divisor has been teetering between protection and development for most of the past decade, but the August 2005 RBI survey and follow-up meetings may have been enough to tip the balance. In April 2006, the Peruvian government declared the entire 1.48-million-hectare area a reserved zone, a preliminary classification that halts all development until the permanent protection status can be determined. However, petroleum exploration leases are still being granted within the protected area, leaving the ultimate fate of the forest and its inhabitants in question. The hope, says Moskovits, is for an area co-managed by conservation groups and indigenous organizations, with strict protection for unique biological and geological resources and for the indigenous groups living in voluntary isolation within its borders. The RBI team remains deeply involved with the planning process, Moskovits says, but it will be up to Peruvians to hammer out the final compromises.

Despite its obvious impact on conservation decisions, there has been debate about the scientific value of rapid assessment data. “We do get criticized — some people say our work isn’t scientific because it’s done so fast,” says Foster, the team’s most experienced member. “People feel that you have to do a quadrant plot and measure each tree to within a millimetre. But for this purpose it’s much better science to sample quick and dirty over several larger areas.”

A one-hectare plot, for example, may contain just a few mature trees, Foster says, “but those canopy trees account for most of the production, most of the insects, most of the fruits that are good for birds, monkeys or peccaries. If you just study your quadrant, you’ll miss the forest for the trees.”

Yet with any short-term study “you’ll get true presences but you can’t know whether the absences are definitive,” says ecologist Michael Willig of the University of Connecticut. “So you’ll almost certainly be underestimating biodiversity.” Given the realities of limited funding and expertise, however, Willig says that rapid assessments are a valuable tool not just for conserving biodiversity, but for understanding it, too. Ultimately, he says, “you just have to respect the limitations of the data.”

It doesn’t take much to see that, even in an area as remote as Sierra del Divisor, the threats are manifold. Although large-scale exploitation has not yet reached Divisor, gas, mining and logging leases overlap with much of the

new reserved zone, and unregulated settlers push closer to the area every day. Seen from a helicopter, the intact forest canopy is breathtaking, with brightly coloured parrots and toucans darting between giant trees. But gaps soon appear in the undulating surface where giant mahogany and tornillo trees have been felled for lumber, and wood smoke billows up from the proliferating slash and burn fields below.

In Pucallpa, a sprawling regional capital along the Ucayali River less than 100 kilometres from Sierra del Divisor, thick smoke often closes the municipal airport for days. The town’s only green space — a strip down the centre of a main road — boasts a sign whose translation reads, “jungle, lungs of the planet.”

Trading standards

Down by the river, settlers pour in from around the region in low-slung wooden boats laden with fish, skins and produce, some of it harvested from near the reserved zone’s boundaries. Downtown, traders display hundreds of peccary and deer hides. One proprietor refuses photographs; another proudly directs a browser to the real prizes — contraband skins of ocelots and other wild cats, barely concealed behind his front door. At the main market, several hundred stalls sell everything from wild palm fruits and desiccated bushmeat to medicinal saps. There are species that have already disappeared from more heavily populated regions of the Amazon, including various fishes as well as tortoises and river turtles. Some of these have already been

butchered; others are propped up and immobile on their backs, and sold alongside plastic buckets of their pickled eggs.

There are wire cages packed tight with bright green parakeets and majestic ruff-necked macaws, but the most wretched pets for sale are the squirrel monkeys and saddle-back tamarins. They can be bought for less than US\$8 — inexpensive,

but evidence of the high cost to local fauna when humans intrude. “The forest still looks so large, people just don’t realize that this is going to be the end of these guys,” says Moskovits. “It’s repeated over and over, every day and in hundreds of places throughout the Amazon. It really has a huge impact, and it makes you worry, are we moving fast enough?”

Thomas Hayden is a science writer in San Francisco, California.

“We’re looking at what’s common, what’s rare, what’s dominant and what’s really weird.” — Corine Vriesendorp

1. Chape, S. *et al.* *United Nations List of Protected Areas* (IUCN/UNEP; 2003).
2. Rodrigues, A. S. L. *et al.* *Nature* **428**, 640–643 (2004).
3. The Field Museum. *Peru: Sierra del Divisor: Rapid Biological Inventories*, 17. (Univ. Chicago Press, Chicago, 2006).

Research on Tasmanian bones raises a number of ethical questions

SIR — Your News story about the repatriation of Tasmanian bones (“Aboriginal remains head for home” *Nature* **444**, 411; 2006) largely ignores the ethics of scientific investigation of these remains. It is my understanding that the Natural History Museum in London is to gather data on these samples before returning them, which is a good compromise in the controversial circumstances. However, it is difficult to agree that — as some researchers seem to suggest — the remains should stay in the museum’s possession indefinitely.

In modern science, for example in the field of medical research, we can proudly say that we strictly control the ethical aspects of our experiments, and do not carry out experiments on human samples obtained unethically or without permission. Not being a historian, I do not know the histories of the items in question. However, Tasmanian remains such as these were typically obtained without consent in circumstances that would now be considered unethical — including theft, grave-robbing and post-mortem mutilation (see Helen MacDonald *Human Remains: Dissection and its Histories* Yale Univ. Press, 2006).

These are not comparable to archaic remains found by archaeologists or palaeoanthropologists. Archaic remains are discovered in the course of science, not displaced at death and relocated to a site for investigation without permission from relatives. These Tasmanian remains are old, but they are not archaic.

Additionally, the scientific value of these remains is unclear. The quoted phrase “Who knows what kind of questions we could ask?” does not provide a solid enough reason for investigating human remains. Scientists have to be specific in order to avoid criticism. If some researchers consider this a blow, they have to change their mindset and find alternative avenues of investigation. Most medical scientists wouldn’t dream of carrying out experiments on human tissue that had been obtained unethically.

As for the issue of ownership, the burden of proof should be on the investigating scientists to show that their samples were obtained ethically, and that continuing investigation is warranted, rather than on descendants to prove ownership.

Is the suggestion that, if nobody can prove a genealogical link with the remains, then any course of investigation is warranted?

If only the Tasmanian Aborigines had been regarded with ethical consideration, they would not have been systematically exterminated. Science was not responsible for their deaths, of course, but we can derive

lessons from this sad history. Perhaps sometimes we have to learn to put ethics and humanity above our scientific curiosity.

Jason Coombes

Centre for Transplant and Renal Research,
University of Sydney at Westmead Millennium
Institute, Westmead, NSW 2145, Australia

Increased funding vital to competitiveness initiative

SIR — Your News story “Power shift stymies US science budget” (*Nature* **445**, 130–131; 2007) states that staff at the US National Institute of Standards and Technology (NIST) are “apparently not too disappointed” by the prospect of Congress passing a continuing resolution that would limit funding to fiscal year (FY) 2006 levels rather than providing the increase of more than 24% in the agency’s laboratory and facilities funding proposed by President Bush’s FY 2007 budget. You quote a NIST spokesman as saying: “Proposed budgets rarely come through as proposed, so there were no emotions here.”

This is not correct. NIST employees care deeply about their budget and these statements misrepresent the agency.

The initiatives proposed in the FY 2007 budget are essential to NIST’s ability to fulfil its mission and are critical to the overall success of the president’s American Competitiveness Initiative. A freeze in funding of NIST’s core programme at 2006 levels would slow progress in a wide range of important areas, including safely exploiting nanotechnologies in a vast range of applications from paints to medicines to electronics; developing the measurement infrastructure required to support hydrogen fuels; and advancing basic physics to realize quantum computing.

There are a number of different ways in which Congress can implement a continuing resolution. Our hope would be that NIST will be allowed to move forward on as many of these critical priorities as possible.

William Jeffrey

National Institute of Standards and Technology,
Gaithersburg, Maryland 20899-1070, USA

Five-point plan to revive and reform Indian science

SIR — To arrest the decline of Indian science, Prime Minister Manmohan Singh promises to double funding for science in the next five years, as you report on your News pages (*Nature* **445**, 134–135; 2007). But there is still a need to make Indian science more attractive to talented young people, in terms of professional opportunities and financial

incentives, free from academic feudalism.

Indian science has suffered a lot from an inward-looking crab mentality, a reluctance to share infrastructure, a disregard for scientific ethics, and the lack of a new generation of science leaders. Expensive instruments can be seen gathering dust in national institutes and universities, in the absence of coordinated planning. Mediocre bosses who grab credit from genuine researchers for their personal glorification are in no position to attract young talent to science. A system that rewards frivolous patents more than peer-reviewed publications has diluted its own quality.

Excessive pressure on scientists to generate income for their labs has forced researchers to deviate from their core competence to cater to the requirements of funding agencies. Self-financing courses have mushroomed, but they lack proper faculty and generate poorly educated graduates. This is good for statistics but bad for quality.

Singh’s warning that increased funding requires better quality science may arouse those who are conscientious and capable, while causing panic among those who do not deserve their high profile. It could pave the way for a science renaissance.

For this to happen, however, certain immediate measures need to be taken. Universities’ core infrastructure needs to be overhauled, with a primary focus on high-quality education. Synergy and collaboration must be promoted between national institutes and centres of excellence in the universities, free from bureaucratic obstacles. Project leaders must have total freedom from unnecessary red tape, in order to attract contract research and competitive grants. Only accomplished, mature scientists must be put in the leadership role of science managers. And a statutory model code of scientific values and ethics must be created.

U. C. Lavanian

Central Institute of Medicinal and Aromatic
Plants, Lucknow 226 015, India

All sizes of needle in that overcrowded haystack

SIR — The few lone top quarks that have been discovered are “60 needles in a pretty large haystack” according to your News in Brief story “Fermilab team finds top quark going solo” (*Nature* **444**, 983; 2006). Just a few pages further on, a Book Review tells us that the discovery of a body in the Kuiper Belt is “a classic case of finding a needle in a haystack” (“The beginning of wisdom” *Nature* **444**, 1006–1007; 2006). That sure is a good few orders of magnitude for a metaphor.

Neville W. Goodman

Department of Anaesthesia,
Southmead Hospital, Bristol BS10 5NB, UK

BOOKS & ARTS



F. WHITNEY/GETTY IMAGES

In the balance: the intensive use of pesticides has benefited agriculture but caused wider environmental damage.

For better or for worse

Science must be applied carefully if we are to reap the benefits but minimize the risks.

Times of Triumph, Times of Doubt: Science and the Battle for Public Trust
by Elof Axel Carlson

Cold Spring Harbor Laboratory Press:
2006. 227 pp. \$39

Ian Wilmut

Scientific research and the associated technical applications have transformed our lifespan and way of life, at least in the West. Public health has been enhanced greatly by good sanitation and by the provision of clean water and adequate food. Immunization and the use of antibiotics have banished diseases that just a few decades ago haunted our grandparents. Neonatal mortality has been dramatically reduced. The benefits arising from biomedicine alone are enormous, and other disciplines have also led to improvements, such as greater opportunities to travel and to communicate. So why do many people view science and innovations with anxiety and concern?

Elof Axel Carlson is a geneticist by training who has taught biology to non-science students for many years. In his thought-provoking book *Times of Triumph, Times of Doubt*, he asks why many of his young students who have turned away from careers in science feel that "science

has let them down through its bad outcomes". In making his analysis he includes in the scientific community not only researchers but also those responsible for the commercialization and regulation of science, such as business executives, ethicists, theologians, legislators, lawyers and journalists.

Carlson has selected a number of areas in which there has been either public controversy or actual harm associated with the application of scientific ideas, and considers how the unfortunate outcome arose, in the hope that the risk of similar outcomes might in future be reduced. He casts his net wide in selecting incidents from which science emerges with less than a perfect reputation. Some are very recent, whereas others began in the nineteenth century. They include eugenics, weapons of mass destruction (in particular the atomic bomb), pesticides, methods of assisted reproduction, and the oversight of procedures for the introduction of new medicines.

It may come as a surprise to many younger readers of this book to find that the scientific community is held responsible for the worst excesses of the Holocaust, but some of the ideas of genetic superiority had their origins in academic genetic research. By a nice twist

of history, one of the major centres of this activity was Cold Spring Harbor Laboratory, New York, where the publishers of this book are based. The laboratory is now distinguished for its research in molecular genetics. But in the early twentieth century, its director, Charles Davenport, developed policies for eugenic protection and the enhancement of our species. Europeans have no cause for complacency because other groups developed similar ideas in Britain, Sweden, Norway, Denmark, Finland and Switzerland. Germany may be the only country that systematically murdered its citizens, but in other countries people were sterilized without consent as a result of policies that had no sound scientific justification and would be judged ethically unacceptable today.

However, the misuse of pesticides seems to me to be a far more representative example of the way knowledge has been used without due care. The intensive use of chemicals that became available in large quantities after the Second World War made it possible for the first time to eliminate insects and weeds. There were medical benefits in some cases, for example in the control of malaria. However, the widespread and sometimes careless use of chemicals in agriculture and domestic

gardens damaged the ecosystem and put people's health at risk.

This danger was first made clear to the public by Rachel Carson in her book *Silent Spring* (Houghton Mifflin, 1962), in which she described the changes in the natural world brought about by the use of chemicals. Since then, in part as a result of Carson's book, there has been a very slow change in our priorities, although many people argue that much more needs to be done to restore an ecosystem in which humans and other species are in a stable relationship. In a few years it may seem obvious to everyone that our pollution of the atmosphere by the consumption of hydrocarbon energy sources was even more reckless than our use of pesticides.

The use of new knowledge, then, is a double-

edged sword. Pesticides led to real benefits, but their careless use was harmful. This is surely the situation in many cases, such as atomic energy and dynamite. It was even the case when a sharp stone was first stuck on a stick to make an axe that could be used to kill animals or chop sticks for firewood, or to kill people.

Carlson ends the book with the interesting suggestion that legal proceedings should be possible in cases of science or technology being misused. He draws on a comparison with the Wall Street crash in 1929, which led to greater regulation of the financial world. In some of the scientific cases he discusses, surely legal redress would already be available if inaccurate information was provided. However, this would not be the position at present if someone merely argued a case in a book or scientific

paper, as was the case in the development of eugenic policies.

Everyone in the scientific community has a responsibility to assess the value of our work realistically and to broadcast both the risks and the benefits, argues Carlson. In determining our attitude to scientific and technological advances, perhaps even more important than the effect of any failures is our tendency to take new things for granted very rapidly. Research has contributed a great deal to our way of life, and none of the sceptics would wish to go back even to the nineteenth century. But it can also do great harm. Let us have ambitious research, but cautious application. ■

Ian Wilmut is director of the Centre for Regenerative Medicine, University of Edinburgh, Edinburgh EH16 4JT, UK.

Painting the whole picture?

Visions of Nature: The Art and Science of Ernst Haeckel

by Olaf Breidbach

Prestel: 2006. 304 pp. \$100, £55

Philip Ball

When *Nature's* centenary issue of 1900 listed the most important scientists of the age, only one German biologist was included: Ernst Haeckel, professor of zoology at the University of Jena. Reckoned to have been instrumental to the introduction of darwinism to Germany, Haeckel has also inspired generations of scientists with his stunning drawings of the natural world. He is perhaps most widely known now as the author and illustrator of *Art Forms in Nature*, a series of plates published between 1899 and 1904 that showed the marvellous forms and symmetries of creatures ranging from radiolarians to antelopes.

Few scientists of his time were more complicated. He was the archetypal German Romantic, who toyed with the idea of becoming a landscape painter and venerated Goethe. He promoted a kind of historical determinism, akin to that of the philosopher G. W. F. Hegel, that sat uncomfortably with Darwin's pragmatic rule of contingency. Haeckel's view of evolution was a search for order, systematization and hierarchy that would reveal far more logic and purpose in life than a mere struggle for survival. His most famous scientific theory, the 'biogenetic law', which argued that organisms retrace evolutionary history as they develop from an egg ('ontogeny recapitulates phylogeny'), was an attempt to

extract such a unifying scheme from the natural world.

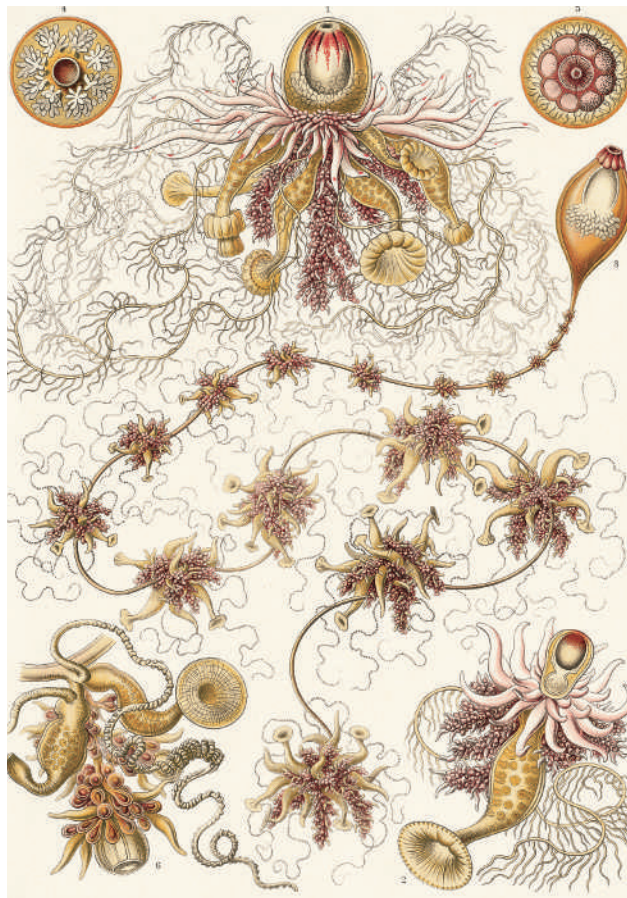
It can be argued that this kind of visionary mindset, with its strong preconceptions about how the world ought to be, does not serve science well. Haeckel supplies a case study in the collision between Romanticism and science, and that tension is played out in his illustrated works. This is something that Olaf Breidbach's

lovingly produced book *Visions of Nature* never really gets to grips with. Indeed, the book has a curiously nineteenth-century flavour itself, declining to grapple with the difficult aspects of Haeckel's life and work.

For example, historian Daniel Gasman and others have proposed that Ernst Haeckel's influence on German culture at the turn of the century was pernicious in its promotion of a 'scientific' racist ideology that fed directly into Nazism. However, Breidbach goes no further than to admit that Haeckel became a "biological chauvinist" during the First World War, and that "sometimes the tone of his writing was overtly racist". Breidbach admits that his book is not a biography as such, more an examination of Haeckel's visual heritage. Yet one could argue that Haeckel's dark side was as much a natural consequence of his world view as was *Art Forms in Nature*.

The claim that Haeckel doctored images to make them fit with his preconceived notions of biology is harder to ignore in this context. He was even accused of this in his own time, particularly by his rival Wilhelm His, and to my eye the evidence looks pretty strong (see *Nature* **410**, 144; 2001 and *Science* **277**, 1435; 1997). But Breidbach skates over this issue, alluding to the allegations only to suggest that the illustrations "instructed the reader how to interpret the shapes of nature properly".

On the whole, Breidbach simply explains Haeckel's reliance on image without assessing it. Haeckel's extraordinary drawings were not made to support his arguments about evolution and morphogenesis; rather, they actually were the arguments. He believed that these truths should be apparent not by analysing the images in depth but simply by



Ernst Haeckel's images portrayed his preconceived view of the world.

Drifting into art

Oil is derived from plankton, those drifting, microscopic organisms in oceans and lakes that so inspired nineteenth-century biologist Ernst Haeckel. In recognition and celebration of his work, the oil company Shell has sponsored this three-dimensional artwork by British fashion embroiderer Karen Nicol. Called *Out of the Blue into the Black*, it emerged from Nicol's observations of plankton at the School of Ocean Sciences at the University of Wales, Bangor.

The embroidery can be seen on 6–8 February as part of the exhibition 'Plankton in Art', which accompanies the American Society of Limnology and Oceanography meeting in Santa Fe, New Mexico.

The exhibition, which pays homage to Haeckel's illustrations, includes the extraordinary photography of Guido Mocafico, as well as items of jewellery, glass, wood carvings and quilting. It also features a video based on the patterns of movement of zooplankton in water, produced by Japanese scientist Ai Nihongi, accompanied by music from jazz musician Akira Sakata.

A rare treat will be the evening performances of the animated documentary *Proteus*, directed by David Lebrun. Named for the sea-god of Greek mythology, the documentary describes the conflicting scientific and romantic visions of the sea in the nineteenth century, using some cleverly animated illustrations from the period.

Proteus pivots around the story of Haeckel and includes fast-spinning sequences of hundreds of his images, each morphing convincingly into the next. But different threads are interspersed, reflecting the contradictory times in which Haeckel lived. The industrial revolution was blasting the romantic notion of nature while at the same time revealing the extent of its wonders. The film pits *The Rime of the Ancient Mariner* by Samuel Taylor Coleridge, for example, against the laying of the first transatlantic telegraphic cables. Broken cables hauled from the pristine deep sea beds revealed the teeming, plankton-rich life at depths previously assumed to be lifeless.

A. A.



K. NICOL/J. JONES

looking at them. "Seeing was understanding," as Breidbach writes. But if that's so, it places an immense burden of responsibility on the veracity of the images.

This is the nub of the matter. Breidbach suggests that Haeckel's drawings are schematic and that, like any illustrator, Haeckel prepared them to emphasize what we are meant to see. But of course, this means we see what Haeckel wants us to see. Quite aside from whether he hid any nascent appendages that challenged his biogenetic law, consider what this implies for the plates of *Art Forms in Nature*. They are some of the most beautiful illustrations ever made in natural history — but it seems clear that Haeckel idealized, abstracted and arranged the elements in such a way that their symmetry and order was exaggerated. They are pictures of platonic creatures, of the ideal forms that Haeckel intuited as he gazed into his microscope. Their very beauty betrays them. They are, as Breidbach says (but seemingly without critical intent), "nature properly organized". In this way, "the labour of the analyst was replaced by the fascination of the image". Absolutely — as 'fascinate' originally meant 'bewitch'.

It is not as if Haeckel did not have the alternative of photography, as microphotography had been used as early as the 1850s. But Breidbach simply recapitulates the arguments against an overreliance on the veracity of photography, pointing out that what one sees is determined by the technology. That is true, and it is apt to give photography a false authority. But are hand-drawn images really any better — let alone those rendered with such apparent skill and realism that their schematic nature is disguised? Indeed, Haeckel felt compelled in 1913 to publish *Nature as an Artist*, a series of photographs of his subjects that demonstrates, he said, that "there can be no talk of reconstruction, touching up, schematization or indeed forgery" in his drawings. It was a remarkable work but it leaves us wondering why Haeckel did not use photographs in the first place.

Another danger of drawings is that they tend to reflect the artistic styles of the day. Haeckel's drawings fed into the florid, nature-inspired designs of the art nouveau and *Jugendstil* schools, but he was more influenced than influential. His medusae look like William Morris prints precisely because they have had

that visual aesthetic imprinted on them. Breidbach says that for Haeckel, as for Goethe, "aesthetics is the foundation of his view of nature". But is that a good thing? As the historian Ernst Gombrich has pointed out, artistic styles create unconscious biases and errors. When Gombrich speaks of the artist who "begins not with his visual impression but with his idea or concept", he might as well be talking of Haeckel. And what happens when the cultural aesthetic moves on — does nature have to follow suit? Breidbach points out that by using the visual language of his age, Haeckel helped to make science accessible to the public. But 20 years later, modernism had rendered his arabesque style old-fashioned.

As director of the Ernst Haeckel Museum at Jena, Breidbach has access to Haeckel's notes and sketchbooks, and he makes good use of them. But perhaps because of his position he felt unable to dig too deeply into the problematic areas his subject raises. So although this is undoubtedly a gorgeous book, and the questions it raises are fascinating, I can't help feeling that it represents an opportunity missed. ■ Philip Ball is a consultant editor for *Nature*.



A twenty-first century science

If handled appropriately, data about Internet-based communication and interactivity could revolutionize our understanding of collective human behaviour.

Duncan J. Watts

Few would deny that many of the major problems currently facing humanity are social and economic in nature. From the apparent wave of religious fundamentalism sweeping the Islamic world (and parts of the Western world), to collective economic security, global warming and the great epidemics of our times, powerful yet mysterious social forces come into play.

But few readers of *Nature* would consider social science to be the science of the twenty-first century. Although economics, sociology, political science and anthropology have produced a plethora of findings regarding human social behaviour, they have been much less successful than the physical and life sciences in producing a coherent theoretical framework that can account for their discoveries. This is not because social scientists are less clever than their peers in other fields, but because social phenomena are among the hardest scientific problems to solve.

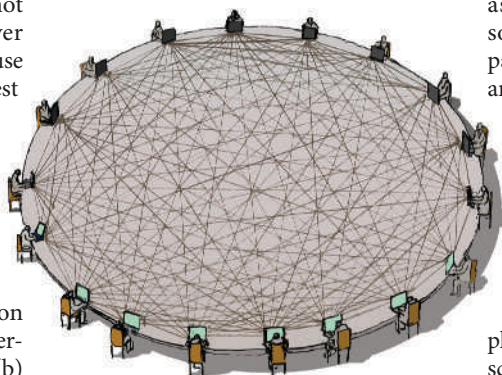
Social phenomena involve the interactions of large (but still finite) numbers of heterogeneous entities, the behaviours of which unfold over time and manifest themselves on multiple scales. It is hard to understand, for example, why even a single organization behaves the way it does without considering (a) the individuals who work in it; (b) the other organizations with which it competes, cooperates and compares itself to; (c) the institutional and regulatory structure within which it operates; and (d) the interactions between all these components. To draw an analogy with physics, one must solve the equivalent of quantum mechanics, general relativity and the multi-body problem at the same time — even string theorists don't have it that bad! Fortunately, recent developments in network science auger some hope for the future.

For the past 50 years or so, sociologists have thought deeply about the importance of interactions between people, institutions and markets in determining collective social behaviour. They have even built a language — network analysis — to describe these interactions in quantitative terms. But the objects of analysis, such as friendship ties, are hard to observe, especially for large numbers of people over extended periods of time. As a result, network data have historically comprised one-time snapshots, often for quite small groups. And most studies have relied on

self-reports from participants, which suffer from cognitive biases, errors of perception and framing ambiguities.

The striking proliferation over the past decade of Internet-based communication and interactivity, however, is beginning to lift these constraints. For the first time, we can begin to observe the real-time interactions of millions of people at a resolution that is sensitive to effects at the level of the individual. Meanwhile, ever-faster computers permit us to simulate large networks of social interactions. The result has been tremendous interest in social networks: thousands of papers and a growing number of books have been published in less than a decade, leading some to herald the arrival of a 'science of networks'.

This label, unsurprisingly, has attracted its share of critics, and with some justifica-



tion. Some of the ideas are not as new as sometimes advertised; many of the popular models are too simplistic to stand up to scrutiny; and even the more sober-looking empirical studies tend to use data that happen to be available, rather than obtained with a specific research question in mind. As a result, despite the avalanche of publications and breathless headlines, it is probably true that little has been learned about real social processes.

Nevertheless, the near future looks promising, especially if a few fundamental features of social networks can be emphasized. First, social networks are not static structures, but evolve in time as a consequence of the social and organizational environments in which they are embedded. Second, they are not unitary, but multiplex, meaning that people maintain a portfolio of types of ties — formal, informal, strong, weak, sexual, business and friendship — each of which serves different functions. And finally, network structure must be understood within the larger

framework of collective social dynamics. People do not just interact: their interactions have consequences for the choices they, and others, make.

Studies that combine all these features are currently beyond the state of the art, but two of my group's recent projects indicate tentative progress. The first used the anonymized e-mail logs of a university community of around 40,000 people to track daily network evolution over a year as a function of existing network structure, shared activities (such as classes) and individual attributes. Dynamic data of this type may shed light on the relative roles of structural constraints and individual preferences in determining, for example, observed homogeneity of friendship circles.

The second was a Web-based experiment in which 14,000 participants were asked to listen to, rate and download songs by unknown bands. Some participants made their decisions independently, and others could see how many times the songs had been downloaded previously.

Experiments of this kind measure not only the influence that individuals have over each others' decisions, but also the consequences of these individual-level effects on macro properties, such as the predictability of 'hit' products.

Clearly, the leap from these still simplistic studies to the 'big questions' of social science remains formidable. In this regard, cooperation between academic researchers and the large Internet companies who currently dominate data collection may be extremely productive. Although such collaborations will encounter challenges, including privacy and intellectual-property issues, the questions are too difficult to be left to intuition, or even experience, alone. We must start asking how the technological revolution of the Internet can lead to a revolution in social science as well. ■

Duncan J. Watts is at the Department of Sociology and the Institute for Social and Economic Research and Policy, Columbia University 420 W. 118th Street, 8th Floor, New York, NY 10027, USA.

FURTHER READING

Heyman, K. *Science* **313**, 604–606 (2006).
Duke, C. B. *Network Science* (The National Academies Press, 2006).
Kossinets, G. & Watts, D. J. *Science* **311**, 88–90 (2006).
Salganik, M. J., Dodds, P. S. & Watts, D. J. *Science* **311**, 854–856 (2006).

For other essays in this series, see <http://nature.com/nature/focus/arts/connections/index.html>

J. KAPUSTA/IMAGES.COM

CONNECTIONS

NEWS & VIEWS

CHEMICAL BIOLOGY

Sticky spices

Michael J. Caterina

The spiciness of foods such as horseradish is perceived through sensory neurons of the pain pathway. The lingering pungency of some such foods results from chemical modification of the channels that trigger these neurons.

Despite their highly dissimilar flavours, garlic, horseradish and cinnamon all share the ability to 'bite back' with a fiery sensation. This pungency is attributable to chemicals that activate a specific ion-channel protein, known as transient receptor potential ankyrin 1 (TRPA1)^{1–4}. Activated TRPA1 mediates the flow of ions into the endings of specialized neurons in the mouth and skin. This excites the neurons, resulting in local inflammation and our perception of burning pain. The activation of many ion channels by chemicals involves a readily reversible binding of the stimulating molecules. But two studies^{5,6} now provide evidence that the spicy compounds found in the foods listed above activate TRPA1 in a different, and often more sustained, manner — by covalently attaching themselves to cysteine amino-acid residues on the channel protein*.

The TRPA1 channel can be activated by an array of chemical and physical signals. The food constituents that act on TRPA1, as well as other chemical activators of this channel such as acrolein⁷ (an environmental irritant) and icilin⁸ (a substance that evokes a cooling sensation), are structurally very diverse (Fig. 1). TRPA1 can also be activated by several other cell-communication pathways, including G-protein-coupled signalling pathways^{1,3} and membrane depolarization⁵, and might even participate in cold-sensing and mechanosensation^{8,9}. How can one channel be activated by so many and such varied stimuli?

On page 541 of this issue, Macpherson *et al.*⁵ note that many TRPA1 stimuli are electrophiles capable of reacting with cysteine residues (albeit by different mechanisms). They reasoned that this property, rather than chemical geometry, might account for their shared activation of TRPA1. To test this hypothesis, they synthesized supercinnamaldehyde, an analogue of cinnamaldehyde (the pungent ingredient in cinnamon oil) predicted to exhibit greater reactivity with cysteine residues. Indeed, supercinnamaldehyde proved to be an even more potent activator of TRPA1 than cinnamaldehyde. Furthermore, the authors showed that iodoacetamide and methanethiosulphonates,

*This article and the paper concerned⁵ were published online on 21 January 2007.

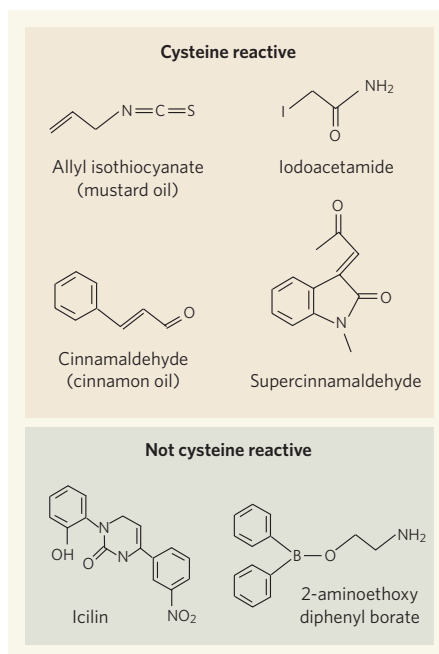


Figure 1 | TRPA1 activators. This structural comparison illustrates the chemical diversity of TRPA1 activators. Macpherson *et al.*⁵ and Hinman *et al.*⁶ find that, despite their geometrical differences, several of these noxious substances act through the common mechanism of covalently attaching themselves to specific cysteine amino-acid residues on the TRPA1 ion channel.

two synthetic compounds that modify cysteines by alternative chemical mechanisms, could also activate TRPA1.

To address more directly whether TRPA1 is covalently modified by cysteine-reactive stimulants (agonists), Macpherson *et al.* exposed cells expressing mouse TRPA1 to agonists that had been adorned with an additional chemical group known as an alkyne. The authors then isolated the TRPA1 protein from the cells, and added a fluorescent molecule that reacts with alkynes. So, in positions where TRPA1 had bound covalently to an agonist, it acquired fluorescence. Using mass spectrometry, the authors then showed more precisely that at least 14 of the 31 cysteine residues of mouse TRPA1 can be bound by iodoacetamide in

living cells. Almost all of these residues are located in the amino (N)-terminal domain of the channel, which is situated in the cytoplasm of the cell. Thus, the cysteine-reactive agonists must enter the cell before activating TRPA1.

Among the 14 modified cysteines, Macpherson *et al.* found three — two close together, and one 200 amino acids away — whose substitution with serine reduced the activation of TRPA1 by cysteine-reactive agonists (Fig. 2, overleaf). These mutations also partially diminished activation of TRPA1 by stimuli such as membrane depolarization that are unlikely to act as covalent cysteine modifiers. Even with correction for this general effect, however, the ability of cysteine-reactive compounds to activate TRPA1 was disproportionately impaired in the mutants. Although this preferential effect might be coincidental, the most likely explanation is that covalent modification of these cysteines — individually, together or in combination with others — accounts for the activation of TRPA1 by electrophiles.

As reported in the *Proceedings of the National Academy of Sciences*, Hinman *et al.*⁶ also used a chemical-biology strategy to arrive at essentially the same conclusions regarding the action of cysteine-modifying agents on TRPA1. Their study identified three neighbouring cysteines on human TRPA1 in which simultaneous mutation negated the channel-activating effects of several cysteine-modifying reagents.

The key cysteines identified by the studies are all among residues conserved between mouse and human TRPA1. Nevertheless, only one cysteine residue was identified as crucial in both studies, possibly reflecting subtle differences between species in overall TRPA1 structure. Aside from the newly identified sites of electrophile action, the TRPA1 N-terminal domain contains 18 ankyrin repeat motifs and an EF-hand domain. These two features have been proposed to contribute to the regulation of the channel by mechanical force and calcium ions, respectively. Clearly, the structural consequences of covalent cysteine modification on these domains and the remainder of the channel will be a fascinating topic for future study.

Another minor discrepancy between

the two studies^{5,6} involves the duration of covalent TRPA1 activation. Although both groups showed that certain activators achieve essentially permanent TRPA1 modification, the longevity of changes evoked by mustard oil differed between the studies. This discrepancy might relate to the use of mouse versus human TRPA1, or to the different systems in which the authors analysed TRPA1 function. It also highlights the fact that the lifetimes of covalent cysteine modifications can vary, depending on the modifying agent and on environmental factors such as pH or redox state¹⁰. This variability, which is exaggerated by non-covalent activation of TRPA1, might lead to differences in the duration, magnitude and qualitative features of TRPA1-mediated food pungency, inflammation and pain^{7,9}.

How general is the covalent regulation of ion channels by cysteine modification? In Hinman and colleagues' study⁶, cysteine-reactive compounds failed to activate several related TRP-family channels or to promote calcium influx into sensory neurons devoid of TRPA1. However, a cysteine-reactive TRPA1 activator from garlic, allicin, was reported in another study to activate TRPV1, through an unknown mechanism⁴. Furthermore, nitric oxide can stimulate certain TRP channels by attaching covalently to cysteines in the vicinity of the channel pore¹¹. Analogous regulation by such nitrosylation also occurs in several other channel families¹². In another twist, Hinman *et al.* found that, at high concentrations, mustard oil can activate TRPA1 through a cysteine-independent, and probably covalent, mechanism requiring a lysine in the N terminus.

These TRPA1 findings^{5,6} will probably evoke a sense of déjà vu among investigators in the cancer research field. Electrophilic

agents can be damaging to DNA and proteins, one potential step towards cancer. But many of the cysteine-reactive compounds that activate TRPA1 induce the expression of the enzymes that detoxify them — protecting against such injury. For instance, KEAP1 is a gene-regulatory protein that binds to and inhibits the actions of NRF2, which would otherwise activate the expression of particular detoxifying enzymes. Covalent modification at two cysteine residues causes pairs of KEAP1 molecules to become crosslinked, and disrupts their interaction with NRF2, resulting in expression of the enzymes¹³. It will be interesting to determine whether crosslinking between subunits also occurs during the activation of TRPA1 by cysteine modification. Perhaps more important will be determining whether the KEAP1 and TRPA1 systems, with their respective biochemical and behavioural outputs, cooperate or have coevolved to fight the war against electrophilic attack. ■

Michael J. Caterina is in the Departments of Biological Chemistry and Neuroscience, and the Center for Sensory Biology, Johns Hopkins School of Medicine, 725 North Wolfe Street, Baltimore, Maryland 21205, USA.
e-mail: caterina@jhmi.edu

1. Bandell, M. *et al.* *Neuron* **41**, 849–857 (2004).
2. Bautista, D. M. *et al.* *Proc. Natl Acad. Sci. USA* **102**, 12248–12252 (2005).
3. Jordt, S. E. *et al.* *Nature* **427**, 260–265 (2004).
4. Macpherson, L. J. *et al.* *Curr. Biol.* **15**, 929–934 (2005).
5. Macpherson, L. J. *et al.* *Nature* **445**, 541–545 (2007).
6. Hinman, A., Chuang, H. H., Bautista, D. M. & Julius, D. *Proc. Natl Acad. Sci. USA* **103**, 19564–19568 (2006).
7. Bautista, D. M. *et al.* *Cell* **124**, 1269–1282 (2006).
8. Story, G. M. *et al.* *Cell* **112**, 819–829 (2003).
9. Kwan, K. Y. *et al.* *Neuron* **50**, 277–289 (2006).
10. Conaway, C. C., Krzeminski, J., Amin, S. & Chung, F. L. *Chem. Res. Toxicol.* **14**, 1170–1176 (2001).
11. Yoshida, T. *et al.* *Nature Chem. Biol.* **2**, 596–607 (2006).
12. Hess, D. T., Matsumoto, A., Kim, S. O., Marshall, H. E. & Stamlir, J. S. *Nature Rev. Mol. Cell Biol.* **6**, 150–166 (2005).
13. Wakabayashi, N. *et al.* *Proc. Natl Acad. Sci. USA* **101**, 2040–2045 (2004).

MATERIALS SCIENCE

Synergy in a superlattice

James R. Heath

Put two types of crystal together in one lattice, and the resulting material can have properties greater than the sum of those of its individual components. Until now, that's been a difficult trick to pull off on a large scale.

Many applications in materials science require the preparation of crystalline solids that are essentially perfect, only for impurities to be added back into them to achieve a particular physical property. Microelectronics is the obvious example: pure silicon is the foundation of modern integrated circuits, but only by adding atomic impurities (dopants) into the silicon lattice can it be tuned from being an insulator to a semiconductor to a metal. This is a relatively simple operation, as it requires the optimization of only one property, electrical conductivity. Optimizing multiple, correlated properties is a trickier business, but one that is essential for many applications. Writing in *Nature Materials*, Urban *et al.*¹ describe progress towards achieving this sort of trade-off — the synergistic combination of two materials' properties in one 'superlattice'.

The material that the authors have developed is an example of a so-called binary nanocrystal superlattice, and could be useful as a 'thermoelectric'. These are materials that convert a heat gradient into a voltage, and can therefore serve as a power generator with no moving parts. The potential of such materials is enormous², but they currently find only niche applications, largely because even the best thermoelectrics are not very efficient. Thermoelectric efficiency is defined by a complex, and frustrating, figure of merit: it depends on the operating

temperature, on the square of the thermopower that the material generates (measured in volts per kelvin), on the material's electrical conductivity and on the inverse of its thermal conductivity. Optimizing one parameter often adversely affects another — the same kind of problem encountered in efforts to design a large, fast car with terrific fuel economy.

Multicomponent materials offer one possible way around such optimization problems. The idea is that individual parameters can be separately optimized in the different components, with the combined material giving the best of all worlds. Superlattices are a promising line of enquiry: they are ordered arrangements of different crystals, most commonly layers of thin films grown with near-atomic perfection on top of each other. A particularly fruitful approach to optimizing thermoelectric efficiency has been to engineer quantum-mechanical interactions. This is done by fine-tuning the thin-film thicknesses in a superlattice so as to hinder lattice vibrations (thus decreasing heat flow) and transmit electrons (increasing electrical conductivity), using materials that intrinsically have a large thermopower³; this generates a thermoelectric material with a particularly high figure of merit.

Similar results can be achieved by using a single-crystal surface to act as a template for the growth of quantum dots, thus forming a

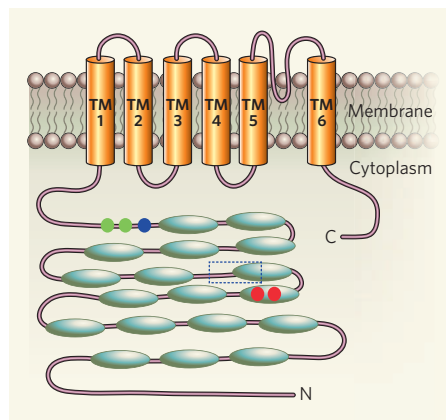


Figure 2 | Structure of one TRPA1 channel subunit. Four identical TRPA1 subunits combine to form a functional channel. As shown here, each subunit spans the plasma membrane six times (transmembrane domains TM1–TM6) and has a long cytoplasmic N-terminal domain. Ovals indicate ankyrin repeat domains; dashed box indicates an EF-hand domain. Filled circles indicate cysteine residues that Macpherson *et al.*⁵ and Hinman *et al.*⁶ identify as being crucial for covalent activation of mouse TRPA1 (red), human TRPA1 (green) or both (blue).

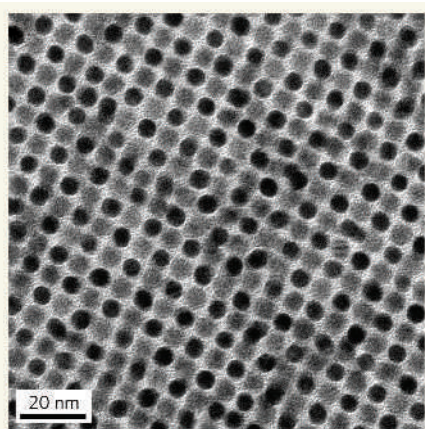


Figure 1 | Binary diversity. Urban *et al.*¹ build on work that has generated a huge variety of binary nanoparticle superlattices incorporating semiconducting, metallic and magnetic building-blocks: here, semiconducting lead selenide (lighter particles) is ordered in a lattice with metallic gold nanoparticles. (Reproduced from ref. 8.)

kind of superlattice embedded in a thin film of a different composition⁴. The dots exhibit size-dependent quantum effects that allow their thermopower to be optimized independently of the thin film⁵. With all these materials, however, there is a significant caveat: they have so far been produced on very small scales, using highly specialized tools. Scaling up such preparations to produce bulk materials remains a daunting challenge.

This is where the binary nanocrystal superlattices exploited by Urban *et al.*¹ come in. A basic nanocrystal superlattice is essentially a 'crystal of crystals' — a regular crystalline array in which the individual components are themselves spherical, chemically synthesized nanoscale crystals consisting of a few hundred to tens of thousands of individual atoms⁶. Binary nanocrystal superlattices follow the same principles, but are formed by the co-crystallization of two different sets of nanocrystals. They could thus potentially combine the desirable attributes of both sets, while also providing a route to a material that can be manufactured on a larger scale.

Two barriers must be overcome. First, binary nanocrystal superlattices are largely limited to a few tightly packed crystal structures, such as those found in naturally occurring opals⁷. That limits their versatility in applications. Second, large 'capping' molecules are required to stabilize the nanocrystal surfaces, preventing them from interacting strongly with each other. Such isolation means that, even if individual physical parameters are optimized in each of the nanocrystal types in the superlattice, the collective properties of the superlattice would be less than the sum of its parts.

These barriers have recently begun to crumble. Many different binary superlattices, including several new crystal structures, have been generated⁸ in the past couple of years using ionic interactions⁹ between nanoparticles

(Fig. 1). That has not only made for fascinating crystallography, but has also dramatically expanded the tool-kit for materials design. This assault on the first obstacle to progress is now followed by Urban and colleagues' offensive¹ on the second. They have made the first binary lattices that show synergistic effects arising from the interactions of separately optimized nanoparticles.

With an eye towards thermoelectric capability, the authors chose lead telluride (PbTe) and silver telluride (Ag₂Te) as their nanocrystal building-blocks. Bulk PbTe has a high thermopower, in that it generates a large voltage from a small heat flow. The addition of Ag₂Te provides silver ions as dopants, thus improving the material's overall electrical conductivity, and so its thermoelectric figure of merit.

The authors prepared two types of binary lattice with differing levels of Ag₂Te dopant. In a later stage, they also replaced the capping molecules that stabilize the nanocrystals in the superlattices with the much smaller molecule hydrazine (N₂H₄). The effect of this second process is to compress the binary lattice so that the individual nanocrystals are in close contact. Although the values for the thermoelectric figure of merit are not reported, the electrical conductivity of the treated binary superlattices was approximately 100 times greater than that of similarly treated superlattices of the individual components. This represents convincing evidence of a property of the bulk solid arising from the collective interactions of its nanocrystal components.

Such multicomponent superlattice approaches to materials design are still in the early stages of development. The generation of truly high-performance materials, requiring the optimization of many competing parameters, is still some way off. Farther away still is proof that these approaches can be scaled up to produce materials for industrial applications. Advances are coming thick and fast, however. With the kind of progress exemplified by Urban and colleagues' work¹, the limited tool-kit for materials engineering is expanding into a treasure trove of resources. ■

James R. Heath is in the Division of Chemistry and Chemical Engineering, Mail Code 127-72, 1200 East California Boulevard, Pasadena, California 91125, USA.
e-mail: heath@caltech.edu

- Urban, J. J., Talapin, D. V., Shevchenko, E. V., Kagan, C. R. & Murray, C. B. *Nature Mater.* **6**, 115–121 (2007).
- Roew, D. M. (ed.) *CRC Handbook of Thermoelectrics* (CRC, New York, 1995).
- Venkatasubramanian, R., Siivola, E., Colpitts, T. & O'Quinn, B. *Nature* **413**, 597–602 (2001).
- Harman, T. C., Taylor, P. J., Walsh, M. P. & LaForge, B. E. *Science* **297**, 2229–2232 (2002).
- Hicks, L. D. & Dresselhaus, M. D. *Phys. Rev. B* **47**, 12727–12731 (1993).
- Collier, C. P., Vossmeier, T. & Heath, J. R. *Annu. Rev. Phys. Chem.* **49**, 371–404 (1998).
- Islam, A. M., Chowdhry, B. Z. & Snowden, M. J. *Adv. Colloid Interf. Sci.* **62**, 109–136 (1995).
- Shevchenko, E. V., Talapin, D. V., Kotov, N. A., O'Brien, S. & Murray, C. B. *Nature* **439**, 55–59 (2006).
- Leunissen, M. E. *et al. Nature* **437**, 235–240 (2005).



50 YEARS AGO

Atomic Quest: A Personal Narrative.

By Dr. Arthur Holly Compton. —

Prof. Compton describes in great detail the agonizing discussions which went on among the scientists of the Metallurgical Laboratory and Los Alamos during 1945 as to whether the bomb should be used against the Japanese. The discussions were brought to the attention of the Secretary of State for War, Mr. Stimson, who appointed a representative 'Interim Committee' to advise him. At this point General Marshall stated that he would advise against its use in the war provided its existence could be kept secret. The general opinion was, however, that it would not be possible to keep its existence secret. A proposal to make a non-military demonstration likely to bring an end to the war was also thought to be impossible. After this, a poll of a hundred scientists of the Metallurgical Laboratory brought an 87 per cent vote in favour of its military use. The decision was taken by President Truman on the advice of Mr. Stimson... Prof. Compton believes that the use of the bomb saved a very large number of lives, since he does not believe that the Japanese would have surrendered without bitter fighting in the next landings.

J. D. Cockcroft

From *Nature* 2 February 1957.

100 YEARS AGO

Dr. Alfred Russel Wallace, in an article entitled "Creation by Law," contributing to the *Quarterly Journal of Science* in October, 1867, alluded to a Madagascar orchid (*Angraecum sesquipedale*) with a nectary varying in length from 10 inches to 14 inches, and prophesied that a hawk-moth will be discovered with a tongue of equal length to fertilise it... Will someone kindly tell me if this prophecy had been fulfilled?

E. W. Swanton

I have not heard of any moth from Madagascar with an exceptionally long proboscis. I think, however, I did hear of one from East Africa with a proboscis nearly the length required.

Alfred Russel Wallace

From *Nature* 31 January 1907.

50 & 100 YEARS AGO



HYDROLOGY

Tropical rain recycling

Thom Rahn

The behaviour of water in the atmosphere is a poorly understood part of the hydrological cycle. Applying the principles of isotope chemistry to satellite data provides a powerful approach for improving the situation.

Water is arguably our most precious resource. It moves through Earth's system in many ways, beginning with its evaporation from the oceans into the atmosphere. There, air masses mix, and droplets coalesce and fall. Some of this precipitation goes straight back into the ocean, while some enters the terrestrial water cycle as rain or snow. Terrestrial water re-evaporates or is stored in glaciers, recharges aquifers or is carried by rivers back to the sea. The processes behind this delivery of a water molecule from ocean to cloud to rain droplet (or snowflake), and eventually back to the ocean, are highly complex. On page 528 of this issue, Worden *et al.*¹ unravel a little more of the mystery behind the journey.

The authors' study takes its cue from the seminal work of Harmon Craig², who in 1961 found that the stable isotopes of hydrogen and oxygen (expressed in terms of the ratios $^2\text{H}/^1\text{H}$ and $^{18}\text{O}/^{16}\text{O}$) follow a simple linear relationship in all precipitation, regardless of where the water was collected. This relationship, along with maps of the distribution of ^2H and ^{18}O in precipitation, has helped to a degree in tracking water through the atmosphere. Along the way, it has illuminated phenomena as diverse as the source regions of groundwater recharge, the pathways of migratory bird species, and the provenance of mineral assemblages resulting from the evaporation of water.

But whereas measuring the isotopic content of rainfall and snow is a straightforward process, analysing isotopic ratios in the vapour

from which this precipitation condensed is another matter altogether. One option is to collect samples with a mechanical cold trap and return them to a laboratory for conventional analysis³; another is to measure isotopes *in situ* using laser-based optical methods^{4,5}. Both approaches have their merits, but have been little used to date. A third option is to determine the isotopes in water from space through satellite-based spectrometric analysis. This has been accomplished previously for ^2H , but only for the upper troposphere (the lowest portion of Earth's atmosphere) and lower stratosphere^{6,7}, or for clear-sky conditions over the Pacific Ocean⁸. Worden *et al.*¹ go one better by retrieving globally distributed profiles of ^2H in water using the Thermal Emission Spectrometer onboard NASA's Aura satellite. These yield the first comprehensive map of the ^2H distribution of water vapour in the troposphere.

The history of this water vapour can be illuminated by comparing Worden and colleagues' measurements with theoretical expectations. In the simplest model, tropical ocean waters evaporate, and are lifted to cloud height by convection and transported poleward, where progressive 'rainout' depletes the air mass of moisture. Because the lighter stable isotopes evaporate preferentially, the initial vapour is depleted in the heavier isotopes ^2H and ^{18}O (Fig. 1, overleaf) when compared with its oceanic origin. As this vapour condenses into clouds to form precipitation, the heavier isotopes become concentrated again in the

liquid phase, further depleting the remaining cloud water vapour (blue curves in Fig. 1) and removing the heavier isotopes from the atmosphere. When the remaining dry and depleted air is mixed with freshly evaporated moist air, its isotopic composition and moisture content move back towards equilibrium with the ocean (the orange curves). In this simple model, air parcels cycling in the atmosphere are represented by the orange and blue regions of Figure 1, depending on whether they are dry or moist.

But as those of us who live in arid regions of the world can verify, rain sometimes does not make it to the ground at all: some of the precipitation is certainly recycled within the atmosphere. If the isotopic composition of a parcel of water vapour is strongly influenced by the re-evaporation of rainfall, it would be expected to be moister, but more depleted in heavy isotopes because of its recycled origin (green area in Fig. 1).

Worden *et al.*¹ identify such an additional ^2H depletion in approximately half of the water vapour in moist air (that is, air in regions dominated by precipitation rather than evaporation) that they sample over tropical oceans. According to their data, on average about 20% of tropical precipitation over the ocean must have re-evaporated before reaching the surface — in some cases, the value exceeds 50%. Although this recycling of precipitation via re-evaporation is not a new idea^{9,10}, it is beautifully illustrated by these measurements.

The degree of re-evaporation depends on the ambient relative humidity. Because a droplet plummets from a cold, saturated cloud through to warmer, generally unsaturated air below, one might expect re-evaporation to be fairly ubiquitous. Perhaps surprisingly, only about half of Worden and colleagues' data from moist tropical air, and very few of their extratropical data, confirm the effect. The lack of re-evaporation in these cases is possibly due to earlier cooling, and the resulting increase in relative humidity,

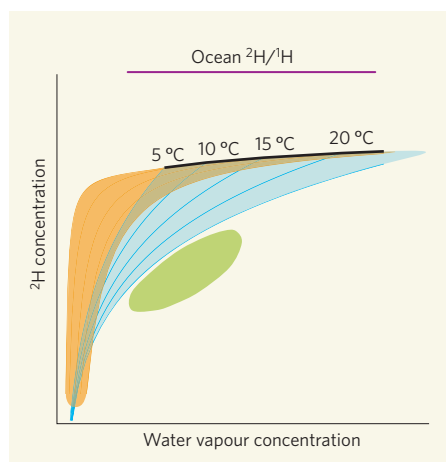


Figure 1 | Stable isotopes in water vapour. The isotopic composition of ocean water defines the baseline ratio of hydrogen isotopes $^2\text{H}/^1\text{H}$ (purple line). As water evaporates from the ocean, its isotopic composition becomes depleted in heavier isotopes, such as ^2H , and moves towards the black curve. Warmer air holds more moisture, as indicated by the sea surface temperatures at the time of evaporation. Condensation in clouds causes the remaining water vapour to become further depleted in the heavy isotopes; the ^2H proportion descends down the blue curves. As dry air high in the atmosphere depleted in ^2H (bottom left-hand corner) mixes with freshly evaporated ocean air, it is moistened; the isotopic composition becomes more enriched in heavy isotopes, moving up along the orange curves. Rainwater that evaporates before it reaches the ocean again is moister and more depleted in heavy isotopes than water vapour resulting from straight evaporation from and condensation into the oceans (green area). These characteristics are detected by Worden *et al.*¹ in about half of their moist-air observations over the tropical oceans.

as the air was advected from warmer regions. By contrast, the water vapour with the greatest signature of re-evaporation is evidence of condensation from local convection.

Potentially even more significant for our understanding of the processes that deliver fresh water to land is that water vapour over tropical continental land masses is, on average, less depleted in ^2H than it is over the tropical oceans. In addition, a proportion is even more enriched than is water vapour in equilibrium with the oceans. These results can be accounted for only by one of two mechanisms. First, relatively enriched water vapour that evaporates from the ocean is transported to land at low altitudes, and is convectively lofted. Alternatively, previous continental precipitation is recycled, with an isotopic composition reflecting a potentially complex history of condensation and evaporation.

Of course, both processes could work in parallel. Future research addressing the seasonal variability of the distribution of ^2H in continental water vapour, and the addition of an ^{18}O data set, will help to resolve the question of whether transport of oceanic air or

recycling of continental precipitation is dominant. Meanwhile, the data provided by Worden *et al.*¹ offer an invaluable insight into the global water cycle. Understanding all aspects of the hydrological cycle will be crucial as we proceed into a future with an uncertain climate, where potable water will become an ever more precious resource.

Thom Rahn is in the Earth and Environmental Sciences Division, Los Alamos National Laboratory, Los Alamos, New Mexico 87545, USA.
e-mail: trahn@lanl.gov

1. Worden, J. *et al.* *Nature* **445**, 528–532 (2007).
2. Craig, H. *Science* **133**, 1702–1703 (1961).
3. Lawrence, J. R. *et al.* *J. Geophys. Res.* **109**, D06115 (2004).
4. Webster, C. R. & Heymsfield, A. J. *Science* **302**, 1742–1745 (2003).
5. Hanisco, T. F. *et al.* *Geophys. Res. Lett.* (in the press).
6. Irion, F. W. *et al.* *Geophys. Res. Lett.* **23**, 2381–2384 (1996).
7. Moyer, E. J., Irion, F. W., Yung, Y. L. & Gunson, M. R. *Geophys. Res. Lett.* **23**, 2385–2388 (1996).
8. Zakharov, V. I., Imasu, R., Gribov, K. G., Hoffmann, G. & Jouzel, J. *Geophys. Res. Lett.* **31**, L12104 (2004).
9. Dansgaard, W. *Tellus* **16**, 436–468 (1964).
10. Rosenfeld, D. & Mintz, Y. *J. Appl. Meteorol.* **27**, 209–215 (1988).

ORGANIC CHEMISTRY

Catalytic gold rush

Steven P. Nolan

Despite gold's reputation as an inert element, chemists have mined a rich seam of catalytic reactions that use this metal. The latest example stakes out gold's claim as a versatile catalyst.

At the turn of the nineteenth century, the small outpost of Dawson, located at the juncture of the Yukon and Klondike rivers, saw a record population explosion. This was caused by a simple cry: "Gold!" A similar gold fever has recently overtaken chemists, who have discovered that this supposedly inert metal can catalyse a wide array of chemical reactions. A striking example of this has now been described by Forsyth and colleagues¹ in *Angewandte Chemie*. They have used a gold-catalysed reaction as the key step in the synthesis of an elaborate organic molecule, so cementing the use of this metal in mainstream chemistry.

It is surprising that gold has taken so long to find a place in catalysis. The reason for the delay is nothing to do with cost, as might be expected — many metals commonly used as catalysts (such as platinum, rhodium and iridium) are much more expensive than gold.

Much of the blame must be attributed to the long-held assumption that gold is unreactive. But gold salts have been known for some time to have a high affinity for carbon–carbon triple bonds (known as alkyne bonds). The simple reactions of these salts with alkynes are the basis of the present gold rush².

Compounds such as gold chloride (AuCl_3) are now frequently assessed by chemists as catalysts for new chemical transformations^{3,4}. This has led to the development of an impressive array of organic reactions^{2–6} that provides a foundation for Forsyth and colleagues' work. Gold salts can promote chemical transformations at room temperature with reaction times of just minutes. This contrasts with other metal-catalysed reactions that require higher temperatures and reaction times of hours or even days.

Forsyth and colleagues¹ now report the use

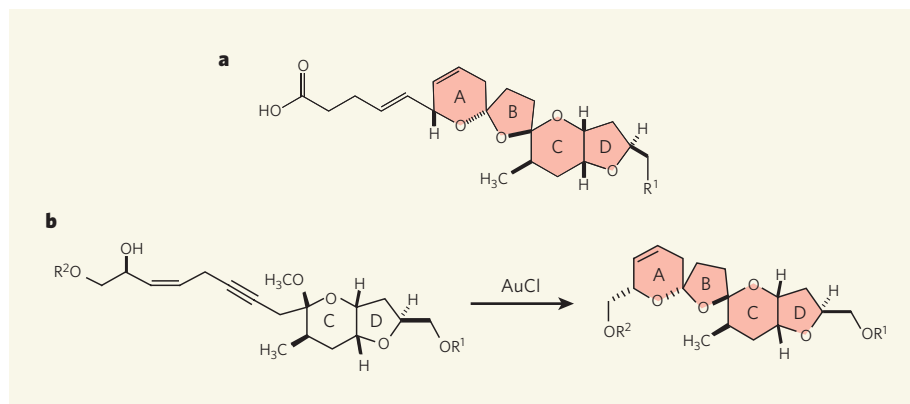


Figure 1 | Gold catalysis in organic synthesis. **a**, Azaspiracids are a family of marine toxins, the core structure of which is shown here. The ring subunits are commonly labelled A–D as shown; R_1 represents the various structures found for each specific azaspiracid. **b**, Forsyth and colleagues¹ use a reaction catalysed by gold chloride (AuCl_3) to construct rings A and B. R_2 represents a chemical group that may be converted into the side chain found in azaspiracids.

of gold chloride as a catalyst in a short and efficient synthesis of part of a naturally occurring compound. This compound, azaspiracid (Fig. 1a), is a member of a family of marine toxins that was found to be the cause of human poisoning in the Netherlands⁷. The first synthesis of azaspiracid⁸ was reported in 2004, but alternative syntheses are always desirable — chemists delight in developing further generations of syntheses that improve on the original, or that offer a completely different strategic approach.

The authors devised their synthetic strategy¹ using retrosynthetic analysis — an approach commonly used by organic chemists, in which elaborate molecules are notionally broken into smaller fragments using a series of simple bond disconnections. This is more easily said than done, as any retrosynthetic analysis requires knowledge of a plethora of assembly protocols. In other words, you can't just disconnect a chemical structure any way you like, as not all disconnections correspond to a workable chemical reaction. Just as in chess, where one has to think many moves ahead, chemists must begin their syntheses by incorporating the chemical groups required to enable later steps. In Forsyth and colleagues' case, they designed a precursor molecule that has chemical groups attached at positions that predispose the molecule to a gold-catalysed reaction.

It turns out that this strategy works remarkably well. The authors report the straightforward assembly of a portion of the azaspiracid molecule, in which the crucial step is the formation of two molecular rings in a gold chloride-catalysed reaction (Fig. 1b). The creation of such molecular complexity in a single step is extraordinary, and provides a clear demonstration of how far gold chemistry has come. The Forsyth group had previously reported another strategy⁹ for assembling this fragment of azaspiracid that required a different precursor molecule designed in an alternative retrosynthetic analysis. But that approach was far from ideal, requiring a step each to form the two rings, and taking up to two days to complete. Contrast this with the gold-catalysed reaction — a single step that takes only 20 minutes.

The mechanism of this elegant dual cyclization reaction is proposed to involve the initial formation of a complex between gold chloride and an alkyne in the precursor molecule. This renders the alkyne prone to chemical attack from an adjacent, strategically positioned hydroxyl group (OH), initiating the sequence that results in the formation of two rings with a spiro configuration — that is, twisted like a spiral staircase.

We are still not at the stage of using gold-mediated catalysis in industrial-scale reactions, such as those that are required for the production of pharmaceutical ingredients. But the cry of "Gold!" has been heard. These catalysts have certainly found their way into the research chemist's synthetic tool-box. It is only a matter

of time before we see them used in commercial applications.

Steven P. Nolan is at the Institute of Chemical Research of Catalonia (ICIQ), Av. Països Catalans 16, 43007 Tarragona, Spain.
e-mail: snolan@icq.es

1. Li, Y., Zhou, F. & Forsyth, C. J. *Angew. Chem. Int. Edn* **46**, 279–282 (2007).
2. Teles, J. H., Brode, S. & Chabanas, M. *Angew. Chem. Int. Edn* **37**, 1415–1418 (1998).

3. Hashmi, A. S. K. *Gold Bull.* **37**, 51–65 (2004).
4. Hoffmann-Röder, N. & Krause, N. *Org. Biomol. Chem.* **3**, 387–391 (2005).
5. Nieto-Oberhuber, C. et al. *Angew. Chem. Int. Edn* **43**, 2402–2406 (2004).
6. Shi, X., Gorin, D. J. & Toste, F. D. *J. Am. Chem. Soc.* **127**, 5802–5803 (2005).
7. McMahon, T. & Silke, J. *Harmful Algae News* **14**, 2 (1996).
8. Nicolaou, K. C. et al. *Angew. Chem. Int. Edn* **43**, 4318–4324 (2004).
9. Gleiser, L. K., Nguyen, S. & Forsyth, C. J. *Org. Lett.* **6**, 4159–4162 (2004).

DEVELOPMENTAL BIOLOGY

Moonlighting at the pole

Tor Erik Rusten and Harald Stenmark

Which end of a fly embryo becomes the head is partly dictated by the accumulation of *bicoid* RNA at the anterior pole. The protein that amasses the RNA turns out to be an old acquaintance from a different context.

Protein production can be restricted to particular areas within cells by targeting the messenger RNAs encoding them to those sites. Such localization of mRNAs can affect the function of single cells, particularly those that have a polarity such as neurons. More dramatically, it can influence the development of whole organisms. In the fruitfly *Drosophila melanogaster*, for instance, the *bicoid* mRNA is moved to the anterior of the oocyte (the developing egg; Fig. 1). This results in a gradient of the encoded protein such that the region with the highest concentration develops into the head region in any resulting embryo¹. Mutant oocytes that lack the *bicoid* gene do not have such anterior organization and form embryos with two posterior ends¹. On page 554 of this issue, Irion and St Johnston² identify a protein complex responsible for *bicoid* mRNA localization, unexpectedly revealing that it is identical to a complex that helps to dictate where certain membrane proteins end up within the cell.

The transport and retention of *bicoid* mRNA in the oocyte's anterior depend on a regulatory region in its sequence called the 3' untranslated region (UTR) and on transport along the microtubule scaffolding of the cell³. An attractive hypothesis to explain how *bicoid* is localized involves mRNA-binding proteins. One of these, Staufen, binds to the *bicoid* 3' UTR and is necessary for *bicoid* retention at the anterior. However, Staufen alone cannot account for specific mRNA localization because it binds to several different mRNAs, including one called *oskar* that localizes to the posterior of the oocyte³. To identify the cellular factors responsible for the anterior localization of *bicoid* mRNA, Irion and St Johnston² developed a clever screen in which the transport of *bicoid* mRNA in oocytes mutated in various genes was followed indirectly using the Staufen protein tagged with green fluorescent protein.



Figure 1 | Rearing a head. In the fruitfly oocyte, *bicoid* mRNA is transported towards the anterior pole where it is retained until after fertilization. In the egg (~500 μm), the *bicoid* RNA (blue) governs development of head structures. (Picture courtesy of U. Irion.)

Surprisingly, the genetic screen showed that the correct transport did not occur when the gene encoding the Vps22 protein was mutated. This protein was already known, but in a completely different context — the process of endosomal protein sorting². Cells regularly take samples of their external environment by sucking in pouches of their membrane and the local extracellular fluid. The bubble-like vesicles are transported into the cytoplasm and end up fusing with a membrane-bounded organelle called the endosome. Sorting in the endosome membrane determines the fate of the various molecules. They are wrapped into packets to send to specialized organelles so they can be digested, expelled from the cell or recycled back to the external membrane. Together with two structurally related proteins, Vps25 and Vps36, Vps22 forms the 'endosomal sorting complex required for transport' (ESCRT)-II (Fig. 2, overleaf)^{4,5}. In conjunction with two other protein complexes, ESCRT-I and ESCRT-III, this evolutionarily conserved protein complex mediates the sorting of particular membrane proteins from endosomes to organelles called lysosomes for digestion^{4,5}.

Analysis of oocytes mutant for Vps25 and Vps36 revealed that these had a similar defect in *bicoid* mRNA localization to the Vps22

REPRODUCTIVE BIOLOGY

Sperm alliance

In 2002, biologists were presented with a vivid account of how sperm of the common wood mouse hook up together in 'trains'. Such trains, it was shown, form a fast vehicle in the race for the great prize — fertilization of an egg. But only one sperm can be successful in that goal. Simone Immler and colleagues have now revisited the question of what prompts the selfless behaviour of the others (*PLoS One* doi:10.1371/journal.pone.0000170; 2007).

A feature of the sperm of wood mice and many of their relatives

among the murine rodents is that their heads carry a hook structure, which varies in shape and size between species, as shown in the picture.

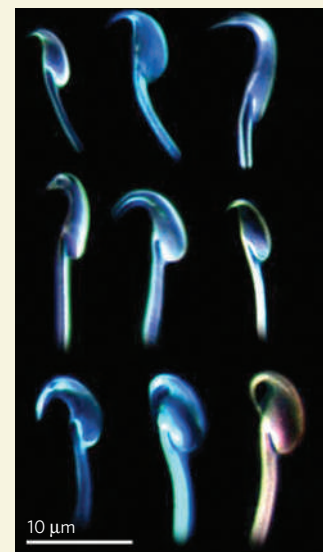
Immler *et al.* carried out a survey of the sperm of 37 species of murine rodent. They find that hook shape and curvature are more pronounced in species in which the female is more likely to mate with different males. The principle of 'together we succeed, divided we fail' makes sense in this situation. These sperm are better equipped to cooperate: so those from any one male are better

able to see off the competition from another male.

The authors also looked at the behaviour of sperm in two of the species, the Norway rat and the house mouse. In both, the sperm formed groups. But in the house mouse, individual sperm outperformed the group in sheer speed. Immler *et al.* speculate that maybe speed isn't everything: perhaps in this case the group can make surer progress in the journey up the female reproductive tract.

And there remains the issue of competition among the collaborators: who gets to claim the envied job of fertilization?

Tim Lincoln



mutants, indicating that the entire ESCRT-II complex is required for *bicoid* localization². Irion and St Johnston also found that the Vps36 protein, and hence ESCRT-II, co-localizes with *bicoid* mRNA at the anterior pole of the oocyte. Importantly, ESCRT-I and ESCRT-III mutants had normal localization of *bicoid* mRNA, suggesting that the function of ESCRT-II in *bicoid* localization is unrelated to its role in endosomal protein sorting.

The involvement of ESCRT-II in two seemingly unrelated processes — RNA guidance and protein sorting — may look surprising. However, the finding that a protein turns out to have an additional activity distinct from its canonical function is not unprecedented. Commonly termed 'moonlighting', this practice is exemplified by several glycolytic enzymes that have taken on jobs in gene regulation in addition to their classical involvement in energy metabolism⁶. Evolutionary pressure may have caused the selection of proteins and complexes capable of multitasking, thereby minimizing the number of genes required to make a fly or a human.

How does ESCRT-II recognize *bicoid* mRNA? Elegant experiments by Irion and St Johnston² showed that a unique part of Vps36 called the GLUE domain binds directly to a specific loop in the *bicoid* 3' UTR. The GLUE domain is indeed a sticky domain as it also binds to a small protein called ubiquitin and to the lipid PtdIns(3)P, which are both associated with the function of ESCRT-II in endosomal protein sorting^{7,8}. Crystallography shows that the ubiquitin-binding and lipid-binding sites of the GLUE domain are separate⁸, and it will be interesting to learn whether the mRNA-binding site overlaps with one or both of these. A mutually exclusive binding to ubiquitin or lipid versus mRNA might provide a mechanism by which ESCRT-II could switch between its functions in endosomal sorting and mRNA guidance.

But how does ESCRT-II find its way to the anterior pole of the oocyte? Previous work identified a group of proteins that start the formation of anterior microtubules during the late stages of oocyte formation, and these too are required for correct localization of *bicoid* mRNA³. The motor protein dynein, which transports many cargoes along microtubules, is a likely candidate for moving *bicoid* mRNA to the anterior pole³, and proteins that attach *bicoid* mRNA to dynein could thus represent the missing link between ESCRT-II and *bicoid* mRNA localization. It is interesting to note that Vps22 in mammalian ESCRT-II binds to the

Rab7-interacting lysosomal protein (RILP), a protein that recruits the dynein motor complex to endosomes⁹. So maybe a RILP-like fruitfly protein participates in the ESCRT-II–RNA complex with dynein, with the latter powering transport to (or retention at) the anterior pole.

Finally, how do these findings relate to other organisms, including humans? The fly Bicoid protein does not have a direct relative in humans, but it does belong to the homeo-domain family, a group of gene regulatory factors that determine body patterning during the development of many organisms, including humans. Also, frog Vps36 can recognize the fruitfly *bicoid* mRNA², indicating that ESCRT-II could play a role in mRNA recognition and localization in vertebrates as well as in flies. Moreover, mammalian ESCRT-II interacts with a protein that stimulates mRNA transcription¹⁰, suggesting that ESCRT-II might associate with selected mRNAs at an early stage of their synthesis. With this in mind, it will be interesting to investigate whether mammalian ESCRT-II can bind to specific mRNAs, and whether their localization is affected by the absence of ESCRT-II.

Tor Erik Rusten and Harald Stenmark are at the Centre for Cancer Biomedicine, Norwegian Radium Hospital and the University of Oslo, Montebello, N-0310 Oslo, Norway.
e-mail: stenmark@ulrik.uio.no

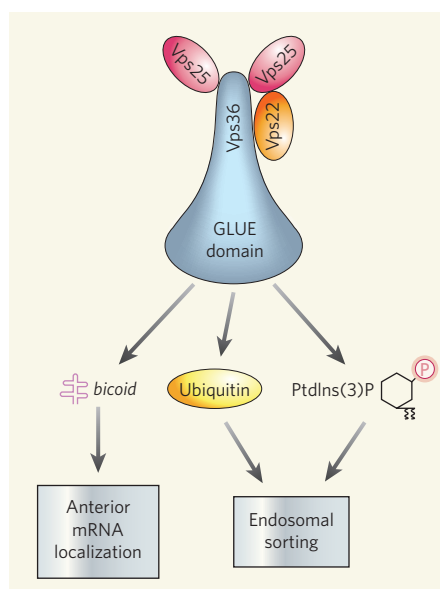


Figure 2 | The functions of ESCRT-II. The ESCRT-II complex is made up of the Vps22, Vps25 and Vps36 proteins. Irion and St Johnston² find that the GLUE domain of Vps36 interacts directly with *bicoid* mRNA to mediate anterior localization of the RNA in the fruitfly embryo. This domain can also bind to ubiquitin and phosphatidylinositol 3-phosphate (PtdIns(3)P) to facilitate protein sorting in the endosome.

1. Driever, W. & Nusslein-Volhard, C. *Cell* **54**, 95–104 (1988).
2. Irion, U. & St Johnston, D. *Nature* **445**, 554–558 (2007).
3. St Johnston, D. *Nature Rev. Mol. Cell Biol.* **6**, 363–375 (2005).
4. Hurley, J. H. & Emr, S. D. *Annu. Rev. Biophys. Biomol. Struct.* **35**, 277–298 (2006).
5. Slagsvold, T., Pattani, K., Malerød, L. & Stenmark, H. *Trends Cell Biol.* **16**, 317–326 (2006).
6. Kim, J. W. & Dang, C. V. *Trends Biochem. Sci.* **30**, 142–150 (2005).
7. Slagsvold, T. *et al.* *J. Biol. Chem.* **280**, 19600–19606 (2005).
8. Teo, H. *et al.* *Cell* **125**, 99–111 (2006).
9. Jordens, I. *et al.* *Curr. Biol.* **11**, 1680–1685 (2001).
10. Shilatfard, A. *J. Biol. Chem.* **273**, 11212–11217 (1998).

QUANTUM PHYSICS

Photon lab in a circuit

Frank K. Wilhelm and Enrique Solano

Electrical circuits might be regarded as rather mundane pieces of classical engineering. But their electromagnetic fields are, like light, a quantum object whose energy comes in discrete units — photons.

Both a coherent light beam and thermal, 'black-body' radiation given out by a heat source are archetypal, classical electromagnetic fields. Such fields can for most purposes satisfactorily be described as waves within the classical theory of electromagnetism formulated by James Clerk Maxwell in the 1860s. But even classical electromagnetic fields have an inherent quantum nature. That much is amply demonstrated by the experiments of Schuster *et al.*¹, set out on page 515 of this issue, which measure the statistics of photons in microwave electromagnetic fields confined within the solidly classical surroundings of an electrical circuit.

Quantum physics owes its origin to Max Planck's postulation in 1900 of the existence of discrete quanta of energy, which were needed to formulate a consistent theory of black-body radiation. Albert Einstein, too, in his *annus mirabilis* of 1905, observed that quantizing light — dividing it up into discrete packets of energy known as photons — could help to explain the photoelectric effect². Since then, countless experiments have confirmed that electromagnetic fields are fundamentally quantized. The quantum theory of coherence, introduced by Roy Glauber in the 1960s, has provided a deeper insight into photonic systems³.

Within this framework, even classical coherent and thermal fields can be described in terms of quantum-mechanical concepts such as phase properties and photon statistics. In a coherent field, the photonic quantum state has a well-defined phase; in an incoherent, thermal field, the phase information is distributed randomly. But on the macroscopic scale — the scale of, for example, an electrical circuit — a quantum-mechanical description of electrodynamics has a fundamental credibility problem. Its probabilistic tenets simply seem irreconcilable with our everyday intuition. For that reason, quantum theories generally tend to be perceived as a theory of only the small and invisible: of photons in free space, and of atoms and molecules.

Schuster and colleagues' work¹ builds on research performed on superconducting circuits, and provides crucial verification that quantum electrodynamics indeed has a role at a macroscopic scale in our everyday life. Their advance uses powerful tools, mainly developed by them earlier⁴, that are inspired by a pivotal innovation known as cavity quantum electrodynamics. Here, an electromagnetic

field is confined inside a resonator as standing waves with discrete frequencies. This allows the study of the interaction between the quantized field and the atoms in the resonator. Major tests, such as the generation and detection of non-classical states, have been performed on electromagnetic fields of microwave wavelengths (in the range of centimetres) confined in such three-dimensional cavities^{5,6}.

The authors' technique uses a microwave field that is not confined in three dimensions in air, as in a standard cavity, but is guided and defined in a one-dimensional, coplanar waveguide — a refined, on-chip version of the coaxial cables common in conventional electronics. According to theory⁷, such guided waves are quantum fields similar to light. The equivalent of a cavity is defined by interrupting the waveguide with capacitors that prevent the electromagnetic wave passing. A Cooper-pair box, a tiny superconducting circuit consisting of a metallic island and a bigger electrode, plays the role of the atom with which the field interacts in a standard cavity (Fig. 2 on page 516).

The physics of this Cooper-pair box can be simplified as two quantum states that differ by a single pair of electrons on the island, and therefore in their electrical dipole moment, which is a measure of the distribution of charge. Because of the greater separation of the charges, the dipole moments involved are huge compared with those of real atoms. Added to the fact that the wave modes supported by the cavity are densely packed in small volumes, this means that the atom-field coupling energy is high. Whereas Schuster and colleagues previously demonstrated just the coherent coupling of the atom and field⁴, they can thus now investigate the precise quantum character of the field.

The authors measure the associated quantum probabilities of the photon numbers in the resonator by imprinting information about the field state on the artificial atom, and then observing the atom reusing the radiation trapped in the cavity. When the artificial probe atom couples to the cavity far from the cavity's resonance frequency, the transition frequency between the atom's two quantum states is shifted — a phenomenon known as the a.c. Stark effect. If the field were completely classical, this frequency shift would be constant, and proportional to the square of the electrical field. But in the quantum world, the discreteness of the field energy and the probabilistic nature of

the field state allow the frequency shift to have only certain values, which are proportional to the number of photons present in the cavity (Fig. 3 on page 517). The height of the peaks corresponding to these frequency shifts reflects the probability of different numbers of photons in the cavity. If the cavity is exposed to a simulated source of thermal radiation, these probabilities follow Planck's thermal law (Fig. 4 on page 517). If the cavity is coherently excited, one obtains a Poisson distribution, as emerges from Glauber's theory of coherence.

For sceptics looking for possible loopholes in quantum theory, this proof of the quantum nature of the confined microwave field is the start of a new generation of tests of its non-classicality. Beyond the significance this set-up has for the foundations of quantum physics on the macroscopic scale, it opens up new perspectives in quantum measurement and its potential use in quantum information processing. The complete measurement of the quantum field — not only photon statistics, but also phase information — is a logical next step, and could be achieved by applying a powerful method known as quantum homodyne tomography. But implementing that technique in the microwave domain will require further work and fresh ideas owing to the lack of effective photodetectors for microwave light⁸.

These kinds of precise measurement would be easier if the field to be measured were separated from the field that does the measuring⁹, and the fact that they are combined is a weakness of Schuster and colleagues' current set-up. The next step is to prepare and verify other genuine quantum objects, such as single microwave photons, entangled multimode fields, and single- and two-mode squeezed states. Schuster and colleagues' work^{1,4} is sparking many theoretical proposals on how to achieve all this, and more. With such impetus, quantum optics on a chip could soon emerge as an exciting new subdiscipline of physics. ■

Frank K. Wilhelm is at the Institute for Quantum Computing and Department of Physics and Astronomy, University of Waterloo, Ontario N2T 2V9, Canada.

Enrique Solano is in the Physics Department, ASC and CeNS, Ludwig-Maximilian-Universität, 80333 Munich, Germany, and in the Sección Física, Pontificia Universidad Católica del Perú, Lima, Peru.

e-mails: f.wilhelm@iqc.ca;
enrique.solano@physik.lmu.de

- Schuster, D. I. *et al.* *Nature* **445**, 515–518 (2007).
- Einstein, A. *Ann. Phys.* **17**, 132–148 (1905).
- Glauber, R. J. *Phys. Rev.* **131**, 2766–2788 (1963).
- Wallraff, A. *et al.* *Nature* **431**, 162–167 (2004).
- Raimond, J.-M. *et al.* *Rev. Mod. Phys.* **73**, 565–582 (2001).
- Walther, H., Varcoe, B. T. H., Englert, B. G. & Becker, T. *Rep. Prog. Phys.* **69**, 1325–1382 (2006).
- Blais, A., Huang, R.-S., Wallraff, A., Girvin, S. M. & Schoelkopf, R. J. *Phys. Rev. A* **69**, 062320 (2004).
- Mariantoni, M. *et al.* preprint at www.arxiv.org/cond-mat/0509737 (2005).
- Storcz, M. J. *et al.* preprint at www.arxiv.org/cond-mat/0612226 (2006).

BIOLOGICAL SCALING

Does the exception prove the rule?

Arising from: P. B. Reich, M. G. Tjoelker, J.-L. Machado & J. Oleksyn *Nature* 439, 457–461 (2006)

Reich *et al.*¹ report that the whole-plant respiration rate, R , in seedlings scales linearly with plant mass, M , so that $R = c_R M^\theta$ when $\theta \approx 1$, in which c_R is the scaling normalization and θ is the scaling exponent. They also state that because nitrogen concentration (N) is correlated with c_R , variation in N is a better predictor of R than M would be. Reich *et al.* and Hedin² incorrectly claim that these “universal” findings question the central tenet of metabolic scaling theory, which they interpret as predicting $\theta = 3/4$, irrespective of the size of the plant. Here we show that these conclusions misrepresent metabolic scaling theory and that their results are actually consistent with this theory.

Reich *et al.* and Hedin do not cite an explicit caveat in metabolic scaling theory that θ will deviate from $3/4$ in plants that violate the secondary optimizing assumptions, including small plants such as seedlings and saplings^{3,4}. The core assumption^{3,5} of this theory states that carbon assimilation by the whole plant, or gross photosynthesis, P , stem fluid flow rate, Q_0 , and that the number (n_L) and mass of leaves (M_L) all co-vary and scale together, as $R \propto P \propto Q_0 \propto n_L \propto M_L \propto M^\theta$, in which θ is derived from vascular network geometry, dynamics and biomechanics. Specifically, $\theta = 1/(2a + b)$, in which a characterizes the branch radii, r , between different branching levels, k (that is, $k: r_{k+1}/r_k \equiv n^{-a}$); b characterizes the ratio of branch lengths, l , between

levels (that is, $l_{k+1}/l_k \equiv n^{-b}$)^{3,6}; and n is the branching ratio. The $\theta = 3/4$ rule then originates from secondary assumptions³, whereby the branching network is volume-filling; hydrodynamic resistance is minimized; the terminal branch (that is, M_L, R_L, P_L, Q_L) is independent of M ; and biomechanical adaptations negate the effects of gravity. Together, these assumptions lead to $a = 1/2$, $b = 1/3$, and consequently, $\theta = 3/4$. Violations of any of these assumptions yield different values^{6,7} of a and/or b , and hence of θ .

Isometric scaling relationships for small plants are the result of such violations. For small plants, gravity is relatively unimportant, so $r_k \approx l_k$ and $a \approx 1/3$, rather than $a = 1/2$ (Fig. 1a). Also, there are few branching levels, so space-filling is incomplete and $b > 1/3$. Thus, metabolic scaling theory predicts that $\theta \approx 1$ for the extreme case of very small plants. However, as plants grow, gravity becomes increasingly important and volume-filling architecture develops³, so metabolic scaling theory predicts a shift in θ from ≈ 1 to $\approx 3/4$ (Fig. 1b).

Independent data sets support these predictions. First, intraspecific scaling of metabolism⁸ from saplings to trees is closer to $3/4$ than to 1. Second, intra- and interspecific scaling of M_L all show⁴ a transition from $\theta \approx 1$ in seedlings to $\theta \approx 3/4$ in larger plants (Fig. 1b). Furthermore, the data of Reich *et al.* for R show a shift from $\theta \approx 1$ for seedlings to $\theta \approx 3/4$ for saplings that

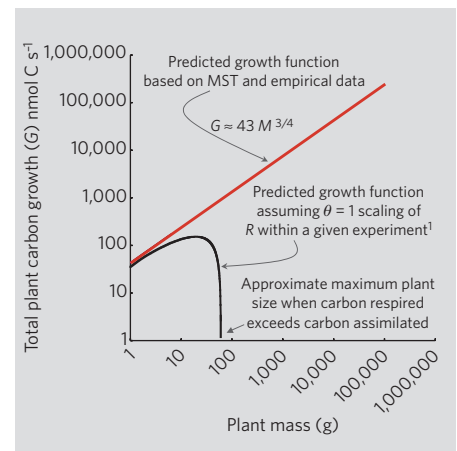


Figure 2 | Plant carbon growth. This is represented by $G = P - R$, in which $P = P_L M_L$, and P_L is the rate of assimilation. Metabolic scaling theory (MST) predicts that $M_L = c_L M^{3/4}$ for plants larger than seedlings. Given that $c_L \approx 0.7 \text{ g}^{3/4} \text{ (Fig. 1b)}$ and that the geometric mean¹⁰ of P_L ($95.5 \text{ nmol C g}^{-1} \text{ s}^{-1}$) yields $P \approx 67 M^{3/4} \text{ (nmol C g}^{-1} \text{ s}^{-1})$, Reich *et al.* claim that, within treatments, $R = c_R M^\theta$, in which $\theta \approx 1$ and $c_R \approx 24 \text{ nmol C g}^{-1} \text{ s}^{-1}$. Thus, $G = P - R \approx 67 M^{3/4} - 24 M$ (nmol C s⁻¹). Growth ceases when $G \rightarrow 0$ (and $P = R$), yielding the erroneous prediction of an unrealistic maximum size (curved black line) of $\sim 1 \text{ kg}$. The red line ($G \approx 67 M^{3/4} - 24 M$), in which c_L has units of $\text{nmol C g}^{-3/4} \text{ s}^{-1}$, is for plants larger than seedlings when $\theta = 3/4$, as predicted by MST (Fig. 1b). Note that, as discussed^{13,14}, the potential variation in c_L and c_R is influenced by nutrient stoichiometry. These results show that isometric scaling within individual experiments cannot continue as plants grow larger than seedlings.

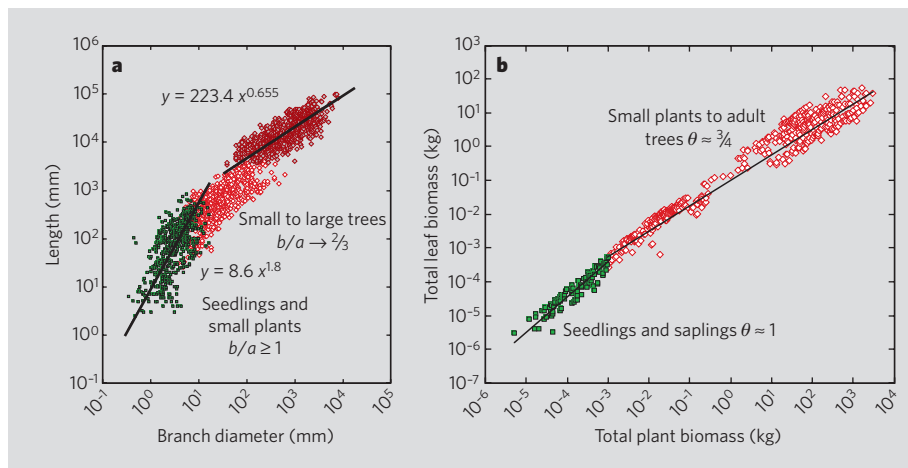


Figure 1 | Metabolic scaling theory (MST) predicts a coordinated shift in allometric exponents. a, Interspecific scaling for branch diameters ($2 \times r$) and lengths (l) from seedlings to trees¹⁵. As predicted, the scaling exponent changes from ≥ 1 for small plants and seedlings (green squares, above-ground biomass $< 1 \text{ g}$, reduced major axis (RMA) fit, $b/a = 1.8 \pm 0.12$; see text) to $b/a = 0.97 \pm 0.048$ for all the larger plants (red and brown diamonds; RMA fit not shown) to $\sim 2/3$ (RMA fit, $b/a = 0.65 \pm 0.02$) for the maximum interspecific heights achieved¹⁵ (brown diamonds). **b,** As the scaling of branch lengths and radii changes, the scaling of total leaf biomass¹², M_L , as well as R and P , are then all predicted to change. Indeed, $\theta = 1.01 \pm 0.7$ ($n = 95$, $r^2 = 0.88$) for plants with a mass of $< 1 \text{ g}$ and $\theta = 0.77 \pm 0.2$ for plants with a mass of $> 1 \text{ g}$ ($n = 563$, $r^2 = 0.959$), which is consistent with the MST-predicted shift from $\theta = 1$ to $\theta = 3/4$ and the scaling relationships in **a**.

have an above-ground biomass of more than 30 g ($\theta = 0.78 \pm 0.08$, $r^2 = 0.86$).

Reich *et al.* do not cite studies of plants larger than seedlings, which show the predicted $3/4$ -power scaling for M_L (Fig. 1b), Q_0 , carbon growth rate ($G = P - R$), and chlorophyll concentration^{5,7}. Thus, within each of their experimental treatments, extrapolation of isometric scaling of R to plants larger than seedlings will erroneously predict that the ratio of R/G should increase, as $R/G \propto M^1/M^{3/4} = M^{1/4}$, and an unrealistic maximum plant size (Fig. 2). Metabolic scaling theory resolves these inconsistencies³ by showing that $R \propto P \propto Q_0 \propto n_L$ so that R/G is invariant with size from seedlings to trees, as observed⁹.

Reich *et al.* point to the correlation between R and N as an alternative scaling mechanism. This is problematic and misleading. First, the literature¹⁰ on leaf-level physiology shows that $R \propto N$ cannot be assumed to apply to whole plants. Nitrogen is present, in varying concentrations, in all structures¹¹, so it is unclear how

N scales. As size increases, the metabolically inert pith and heartwood constitute an increasing fraction of biomass¹², but the fraction of nitrogen-rich leaves decreases as $M^{-1/4}$. Second, work extending metabolic scaling theory^{13,14} anticipated their result by showing how variation in nutrients influence R and related rates by changing the intercept of the predicted c_R , as observed¹.

For both plants and animals, metabolic scaling theory provides a general mechanistic baseline theory to predict how the scaling of metabolism is linked to the geometry and scaling of branching vascular networks, θ , temperature and nutrient stoichiometry — that is, nitrogen concentration. As a result, metabolic scaling theory can successfully resolve apparent exceptions and deviations^{3,6}, including isometric scaling in seedlings.

Brian J. Enquist^{*†}, Andrew P. Allen[‡],
James H. Brown^{†§}, James F. Gillooly^{||},

Andrew J. Kerkhoff[¶], Karl J. Niklas[#],
Charles A. Price^{*}, Geoffrey B. West[†]

^{*}Department of Ecology and Evolutionary Biology,
University of Arizona, Tucson, Arizona 85721, USA
e-mail: benquist@email.arizona.edu

[†]The Santa Fe Institute, Santa Fe, New Mexico
87501, USA

[‡]National Center for Ecological Analysis and
Synthesis, University of California, Santa Barbara,
California 93101, USA

[§]Department of Biology, University of New
Mexico, Albuquerque, New Mexico 87131, USA

^{||}Department of Zoology, University of Florida,
Gainesville, Florida 32611, USA

[¶]Department of Biology and Department of
Mathematics, Kenyon College, Gambier, Ohio
43022, USA

[#]Department of Plant Biology, Cornell University,
Ithaca, New York 14853, USA

1. Reich, P. B., Tjoelker, M. G., Machado, J.-L. & Oleksyn, J.
Nature **439**, 457–461 (2006).

2. Hedin, L. O. *Nature* **439**, 399–400 (2006).
3. West, G. B., Brown, J. H. & Enquist, B. J. *Nature* **400**, 664–667 (1999).
4. Sack, L., Marañón, T., Grubb, P. J., Enquist, B. J. & Niklas, K. J. *Science* **296**, 1923 (2002).
5. Niklas, K. J. & Enquist, B. J. *Proc. Natl Acad. Sci. USA* **98**, 2922–2927 (2001).
6. Price, C. A. & Enquist, B. J. *Ecology* (in the press).
7. Enquist, B. J. *Tree Physiol.* **22**, 1045–1064 (2002).
8. Hemmingsen, A. M. *Rep. Steno Memorial Hosp. Nord. Insulinlab.* **4**, 7–51 (1950).
9. Gifford, R. M. *Funct. Plant Biol.* **30**, 171–186 (2003).
10. Wright, I. J. *et al. Nature* **428**, 821–827 (2004).
11. Kerkhoff, A. J., Fagan, W. F., Elser, J. J. & Enquist, B. J. *Am. Nat.* **168**, E103–E122 (2006).
12. Enquist, B. J. & Niklas, K. J. *Science* **295**, 1517–1520 (2002).
13. Kerkhoff, A. J., Enquist, B. J., Elser, J. J. & Fagan, W. F. *Glob. Ecol. Biogeogr.* **14**, 585–598 (2005).
14. Gillooly, J. F., Charnov, E. L., West, G. B., Savage, V. M. & Brown, J. H. *Nature* **417**, 70–73 (2002).
15. Niklas, K. J. & Spatz, H. C. *Proc. Natl Acad. Sci. USA* **101**, 15661–15663 (2004).

Competing interests: declared none.
doi:10.1038/nature05548

BIOLOGICAL SCALING

Reich et al. reply

Replying to: B. J. Enquist *et al. Nature* **445**, doi: 10.1038/nature05548 (2007)

Enquist *et al.*¹ raise several points that they claim cast doubt on our findings and interpretation² regarding whole-plant relations of respiration, R , with plant mass, M , and total plant nitrogen content, N . We agree with Enquist *et al.* that R does not scale isometrically with M across all plants. However, their assertion that we claim that isometric scaling ($R \propto M^\theta$, with $\theta = 1$) is universal in plants of all sizes is incorrect — in fact, we conclude the opposite², noting that there is isometric scaling within individual experiments, non-isometric scaling of respiration versus mass across all data pooled, and no common relation across all data².

Enquist *et al.*¹ also claim that isometric scaling is evident only for very small seedlings that have a dry mass of less than 3 g (for example, see their Fig. 1b), but that leaf mass in larger plants is proportional to $M^{3/4}$ and $R \propto M^{3/4}$. By contrast, our results show that $R \propto M^{1.0}$ for plants ranging from 0.01 to 50 g, and from 1 to 1,000 g, within individual studies (Fig. 1a in ref. 2) and that there are significant differences in the intercepts of these relationships². Thus, $\theta < 1$ for all plants pooled and differs in individual studies, such that no single $R \propto M$ scaling model can apply, whereas $R \propto N^{1.0}$ reconciles all such differences². Enquist *et al.*¹ also criticize us for not noting their earlier suggestion³ that θ might deviate from $\theta = 3/4$ for small plants, although they themselves predicted $3/4$ metabolic scaling in plants of all sizes^{3–5}.

The allometry presented in Fig. 1 of Enquist *et al.*¹ does not address our findings, which

directly test their prediction^{3–5} that $R \propto M^{3/4}$. These allometric relations are not equivalent to measures of plant metabolism and are, at best, only indirectly relevant. Irrespective of its relevance to scaling, Enquist *et al.* claim that allometric relations (their Fig. 1) for leaf $M \propto$ total M^θ show isometric scaling for seedlings of less than 1 g and $\theta \approx 3/4$ for larger plants, although their Fig. 1 shows a θ that changes continuously across the entire gradient of size. As noted previously in a critique⁶ of the works of West, Brown and Enquist, arbitrary data parsing such as in Fig. 1 of Enquist *et al.*¹ can lead to widely varying θ values: for instance, in their Fig. 1b, leaf $M \propto$ total M^θ has $\theta \approx 0.70$ for plants of less than 1,000 g ($n = 334$), 1.10 for plants from 50,000 to 500,000 g ($n = 158$), and 2.20 for plants of more than 1,000,000 g ($n = 25$). Furthermore, an empirical study⁷ of leaf to whole-tree allometry for large trees showed that θ could vary from much lower than $3/4$ to much more than 1.0 depending on the nature of the data set, further refuting any notion of a constant allometry of leaf M to total plant M following $3/4$ scaling rules.

Nonetheless, the work by Enquist and colleagues has stimulated the field by providing testable predictions³, such as a universal $R \propto M^{3/4}$ relationship⁴. The plant data of Gillooly *et al.*⁴ ($n = 20$) were mostly for fruits or tubers (not plants) such as bananas, lemons, strawberries and carrots, with data on R and M obtained from unrelated sources. Given the general importance of this predicted relationship, including in subsequent synthesis and

modelling by this group^{5,8}, we tested it using a comprehensive data set² that included coupled whole-plant mass and respiration measures. Those data do not support predictions of a universal $R \propto M^{3/4}$ scaling in plants.

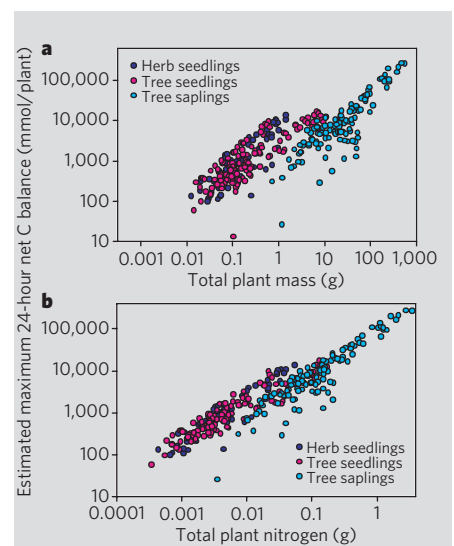


Figure 1 | Evidence for positive carbon balance across all plant sizes. **a, b**, Estimated maximum 24-hour net carbon balance in relation to total plant mass (**a**) and total plant nitrogen (**b**) for the plants in ref. 2. The 24-hour net carbon balance is based on predicting light-saturated rates of net photosynthesis from photosynthesis–nitrogen relationships¹¹, and scaling carbon gain and respiratory carbon loss to the whole plant based on tissue nitrogen and biomass distribution.

Enquist *et al.* largely sidestep our main findings, namely the whole-plant scaling of $R \propto N^{1.0}$. This finding is supported across five orders of magnitude in plant size and, unlike $R \propto M^{3/4}$ or $R \propto M^{1.0}$, is consistent within as well as across all data sets. They claim¹ that the idea of general scaling of R in relation to N is problematic and misleading, which ignores abundant evidence of globally convergent mass-specific scaling relations in terms of both photosynthesis and respiration being proportional to tissue nitrogen concentration^{9–11}.

Our findings² are misrepresented by Enquist *et al.*¹ when they suggest that these are incompatible with the existence of plants over 60 g, because such plants will respire more carbon than they can acquire (although we did in fact present data for R in much larger plants²). Their simulation creates a problem that does not exist by using assumptions we both agree are incorrect, including universal $R \propto M^{1.0}$ scaling, which the data do not support², and by arbitrary selection of photosynthesis and respiration rates without regard to whether these are appropriately scaled to each other or to plant nitrogen concentrations. Thus, the “erroneous prediction of an unrealistic maximum plant size”, incorrectly attributed to our findings², is solely a result

of their model assumptions¹, is unsupported by published data and cannot be reconciled with data in Fig. 1a. By contrast, net photosynthetic rates generally scale with tissue nitrogen¹¹ and are about ten times higher than respiration rates at any given leaf nitrogen concentration¹¹. Modelling net photosynthesis for plants in ref. 2 from these relationships¹¹, and scaling carbon gain and respiratory carbon loss to the whole plant based on tissue nitrogen and biomass distribution, we find positive maximum 24-hour whole-plant net carbon gain across plants of all sizes (Fig. 1a). In addition, the maximum whole-plant carbon gain is positively related to total plant nitrogen (Fig. 1b), indicating that a nitrogen-based scaling approach is consistent with observations on plants that maintain a positive carbon balance.

A debate aimed at reconciling models that focus on generality in scaling relationships^{3,4}, mechanistic understanding of the underlying biology^{5,12–14}, and uncertainties regarding statistical approaches^{6,14} is sorely needed to advance this field.

Peter B. Reich*, **Mark G. Tjoelker†**,
Jose-Luis Machado‡, **Jacek Oleksyn§**

*Department of Forest Resources, University of Minnesota, St Paul, Minnesota 55108, USA

e-mail: preich@umn.edu

†Department of Forest Science, Texas A&M University, College Station, Texas 77843, USA

‡Department of Biology, Swarthmore College, Swarthmore, Pennsylvania 19081, USA

§Polish Academy of Sciences, Institute of Dendrology, 62-035 Kornik, Poland

1. Enquist, B. J. *et al.* *Nature* **445**, doi:10.1038/nature05548 (2007).
2. Reich, P. B., Tjoelker, M. G., Machado, J.-L. & Oleksyn, J. *Nature* **439**, 457–461 (2006).
3. West, G. B., Brown, J. H. & Enquist, B. J. *Nature* **400**, 664–667 (1999).
4. Gillooly, J. F., Brown, J. H., West, G. B., Savage, V. M. & Charnov, E. L. *Science* **293**, 2248–2251 (2001).
5. Brown, J. H., Gillooly, J. F., Allen, A. P., Savage, V. M. & West, G. B. *Ecology* **85**, 1771–1789 (2004).
6. Kozłowski, J. & Konarzewski, M. *Funct. Ecol.* **19**, 739–743 (2005).
7. Mäkelä, A. & Valentine, H. T. *Ecology* **87**, 2967–2972 (2006).
8. Enquist, B. J. *et al.* *Nature* **423**, 639–642 (2003).
9. Field, C. & Mooney, H. A. in *On the Economy of Plant Form and Function* (ed. Givnish, T. J.) 25–55 (Cambridge University Press, Cambridge, 1986).
10. Ryan, M. G. *Ecol. Appl.* **1**, 157–167 (1991).
11. Wright, I. J. *et al.* *Nature* **428**, 821–827 (2004).
12. Mencuccini, M. *Plant Cell Envir.* **26**, 163–182 (2003).
13. Meinzer, F. C., Bond, B. J., Warren, J. M. & Woodruff, D. R. *Funct. Ecol.* **19**, 558–565 (2005).
14. Glazier, D. S. *BioScience* **56**, 325–332 (2006).

doi:10.1038/nature05549

BIOLOGICAL SCALING

Hedin replies

Replying to: B. J. Enquist *et al.* *Nature* **445**, doi:10.1038/nature05548 (2007)

In my News & Views article¹, I argued for the need to include factors other than body size to create a truly universal theory of plant scaling. I based my expectations for the metabolic scaling theory on Enquist's own conclusion that “unlike animal clades...all plants comply with a single allometric formula that spans 20 orders of magnitude in body mass”². Because in this recent analysis the authors applied a $3/4$ scaling slope across plants ranging in size from unicellular algae ($< 10^{-7}$ g body mass), to duckweed (10^{-5} to 10^{-2} g), to forest herbs and trees including giant *Sequoia* (10^{-1} to 10^7 g), I found the comparison to the data of Reich *et al.*³ entirely reasonable. Nevertheless, I explicitly discussed my concern about whether and how the findings of Reich *et al.* could extend to mature trees¹.

I am glad to see the more nuanced state-

ment of metabolic scaling theory by Enquist *et al.*⁴, which now explicitly introduces the idea of scale dependence in scaling slope between smaller and larger plants. This seems to be an important improvement, especially as many of Earth's plant species are smaller than adult trees, and within the size range considered by Reich *et al.* ($< 10^4$ g). What is less clear, however, is whether the proposed change in slope is abrupt or gradual, and across what size range it takes place. However, this revision by Enquist *et al.* does not address the effect of nitrogen on plant respiration⁵ shown by Reich *et al.*, an effect that is well documented theoretically and experimentally at the scale of individual leaves as well as of whole plants^{5,6}. It is interesting that there is even recent evidence that plant hydraulic architecture varies as a function of nitrogen supply⁷. Future investigations should seek to

resolve this vexing interaction of body size, nutrient status and metabolic scaling slopes.

Lars O. Hedin

Department of Ecology and Evolutionary Biology, Princeton University, Princeton, New Jersey 08540, USA

e-mail: lhedin@princeton.edu

1. Hedin, L. O. *Nature* **439**, 399–400 (2006).
2. Niklas, K. J. & Enquist, B. J. *Proc. Natl Acad. Sci. USA* **98**, 2922–2927 (2001).
3. Reich, P. B., Tjoelker, M. G., Machado, J.-L. & Oleksyn, J. *Nature* **439**, 457–461 (2006).
4. Enquist, B. J. *et al.* *Nature* **445**, doi:10.1038/nature05548 (2007).
5. Cannell, M. G. R. & Thornley, J. H. M. *Ann. Bot.* **85**, 45–54 (2000).
6. Ryan, M. G., Hubbard, R. M., Pongracic, S., Raison, R. J. & McMurtrie, R. E. *Tree Physiol.* **16**, 333–343 (1996).
7. Bucci, S. J. *et al.* *Plant Cell Envir.* **29**, 2153–2167 (2006).

doi:10.1038/nature05550

Termination of asymmetric cell division and differentiation of stomata

Lynn Jo Pillitteri¹, Daniel B. Sloan¹, Naomi L. Bogenschutz¹ & Keiko U. Torii^{1,2,3}

Stomata consist of a pair of guard cells that mediate gas and water-vapour exchange between plants and the atmosphere. Stomatal precursor cells—meristemoids—possess a transient stem-cell-like property and undergo several rounds of asymmetric divisions before further differentiation. Here we report that the *Arabidopsis thaliana* basic helix–loop–helix (bHLH) protein MUTE is a key switch for meristemoid fate transition. In the absence of MUTE, meristemoids abort after excessive asymmetric divisions and fail to differentiate stomata. Constitutive overexpression of MUTE directs the entire epidermis to adopt guard cell identity. MUTE has two paralogues: FAMA, a regulator of guard cell morphogenesis, and SPEECHLESS (SPCH). We show that SPCH directs the first asymmetric division that initiates stomatal lineage. Together, SPCH, MUTE and FAMA bHLH proteins control stomatal development at three consecutive steps: initiation, meristemoid differentiation and guard cell morphogenesis. Our findings highlight the roles of closely related bHLHs in cell type differentiation in plants and animals.

A key developmental innovation of land plants was the evolution of specialized epidermal structures called stomata. In *Arabidopsis*, a stomatal lineage arises from an undifferentiated protodermal cell called a meristemoid mother cell (MMC), which divides asymmetrically to give rise to two daughter cells with distinct identities: a pavement cell and a meristemoid. The meristemoid undergoes several rounds of asymmetric division before differentiating into a round, guard mother cell (GMC). The GMC divides symmetrically to generate a pair of guard cells that surround a microscopic pore¹. Density and distribution of stomata are influenced by environmental factors as well as developmental programmes^{2,3}. Recent studies have revealed that stomatal patterning is controlled by positional cues. The current model suggests that the subtilisin-like protease STOMATAL DENSITY AND DISTRIBUTION 1 (SDD1) generates a cell–cell signal that is interpreted by the transmembrane receptor TOO MANY MOUTHS (TMM) and three ERECTA family receptor-like kinases ERECTA, ERECTA-LIKE 1 (ERL1) and ERL2. This signalling pathway is proposed to be mediated via mitogen-activated protein kinase (MAP kinase) cascades^{4–8}. Loss-of-function mutations in these loci disrupt epidermal patterning with stomata produced adjacent to each other or in clusters. In addition, two putative transcription factors FAMA and FOUR LIPS (FLP) regulate the final differentiation of guard cells: their loss-of-function mutations result in reiterative symmetric divisions of GMCs^{7,9}.

Although our understanding of genes regulating stomatal development has greatly advanced, an intrinsic factor that specifies differentiation of a meristemoid had not yet been discovered. If such a gene exists, then the loss-of-function mutation may extend the lifespan of meristemoids, such that mutant plants should exhibit excessive rounds of asymmetric division but no GMC differentiation. On the basis of this hypothesis, we conducted a sensitized genetic screen and identified *MUTE*.

Key switch for meristemoid transition

The loss-of-function *mute* mutation resulted in the complete absence of stomata. *mute* plants are small, pale and sterile, presumably owing

to severe defects in gas exchange and transpiration (Fig. 1a). Wild-type meristemoids undergo 1–3 rounds (mean = 2.23 ± 0.13) of asymmetric division before differentiating into a GMC (Fig. 1b, d)¹. In contrast, *mute* meristemoids undergo 3–6 rounds (mean = 4.46 ± 0.20) of asymmetric division, suggesting that *mute* meristemoids have an extended period of replication (Fig. 1c, d). The inward-spiral nature of the reiterative asymmetric divisions created a rosette pattern in the *mute* epidermis with an arrested, small triangular meristemoid at the centre (Fig. 1).

The molecular character of arrested meristemoids was investigated using stomatal cell-type-specific markers (Fig. 1e–l). *TMM* and *ERL1* mark stomatal lineage cells with the highest expression in meristemoids (Fig. 1e, f)^{6,8}. The arrested *mute* meristemoids expressed high levels of *TMM::TMM-GFP*, a translational fusion of *TMM* with a green fluorescent protein, and *ERL1::GUS*, a reporter β -glucuronidase driven by the *ERL1* promoter^{6,8} (Fig. 1i and j, respectively). In addition, the rosette of cells surrounding the arrested meristemoid exhibited faint expression of these reporters (Fig. 1e, f, i, j), suggesting their identity as stomatal lineage ground cells (SLGCs)—larger daughter cells derived from the reiterative asymmetric divisions of a single meristemoid⁸.

To investigate whether arrested meristemoids progress into GMCs, we further examined the expression of *FAMA::FAMA-GFP*, a translational fusion of GFP and FAMA (Supplementary Methods). In the wild-type leaf epidermis, FAMA-GFP was specifically detected in the nuclei of GMCs and early, immature guard cells, but not in meristemoids (Fig. 1g). In *mute*, no FAMA-GFP expression was detected (Fig. 1k). Likewise, the arrested meristemoids in *mute* did not express the mature-guard-cell-specific GFP marker E994 (Fig. 1h, l)¹⁰, suggesting that these cells failed to establish either GMC or guard cell identity^{7,9}. On the basis of these findings, we conclude that *MUTE* controls differentiation of meristemoids to GMCs.

Genetic interactions

To place *MUTE* within the context of genetic pathways for stomatal patterning and differentiation, we next investigated genetic

¹Department of Biology and ²Institute for Stem Cell and Regenerative Medicine, University of Washington, Seattle, Washington 98195, USA. ³CREST, Japan Science and Technology Agency, Saitama, 332-0012, Japan.

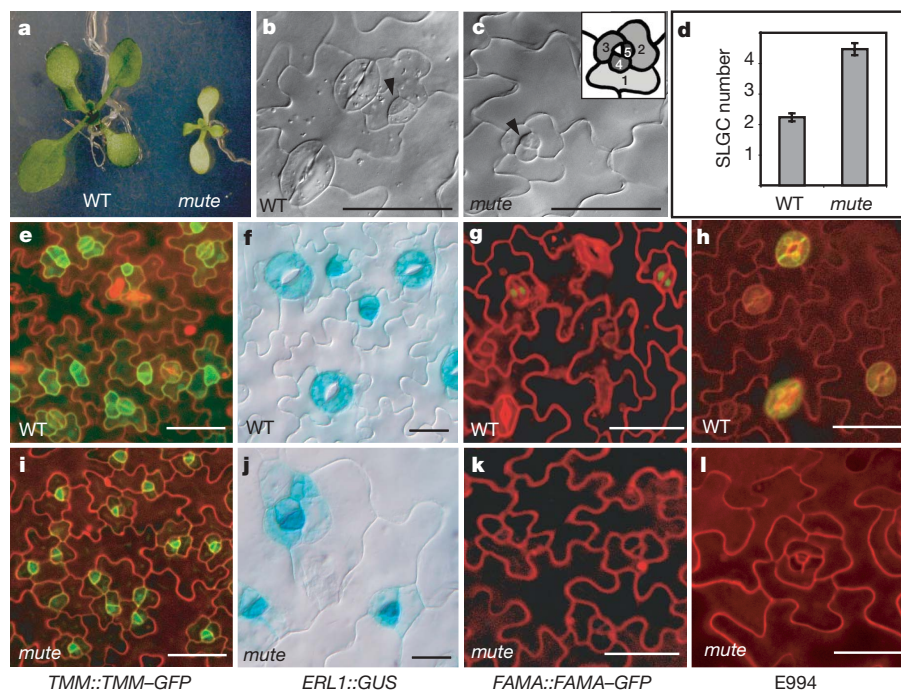


Figure 1 | *MUTE* is required for meristemoid differentiation. **a**, *mute* phenotype. Unlike the wild type (WT), the *mute* plant is pale and stunted. **b**, **c**, Abaxial leaf epidermis of WT (**b**) and *mute* (**c**), with meristemoids indicated by arrowheads. Inset, tracing of a *mute* meristemoid with successive numbering of SLGCs. **d**, Mean numbers of SLGCs surrounding an immature stoma (WT) or an arrested meristemoid (*mute*). Mean is \pm s.e.m., $n = 25$ (t -test, $P < 0.00001$). **e–l**, Expression of molecular markers in WT

(**e–h**) and *mute* (**i–l**). Arrested meristemoids in *mute* express high levels of stomatal lineage markers TMM::TMM-GFP (green; **i**) and ERL1::GUS (blue; **j**), but does not express GMC/immature guard cell marker FAMA::FAMA-GFP (**k**) and mature guard cell marker E994 (**l**). For **e**, **g–i**, **k**, **l**, the epidermal cell periphery is highlighted by propidium iodide (red). Scale bars, 20 μ m.

interactions of *MUTE* with known regulators of stomatal development. First, double and quadruple mutants were produced between *mute* and cell–cell signalling mutants *tmm*, *sdd1* and *erecta*; *erl1*; *erl2* (Fig. 2a–f). The leaf epidermis of *tmm* or *erecta*; *erl1*; *erl2* mutants exhibits clusters of adjacent stomata (Fig. 2a, e), whereas that of *sdd1* shows increased overall stomatal density with a few

stomatal clusters (Fig. 2c). ‘Bubble-like’ clusters of small cells were observed in the epidermis of *mute*; *tmm* and *mute*; *erecta*; *erl1*; *erl2* (Fig. 2b, f). These small cells expressed TMM::GUS and ERL1::GUS at high levels, indicating that they are stomatal lineages, most probably meristemoids and SLGCs (Fig. 2b inset; Supplementary Fig. 1). The cells in these clusters are oriented in random angles, indicating the

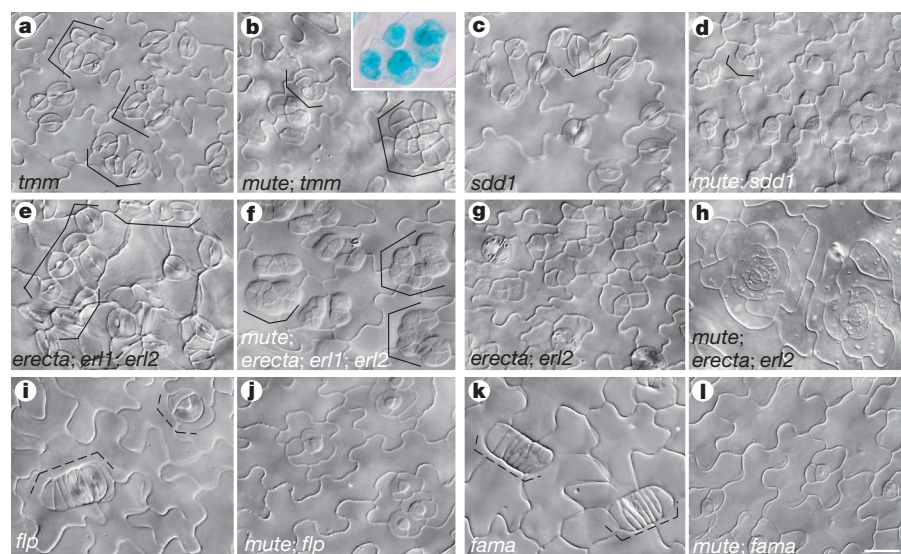


Figure 2 | Genetic interactions between *MUTE* and known regulators of stomatal patterning and differentiation. **a–l**, Abaxial leaf epidermis of *tmm* (**a**), *mute*; *tmm* (**b**), *sdd1* (**c**), *mute*; *sdd1* (**d**), *erecta*; *erl1*; *erl2* (**e**), *mute*; *erecta*; *erl1*; *erl2* (**f**), *erecta*; *erl2* (**g**), *mute*; *erecta*; *erl2* (**h**), *flp* (**i**), *mute*; *flp* (**j**), *fama* (**k**) and *mute*; *fama* (**l**). Solid brackets indicate clusters of stomata (**a**, **c**, **e**) or meristemoids (**b**, **d**, **f**). Dashed brackets indicate stacks of symmetrically

divided GMC or guard cells (**i**, **k**). The bubble-like clusters of cells in *mute*; *tmm* exhibit high expression of ERL1::GUS (**b**, inset). For the phenotypes of wild type and *mute*, see Fig. 1b, c. For expression of ERL1::GUS and TMM::GUS in wild type, *mute* and *tmm*; *mute*, see Supplementary Fig. 1. Images are taken under the same magnification. Scale bar, 20 μ m.

occurrence of randomized asymmetric division. This is consistent with the roles of *TMM* and the three *ERECTA*-family genes in regulating the frequency and orientation of asymmetric division in stomatal lineages^{8,11}. The epidermis of *mute; sdd1* has an increased density of arrested meristemoids with two meristemoids adjacent to each other observed occasionally (Fig. 2d). Overall, these results suggest that *MUTE* and the cell-cell signalling genes interact additively, whereas *MUTE* is epistatic with regard to guard cell differentiation.

erecta; erl2 double mutants exhibit an increased frequency of asymmetric divisions with occasional patches of SLGCs that do not include stomata (Fig. 2g). The phenotype is due to inhibitory effects of *ERL1* in the binary fate decision of a meristemoid to be a GMC rather than an SLGC⁸. Interestingly, the *erecta; erl2* double mutation

increased the number of SLGCs surrounding the single, arrested *mute* meristemoid, resulting in a striking, 'large rosette' phenotype (Fig. 2h). Therefore, *ERL1* may enhance the longevity of meristemoids in the *mute* background.

In *flp* and *fama*, differentiation of a meristemoid to a GMC occurs normally. However, subsequent guard cell differentiation is abnormal; the GMC reiterates symmetric divisions and forms stacks of cell clusters (Fig. 2i, k)^{7,9}. The phenotypes of *mute; flp* and *mute; fama* double mutants were indistinguishable from that of *mute* (Fig. 2i–l). The epistasis of *MUTE* over *FLP* and *FAMA* is consistent with *MUTE* acting at an earlier step of stomatal differentiation.

MUTE triggers stomatal differentiation

By map-based cloning, we identified the *MUTE* gene as At3g06120, which encodes the putative bHLH transcription factor bHLH45 (Supplementary Methods; Supplementary Fig. 2)¹². *mute* possesses a single G→A nucleotide substitution at the splice donor site of the first intron (Fig. 3a). This abolishes the proper splicing of transcripts and results in splicing variants, which confer premature truncations at various positions within the bHLH domain (Fig. 3b, c). The bHLH domain is required for both DNA binding and dimerization¹³, and therefore *mute* is most probably a null allele. Introduction of the *bHLH45* open reading frame with its native promoter into *mute* plants fully restored the wild-type phenotype, confirming that *bHLH45* is *MUTE* (Supplementary Fig. 3).

To examine promoter activity and subcellular localization, we used the native *MUTE* promoter to drive expression of the GUS reporter (*MUTE::GUS*) and the translational fusion of a full-length *MUTE* protein and GFP (*MUTE::MUTE-GFP*). The latter construct complemented the *mute* phenotype, indicating that the *MUTE*–GFP fusion protein is functional (Supplementary Fig. 3). *MUTE::GUS* expression was highest in a subset of meristemoids that have undergone a few rounds of asymmetric division, with residual activity in GMC and immature guard cells (Fig. 3d). The *MUTE*–GFP fusion protein was localized in the nuclei of a subset of meristemoids that have undergone a few rounds of asymmetric division and in recently transitioned GMCs (Fig. 3e). No GFP signal was detected in other epidermal cells, including newly formed meristemoids and both immature and mature guard cells (Fig. 3e). These findings support the hypothesis that *MUTE* acts as an intrinsic transcription factor that creates changes in meristemoids to terminate their stem-cell-like properties and trigger GMC differentiation.

We next ectopically overexpressed *MUTE*. *CaMV35S::MUTE* plants exhibited a striking phenotype, converting all epidermal cells into stomata (Fig. 3f). Many of these ectopic stomata expressed the mature guard cell marker E994 (Fig. 3g). In less severe lines, a subset of epidermal pavement cells adopted partial guard cell identity. These

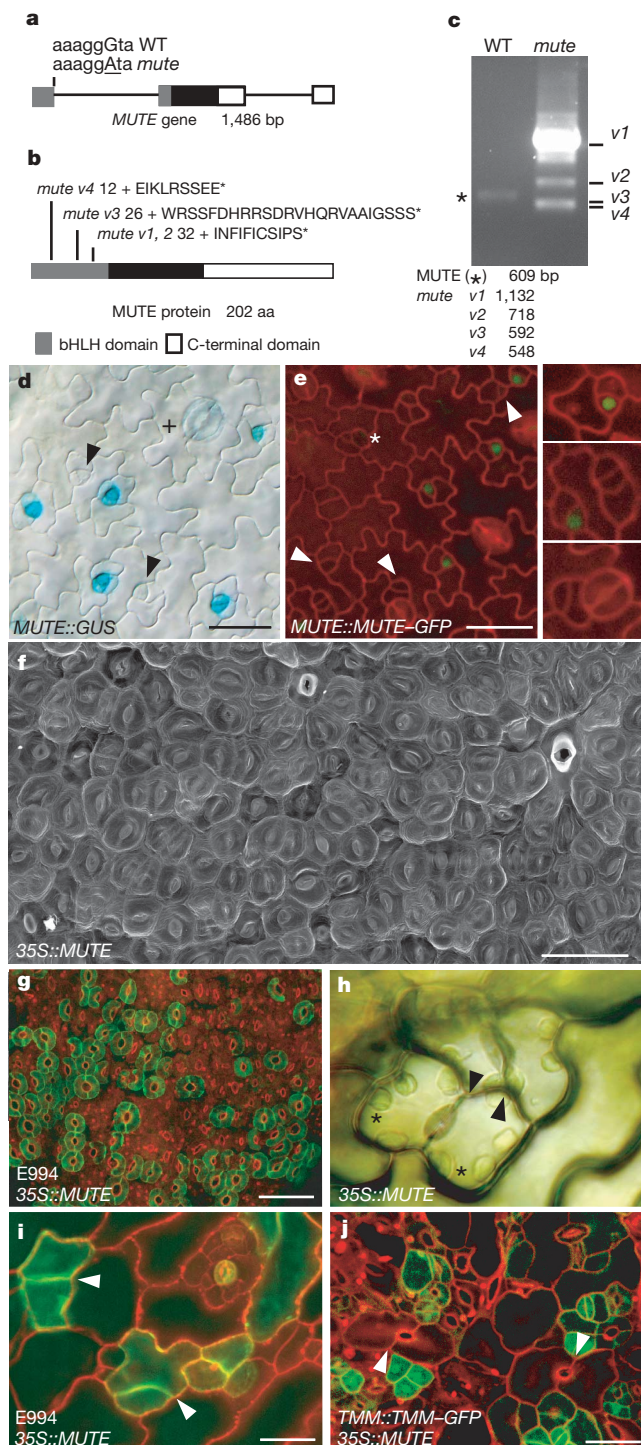


Figure 3 | MUTE bHLH protein triggers stomatal differentiation. **a**, *MUTE* gene structure. In *mute*, the G→A substitution occurred at the first intron splice donor site (underlined). **b**, *MUTE* protein structure. Four *mute* splicing variants (see **c**) result in a truncation within the bHLH domain. Position of frame shifts and the out-of-frame amino acid (aa) sequence up to the stop codon (asterisk) are indicated. For wild-type *MUTE* protein sequence, see Supplementary Fig. 4. **c**, PCR with reverse transcription (RT–PCR) analysis of splicing variants. Size of each transcript indicated. **d**, *MUTE::GUS* marks a subset of meristemoids and GMCs with residual activity in guard cells (+). Young meristemoids (arrowhead) do not express GUS activity. **e**, A functional, translational fusion protein *MUTE*–GFP is detected in the nuclei of meristemoids that have undergone asymmetric divisions, but not in newly formed meristemoids (arrowhead), immature guard cells (asterisk) or mature guard cells. Insets: enlargements. **f**, **g**, Ectopic overexpression of *MUTE* converts the entire epidermis to guard cells. **f**, Scanning electron microscope image. **g**, Mature guard cell marker E994. **h–j**, Weak overexpression lines. Epidermal cells with mixed pavement–guard-cell identity possess chloroplasts (asterisks, **h**), express E994 (**i**), and form a symmetric division plane with a 'faux pore' (**h–j**, arrowheads). Scale bars, 20 μ m.

pavement cells contain chloroplasts, express the mature guard cell marker E994, and produce a symmetric division plane with a 'faux pore' (Fig. 3h–j). Together, these results demonstrate that *MUTE* is capable of directing all protoderm cells to differentiate into guard cells and, depending on the strength of *MUTE* action, these cells may express characteristics of both pavement and guard cells.

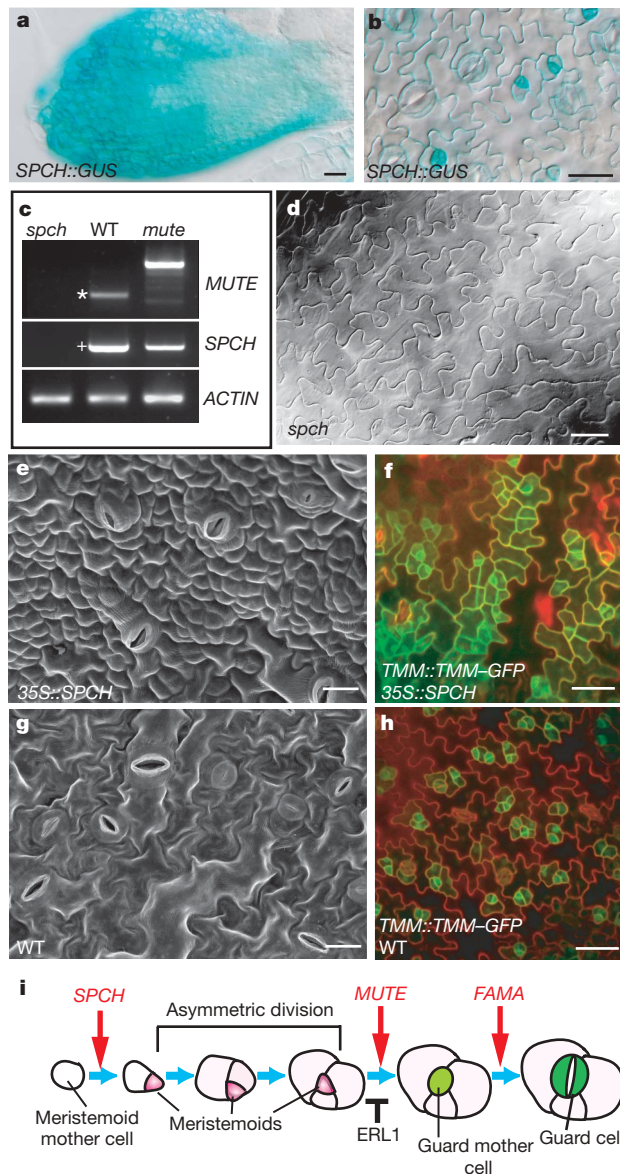


Figure 4 | *SPCH*, a paralogue of *MUTE*, initiates stomatal cell lineages. a, b, *SPCH::GUS* expression in the first leaf primordia of a 4-day-old seedling (a) and in the abaxial leaf epidermis of a 3-week-old seedling (b). c, RT-PCR analysis. The T-DNA insertion *spch* mutant does not accumulate *SPCH* (+) or *MUTE* (asterisk) transcripts. Note that *mute* produces aberrant splice variants. *ACTIN* serves as a positive control. d, *spch* develops an epidermis solely made of pavement cells. e–h, Ectopic overexpression of *SPCH* confers a highly divided epidermis with small cells. e, Scanning electron microscope image. f, These small cells express high levels of *TMM::TMM-GFP*. g, h, Control WT epidermis. Scale bars, 20 μ m. i, A model for consecutive actions of three bHLH genes. *SPCH* drives the first asymmetric division that initiates stomatal development. *MUTE* controls termination of asymmetric division and differentiation of meristemoids into GMCs. *FAMA* regulates differentiation of mature guard cells from GMCs. *ERL1* affects the binary decision of meristemoid versus GMC identity and hence inhibits GMC differentiation. Red arrow, positive regulation; black T-bar, negative regulation.

Consecutive actions of three bHLH proteins

The genome-wide molecular phylogenetic analysis of *Arabidopsis* bHLH family showed that *MUTE* belongs to subfamily III with two closely related paralogues, *SPEECHLESS* (*SPCH*)/bHLH98 (At5g53210) and *FAMA*/bHLH97 (At3g24140)^{12,14–16} (Supplementary Fig. 4). They share high sequence similarity in the bHLH domain and carboxy-terminal region. However, the *MUTE* protein lacks the amino-terminal extension domain (Supplementary Fig. 4). *FAMA* is expressed in GMCs and immature guard cells (Supplementary Fig. 5; Fig. 1g), consistent with its known role in controlling the transition from GMC to guard cells⁷.

To unravel the developmental function of *SPCH*, the closest paralogue of *MUTE*, we next investigated its expression pattern as well as loss-of-function and gain-of-function phenotypes. *SPCH* promoter activity (*SPCH::GUS*) was observed broadly in the protoderm of leaf primordia and localized in stomatal lineage cells later in development (Fig. 4a, b; Supplementary Fig. 5). The T-DNA insertion *spch* loss-of-function mutant exhibited an intriguing epidermal phenotype consisting solely of jigsaw-puzzle-shaped pavement cells, thus lacking any stomatal lineage cells (Fig. 4c, d). In contrast, ectopic overexpression of *SPCH* by the *CaMV35S* promoter produced a highly divided epidermis with numerous small cells (Fig. 4e, g). These cells strongly express *TMM::TMM-GFP*, indicating that they probably have the identity of stomatal lineage cells (Fig. 4f, h). On the basis of these results, we conclude that *SPCH* directs the first asymmetric division that initiates the stomatal lineage. The *spch* mutant does not express *MUTE* transcripts, consistent with *SPCH* acting before *MUTE* at the initial step of stomatal development (Fig. 4c).

Discussion

We have shown that *MUTE* is a key switch gene for meristemoids to acquire GMC identity and that ectopic *MUTE* expression triggers stomatal differentiation. Our findings highlight both similarities and differences in the control of asymmetric division and cell type differentiation between plants and animals. During *Drosophila melanogaster* central nervous system development, a neuroblast divides asymmetrically to produce another neuroblast and a differentiated ganglion mother cell¹⁷. A transcription factor, Prospero, is unequally allocated during asymmetric division to specify cell fate¹⁸. In contrast, *MUTE* protein is first detected in the nuclei of meristemoids just before GMC differentiation. This suggests that plants are able to monitor the age of meristemoids, possibly by tracking the rounds of asymmetric division, and subsequently induce *MUTE* (Fig. 3e). The longevity of meristemoids in *mute*; *erecta*; *erl2* triple mutants (Fig. 2h) implies that positional signals mediated by *ERL1* might intersect with this fate decision (Fig. 4i).

We and others¹⁹ discovered that three closely related bHLH proteins control three critical steps of stomatal development: initiation by *SPCH*, meristemoid differentiation by *MUTE*, and final guard cell differentiation by *FAMA* (Fig. 4i; ref. 19). *SPCH* triggers asymmetric division whereas *MUTE* terminates asymmetrically dividing meristemoids. Therefore, these bHLH proteins may act in an opposing manner in cell division control, but cooperate in stomatal differentiation. The basal lineages of extant land plants, such as *Selaginella* sp., seem to differentiate GMCs without reiterative asymmetric divisions of a precursor cell^{20,21}. Diversification of this subfamily of bHLH proteins, possibly by gene duplication, may have allowed plants to acquire complex stomatal patterning as they conquered terrestrial environments.

Our discoveries emphasize the roles of bHLH proteins in cell type determination and differentiation in plants and animals. During myogenesis and neurogenesis in animals, a series of closely related bHLH proteins, such as the four mammalian myogenic regulatory proteins, MyoD, Myf-5, myogenin and MRF4, as well as the *Drosophila* achaete–scute complex, regulate sequential events in a hierarchical fashion^{22–24}. Muscle fibres and neurons are specialized cell types, numbers of which are tightly regulated by extrinsic cell–cell signals²⁵. Similarly, proper spacing and density of stomata, which is

critical for plant physiology and function, are controlled by positional signals mediated by receptor kinases and MAP kinase cascades. Understanding the interplay between cell–cell signals and SPCH, MUTE and FAMA function, as well as tracing evolutionary origins of the three paralogous bHLH proteins, may elucidate the conservation and innovation of asymmetric division and cell type differentiation adopted by land plants.

METHODS

Plant materials. The *Arabidopsis thaliana* Columbia (Col) accession was used as a wild type. All mutants are in the Col background, except for *flp-7*, which is in the Landsberg *erecta* background. *sdd1* was originally in C24 and was outcrossed into Col twice. The *mute* mutant was backcrossed into Col three times before analysis. T-DNA insertion alleles of *FAMA* (Salk_100073) and *SPCH* (SAIL_36_B06) were obtained from SIGnAL (Salk Institute) and ABRC (Ohio State University). For details, see Supplementary Methods.

Genetic screen and map-based cloning. *mute* was identified as a novel, arrested-meristemoid phenotype from an ethyl-methanesulphonate-treated M₁ population of *erecta-105; erl2*. A subsequent test cross revealed that *mute* segregates as a single recessive trait: 14 of 32 F₁ plants (43.8%) carried the *mute* gene on the basis of the segregation in the next generation ($\chi^2 = 0.5$, $P = 0.48$), and 207 of 851 F₂ plants (24.3%) showed the *mute* phenotype ($\chi^2 = 0.21$, $P = 0.65$). F₂ mapping populations were generated from a single cross of M₃ *mutel* +; *erecta-105; erl2* × *Ler*. For details, see Supplementary Methods. A list of primer sequences is available as Supplementary Tables 1 and 2.

Plasmids and transgenic plants. The following constructs were generated for this study: *SPCH::GUS* (pLJP149), *MUTE::GUS* (pLJP138), *FAMA::GUS* (pLJP146), *MUTE::MUTE-GFP* (pLJP155), *FAMA::FAMA-GFP* (pLJP156), *MUTE::MUTE-HA* (pLJP158), *CaMV35S::SPCH* (pLJP152), and *CaMV35S::MUTE* (pLJP151). See Supplementary Table 3 for a list of primer sequences used for plasmid construction. For details, see Supplementary Methods.

Quantitative analysis of SLGCs. The number of asymmetric divisions per stomatal lineage between *mute* and wild-type plants was quantified using a *TMM::GUS* reporter line⁸. Cells surrounding a meristemoid (*mute*) or an immature stoma (wild type) expressing β -glucuronidase were considered SLGCs and counted for the analysis.

Microscopy. Detailed protocols, sample preparations, microscopy, and histochemical staining for β -glucuronidase activity are available in Supplementary Methods.

Received 17 October; accepted 21 November 2006.

Published online 20 December 2006.

- Nadeau, J. A. & Sack, F. D. Stomatal development in *Arabidopsis*. In *The Arabidopsis Book* (eds Somerville, C. & Meyerowitz, E. M.) doi:10.1199/tab.0066 (American Society of Plant Biologists, 2002).
- Hetherington, A. M. & Woodward, F. I. The role of stomata in sensing and driving environmental change. *Nature* **424**, 901–908 (2003).
- Gray, J. E. *et al.* The *HIC* signalling pathway links CO₂ perception to stomatal development. *Nature* **408**, 713–716 (2000).
- Berger, D. & Altmann, T. A subtilisin-like serine protease involved in the regulation of stomatal density and distribution in *Arabidopsis thaliana*. *Genes Dev.* **14**, 1119–1131 (2000).
- von Groll, U., Berger, D. & Altmann, T. The subtilisin-like serine protease SDD1 mediates cell-to-cell signaling during *Arabidopsis* stomatal development. *Plant Cell* **14**, 1527–1539 (2002).
- Nadeau, J. A. & Sack, F. D. Control of stomatal distribution on the *Arabidopsis* leaf surface. *Science* **296**, 1697–1700 (2002).
- Bergmann, D. C., Lukowitz, W. & Somerville, C. R. Stomatal development and pattern controlled by a MAPKK kinase. *Science* **304**, 1494–1497 (2004).

- Shpak, E. D., McAbee, J. M., Pillitteri, L. J. & Torii, K. U. Stomatal patterning and differentiation by synergistic interactions of receptor kinases. *Science* **309**, 290–293 (2005).
- Lai, L. B. *et al.* The *Arabidopsis* R2R3 MYB proteins FOUR LIPS and MYB88 restrict divisions late in the stomatal cell lineage. *Plant Cell* **17**, 2754–2767 (2005).
- Poethig, R. S. EnhancerTraps (<http://enhancertraps.bio.upenn.edu/>) (2006).
- Geisler, M. J., Deppong, D. O., Nadeau, J. A. & Sack, F. D. Stomatal neighbor cell polarity and division in *Arabidopsis*. *Planta* **216**, 571–579 (2003).
- Toledo-Ortiz, G., Huq, E. & Quail, P. H. The *Arabidopsis* basic/helix-loop-helix transcription factor family. *Plant Cell* **15**, 1749–1770 (2003).
- Murre, C., McCaw, P. S. & Baltimore, D. A new DNA binding and dimerization motif in immunoglobulin enhancer binding, *daughterless*, *MyoD*, and *myc* proteins. *Cell* **56**, 777–783 (1989).
- Bailey, P. C. *et al.* Update on the basic helix-loop-helix transcription factor gene family in *Arabidopsis thaliana*. *Plant Cell* **15**, 2497–2502 (2003).
- Buck, M. J. & Atchley, W. R. Phylogenetic analysis of plant basic helix-loop-helix proteins. *J. Mol. Evol.* **56**, 742–750 (2003).
- Heim, M. A. *et al.* The basic helix-loop-helix transcription factor family in plants: a genome-wide study of protein structure and functional diversity. *Mol. Biol. Evol.* **20**, 735–747 (2003).
- Doe, C. Q. & Bowerman, B. Asymmetric cell division: fly neuroblast meets worm zygote. *Curr. Opin. Cell Biol.* **13**, 68–75 (2001).
- Ikeshima-Kataoka, H., Skeath, J. B., Nabeshima, Y., Doe, C. Q. & Matsuzaki, F. Miranda directs Prospero to a daughter cell during *Drosophila* asymmetric divisions. *Nature* **390**, 625–629 (1997).
- MacAlister, C. A., Ohashi-Ito, K. & Bergmann, D. C. Transcription factor control of asymmetric cell divisions that establish the stomatal lineage. *Nature* doi:10.1038/nature05491 (this issue).
- Dengler, N. The developmental basis of anisophylly in *Selaginella martensii*. II. Histogenesis. *Am. J. Bot.* **70**, 193–206 (1983).
- Brown, R. & Lemmon, B. Development of stomata in *Selaginella*: Division polarity and plastid movements. *Am. J. Bot.* **72**, 1914–1925 (1985).
- Weintraub, H. The MyoD family and myogenesis: redundancy, networks, and thresholds. *Cell* **75**, 1241–1244 (1993).
- Olson, E. N. MyoD family: a paradigm for development? *Genes Dev.* **4**, 1454–1461 (1990).
- Campuzano, S. & Modolell, J. Patterning of the *Drosophila* nervous system: the *achaete-scute* gene complex. *Trends Genet.* **8**, 202–208 (1992).
- Olson, E. N. Interplay between proliferation and differentiation within the myogenic lineage. *Dev. Biol.* **154**, 261–272 (1992).

Supplementary Information is linked to the online version of the paper at www.nature.com/nature.

Acknowledgements We thank C. Doe, B. Wakimoto, J. McAbee, and T. Kakimoto for commenting on the manuscript; F. Sack and T. Altmann for a gift of *flp*, *sdd1* and *TMM::TMM-GFP*; S. Poethig and D. Bergmann for E994; T. Nakagawa and ABRC for cloning vectors; SIGnAL and ABRC for T-DNA insertion lines; and P. Chan for confocal microscopy expertise. Our thanks to D. Bergmann for sharing unpublished results and discussion about stomatal development. This work was supported in part by the grants from DOE and NSF to K.U.T. L.J.P. was supported by the NRI USDA/CSREES fellowship, and K.U.T. is a CREST JST investigator.

Author Contributions K.U.T. supervised the entire project. K.U.T. and L.J.P. conceived and designed the experiments, and wrote the manuscript with comments from co-authors. L.J.P. isolated the *mute* mutant and performed characterization of mutants and transgenic plants with N.L.B. D.B.S. identified the *MUTE* gene by map-based cloning.

Author Information The NCBI/GenBank accession numbers for the genes described in this manuscript are: DQ863645 (*MUTE* mRNA), DQ864972 (*MUTE* genomic) and DQ868373 (*SPCH* mRNA). Reprints and permissions information is available at www.nature.com/reprints. The authors declare no competing financial interests. Correspondence and requests for materials should be addressed to K.U.T. (ktorii@u.washington.edu).

ARTICLES

The POT1–TPP1 telomere complex is a telomerase processivity factor

Feng Wang¹, Elaine R. Podell², Arthur J. Zaug², Yuting Yang¹, Paul Baciú¹, Thomas R. Cech² & Ming Lei¹

Telomeres were originally defined as chromosome caps that prevent the natural ends of linear chromosomes from undergoing deleterious degradation and fusion events. POT1 (protection of telomeres) protein binds the single-stranded G-rich DNA overhangs at human chromosome ends and suppresses unwanted DNA repair activities. TPP1 is a previously identified binding partner of POT1 that has been proposed to form part of a six-protein shelterin complex at telomeres. Here, the crystal structure of a domain of human TPP1 reveals an oligonucleotide/oligosaccharide-binding fold that is structurally similar to the β -subunit of the telomere end-binding protein of a ciliated protozoan, suggesting that TPP1 is the missing β -subunit of human POT1 protein. Telomeric DNA end-binding proteins have generally been found to inhibit rather than stimulate the action of the chromosome end-replicating enzyme, telomerase. In contrast, we find that TPP1 and POT1 form a complex with telomeric DNA that increases the activity and processivity of the human telomerase core enzyme. We propose that POT1–TPP1 switches from inhibiting telomerase access to the telomere, as a component of shelterin, to serving as a processivity factor for telomerase during telomere extension.

Telomeres, the specialized DNA–protein complexes found at the termini of all linear eukaryotic chromosomes, protect chromosomes from degradation and end-to-end fusion¹. Telomeric DNA typically consists of tandem repeats of a short G-rich sequence oriented 5' to 3' towards the chromosome terminus, with the G-rich strand extending beyond its complement to form a 3' overhang. In most eukaryotes, telomere length is maintained by telomerase, a specialized reverse transcriptase that adds telomeric DNA to the 3' ends of chromosomes to ensure complete genome replication². Telomerase is strongly upregulated in most cancer cells and has been studied as a plausible anti-cancer target³.

A six-protein complex is thought to protect the telomeres of human chromosomes. TRF1 and TRF2 directly bind double-stranded telomeric DNA^{4,5}, POT1 directly binds the single-stranded 3' extension at the chromosome end^{6–11}, and these are bridged through protein–protein interactions involving TIN2 and TPP1 (refs 12–19). The sixth protein, RAP1, binds mostly to TRF2 (refs 18, 20). Two functions have been proposed for this complex: protecting the natural chromosome end from being mistaken for a broken end and being subjected to DNA repair, and negative regulation of telomerase by sequestration of its telomeric DNA substrate. Both functions of this complex are captured by the name shelterin²¹.

Because POT1–TPP1 has been viewed as a structural component of the telomere, we were surprised to find that it increases both the activity and processivity of core telomerase. This is the first protein complex shown to substantially activate telomerase processivity. The crystal structure of TPP1 shows high structural similarity to the β -subunit of TEBP (telomere end-binding protein) from *Oxytricha nova*, a ciliated protozoan^{22–24}. Because POT1 is the human homologue of TEBP α ^{6,7,10,25}, it now appears that capping of telomeres by a TEBP α – β dimer is more conserved evolutionarily than had been expected.

TPP1 and POT1 form ternary complexes with ssDNA

Recombinant human TPP1 protein with an N-terminal deletion, TPP1(90–544) (Fig. 1a), was overexpressed and purified from

Escherichia coli. TPP1(90–544) was chosen because the 87 N-terminal residues of TPP1 are functionally dispensable in human cells^{12–14} and are not conserved among TPP1 proteins of different organisms^{12,13}. For simplicity, we hereafter use TPP1 to represent TPP1(90–544) unless stated otherwise.

An 18-nucleotide single-stranded telomeric DNA (primer a, (TTAGGG)₃) was incubated with increasing amounts of TPP1 with or without POT1, and binding was analysed by electrophoretic mobility shift assay (EMSA). POT1 protein bound to the DNA, whereas TPP1 on its own did not, even at a high protein concentration (375 nM) (Fig. 1b, lanes 1–5). When TPP1 was added to the POT1–DNA mixture, however, an additional complex formed that migrated above the POT1–DNA complex (Fig. 1b, lanes 6–11). By two criteria, this more slowly migrating complex contained TPP1. First, two size variants of TPP1, both of which contain the POT1-binding domain (Fig. 1a), produced electrophoretically distinct complexes (Fig. 1c). Second, addition of an anti-His antibody confirmed that the slower complex contained His-tagged TPP1 (Fig. 1d). The amount of DNA in the ternary complex was increased compared with the amount of DNA bound to POT1 alone (compare lanes 5 and 11 in Fig. 1b), suggesting higher affinity.

The equilibrium dissociation constants (K_d) of the protein complexes with various telomeric single-stranded (ss)DNAs were determined. Primer a (Fig. 2a) bound POT1 with a K_d of 26 nM, and the stability of this complex was increased sixfold by addition of TPP1 (Supplementary Fig. 1). Primers a5 and a3 (Fig. 2a) contain single-nucleotide substitutions that force POT1 to bind either to a 5' site (corresponding to an internal site on a long telomeric G-overhang) or to a 3'-proximal site (corresponding to end-capping)²⁶. The POT1–TPP1 complex showed a substantial preference for 3'-end binding ($K_d = 0.7$ versus 7.4 nM; compare circles in Fig. 2b, c). Notably, the dissociation constant of POT1–a5 is also tenfold higher than that of POT1–a3 (8.3 versus 89 nM) (compare triangles in Fig. 2b, c), suggesting that the 3' end preference of the POT1–TPP1 complex is mainly dictated by POT1. Measurements of the

¹Department of Biological Chemistry, University of Michigan Medical School, MSRBIII 5301D, 1150 W. Medical Center Drive, Ann Arbor, Michigan 48109, USA. ²Howard Hughes Medical Institute, Department of Chemistry and Biochemistry, University of Colorado, Boulder, Colorado 80309, USA.

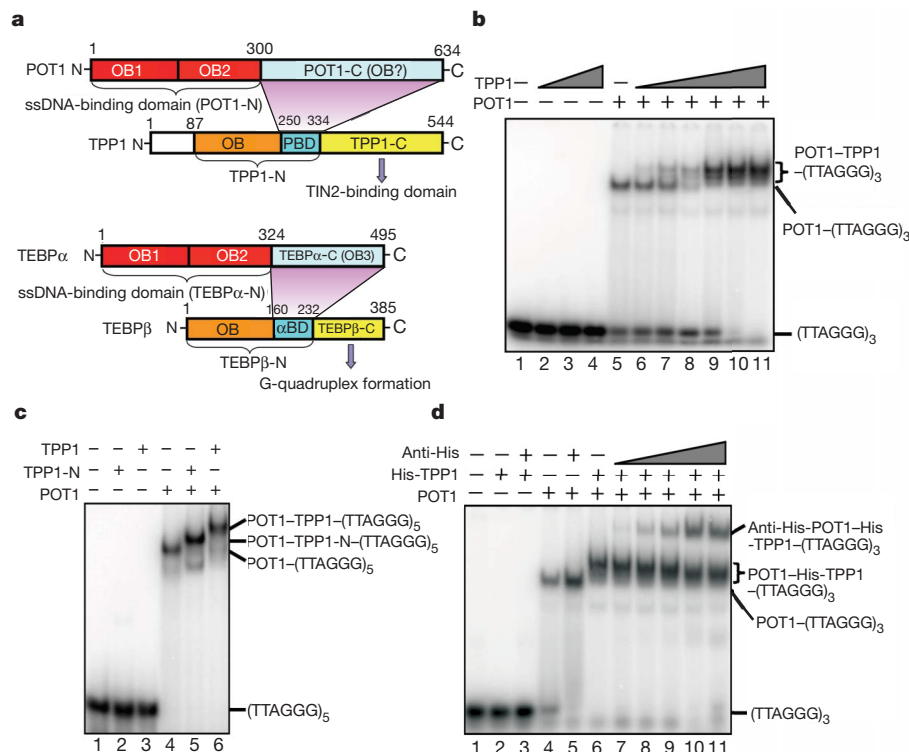


Figure 1 | TPP1 binds to the POT1-ssDNA complex and enhances the POT1-ssDNA interaction. **a**, Human POT1-TPP1 and *O. nova* TEBP α - β complexes share similar domain organization. In POT1 and TEBP α , the N-terminal ssDNA-binding domains are coloured in red, and the C-terminal TPP1/TEBP β -binding domains are in light blue. In TPP1 and TEBP β , the N-terminal OB folds are in orange, the central α -subunit-binding region (PBD in TPP1 and α BD in TEBP β) is in cyan, and the C-terminal domains are in yellow. Numbers indicate amino acid positions at the boundaries of

various subdivisions. **b**, TPP1 requires POT1 in order to interact stably with telomeric DNA. Primer a (50 nM) was incubated with increasing amounts of TPP1 (2, 10 and 50 nM in lanes 2–4, 2–100 nM in lanes 6–11) in the absence or presence of 150 nM POT1. **c**, Both TPP1 and TPP1-N generate super-shifted species but with different mobility; use of a longer primer enhanced the separation. **d**, The addition of anti-His antibody TPP1 detected the existence of His-tagged TPP1 in the slower migrating complex.

kinetic stabilities of the various complexes confirmed that the off rate of the POT1-DNA complex was decreased by addition of equimolar TPP1 (Supplementary Fig. 1). Furthermore, the complexes with a3 were kinetically about tenfold more stable than those with a5 (Supplementary Fig. 1). Taken together, these data indicate two

POT1-TPP1 binding modes on telomeric DNA, a lower affinity one at internal sequences and a higher affinity one at the 3' end.

Structural conservation between TPP1 and TEBP β

Functional and structural studies have established that POT1 is the human homologue of the *O. nova* TEBP α -subunit^{6,7,10,25}. Although there has been no report of a TEBP β -subunit in any organism besides *O. nova* and a related ciliate, *Stylonychia mytilis*²⁷, the DNA-binding properties of POT1-TPP1 closely resembled those of *O. nova* TEBP α - β ²⁸, consistent with TPP1 being the human homologue of TEBP β . In addition, their domain organizations revealed clear similarities (Fig. 1a). First, both TPP1 and TEBP β use a central region (PBD in TPP1 and α BD in TEBP β) to interact with the carboxy-terminal domains of their binding partners (POT1-C and TEBP α -C). Second, primary sequence analysis of the N-terminal domain of TPP1 (residues 90–250) predicted a secondary structure pattern of α - β - β - α - β - β - α (data not shown), where the bold region is characteristic of oligonucleotide/oligosaccharide-binding (OB) folds found in many telomere-binding proteins including TEBP β ^{10,23}. Third, the C-terminal domains of both TPP1 and TEBP β (TPP1-C and TEBP β -C) are not involved in the interaction with the α -subunits (POT1 and TEBP α) and have evolved to have distinct functions^{13,14,18,29,30} (Fig. 1a).

For crystallization studies, we first purified the N-terminal fragment TPP1-N (Fig. 1a), which can interact with POT1 and would correspond to the TEBP β fragment in the TEBP α - β -ssDNA crystal structure²³. However, TPP1-N was unstable by itself. Limited proteolysis and matrix-assisted laser desorption/ionization (MALDI) mass spectrometry identified a protease-resistant core domain of TPP1-N containing residues 90–260 (Supplementary Fig. 2); this domain corresponds to the predicted OB fold (Fig. 1a).

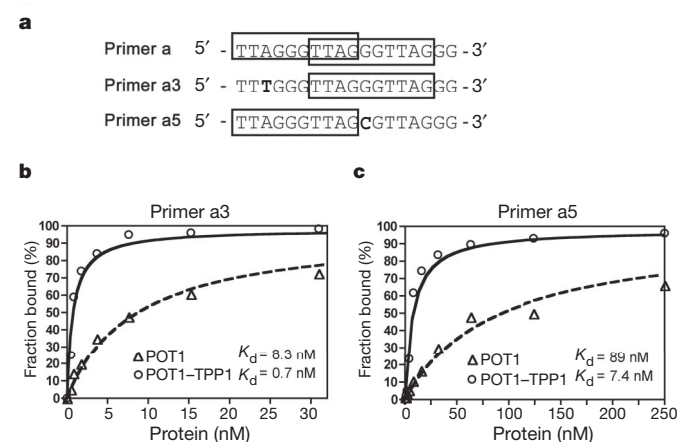


Figure 2 | The POT1-TPP1 complex binds to the single-stranded telomeric overhang with 3' end preference. **a**, Sequences of primers a, a5 and a3. The bold letters are the point mutations. The POT1-binding sites are denoted by boxes²⁶. **b**, **c**, Equilibrium binding curves for primers a3 (**b**) and a5 (**c**) binding to POT1 and the POT1-TPP1 complex. The solid and dashed lines represent theoretical binding curves fit to the data for POT1 and POT1-TPP1, respectively. The calculated equilibrium dissociation constant (K_d) values are indicated. The binding curves and K_d values for primers a, b and hT10 (TTAGGGTTAG) are shown in Supplementary Fig. 1.

Recombinant TPP1(90–250) expressed from *E. coli* was crystallized, and the structure was solved by single anomalous dispersion (SAD) and refined to a resolution of 2.7 Å (Supplementary Table 1). The final model contains residues 90–243 (Fig. 3a).

The structure of TPP1(90–250) reveals a typical OB-fold architecture comprising a highly curved five-stranded β -barrel (Fig. 3a)^{31,32}. Hereafter, we will refer to TPP1(90–250) as TPP1-OB (Fig. 1a). An unbiased search for structurally homologous proteins using Dali³³ revealed that the structure of TPP1-OB is most similar to that of the OB fold of the *O. nova* TEBP β -subunit²³. The two structures can be superimposed with a root-mean-square deviation of 2.0 Å in the positions of 144 equivalent C α atoms (Fig. 3b). Notably, this structurally conserved region includes not only the central β -barrel, but also three peripheral α -helices, suggesting that TPP1 and TEBP β are homologous proteins (Fig. 3b); other OB folds, such as that of TEBP α , are more distantly related (Fig. 3c). In addition to the overall structural similarity, the OB folds of TPP1 and TEBP β share several unique features. First, the loop connecting β 5 and α C (L_{5C}), unlike in the OB folds of POT1 and TEBP α , adopts an extended conformation and packs across one side of the β -barrel, forcing helix α C to cap the bottom of the barrel (Fig. 3b). Second, helix α B is in a modified position, rotated almost 90° relative to the orientation normally observed in OB folds. Taken together, these structural similarities strongly support the notion that TPP1 is the human homologue of *O. nova* TEBP β . Given that TPP1 has been identified in many other eukaryotes^{12,13}, TPP1/TEBP β may be an evolutionarily conserved telomere protein.

Despite the high degree of structural conservation, the sequences of OB folds of TPP1 and TEBP β are markedly divergent and share only 11% identity (Supplementary Fig. 3). Significant sequence and structural variation is particularly evident in the connecting loop regions. TPP1-OB has a very long loop (20 residues), L₁₂, between strands β 1 and β 2, which packs on helix α A and covers one end of the barrel (Fig. 3a, b). In contrast, strands β 1 and β 2 of TEBP β are connected by a short two-residue turn (Fig. 3b). These marked variations in the loop regions explain the failure to detect the similarity between these OB folds by bioinformatics.

POT1–TPP1 is a telomerase processivity factor

We investigated the ability of telomerase to extend the POT1–TPP1–ssDNA ternary complex, expecting some inhibition consistent with the shelterin model²¹. Human core telomerase was reconstituted *in vitro* and immunopurified via the haemagglutinin (HA) tag on the telomerase catalytic subunit (TERT). Primer a5 has a single-nucleotide mutation that forces POT1 to bind to its 5' end (Fig. 2a), leaving a telomerase-extendible 3' tail²⁶. Addition of POT1 and TPP1 to primer a5 markedly increased the telomerase product size distribution. Primer a5 was extended via more than 30 cycles of template

copying (Fig. 4a, lane 4), whereas in the absence of the POT1–TPP1 complex, the first three cycles accounted for most of the extension (lane 1). Under conditions of vast primer excess, longer extension products result from processive extension, not from rebinding of previously extended products³⁴. We confirmed that this condition still pertained in the case of the ternary complexes by showing that the extension was independent of concentration over a 2,000-fold range (Supplementary Fig. 4).

These data emphasize the longer extension products, because ³²P-GMP incorporation increases with product size. Quantification showed that POT1–TPP1 provided a threefold increase in activity (Fig. 4b) and, after dividing each product by the amount of GMP incorporated, a fourfold increase in processivity (Fig. 4c). $R_{1/2}$, the number of repeats synthesized before half of the chains have dissociated, increased from 0.78 repeats with DNA primer a5 to 3.3 repeats with the POT1–TPP1–DNA complex. Because this fourfold increase in processivity is cumulative, it has a very large effect on the production of longer products (see double-headed arrows in Fig. 4c–e). POT1 by itself produced a more modest stimulation of processivity, consistent with earlier results²⁶, and TPP1 by itself had a similar effect (Fig. 4c–e).

The increase in telomerase processivity with the POT1–TPP1 complex was unexpected, and we were concerned that it might be due to a small molecule accompanying the protein. However, when we fractionated TPP1 by gel filtration chromatography, the processivity activity clearly co-migrated with the main protein peak (Supplementary Fig. 5), indicating that the enhanced processivity was TPP1-specific.

The effects of POT1 and TPP1 were even more dramatic with other DNA primers. Primer a3 binds POT1 mainly at its 3' end (Fig. 2a), as does primer b ((GGTTAG)₃)²⁶. As expected, the addition of POT1 almost completely blocked the extension of these primers (Fig. 4a, lanes 6 and 10). When TPP1 was also added, however, telomere extension was rescued and processivity was increased five- to sixfold (Fig. 4a, lanes 8 and 12; see also Fig. 4d, e). To test the possibility that TPP1 induced sliding of POT1 from the preferred 3' binding site to the 5' site, we mapped the position of the leading edge of the POT1–TPP1 complex on the DNA using snake-venom phosphodiesterase I, which degrades ssDNA exonucleolytically from the 3' end. Complexes of primer a3 or primer a with the POT1–TPP1 heterodimer showed that the protein mostly occupied the DNA 3' end, with a local change in accessibility relative to the POT1–DNA complexes where the 3' end of the DNA protrudes from the protein (Supplementary Fig. 6). Although TPP1 did not relocate the bulk of POT1 to an internal site on the DNA, we propose that the proteins are in fact binding internally in a minority of the complexes²⁶; the resulting 3' overhang is then extended by telomerase with the enhanced processivity characteristic of POT1–TPP1 complexes.

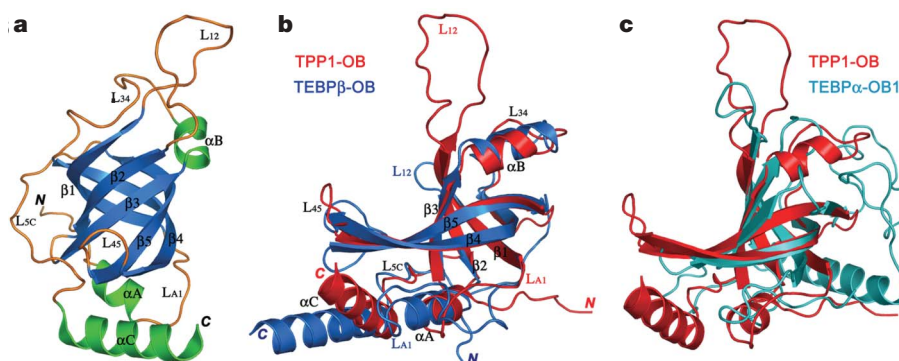


Figure 3 | The crystal structure of TPP1-OB indicates that TPP1 is the homologue of *O. nova* TEBP β . **a**, Ribbon diagram of TPP1-OB with β -strands coloured in blue, α -helices green, and loops orange. The secondary structure elements are labelled. **b**, Superposition of TPP1-OB on the crystal

structure of the OB fold of TEBP β ²³. TPP1 is in red and TEBP β in blue. **c**, Superposition of TPP1-OB on the crystal structure of the first OB fold of TEBP α ²³. TPP1 is in red and TEBP α in cyan. Figures were generated by using the program Pymol (<http://pymol.sourceforge.net>).

Primer AGGG-a (AGGG(TTAGGG)₃) has four blocks of GGG and therefore folds into Hoogsteen base-paired G-quadruplex structures, which are inhibitory for telomerase extension (Fig. 4a, lane 13)³⁵. POT1 can trap an open form of this DNA, allowing telomerase extension³⁵ (lane 14). TPP1 by itself (lane 15) gave the typical twofold increase in telomerase activity seen with all the primers (Fig. 4b), but telomerase still stalled after every nucleotide added to the G-quadruplex. POT1–TPP1 again stimulated highly processive extension by telomerase (lane 16).

We next asked whether the enhanced telomerase processivity and activity were dependent on the POT1–TPP1 interaction by using a panel of POT1 and TPP1 deletion mutant proteins. POT1-N, which lacks the TPP1 interaction domain, and TPP1-OB, which lacks the POT1 interaction domain, both failed to endow telomerase with increased processivity and activity (Supplementary Fig. 7). Only when both proteins had intact interaction domains was the processivity greatly stimulated (Supplementary Fig. 7), confirming the important role of the POT1–TPP1 interaction in this activity. The purified POT1 interaction domain of TPP1, TPP1-PBD, was insufficient to activate telomerase in the presence of POT1 (Supplementary Fig. 8).

Discussion

E. coli DNA polymerase achieves high processivity by means of an accessory protein that serves as a ‘sliding clamp’, encircling the DNA

and preventing dissociation³⁶. By analogy, the POT1–TPP1 complex might move with telomerase, binding the DNA just upstream from its 3' end and inhibiting dissociation. Given the DNA sequence-specificity of POT1–TPP1 binding, the protein would not slide continuously along the DNA but would ratchet in 6- or 12-nucleotide steps. On the other hand, ssDNA is intrinsically much more flexible than double-stranded (ds)DNA. Thus, a clamp would not need to slide or ratchet to keep the ssDNA associated with telomerase, but could instead remain fixed while the newly synthesized telomeric repeats formed a larger and larger protruding loop. Another question for future research is whether a single POT1–TPP1 complex clamp is sufficient for increased processivity, or whether the proteins must coat the elongating telomeric DNA.

In normal human somatic cells that lack telomerase, telomeres shrink by about 30–100 base pairs per replication cycle³⁷. This provides a plausible estimate for the amount of DNA synthesized by telomerase at each chromosome end, and is similar to more direct measurements in yeast³⁸. Whether such extension is processive or distributive *in vivo* is unknown. However, we note that the telomerase processivity achieved here in the presence of POT1–TPP1 is around four repeats or 24 nucleotides, which would mean that one or a few rounds of telomerase extension per cell cycle would be sufficient to maintain human telomeres.

Given that POT1 and TPP1 are components of a negative feedback loop of telomere length control^{11–14}, we were surprised to find that the

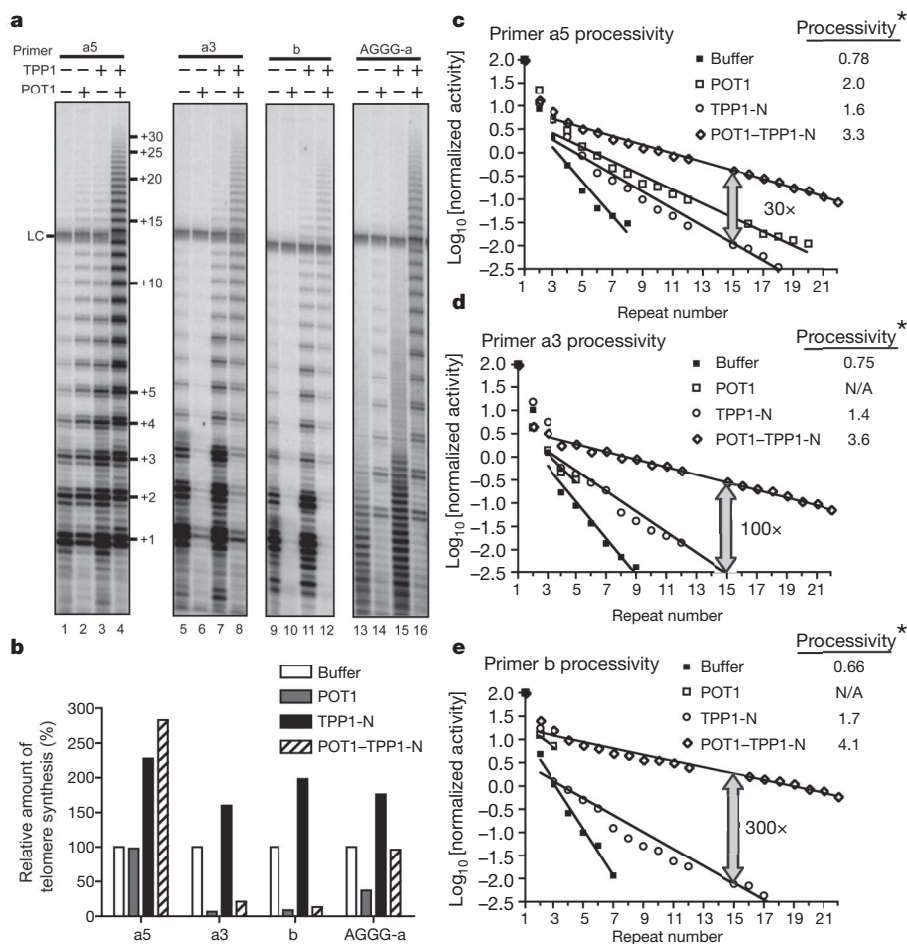


Figure 4 | The POT1–TPP1 complex functions as a telomerase processivity factor. **a**, Direct telomerase activity assays³⁴ were performed with 100 nM primer a5 (lanes 1–4), a3 (lanes 5–8), b (lanes 9–12), or AGGG-a (lanes 13–16) in the presence of a saturating concentration of POT1, TPP1, or POT1–TPP1. Reaction products were then analysed by gel electrophoresis (LC, loading control). Three independent sets of experiments gave equivalent

results. **b**, Quantification of total DNA synthesis relative to synthesis in the presence of protein buffer alone. **c–e**, Activity in each repeat shown in **a** was measured, corrected for the number of radiolabelled nucleotides incorporated, and then plotted. *Processivity = $R_{1/2} = -\ln 2 / (2.303k)$, where k is the slope and $R_{1/2}$ is the number of repeats synthesized before half of the chains have dissociated, analogous to $t_{1/2}$ in radioactive decay.

POT1–TPP1 complex can also function as a positive telomerase processivity factor. We propose a three-state model of telomere length regulation that can reconcile the two apparently opposite functions of POT1–TPP1. (1) When POT1–TPP1 covers the 3' terminus of the G-overhang, it sequesters the telomere and prevents binding of telomerase. (2) POT1–TPP1 is removed from its high-affinity 3' binding site by an unidentified mechanism, which might, for example, involve post-translational modification and disruption of the shelterin complex. (3) The POT1–TPP1 complex then serves as a telomerase processivity factor during telomere extension. As the telomere is elongated and reaches a certain threshold, the newly synthesized repeats bind shelterin complexes, the 3' end of the overhang is re-bound by POT1–TPP1, and further telomerase extension is inhibited (back to state 1). Further work will be needed to understand how switching between such telomere and telomerase complexes is achieved and regulated *in vivo*.

METHODS

Details of recombinant protein cloning, expression and purification can be found in Supplementary Methods. Telomeric ssDNAs used in the DNA-binding assay were purchased from IDT and Invitrogen and 5'-end-labelled using polynucleotide kinase. Protein binding proceeded for 1 h at room temperature in 90 mM NaCl, 50 mM Tris-HCl, pH 8.0, 6 mM dithiothreitol and 5% glycerol, followed by EMSA on native 6% polyacrylamide gels¹⁰. For *in vitro* telomerase activity assays²⁶, C-terminal HA-tagged human TERT was expressed from pHRT-HA2 and hTR from pHTR³⁴ using the TnT quick-coupled transcription/translation system (Promega), and the reconstituted core telomerase was affinity-purified on anti-HA F7-agarose beads (Santa Cruz Biotechnology)²⁶. Details of crystallization, data collection and structure determination of TPP1–OB can be found in Supplementary Methods.

Received 17 August; accepted 17 November 2006.

Published online 21 January 2007.

- Blackburn, E. H. Switching and signaling at the telomere. *Cell* **106**, 661–673 (2001).
- Cech, T. R. Beginning to understand the end of the chromosome. *Cell* **116**, 273–279 (2004).
- Shay, J. W. & Wright, W. E. Telomerase: a target for cancer therapeutics. *Cancer Cell* **2**, 257–265 (2002).
- Chong, L. *et al.* A human telomeric protein. *Science* **270**, 1663–1667 (1995).
- Broccoli, D., Smogorzewska, A., Chong, L. & de Lange, T. Human telomeres contain two distinct Myb-related proteins, TRF1 and TRF2. *Nature Genet.* **17**, 231–235 (1997).
- Baumann, P. & Cech, T. R. Pot1, the putative telomere end-binding protein in fission yeast and humans. *Science* **292**, 1171–1175 (2001).
- Baumann, P., Podell, E. & Cech, T. R. Human Pot1 (protection of telomeres) protein: cytolocalization, gene structure, and alternative splicing. *Mol. Cell. Biol.* **22**, 8079–8087 (2002).
- Hockemeyer, D., Daniels, J. P., Takai, H. & de Lange, T. Recent expansion of the telomeric complex in rodents: Two distinct POT1 proteins protect mouse telomeres. *Cell* **126**, 63–77 (2006).
- Wu, L. *et al.* Pot1 deficiency initiates DNA damage checkpoint activation and aberrant homologous recombination at telomeres. *Cell* **126**, 49–62 (2006).
- Lei, M., Podell, E. R. & Cech, T. R. Structure of human POT1 bound to telomeric single-stranded DNA provides a model for chromosome end-protection. *Nature Struct. Mol. Biol.* **11**, 1223–1229 (2004).
- Loayza, D. & de Lange, T. POT1 as a terminal transducer of TRF1 telomere length control. *Nature* **423**, 1013–1018 (2003).
- Ye, J. Z. *et al.* POT1-interacting protein PIP1: a telomere length regulator that recruits POT1 to the TIN2/TRF1 complex. *Genes Dev.* **18**, 1649–1654 (2004).
- Liu, D. *et al.* PTOP interacts with POT1 and regulates its localization to telomeres. *Nature Cell Biol.* **6**, 673–680 (2004).
- Houghtaling, B. R., Cuttonaro, L., Chang, W. & Smith, S. A dynamic molecular link between the telomere length regulator TRF1 and the chromosome end protector TRF2. *Curr. Biol.* **14**, 1621–1631 (2004).
- Kim, S. H., Kaminker, P. & Campisi, J. TIN2, a new regulator of telomere length in human cells. *Nature Genet.* **23**, 405–412 (1999).
- Liu, D., O'Connor, M. S., Qin, J. & Songyang, Z. Telosome, a mammalian telomere-associated complex formed by multiple telomeric proteins. *J. Biol. Chem.* **279**, 51338–51342 (2004).
- Ye, J. Z. *et al.* TIN2 binds TRF1 and TRF2 simultaneously and stabilizes the TRF2 complex on telomeres. *J. Biol. Chem.* **279**, 47264–47271 (2004).
- O'Connor, M. S., Safari, A., Xin, H., Liu, D. & Songyang, Z. A critical role for TPP1 and TIN2 interaction in high-order telomeric complex assembly. *Proc. Natl Acad. Sci. USA* **103**, 11874–11879 (2006).
- Kim, S. H. *et al.* TIN2 mediates functions of TRF2 at human telomeres. *J. Biol. Chem.* **279**, 43799–43804 (2004).
- Li, B., Oestreich, S. & de Lange, T. Identification of human Rap1: implications for telomere evolution. *Cell* **101**, 471–483 (2000).
- de Lange, T. Shelterin: the protein complex that shapes and safeguards human telomeres. *Genes Dev.* **19**, 2100–2110 (2005).
- Hicke, B. J., Celander, D. W., MacDonald, G. H., Price, C. M. & Cech, T. R. Two versions of the gene encoding the 41-kilodalton subunit of the telomere binding protein of *Oxytricha nova*. *Proc. Natl Acad. Sci. USA* **87**, 1481–1485 (1990).
- Horvath, M. P., Schweiker, V. L., Bevilacqua, J. M., Ruggles, J. A. & Schultz, S. C. Crystal structure of the *Oxytricha nova* telomere end binding protein complexed with single strand DNA. *Cell* **95**, 963–974 (1998).
- Gray, J. T., Celander, D. W., Price, C. M. & Cech, T. R. Cloning and expression of genes for the *Oxytricha* telomere-binding protein: specific subunit interactions in the telomeric complex. *Cell* **67**, 807–814 (1991).
- Loayza, D., Parsons, H., Donigian, J., Hoke, K. & de Lange, T. DNA binding features of human POT1: a nonamer 5'-TAGGGTTAG-3' minimal binding site, sequence specificity, and internal binding to multimeric sites. *J. Biol. Chem.* **279**, 13241–13248 (2004).
- Lei, M., Zaug, A. J., Podell, E. R. & Cech, T. R. Switching human telomerase on and off with hPOT1 protein *in vitro*. *J. Biol. Chem.* **280**, 20449–20456 (2005).
- Fang, G. W. & Cech, T. R. Molecular cloning of telomere-binding protein genes from *Stylonychia mytilis*. *Nucleic Acids Res.* **19**, 5515–5518 (1991).
- Fang, G., Gray, J. T. & Cech, T. R. *Oxytricha* telomere-binding protein: separable DNA-binding and dimerization domains of the α -subunit. *Genes Dev.* **7**, 870–882 (1993).
- Fang, G. & Cech, T. R. The β subunit of *Oxytricha* telomere-binding protein promotes G-quartet formation by telomeric DNA. *Cell* **74**, 875–885 (1993).
- Paeschke, K., Simonsson, T., Postberg, J., Rhodes, D. & Lipps, H. J. Telomere end-binding proteins control the formation of G-quadruplex DNA structures *in vivo*. *Nature Struct. Mol. Biol.* **12**, 847–854 (2005).
- Dietmann, S. & Holm, L. Identification of homology in protein structure classification. *Nature Struct. Biol.* **8**, 953–957 (2001).
- Theobald, D. L., Mitton-Fry, R. M. & Wuttke, D. S. Nucleic acid recognition by OB-fold proteins. *Annu. Rev. Biophys. Biomol. Struct.* **32**, 115–133 (2003).
- Holm, L. & Sander, C. Database algorithm for generating protein backbone and side-chain co-ordinates from a C α trace application to model building and detection of co-ordinate errors. *J. Mol. Biol.* **218**, 183–194 (1991).
- Chen, J. L. & Greider, C. W. Determinants in mammalian telomerase RNA that mediate enzyme processivity and cross-species incompatibility. *EMBO J.* **22**, 304–314 (2003).
- Zaug, A. J., Podell, E. R. & Cech, T. R. Human POT1 disrupts telomeric G-quadruplexes allowing telomerase extension *in vitro*. *Proc. Natl Acad. Sci. USA* **102**, 10864–10869 (2005).
- Kuriyan, J. & O'Donnell, M. Sliding clamps of DNA polymerases. *J. Mol. Biol.* **234**, 915–925 (1993).
- Counter, C. M. *et al.* Telomere shortening associated with chromosome instability is arrested in immortal cells which express telomerase activity. *EMBO J.* **11**, 1921–1929 (1992).
- Teixeira, M. T., Arneric, M., Sperisen, P. & Lingner, J. Telomere length homeostasis is achieved via a switch between telomerase-extendible and -nonextendible states. *Cell* **117**, 323–335 (2004).

Supplementary Information is linked to the online version of the paper at www.nature.com/nature.

Acknowledgements We thank Y. Chen and K. Wan for help at various stages of the project; N. F. Lue for the His-SUMO protein expression vector; Z. Songyang and T. de Lange for TPP1 cDNA; D. Yoder of beamline 23-ID at APS for assistance with data collection; and J. L. Chen and C. W. Greider for the human TERT and TER plasmids. Work in the laboratory of M.L. is supported by the American Cancer Society and the Sidney Kimmel Foundation. E.R.P., A.J.Z. and T.R.C. are supported by the Howard Hughes Medical Institute.

Author Contributions F.W. is responsible for the bulk of the experiments; Y.Y. for structural determination of TPP1–OB; P.B. for crystallization of TPP1–OB; E.R.P. and A.J.Z. for the telomerase activity assays and some of the EMSA experiments; and T.R.C. and M.L. contributed to overall design and interpretation of the studies.

Author Information The atomic coordinates and structure factors of TPP1–OB have been deposited in the RCSB Protein Data Bank with accession code 2146. Reprints and permissions information is available at www.nature.com/reprints. The authors declare no competing financial interests. Correspondence and requests for materials should be addressed to M.L. (leim@umich.edu).

The signature of hot hydrogen in the atmosphere of the extrasolar planet HD 209458b

Gilda E. Ballester¹, David K. Sing^{1,2} & Floyd Herbert¹

About ten per cent of the known extrasolar planets are gas giants that orbit very close to their parent stars. The atmospheres of these 'hot Jupiters' are heated by the immense stellar irradiation^{1–5}. In the case of the planet HD 209458b, this energy deposition results in a hydrodynamic state in the upper atmosphere, allowing for sizeable expansion and escape of neutral hydrogen gas^{2–6}. HD 209458b was the first extrasolar planet discovered that transits in front of its parent star⁷. The size of the planet can be measured using the total optical obscuration of the stellar disk during an observed transit, and the structure and composition of the planetary atmosphere can be studied using additional planetary absorption signatures in the stellar spectrum. Here we report the detection of absorption by hot hydrogen in the atmosphere of HD 209458b. Previously, the lower atmosphere and the full extended upper atmosphere of HD 209458b have been observed^{2,6,8}, whereas here we probe a layer where the escaping gas forms in the upper atmosphere of HD 209458b.

An extensive study of HD 209458 planetary transits with the Hubble Space Telescope (HST) was first performed at optical wavelengths using the G750M grating of the Space Telescope Imaging Spectrograph (STIS) and the CCD camera detector⁹. A similar STIS study has recently been reported¹⁰ with the G430L and G750L gratings spanning the full 2,900–10,300 Å region. This latter study refined the system parameters of HD 209458 by assuming a limb-darkening law for the star (based on a stellar model from ref. 11) and simultaneously fitting the shapes of the planetary transit curves over ten different bandpasses. In particular, a new, significantly smaller planetary radius $R_{\text{pl}} = 1.320R_{\text{Jup}}$ (where R_{Jup} is Jupiter's radius) was obtained, as compared to the $1.35R_{\text{Jup}}$ value previously used in the literature. We adopt the new system parameters in our work, and use the same G430L data set (now public) to present a transit flux ratio spectrum, which is useful for identifying specific spectral features from atmospheric absorption. The present work was started while using the G430L data set to calibrate independent transit observations of HD 209458 made with the HST Advance Camera for Surveys (ACS) near-ultraviolet (UV) prism at the overlap 3,000–5,500 Å region (A. Vidal-Madjar *et al.*, unpublished results).

The far-UV H I Lyman- α line is the strongest absorption line of atomic hydrogen. Far-UV HST transit observations of HD 209458b revealed a hydrogen obscuring disk which is $\sim 15\%$ of the size of the stellar disk², much larger than the $\sim 1.5\%$ planetary disk seen in the optical. This material encompasses an enormous obscuring area, larger than that defined by the Roche lobe, outside of which the stellar gravity overpowers the planet's gravitational pull. Furthermore, the spectrally-resolved H I Lyman- α line clearly showed blue-shifted absorption, indicating that absorbing hydrogen atoms are moving away from the star due mainly to radiation pressure^{2,3}, forming a comet-like tail. The estimated hydrogen escape rate is enormous,

10^{10} g s^{-1} or larger, while the upper atmospheric temperature ($\sim 10,000 \text{ K}$; refs 1–5) is not high enough to produce significant thermal (Jeans) escape. This atmosphere must have a hydrodynamic outflow^{3–6}, similar to the solar corona. Instead of hydrostatic equilibrium, there is a net upward velocity of the dominant light hydrogen gas. This outflow is maintained by the continual energy input supplied by the strong extreme-UV flux from the star located only nine stellar radii away (0.045 AU). If the hydrodynamic outflow is real and robust enough (for example, 'blow-off'), then the lighter gas could drag along heavier species, and indeed, an extended atmosphere has also been detected in HD 209458b in the abundant O I and C II species by their far-UV absorption⁶. In contrast, a small 0.02% absorption by atomic sodium in the strong yellow D lines has been detected in HD 209458b (ref. 8), and this absorption must be produced in the lower atmosphere. Here we also present a small 0.03% absorption, by atomic hydrogen in the Balmer jump and continuum, but as we demonstrate below, to produce this absorption a significant hot hydrogen population is needed at higher atmospheric altitudes. (The Balmer jump is the abrupt transition to the ionization continuum absorption from the $n = 2$ state of atomic hydrogen. For the purposes of this Letter we also include in this term the Balmer lines lying very close to the ionization edge.)

The small 0.03% extra absorption can be seen in a photometric transit light curve and in a transit flux ratio spectrum, both derived from the HST G430L spectroscopic data set. Details of the data reduction and stellar limb-darkening corrections necessary^{9–12} can be found in Supplementary Information. We derive what would be a larger planetary radius for the near-UV/violet region 3,000–4,000 Å compared to that from the blue 4,500–5,500 Å region. The corresponding photometric light curves (data and model) are depicted in Fig. 1, along with model curves corrected for limb-darkening. We fit a planetary radius of $1.3200 \pm 0.0002 R_{\text{Jup}}$ for the blue light curve and $1.3300 \pm 0.0006 R_{\text{Jup}}$ for the near-UV/violet curve. The errors correspond to the relative uncertainty between the two bandpasses, not the total uncertainty which depends on the stellar radius and mass¹⁰. Our results are consistent with the independent analysis in ref. 10, in which the data were used to refine the planetary radius based on broadband photometric results.

A transit flux ratio spectrum shows the wavelength dependence of the absorption features; this is valuable information that is lost when integrating the flux over spectral bandpasses for the photometric studies. Any wavelength-dependent increase in absorption will appear as a flux ratio lower than 0.9855 during mid-transit. Figure 2 shows the mid-transit flux ratio spectrum derived from the data. No obvious narrow absorption lines are evident, but there does appear to be a broadband absorption at wavelengths shorter than about 4,000 Å, consistent with the photometric results. The

¹Lunar and Planetary Laboratory, University of Arizona, Sonett Space Sciences Building, Tucson, Arizona 85721-0063, USA. ²Institut d'Astrophysique de Paris, CNRS/UPMC, 98 bis Boulevard Arago, F-75014 Paris, France.

broad absorption appears to be relatively flat between 3,000 and 3,800 Å, where we find an average transit flux ratio of 0.98523 ± 0.00006 (s.e.m.) which is below the 0.98545 ± 0.00002 we derive for the blue region. The short-wavelength absorption is 0.03 ± 0.006 below the value of 0.9855 calculated from the latest value for the radius of the planet ($1.320R_{\text{Jup}}$)¹⁰.

The simplest candidate for creating the broadband absorption observed is bound-free absorption by atomic hydrogen in the first excited state. The observed absorption starts around 3,900 Å, and remains relatively flat below 3,650 Å. This region corresponds to the Balmer jump, which occurs at 3,646 Å, although in practice there is significant absorption at wavelengths longer than 3,646 Å due to the pile-up of Balmer transition lines. In order to have a significant bound-free absorption by H I at near-UV and optical wavelengths, there must be a significant population of H I in the first excited state ($n = 2$). The relative population of $n = 2$ hydrogen atoms is very sensitive to temperature, and peaks around 10,000 K (refs 13, 14). In general, at temperatures of a few thousand kelvins the thermal $n = 2$ population is very small, and above $\sim 15,000$ K the ionized (H^+) population with its associated free-free absorption becomes dominant. The upper atmosphere of this hot Jupiter should reach temperatures of 10,000 K or more owing to the immense heating by the stellar extreme-UV input¹⁻⁵.

In order to check whether there is a significant population of excited H I and the amount of absorption it would produce during planetary transit, we numerically evaluated the equation of radiative

transfer using the most detailed model to date of the HD 209458b upper atmosphere^{4,5} (see Supplementary Information for calculation details). In this one-dimensional aeronomy model, many aspects are explicitly calculated, including the effects of the immense stellar extreme-UV heating, hydrogen and helium photochemistry, ionization and hydrodynamics, as well as the atmospheric escape rate. (The atmospheric escape rate derived from this model⁴ was recently clarified⁵ to be in the same regime found from the H I Lyman- α HST observations².) The model shows a sharp temperature rise from ~ 750 K at a radius of $r = 1R_{\text{pl}}$ to $\sim 10,000$ K at $r = 1.14R_{\text{pl}}$, at which point H I becomes the dominant species in the atmosphere. At higher radial distances the temperature increases further and the H^+ population becomes dominant. Our calculation based on the model of refs 4 and 5 yields a net absorption contrast of 0.03% beginning at the Balmer jump, with similar values in the continuum down to $\sim 3,000$ Å. The absorption contrast that we derive from the HST data is also $\sim 0.03\%$ on average. The similarity may be coincidental, but the results show that we are in the correct regime and such absorption should be detectable. As the model suggests, the data show that the upper escaping atmosphere of HD 209458b should have a hot enough layer at high enough densities to produce a Balmer jump and continuum absorption signature.

Various studies¹⁵ indicate that the lower atmosphere of the hot-Jupiter HD 209458b has a temperature on the order of 1,200 K (at least on the dayside), which is too low to produce any significant $n = 2$ H I population. Our results therefore indicate that this planet

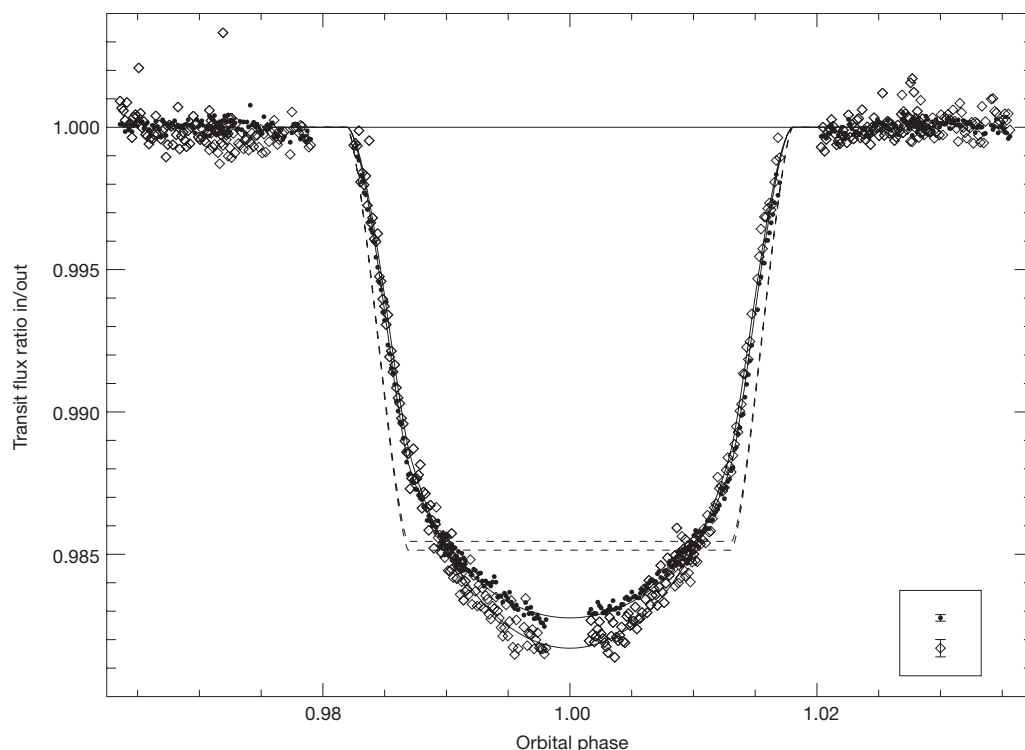


Figure 1 | Photometric transit light curves of HD 209458. Plotted are the STIS G430L transit light curves for the near-UV/violet 3,000–4,000 Å (diamonds) and blue 4,500–5,500 Å (filled circles) photometric bandpasses. The data have been corrected for systematic instrumental effects. The error bars shown in the bottom right inset represent 1 standard error estimated from the pipeline data errors (dominated by photon counting statistics), and propagated while integrating the flux in each photometric bandpass per exposure. As the integrated counts per bandpass are very similar per exposure, the errors bars are all basically the same for each bandpass, 0.00061 and 0.00023 for the near-UV/violet and blue bandpasses, respectively. The corresponding curved solid lines are the theoretical limb-darkened models for comparison with the data. The dashed curves are the

theoretical transit light curves for zero stellar limb-darkening using the two different planetary sizes found for the two photometric bandpasses. The bottom curve corresponds to a larger planetary radius derived for the near-UV/violet. Note that the near-UV/violet radius is an interpretation, because we find in the modelling of the data that the absorption should arise from a relatively thin high-altitude isolated layer (see text). The limb-darkening correction reduces the difference between the two light curves but is inconsistent with a zero difference, as we explain in Fig. 2 legend. For fitting the theoretical transit curves we used the system parameters derived¹⁰ from the full G430L and G750M STIS data set: orbital inclination $i = 86.929^\circ$, orbital period = 3.52474859 d, zero transit time 2452826.628521 HJD, stellar mass $M_{\text{star}} = 1.101M_{\text{Sun}}$, and stellar radius $R_{\text{star}} = 1.125R_{\text{Sun}}$.

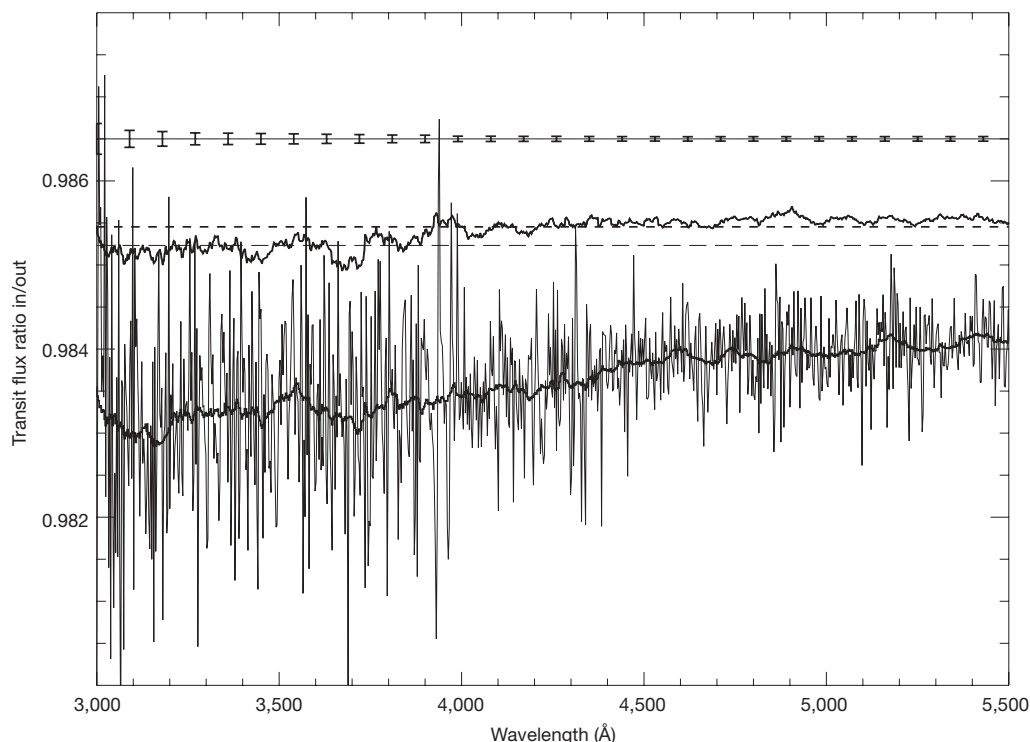


Figure 2 | Transit flux ratio spectrum. Middle trace, smoothed and with stellar limb-darkening correction (dark, thick line); bottom trace, without limb-darkening correction both smoothed (dark, thick line) and unsmoothed (light, thin line). The transit flux ratio spectrum was obtained by co-adding the spectra between orbital phases 0.987 and 1.012 (around mid-transit) and dividing the resulting spectrum by that from the co-added, out-of-transit spectra. Errors were estimated by propagating the pipeline data errors while co-adding the spectra and deriving the spectral flux ratio. The smoothed spectral ratios depicted are boxcar smoothed over 33 points for clarity, and the corresponding error bars (1 standard error) propagated in the smoothing are plotted at the top. Overplotted are also the mid-transit flux ratio values derived from the two planetary radii using the photometric light curves for the near-UV/violet 3,000–4,000 Å (thin, long-dash line) and

blue 4,500–5,500 Å (thick, short-dash line) bandpasses, respectively. The derived limb-darkening-corrected transit flux ratio spectrum (middle trace; dark, thick line) is relatively flat, but shows an extra broadband absorption at wavelengths shorter than 3,900 Å, consistent with the photometry. This extra absorption is measured at $\sim 0.03\%$ and identified to be due to absorption in the Balmer edge by hot hydrogen in the planetary atmosphere (see text). The extra absorption cannot be an artefact due to improper correction of the stellar limb-darkening because this would require a reduction of the stellar temperature outside the error limits of the assumed value. Following ref. 16, we would need to reduce the stellar temperature by roughly 300 K to produce a $\sim 0.03\%$ effect, and this is too large a drop given the well-known temperature of $6,117 \pm 26$ K for HD 209458, an F9/G0 star.

possesses a hot, dense region at higher altitudes, producing a 0.03% Balmer-continuum absorption, which is a new constraint for atmospheric models. Using the upper atmospheric model^{4,5} of HD 209458b, we find that the absorption can be readily produced in a 5,000 K layer that is 1,000 km thick at an altitude of 8,500 km, in agreement with the observations. This absorption layer is in a region of rising temperatures and accelerating outflow, between the lower, colder atmosphere and the hotter (10,000 K or more) upper thermospheric region of the hydrodynamically escaping atmosphere. This layer is only a small fraction of the full escaping upper atmosphere that produces a 15% Lyman- α absorption by the most prevalent $n = 1$ (ground state) H I population².

Finally, we point out that we cannot detect the absorption from isolated narrow Balmer lines, in particular H β at 4,861 Å and H γ at 4,340 Å, which are included in our spectral window. At the relatively high temperature ($\sim 5,000$ K) found for the peak absorbing layer of the Balmer continuum, the thermal line broadening is approximately ten times smaller than our spectral resolution, so the individual lines cannot be resolved. Unsuccessful attempts have been made to detect the strongest Balmer line, H α at 6,563 Å. The optical depth of H α would be very high in the absorbing layer, producing an opaque disk with a radius of $1.09 R_{\text{p}}$. However, this disk would only produce a $\sim 0.3\%$ absorption in H α , and this, combined with the narrow ~ 0.3 Å thermal width of the line, makes detection very difficult. Our detection of the 0.03% absorption in the Balmer continuum is possible because it spans a large ~ 550 Å wavelength range and the

data were taken with HST, which has numerous advantages over ground-based telescopes.

The HST observations presented here constitute the first detection of Balmer jump and continuum absorption in a planetary atmosphere, and the first detection of an isolated hot layer in the lower thermosphere of the transiting planet HD 209458b. These discoveries provide a valuable tool to probe the thermospheres of hot-giant extrasolar planets that orbit close to their parent stars, by placing empirical constraints on the thermosphere.

Received 3 October; accepted 8 December 2006.

- Burrows, A. & Lunine, J. Extra-solar planets — astronomical questions of origin and survival. *Nature* **378**, 333 (1995).
- Vidal-Madjar, A. *et al.* An extended upper atmosphere around the extrasolar planet HD209458b. *Nature* **442**, 143–146 (2003).
- Lecavelier des Etangs, A., Vidal-Madjar, A., McConnell, J. C. & Hebrard, G. Atmospheric escape from hot Jupiters. *Astron. Astrophys.* **418**, L1–L4 (2004).
- Yelle, R. Aeronomy of extra-solar giant planets at small orbital distances. *Icarus* **170**, 167–179 (2004).
- Yelle, R. Corrigendum to “Aeronomy of extra-solar giant planets at small orbital distances [*Icarus* 170 (2004) 167–179].” *Icarus* **183**, 508 (2006).
- Vidal-Madjar, A. *et al.* Detection of oxygen and carbon in the upper atmosphere of the extrasolar planet HD 209458b. *Astrophys. J.* **604**, L69–L72 (2004).
- Henry, G. W., Marcy, G. W., Butler, R. P. & Vogt, S. S. A transiting “51-Peg-like” planet. *Astrophys. J.* **529**, L41–L44 (2000).
- Charbonneau, D., Brown, T. M., Noyes, R. W. & Gilliland, R. L. Detection of an extrasolar planet atmosphere. *Astrophys. J.* **568**, 377–384 (2002).
- Brown, T. M., Charbonneau, D., Gilliland, R. L., Noyes, R. W. & Burrows, A. Hubble Space Telescope time-series photometry of the transiting planet of HD209458. *Astrophys. J.* **552**, 699–709 (2001).

10. Knutson, H., Charbonneau, D., Noyes, R. W., Brown, T. M. & Gilliland, R. L. Using stellar limb-darkening to refine the properties of HD 209458b. *Astrophys. J.* **655**, 564–575 (2007).
11. Kurucz, R. HD209458 stellar model and associated spectra. (<http://kurucz.harvard.edu/stars/HD209458/>) (2005).
12. Mandel, K. & Agol, E. Analytic light curves for planetary transit searches. *Astrophys. J.* **580**, L171–L175 (2002).
13. Carroll, B. W. & Ostlie, D. A. *An Introduction to Modern Astrophysics* Ch. 8 (Addison-Wesley, San Francisco, 1996).
14. Mihalas, D. *Stellar Atmospheres* 2nd edn, 99 (W.H. Freeman & Company, New York, 1978).
15. Deming, D., Seager, S., Richardson, L. J. & Harrington, J. Infrared radiation from an extrasolar planet. *Nature* **434**, 740–743 (2005).
16. Claret, A. A new non-linear limb-darkening law for LTE stellar atmosphere models. *Astron. Astrophys.* **363**, 1081–1190 (2000).

Supplementary Information is linked to the online version of the paper at www.nature.com/nature.

Acknowledgements We thank J. Holberg for discussions, as well as R. Yelle for the atmospheric model of HD 209458b. Support for this work was provided by NASA through a grant from the Space Telescope Science Institute which is operated by AURA, under NASA contract.

Author Contributions The work required for this paper was equally shared between D.K.S. and G.E.B. F.H. suggested the Balmer jump spectral identification, and joined discussions.

Author Information Reprints and permissions information is available at www.nature.com/reprints. The authors declare no competing financial interests. Correspondence and requests for materials should be addressed to G.E.B. (gilda@vega.LPL.arizona.edu).

Resolving photon number states in a superconducting circuit

D. I. Schuster^{1*}, A. A. Houck^{1*}, J. A. Schreier¹, A. Wallraff^{1†}, J. M. Gambetta¹, A. Blais^{1†}, L. Frunzio¹, J. Majer¹, B. Johnson¹, M. H. Devoret¹, S. M. Girvin¹ & R. J. Schoelkopf¹

Electromagnetic signals are always composed of photons, although in the circuit domain those signals are carried as voltages and currents on wires, and the discreteness of the photon's energy is usually not evident. However, by coupling a superconducting quantum bit (qubit) to signals on a microwave transmission line, it is possible to construct an integrated circuit in which the presence or absence of even a single photon can have a dramatic effect. Such a system¹ can be described by circuit quantum electrodynamics (QED)—the circuit equivalent of cavity QED, where photons interact with atoms or quantum dots. Previously, circuit QED devices were shown to reach the resonant strong coupling regime, where a single qubit could absorb and re-emit a single photon many times². Here we report a circuit QED experiment in the strong dispersive limit, a new regime where a single photon has a large effect on the qubit without ever being absorbed. The hallmark of this strong dispersive regime is that the qubit transition energy can be resolved into a separate spectral line for each photon number in the cavity. This effect is used to distinguish between coherent and thermal fields, and could be used to create a photon statistics analyser. As no photons are absorbed by this process, it should be possible to generate non-classical states of light by measurement and perform qubit–photon conditional logic, the basis of a logic bus for a quantum computer.

Cavity QED³ is a test-bed system for quantum optics⁴ that allows investigation of fundamental questions about quantum measurement and decoherence, and enables applications such as squeezed light sources and quantum logic gates. To achieve it, an atom is placed between two mirrors, forming a cavity that confines the electromagnetic field and enhances the atom–photon interaction strength. Cavity QED can be characterized by this interaction strength, g , and the atom cavity detuning, Δ , resulting in several regimes that we represent with the parameter space diagram in Fig. 1. Resonance occurs when the detuning is less than the interaction strength ($\Delta < g$, blue region in Fig. 1), allowing real excitations to be exchanged between the atom and the cavity, resulting in phenomena such as enhanced spontaneous emission into the cavity mode (the Purcell effect⁵). The resonant strong coupling regime of cavity QED is achieved when the coupling rate, g , is larger than the inverse atom transit time through the cavity, $1/T$, and larger than the decay rates of the atom, γ , and the cavity, κ . In this regime, the photon and atom are coherently coupled, and a single photon is periodically absorbed and re-emitted (the vacuum Rabi oscillations) at a rate $2g$. Strong coupling has traditionally been studied in atomic systems using alkali atoms⁶, Rydberg atoms⁷, or ions^{8,9}. More recently, strong coupling

with solid state systems has been achieved with superconducting circuits^{2,10,11} and approached in semiconducting quantum dots^{12,13}. The resonant strong regime of cavity QED is interesting because the joint system becomes anharmonic, allowing experiments in nonlinear optics and quantum information at the single photon level.

In the dispersive (off-resonant) limit, the atom cavity detuning is larger than the coupling, $\Delta \gg g$, and only virtual photon exchange is allowed, keeping the atom and photon largely separable (red and white regions in Fig. 1). The atom (photon) now acquires only a small photonic (atomic) component of magnitude $(g/\Delta)^2$, and an accompanying frequency shift, $2\chi = 2g^2/\Delta$. In this case, the dispersive and rotating wave approximations apply, and the system is described to second order in g/Δ by the quantum version of the a.c. Stark hamiltonian¹:

$$H = \hbar\omega_r(a^\dagger a + 1/2) + \hbar\omega_a\sigma_z/2 + \hbar\chi(a^\dagger a + 1/2)\sigma_z$$

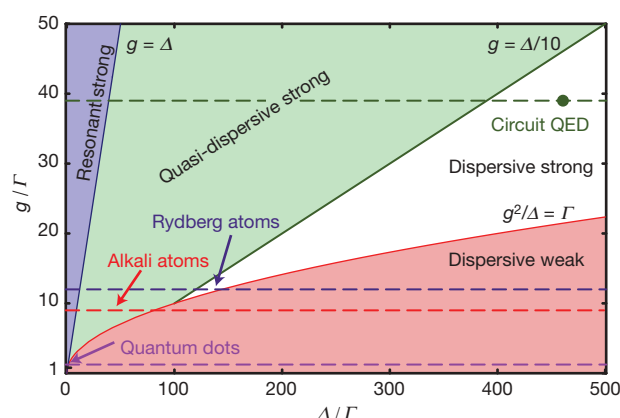


Figure 1 | A parameter space diagram for cavity QED. The space is described by the atom–photon coupling strength, g , and the detuning Δ between the atom and cavity frequencies, normalized to the rates of decay represented by $\Gamma = \max[\gamma, \kappa, 1/T]$. Different cavity QED systems, including Rydberg atoms, alkali atoms, quantum dots, and circuit QED, are represented by dashed horizontal lines. The dark green filled circle represents the parameters used in this work. In the blue region the qubit and cavity are resonant, and undergo vacuum Rabi oscillations. In the red, weak dispersive, region the a.c. Stark shift $g^2/\Delta < \Gamma$ is too small to dispersively resolve individual photons, but a QND measurement of the qubit can still be realized by using many photons. In the white region QND measurements are in principle possible with demolition less than 1%, allowing 100 repeated measurements. In the green region single photon resolution is possible but measurements of either the qubit or cavity occupation cause larger demolition.

¹Departments of Applied Physics and Physics, Yale University, New Haven, Connecticut 06520, USA. [†]Present addresses: Department of Physics, ETH Zurich, CH-8093 Zürich, Switzerland (A.W.); Département de Physique et Regroupement Québécois sur les Matériaux de Pointe, Université de Sherbrooke, Sherbrooke, Québec, Canada J1K 2R1 (A.B.).

*These authors contributed equally to this work.

The first term describes a single photon mode (a) as a harmonic oscillator of frequency ω_r . The second term describes an atom or qubit, with transition frequency ω_a , as a two-level pseudo-spin (σ_x) system. The third term is a dispersive interaction that can be viewed as either an atom-state-dependent shift of the cavity frequency or a photon-number-dependent light shift (the Stark plus Lamb shifts) of the atom transition frequency. This interaction means that when the atom state is changed, an energy $2\hbar\chi$ is added to or removed from each cavity photon. The form of the interaction is of particular interest because it commutes with the individual atom and photon terms, meaning that it is possible to do a quantum non-demolition^{14,15} (QND) measurement of either the atom state by measuring the phase shift of photons in the cavity¹⁶ or photon number using the atomic Stark shift^{17,18}.

A QND measurement protocol to measure photon number might drive the atom at the Stark shifted atom frequency $\omega_n = \omega_a + 2n\chi$, followed by an independent measurement of the atom state. If the atom is excited, the field must have exactly n photons. Because the photon number is not changed in this process, the QND protocol can be repeated indefinitely. In practice, all measurements have some demolition, which limits the number of repetitions before the measurement changes the measured variable (the number of photons). In our experiment, the cavity transmission is used to measure the atom state, so while the interaction is QND, the detection performed here is not. Any cavity QED experiment that employs a fixed coupling will have demolition arising from the overlap of the atomic and photonic wavefunctions, creating a probability, $(g/\Delta)^2$, that a measurement of photon number will absorb a photon or a measurement of the atomic state will induce a transition, demolishing the measured state. This source of demolition could be minimized by adiabatically changing the coupling strength, as happens in the case of a Rydberg or alkali atom slowly passing through a cavity.

In analogy with the strong resonant case, the strong dispersive limit can be entered when the Stark shift per photon is much larger than the decoherence rates ($2\chi > \gamma, \kappa, 1/T$; the white region in Fig. 1), while the demolition remains small ($(g/\Delta)^2 \ll 1$). The small number-

dependent frequency shift present in the weak dispersive regime (red region in Fig. 1) becomes so large that each photon number produces a resolvable peak in the atomic transition spectrum, allowing the measurement we report here. It has been proposed that the dispersive photon shift could be used to make a QND measurement of the photon number state of the cavity using Rydberg atoms¹⁹. Previously attainable interaction strengths required photon number detection experiments to employ absorptive quantum Rabi oscillations in the resonant regime²⁰, allowing a QND measurement²¹ restricted to distinguishing only between zero and one photon. More recently, a non-resonant Rydberg atom experiment entered the strong dispersive limit, measuring the single photon Wigner function with demolition $(g/\Delta)^2 = 6\%$, in principle allowing ~ 15 repeated measurements²². We present here a circuit QED experiment clearly demonstrating the strong dispersive regime, resolving states of up to ten photons, and having demolition $(g/\Delta)^2 < 1\%$, which should allow up to ~ 100 repeated QND measurements.

In circuit QED^{1,16} the 'atom'–photon interaction is implemented by a Cooper pair box (CPB)²³, chosen for its large dipole moment, capacitively coupled to a full-wave one-dimensional transmission line resonator (Fig. 2). The reduced mode volume of a one-dimensional resonator compared with that of a three-dimensional cavity⁷ of similar wavelength ($w^2\lambda \approx 10^{-6} \text{ cm}^3$ versus $\lambda^3 \approx 1 \text{ cm}^3$), where w is the transverse dimension of the resonator, yields 10^6 times larger energy density. This large energy density, together with the large geometric capacitance (dipole moment) of the CPB, yields an interaction strength that is $g/\omega_{a,r} = 2\%$ of the total photon energy. This dimensionless coupling, 10^4 times larger than currently attainable in atomic systems, allows circuit QED to overcome the larger decoherence rates present in the solid-state environment, maintaining $g/\gamma_{\text{eff}} = 40$ possible coherent vacuum Rabi oscillations in the strong resonant regime, where $\gamma_{\text{eff}} = (\gamma + \kappa)/2$ is the combined photon-qubit decay rate. The equivalent comparison of the dispersive interaction to decoherence examines the Stark shift per photon in relation to the qubit decay, $2\chi/\gamma = 6$, and determines the resolution of photon number peaks. Comparing instead to the cavity lifetime yields an

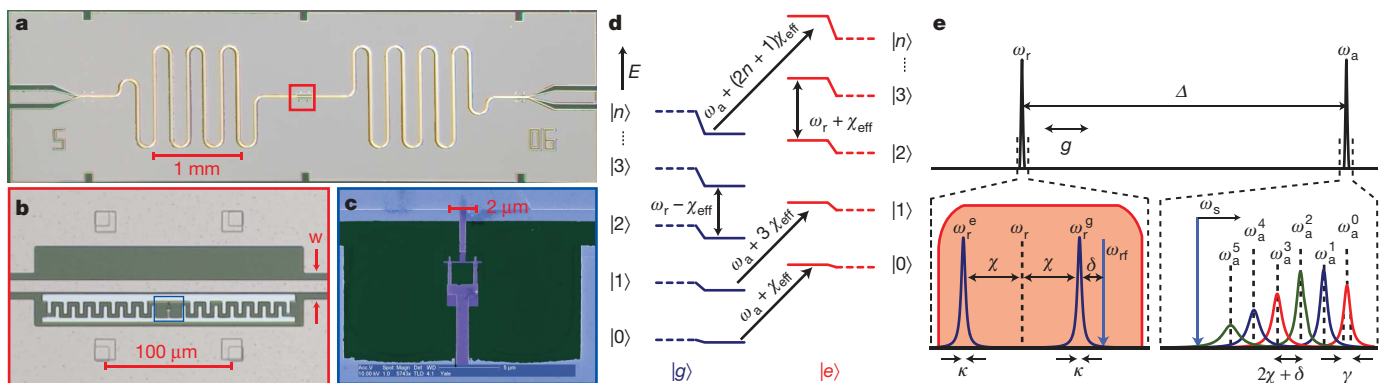


Figure 2 | A Cooper pair box inside a cavity, and spectral features of the circuit QED system. **a**, An on-chip coplanar waveguide (CPW) cavity with resonant frequency $\omega_r/2\pi = 5.7$ GHz. The area within the red box is shown magnified in **b**. **b**, The Cooper pair box (CPB), placed at a voltage antinode of the CPW (metal is beige, substrate is dark), consists of two superconducting islands (light blue) connected by a pair of Josephson tunnel junctions (purple in **c**). Both the CPB and cavity are made from aluminium. The transition frequency between the lowest two CPB levels is $\omega_a/2\pi \approx \sqrt{8E_J E_C}/\hbar = 6.9$ GHz, where the Josephson energy $E_J/\hbar = 11.5$ GHz and the charging energy $E_C/\hbar = e^2/2C_\Sigma \hbar = 520$ MHz, where C_Σ is the total capacitance between the islands. Both the large dipole coupling, $g/2\pi = 105$ MHz, and the small charging energy are due to the large geometric capacitance of the CPB to the resonator. The anharmonicity is 10%, allowing the first two levels to be addressed uniquely, though higher levels do contribute dispersive shifts, resulting in a negative effective Stark shift per photon, $\chi_{\text{eff}}/\pi = -17$ MHz. **d**, Dispersive cavity-qubit energy levels. Each level is labelled by the qubit state, $|g\rangle$ or $|e\rangle$, and photon number $|n\rangle$.

Dashed lines are qubit-cavity energy levels with no interaction ($g = 0$), where solid lines show eigenstates dressed by the dispersive interaction. Transitions from $|n\rangle \rightarrow |n+1\rangle$ show the qubit-dependent cavity shift. Transitions at constant photon number from $|g\rangle |n\rangle \rightarrow |e\rangle |n\rangle$ show a photon-number-dependent frequency shift, $2n\chi_{\text{eff}}$. **e**, Cavity-qubit spectral response. To measure the qubit state and populate the cavity, a coherent tone is driven at ω_{rf} (bottom left), which is blue detuned from the cavity by several linewidths, reducing any cavity nonlinearity. Thermal fields are generated with gaussian noise applied in the red envelope, spanning the cavity. The qubit spectrum (bottom right) is detuned from the cavity by $\Delta/2\pi = 1.2$ GHz $\gg g/2\pi$. Information about photon number is measured by monitoring transmission at ω_{rf} while driving the qubit with a spectroscopy tone at ω_s . Each photon shifts the qubit transition by more than a linewidth ($|\chi_{\text{eff}}|/2\pi > \gamma/2\pi = 1.9$ MHz, $\kappa/2\pi = 250$ kHz), giving a distinct peak for each photon number state. The maximum number of resolvable peaks is $2|\chi_{\text{eff}}|/\kappa$.

estimate of the maximum number of peaks that could possibly be resolved, $2\chi/\kappa = 70$, and determines the contrast of a qubit measurement by the cavity. These values of our parameters place the system well into the strong dispersive regime.

The photon-number-dependent frequency shift of the qubit is detected by performing spectroscopy on the qubit–cavity system (Fig. 2e). The cavity is coherently excited by applying a microwave signal (the cavity tone) at a frequency (ω_{eff}) near the cavity resonance (Fig. 2e). A spectrum is taken by sweeping the frequency (ω_s) of a second microwave signal (the spectroscopy tone), which probes the qubit absorption without significantly populating the resonator as it is detuned by many linewidths ($\omega_s - \omega_r \gg \kappa$). The detection is completed by exploiting the dual nature of the qubit–photon coupling, reusing the cavity photons as a measure of cavity transmission, demonstrated previously^{1,2,16,18} to measure the qubit excited state population. The measured transmission amplitude (Figs 3 and 4) is an approximate measure of the actual qubit population, which could in principle be measured independently. For clarity, the transmission

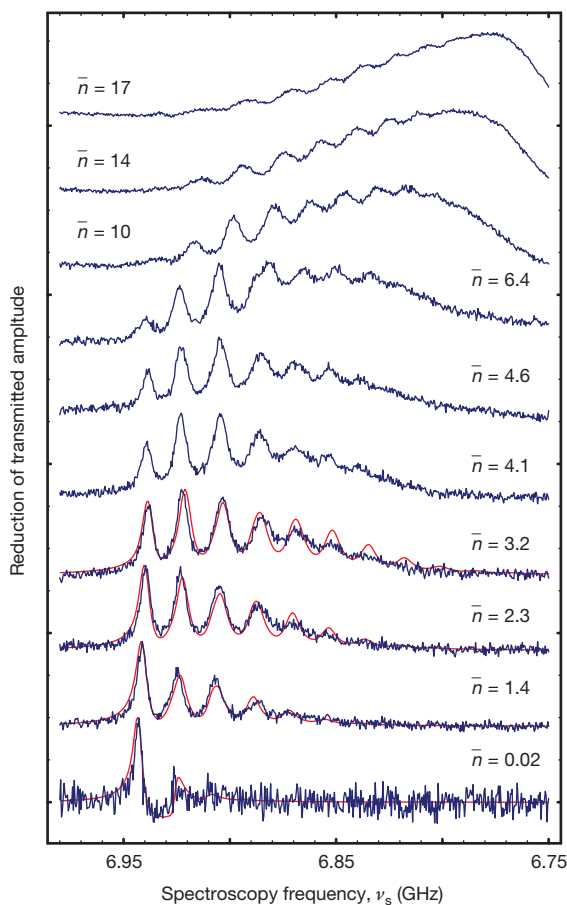


Figure 3 | Direct spectroscopic observation of quantized cavity photon number. Shown are qubit spectra with coherent cavity drive at different average cavity occupations (\bar{n}). The spectra have resolved peaks corresponding to each photon number. The peaks are separated by $2|\chi_{\text{eff}}|/2\pi = 17$ MHz. Approximately ten peaks are distinguishable. The data (blue) are well described by numerical simulations (red) with all parameters predetermined except for a single frequency offset, overall power scaling, and background thermal photon number ($n_{\text{th}} = 0.1$) used for all traces. Computational limitations prevented simulations of photon numbers beyond ~ 3 . At the lowest power nearly all of the weight is in the $|0\rangle$ peak, meaning that the cavity has a background occupation less than ($n_{\text{th}} < 0.1$). Peaks broaden as $(n + \bar{n})\kappa/2$ plus some additional contributions due to charge noise. At higher powers the peaks blend together and the envelope approaches a gaussian shape for a coherent state. As $\chi_{\text{eff}} < 0$, spectra are displayed from high to low frequency, and also have been normalized and offset for clarity.

amplitude in Figs 3 and 4 is plotted from high to low frequency. In order to reduce nonlinearities in the response, the cavity tone was applied at a small detuning $\delta/2\pi = (\omega_{\text{eff}} - \omega_r^g)/2\pi = 2$ MHz from the resonator frequency when the qubit is in the ground state. This also slightly modifies the peak splitting²⁴ (Fig. 2e).

The measured spectra reveal the quantized nature of the cavity field, containing a separate peak for each photon number state (Fig. 3)^{24,25}. These peaks approximately represent the weight of each Fock state in a coherent field with mean photon number \bar{n} , which is varied from zero to 17 photons. At the lowest photon powers, nearly all of the weight is in the first peak, corresponding to no photons in the cavity, and confirming that the background cavity occupancy is $n_{\text{th}} < 0.1$. As the input power is increased, more photon number peaks can be resolved and the mean of the distribution shifts proportional to \bar{n} . The data agree well with numerical solutions at low powers (solid lines in Fig. 3) to the markovian master equation^{4,24} with three damping sources, namely the loss of photons at rate $\kappa/2\pi = 250$ kHz, energy relaxation in the qubit at rate $\gamma/2\pi = 1.8$ MHz and the qubit dephasing rate $\gamma_\phi/2\pi = 1.0$ MHz. However, adequate numerical modelling of this strongly coupled system at higher photon numbers is quite difficult and has not yet been achieved.

In earlier work^{17,18} in the weak dispersive limit ($\chi/\gamma < 1$), the measured linewidth resulted from an ensemble of Stark shifts blurring the transition, whereas here in the strong limit ($\chi/\gamma > 1$) each member of the ensemble is individually resolved. In the spectra measured here (Fig. 3), the linewidth of a single peak can be much less than the frequency spread of the ensemble, but changes in photon number during a single measurement can still completely dephase the qubit. Taking this into account yields a predicted photon-number-dependent linewidth, $\gamma_n = \gamma/2 + \gamma_\phi + (\bar{n} + n)\kappa/2$ for the n th peak²⁴. The lowest power peak (in the $\bar{n} = 0.02$ trace) corresponds to zero

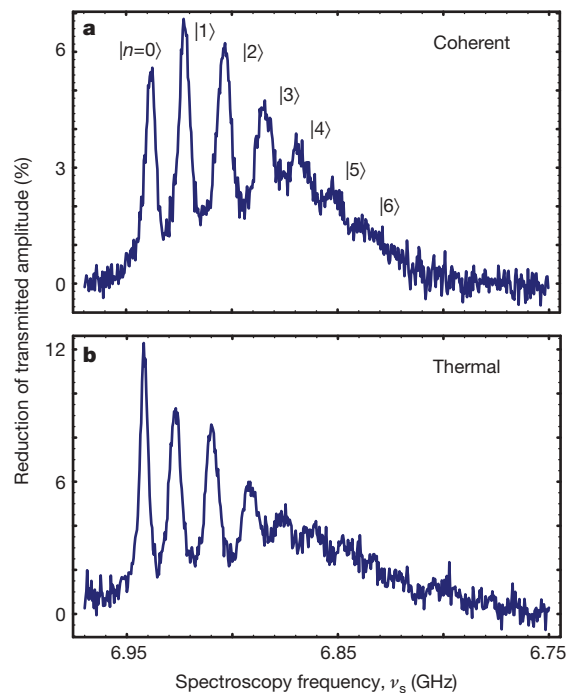


Figure 4 | Qubit spectrum distinguishes between coherent and thermal distributions. **a**, Reduction in transmitted amplitude is plotted as a proxy for qubit absorption for the case of a coherent drive with $\bar{n} = 3$ photons. **b**, Spectrum when cavity is driven with gaussian white noise approximating a thermal state also with $\bar{n} = 3$. The coherent spectrum is clearly non-monotonic and qualitatively consistent with the Poisson distribution, $P(n) = e^{-\bar{n}}\bar{n}^n/n!$, while the thermal spectrum monotonically decreases in a fashion consistent with the Bose–Einstein distribution $P(n) = \bar{n}^n/(\bar{n} + 1)^{n+1}$.

photons and measures the unbroadened linewidth, $\gamma_0/2\pi = 1.9$ MHz. When $\bar{n} = 2\chi_{\text{eff}}/\kappa$, the peaks should begin to overlap once more, returning the system to the classical field regime. If this effect were the only limitation, we might hope to count as many as 70 photon number peaks before they merge. In practice, the higher number peaks are also more sensitive to charge fluctuations in the Cooper pair box, which limits us to about 10 resolvable photon states in this measurement.

The relative area under each peak in the transmission amplitude (Fig. 4) contains information about the photon statistics of the cavity field. We can compare two cases having the same average cavity occupation ($\bar{n} \approx 3$), but containing either a coherent field (Fig. 4a) or a thermal field (Fig. 4b). To create the thermal field, gaussian noise was added in a wide band around the cavity (red in Fig. 2e). The coherent and thermal states are clearly distinguishable. The weights of the peaks are non-monotonic for a coherent distribution, whereas in the thermal distribution they monotonically decrease²⁶ for all noise intensities measured. However, for the sample parameters and measurement protocols used here, several effects prevent quantitative extraction of photon number probabilities from the data. First, the inhomogeneous broadening of the higher number peaks due to charge noise prevents independent extraction of their areas. Second, though it has been analytically shown that the qubit absorption spectrum should accurately represent the cavity photon statistics²⁴, this experiment did not have an independent means to measure the qubit, and there are imperfections in mapping the qubit spectrum onto the cavity transmission. Last, numerical simulations show that spectroscopic driving of the qubit results in complex dynamics that squeezes the cavity photon number, pointing to a path to create exotic states of light, but also partially obscuring the initial photon statistics. The measured data are consistent with numerical predictions that do take into account such squeezing effects (see Fig. 3) for photon numbers ($\bar{n} \leq 3$) that we could simulate. Although these effects are large in the present experiment, an independent measurement of the qubit could be introduced using a second cavity or Josephson-bifurcation amplifier²⁷, allowing the realization of a quantitative photon statistics analyser. Previous experiments have also measured analogous statistics of other bosonic systems, including phonons in an ion trap^{8,9}, excitations in a single electron cyclotron oscillator²⁸, and the number of atoms in a Bose–Einstein condensate passing through a cavity²⁹.

The results obtained here also suggest a method for photon–qubit conditional logic. The qubit response is now strongly dependent on the number of photons in the cavity. For example, a controlled-not (CNOT) gate between a photon and a qubit could be implemented by applying a π control pulse at the frequency corresponding to one photon in the cavity. This would flip the qubit if there were exactly one photon in the cavity, but do nothing in any other photon number state. Though the resulting qubit state is determined by the presence or absence of a cavity photon, no photons are created or destroyed. The photon can thus be reused to entangle with another distant qubit. A photon-number-based gate is analogous to the phonon common mode coupling used in ion-traps³⁰, but as the photons travel along transmission lines and not through qubits themselves, many qubits can be placed in a single wavelength, and the photons could be sent to distant qubits, including those in other cavities.

The observation of resolved photon number peaks in the qubit spectrum demonstrates a new regime for cavity QED systems, the strong dispersive limit. Measurement of the spectrum directly reveals the discrete particle nature of the microwave field inside the on-chip cavity, and is used to distinguish field states with different photon statistics. Further exploitation of this exceptionally large vacuum Rabi coupling should enable quantum computing using transmission line cavities as a quantum bus, and allow preparation of quantum states of light for use in quantum communication and nonlinear optics.

Received 20 August; accepted 20 November 2006.

- Blais, A., Huang, R., Wallraff, A., Girvin, S. & Schoelkopf, R. J. Cavity quantum electrodynamics for superconducting electrical circuits: an architecture for quantum computation. *Phys. Rev. A* **69**, 062320 (2004).
- Wallraff, A. *et al.* Strong coupling of a single photon to a superconducting qubit using circuit quantum electrodynamics. *Nature* **431**, 162 (2004).
- Mabuchi, H. & Doherty, A. C. Cavity quantum electrodynamics: Coherence in context. *Science* **298**, 1372–1377 (2002).
- Walls, D. F. & Milburn, G. J. *Quantum Optics* (Springer, Berlin, 2006).
- Purcell, E. M. Spontaneous emission probabilities at radio frequencies. *Phys. Rev.* **69**, 681 (1946).
- Thompson, R. J., Rempe, G. & Kimble, H. J. Observation of normal-mode splitting for an atom in an optical cavity. *Phys. Rev. Lett.* **68**, 1132–1135 (1992).
- Raimond, J. M., Brune, M. & Haroche, S. Manipulating quantum entanglement with atoms and photons in a cavity. *Rev. Mod. Phys.* **73**, 565–582 (2001).
- Leibfried, D. *et al.* Experimental determination of the motional quantum state of a trapped atom. *Phys. Rev. Lett.* **77**, 4281–4285 (1996).
- Leibfried, D. *et al.* Experimental preparation and measurement of quantum states of motion of a trapped atom. *J. Mod. Opt.* **44**, 2485–2505 (1997).
- Chiorescu, I. *et al.* Coherent dynamics of a flux qubit coupled to a harmonic oscillator. *Nature* **431**, 159–162 (2004).
- Johansson, J. *et al.* Vacuum Rabi oscillations in a macroscopic superconducting qubit LC oscillator system. *Phys. Rev. Lett.* **96**, 127006 (2006).
- Reithmaier, J. P. *et al.* Strong coupling in a single quantum dot-semiconductor microcavity system. *Nature* **432**, 197–200 (2004).
- Yoshie, T. *et al.* Vacuum Rabi splitting with a single quantum dot in a photonic crystal nanocavity. *Nature* **432**, 200–203 (2004).
- Grangier, P., Levenson, J. A. & Poizat, J. P. Quantum non-demolition measurements in optics. *Nature* **396**, 537–542 (1998).
- Caves, C. M., Thorne, K. S., Drever, R. W. P., Sandberg, V. D. & Zimmermann, M. On the measurement of a weak classical force coupled to a quantum-mechanical oscillator. *Rev. Mod. Phys.* **52**, 341–392 (1980).
- Wallraff, A. *et al.* Approaching unit visibility for control of a superconducting qubit with dispersive readout. *Phys. Rev. Lett.* **95**, 060501 (2005).
- Brune, M. *et al.* From Lamb shift to light shifts: vacuum and subphoton cavity fields measured by atomic phase-sensitive detection. *Phys. Rev. Lett.* **72**, 3339–3342 (1994).
- Schuster, D. I. *et al.* AC-Stark shift and dephasing of a superconducting qubit strongly coupled to a cavity field. *Phys. Rev. Lett.* **94**, 123602 (2005).
- Brune, M., Haroche, S., Lefevre, V., Raimond, J. M. & Zagury, N. Quantum nondemolition measurement of small photon numbers by Rydberg-atom phase-sensitive detection. *Phys. Rev. Lett.* **65**, 976–979 (1990).
- Brune, M. *et al.* Quantum Rabi oscillation: A direct test of field quantization in a cavity. *Phys. Rev. Lett.* **76**, 1800–1803 (1996).
- Nogues, G. *et al.* Seeing a single photon without destroying it. *Nature* **400**, 239–242 (1999).
- Bertet, P. *et al.* Direct measurement of the Wigner function of a one-photon Fock state in a cavity. *Phys. Rev. Lett.* **89**, 200402 (2002).
- Bouchiat, V., Vion, D., Joyez, P., Esteve, D. & Devoret, M. H. Quantum coherence with a single Cooper pair. *Phys. Scripta* **T76**, 165–170 (1998).
- Gambetta, J. *et al.* Qubit-photon interactions in a cavity: Measurement induced dephasing and number splitting. *Phys. Rev. A* **74**, 042318 (2006).
- Irish, E. K. & Schwab, K. Quantum measurement of a coupled nanomechanical resonator-Cooper pair box system. *Phys. Rev. B* **68**, 155311 (2003).
- Dykman, M. I. & Krivoglaz, M. A. Profiles of no-phonon lines of impurity centers interacting with local quasiloc vibrations. *Sov. Phys. Solid State* **29**, 210–214 (1987).
- Siddiqi, I. *et al.* Dispersive measurements of superconducting qubit coherence with a fast latching readout. *Phys. Rev. B* **73**, 054510 (2006).
- Peil, S. & Gabrielse, G. Observing the quantum limit of an electron cyclotron: QND measurements of quantum jumps between Fock states. *Phys. Rev. Lett.* **83**, 1287–1290 (1999).
- Ottl, A., Ritter, S., Kohl, M. & Esslinger, T. Correlations and counting statistics of an atom laser. *Phys. Rev. Lett.* **95**, 090404 (2005).
- Monroe, C., Meekhof, D. M., King, B. E., Itano, W. M. & Wineland, D. J. Demonstration of a fundamental quantum logic gate. *Phys. Rev. Lett.* **75**, 4714–4717 (1995).

Acknowledgements This work was supported in part by the National Security Agency under the Army Research Office, the NSF, the W. M. Keck Foundation and Yale University. A.A.H. acknowledges support from Yale University via a Quantum Information and Mesoscopic Physics Fellowship. A.B. was supported by NSERC, CIAR and FQRNT. Numerical simulations were performed on a RQCHP cluster.

Author Information Reprints and permissions information is available at www.nature.com/reprints. The authors declare no competing financial interests. Correspondence and requests for materials should be addressed to R.J.S. (Robert.Schoelkopf@yale.edu).

Label-free immunodetection with CMOS-compatible semiconducting nanowires

Eric Stern¹, James F. Klemic², David A. Routenberg², Pauline N. Wyrembak⁵, Daniel B. Turner-Evans², Andrew D. Hamilton⁵, David A. LaVan³, Tarek M. Fahmy¹ & Mark A. Reed^{2,4}

Semiconducting nanowires have the potential to function as highly sensitive and selective sensors for the label-free detection of low concentrations of pathogenic microorganisms^{1–10}. Successful solution-phase nanowire sensing has been demonstrated for ions³, small molecules⁴, proteins^{5,6}, DNA⁷ and viruses⁸; however, ‘bottom-up’ nanowires (or similarly configured carbon nanotubes¹¹) used for these demonstrations require hybrid fabrication schemes^{12,13}, which result in severe integration issues that have hindered widespread application. Alternative ‘top-down’ fabrication methods of nanowire-like devices^{9,10,14–17} produce disappointing performance because of process-induced material and device degradation. Here we report an approach that uses complementary metal oxide semiconductor (CMOS) field effect transistor compatible technology and hence demonstrate the specific label-free detection of below 100 femtomolar concentrations of antibodies as well as real-time monitoring of the cellular immune response. This approach eliminates the need for hybrid methods and enables system-scale integration of these sensors with signal processing and information systems. Additionally, the ability to monitor antibody binding and sense the cellular immune response in real time with readily available technology should facilitate widespread diagnostic applications.

We demonstrate here that the limitations of fabricated nanowire-type devices can be overcome and that nanometre-scale sensors with little mobility degradation from bulk can be achieved. We have used ultrathin silicon-on-insulator wafers^{9,10,18,19}, which require only lateral (in-plane, two-dimensional) active layer definition to achieve the nanometre dimensions needed for a nanowire-type device. Previous attempts with this approach used reactive-ion etching (RIE) of the active silicon layer, which unacceptably degraded device performance^{9,10}. To achieve the nanometre-scale dimensions necessary for sensitivity, we developed a fabrication process using an anisotropic wet etch: specifically, tetramethylammonium hydroxide, TMAH, which etches Si (111) planes about 100 times more slowly than all other planes²⁰. This approach allows retention of pattern definition (of a masking oxide layer), and smoothes edge imperfections not aligned to the (111) plane. Previous work on TMAH-defined electronic devices has shown excellent retention of electrical properties¹⁸, although not in configurations suitable for sensing. We show that ‘nanowire’ devices capable of sensing can be defined by TMAH etching. Our approach uses commercially available (100) silicon-on-insulator wafers that yield trapezoidal cross-section nanowires with dominant Si (111) exposed planes, the preferred surface for selective surface functionalization²¹.

First, we show that this process can be used reproducibly to generate non-degraded devices that are narrower than their lithographic pattern definition¹⁹. A schematic depicting a completed device before

removal of the masking oxide is shown in Fig. 1a. The anisotropic wet etch undercuts this masking oxide, whose lateral dimensions can be achieved with optical lithography, although it does not appreciably etch the degenerately doped ($>10^{20} \text{ cm}^{-3}$) boron contacts²⁰. A top-view scanning electron micrograph of a device with the oxide mask

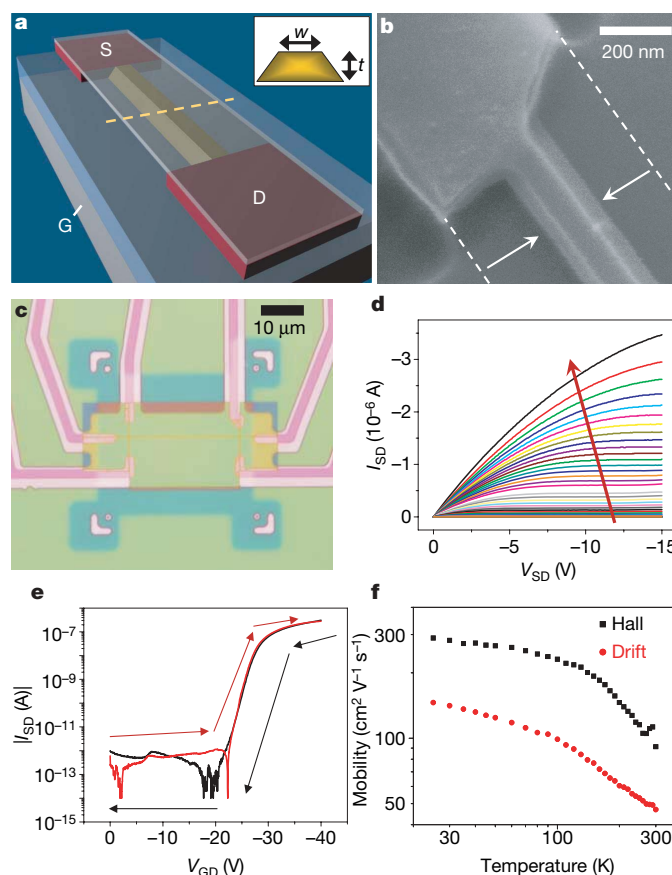


Figure 1 | Device fabrication and electrical performance. **a**, Schematic after anisotropic etch. The silicon-on-insulator active channel (yellow, width w and thickness t) is undercut etched, whereas degenerate leads (red) are etch-resistant. The source (S), drain (D), and underlying backgate (G) are labelled. **b**, **c**, Scanning electron micrograph (**b**) and optical micrograph (**c**) of a completed device. **d**, $I_{SD}(V_{SD})$ ($w = 50 \text{ nm}$, $t = 25 \text{ nm}$) for varying V_{GD} (0 to -40 V , $\Delta V = -1 \text{ V}$), illustrating p-type accumulation mode behaviour. **e**, $|I_{SD}|(V_{GD})$ for $V_{SD} = -1 \text{ V}$ for forward (red) and reverse (black) sweep. **f**, Accumulation-mode Hall and drift mobilities versus temperature ($w = 300 \text{ nm}$, $t = 25 \text{ nm}$).

¹Department of Biomedical Engineering, ²Department of Electrical Engineering, ³Department of Mechanical Engineering, ⁴Department of Applied Physics, Yale University, P O Box 208284 New Haven, Connecticut 06511, USA. ⁵Department of Chemistry, Yale University, P O Box 208107, New Haven, Connecticut 06511, USA.

removed (Fig. 1b) illustrates its trapezoidal shape. Although pattern-definition roughness is evident at the contact regions, the nanowire has no such roughness, owing to the planarization of the etch. Reproducible and well-controlled device narrowing (Supplementary Fig. 3) is achieved owing to the slow Si (111) etch rate. The fabrication approach is flexible, allowing for the configuration of a variety of nanowire geometries, such as a six-point, Hall bar device (see optical micrograph in Fig. 1c). The CMOS compatibility of the technique enables the simultaneous fabrication of sensor arrays, complementary error detection^{9,10}, and integrated signal processing electronics. Although nanowire arrays fabricated with this process may not be capable of achieving the ultrahigh densities attainable with other approaches, considerations including Debye screening length (λ_D)⁹, length of functionalization molecules, and macromolecular size may render ultrahigh density arrays suboptimal for sensing applications.

Electrical characterization verifies that this fabrication approach produces high-quality devices. The source–drain current (I_{SD}) versus source–drain voltage (V_{SD}) dependence for varying gate–drain voltage (V_{GD}) is shown in Fig. 1d, and the $I_{SD}(V_{GD})$ dependence for constant V_{SD} in Fig. 1e, for a representative p-type device. The small hysteresis between forward and reverse $I_{SD}(V_{GD})$ slopes suggests minimal defect-induced charge trapping. Peak drift mobilities were calculated from the measured $I_{SD}(V_{GD})$ dependence and a self-consistent device simulation (Silvaco program; www.silvaco.com); averaged across 12 devices, we obtain $54 \text{ cm}^2 \text{ V}^{-1} \text{ s}^{-1}$, with a maximum of $139 \text{ cm}^2 \text{ V}^{-1} \text{ s}^{-1}$. These results compare favourably with p-type silicon doped to 10^{15} cm^{-3} , which has a bulk mobility of $450 \text{ cm}^2 \text{ V}^{-1} \text{ s}^{-1}$ at 300 K (ref. 22), and the known decrease in mobility for high field and anisotropically defined Si (111) planes²³. The ability to produce nanowires in a Hall bar geometry allows measurement of the Hall mobility in a nanowire for the first time to our knowledge, Fig. 1f. Ongoing studies are examining drift

versus Hall mobilities and their utility in determining scattering mechanisms.

To characterize liquid-phase sensor response, a macro-scale solution chamber was designed specifically to avoid the well-characterized limits on sensitivity and response time inherent in diffusion-limited systems such as microchannels²⁴. Our design (Fig. 2a) is experimentally simple and induces mixing during fluid exchange, and was used for all solution-based sensor measurements.

Unfunctionalized devices were characterized as hydrogen ion sensors; the oxide that coats the exposed silicon nanowire surfaces (top and sides) can be protonated and deprotonated by varying pH, which in turn gates the underlying device, thereby modulating I_{SD} (refs 3, 25). The response of a large and small device to five solutions with pH values varying from 6.0–8.0 is displayed in Fig. 2b. Consistent with p-type semiconducting behaviour, the source–drain conduction decreases as the acidity of the solution increases. Both devices respond appropriately to pH changes (linearly on a logarithmic current scale), with the smaller device exhibiting greater sensitivity: the pH 8.0/pH 6.0 current ratio is 43.8 versus 11.4 (for the smaller versus the larger device, respectively). The impact of scaling on sensitivity is illustrated in Fig. 2c and the TMAH-etched devices were found to scale with inverse surface area. The sensor response of a 3- μm -wide RIE edge-defined control structure processed simultaneously with the TMAH-etched devices is also shown in Fig. 2c. This device is nominally identical with the exception of channel definition, and illustrates RIE-induced degradation of sensing performance.

To demonstrate the efficacy of these sensors in monitoring real-time cellular responses, we analysed the well-characterized system of T-lymphocyte activation²⁶. Antibody-mediated crosslinking of cell-surface CD3 ligands triggers activation of T cells, inducing intracellular signalling and subsequent effector mechanisms. One consequence of such activation includes the release of acid²⁷. Addition of species-specific antibody directed against the mouse CD3 complex

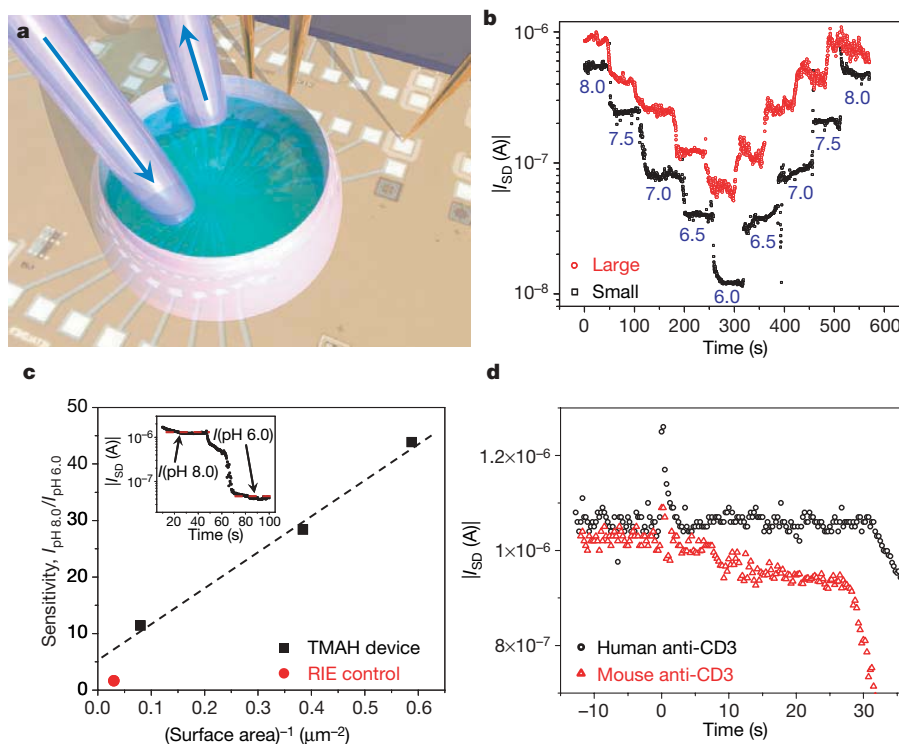


Figure 2 | Unfunctionalized device sensing. **a**, Schematic of fluid exchange system superimposed on chip optical micrograph. Fluid supply and return (arrows) are provided by Tygon tubes. **b**, Response of two sensors to five solutions of different pH (indicated in blue). Large sensor: $w = 1,000 \text{ nm}$, $t = 80 \text{ nm}$. Small sensor: $w = 100 \text{ nm}$, $t = 25 \text{ nm}$. **c**, Device sensitivity versus

inverse device surface area. The inset shows the sensitivity definition. **d**, Response of devices with $w = 100 \text{ nm}$ and $t = 40 \text{ nm}$ to changes in extracellular pH. A non-immune (human anti-CD3, black) and immune (mouse anti-CD3, red) stimulant were added to $\sim 6,000$ mouse-derived T cells at time zero.

(mouse-anti-CD3) to a suspension of mouse splenocytes containing T cells caused a current decrease after ~ 10 s and a continued negative derivative, Fig. 2d. In contrast, a control experiment with a species-specific antibody to human CD3 showed no response. Device instability was observed at ~ 30 s, although preliminary measurements have indicated that unintentional solution-to-backgate leakage in the present device design may be the cause. These data are consistent with previous results obtained with a microphysiometer²⁷ and with expectations regarding early signals responsible for T-cell activation that involve clustering of CD3 receptors²⁶.

Another powerful application of these devices is the direct detection of macromolecules without the need for the a priori attachment of fluorescent, radioactive or other probes to those macromolecules, that is, label-free sensing. Specific detection using this approach therefore requires that the nanowire be functionalized with a receptor for the unlabelled macromolecule. To maximize device sensitivity, only the nanowire should be functionalized, because nonspecific functionalization of both the nanowire and the underlying oxide will greatly diminish sensitivity owing to binding competition^{3,4,6–8,10}. We used dec-9-enyl-carbamic acid tert-butyl ester for functionalization because this molecule has previously been shown to confer amine functionality selectively to silicon²⁸, and we found that device performance is preserved after functionalization with this olefin (Supplementary Fig. 5b). Electrically directed functionalization²¹ was achieved (Supplementary Fig. 6) but was found to unacceptably degrade device performance (Supplementary Fig. 5e), most probably by creating redox-active surface traps.

Sensitivity to protein binding was characterized using the well-known biotin-avidin/streptavidin interaction. To avoid the problem of Debye screening⁹, the salt concentrations in the buffers used for macromolecular sensing experiments were chosen such that λ_D was sufficiently long to enable sensing, but sufficiently short to screen unbound macromolecules²⁹. We first determined biotinylated³⁰

device responses to streptavidin, biotin-quenched streptavidin (streptavidin pre-treated with five equivalents of biotin), and avidin (all 1 nM); see Fig. 3a. The addition of streptavidin resulted in a current increase due to the protein's negative charge, whereas the previously quenched streptavidin elicited no response (separately, fluorescently conjugated streptavidin was bound and fluorescently imaged; see inset to Fig. 3a). In contrast, upon introduction of avidin, the current decreased due to the protein's positive charge. A poly(ethylene glycol) (PEG)-functionalized control device yielded no response to 1 nM streptavidin addition with the exception of injection transient noise, which is observed in all measurements. Complementary devices, necessary for error detection, demonstrated opposite polarity (Supplementary Fig. 7).

To demonstrate unequivocally that the biotin–streptavidin interaction was responsible for sensor response, biotinylation of one device was performed with a cleavable molecule (SS-biotin), while a second device was biotinylated with a non-cleavable molecule (LC-biotin)³⁰. The initial response of each sensor to 1 nM streptavidin is similar (Fig. 3b). The subsequent addition of a reducing agent cleaved the disulphide bond²¹, with the resultant current for the SS-biotinylated device returning to the original baseline value, whereas the LC-biotinylated control was insensitive to the reducing agent.

Device sensitivity to protein charge and concentration, the hallmarks of nanowire-field effect transistor sensing, were also studied. Avidin is positive in neutral solutions owing to its high isoelectric point ($pI \approx 10.5$), but its effective charge can be decreased by increasing solution pH. Figure 3c demonstrates decreased device sensitivity with increasing solution pH (1 nM avidin). Thus, to optimize protein sensing, it is imperative that the $|pH_{\text{solution}} - pI|$ be maximized. (Alternatively, with the use of a linear solution pH gradient, this platform could be used to determine unknown protein pI values.)

An exploration of the detection limit of these sensors is shown in Fig. 3d, where streptavidin concentrations are decreased from 1 nM to 10 fM. Close inspection of the post-transition current reveals that the response at the highest protein concentrations saturates (probably fully coating the sensor with bound protein during solution exchange), whereas the signal continues to increase for proteins in the solutions of lower concentration, probably owing to continued diffusion and binding to the devices after initial mixing. The 10 fM solution has an initial signal-to-noise response of 140, implying a detection floor of ~ 70 aM.

Device utility for immunodetection applications using antibodies was demonstrated with commercially available antibodies to mouse immunoglobulin G (IgG) and mouse immunoglobulin A (IgA) proteins. A cross-comparison assay was performed by first functionalizing two devices with goat anti-mouse IgG and two additional devices with goat anti-mouse IgA³⁰. Devices from each group were then used to sense 100 fM antigen. Figure 4 shows clear discrimination (after injection transient noise) of the specific antigen over the nonspecific

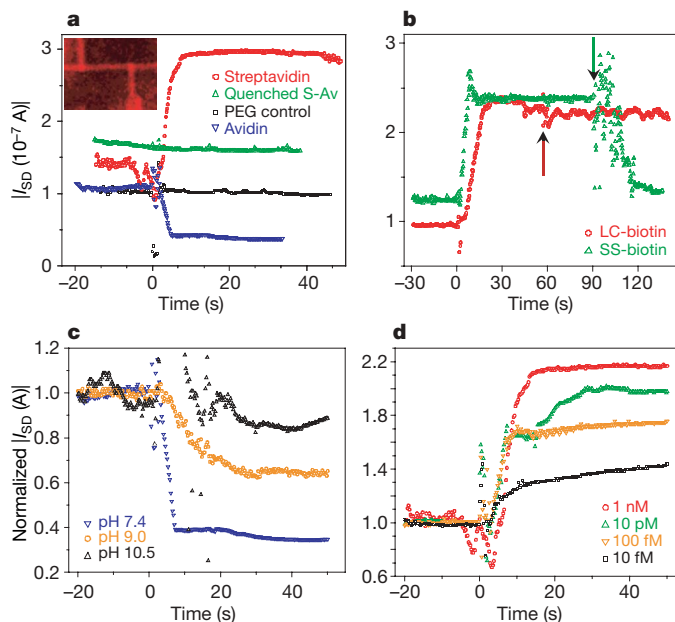


Figure 3 | Protein detection and sensitivity. Solution exchange occurs at time zero. **a**, Specific recognition and protein charge determination of avidin/streptavidin. All additions used 1 nM solutions. Inset shows fluorescence micrograph of biotin-functionalized device after fluorescently labelled streptavidin addition. **b**, Verification of surface charge by cleavage. Streptavidin (1 nM) addition to LC-biotin- or SS-biotin-functionalized devices. The arrow indicates reducing agent (TCEP) addition. **c**, Biotinylated sensor response to protein charge, by addition of 1 nM avidin in buffers with different pH values. **d**, Detection response with decreasing streptavidin concentration. For **c** and **d**, currents were normalized by dividing the measured I_{SD} by the pre-addition average current.

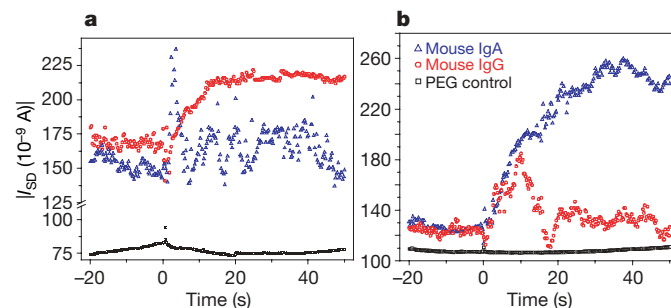


Figure 4 | Demonstration of immunodetection. All solution exchanges occurred at time zero. Sensor responses to 100 fM mouse-IgG (red) or 100 fM mouse-IgA (blue) for goat anti-mouse IgG-functionalized sensor (**a**) or goat anti-mouse IgA-functionalized sensor (**b**). The PEG-functionalized sensor control is shown in black.

control for the reciprocal cases, demonstrating selective immunodetection. Thus, the ability of this approach to specifically detect antibodies at less than 100 fM concentrations (also with complementary electronic response; see Supplementary Fig. 7c) has been shown.

We have thus demonstrated a novel approach for realizing integrable silicon nanowire sensors for less than 100 fM specific label-free antibody detection, as well as for monitoring real-time live cellular response. Although this study focused on device and sensor performance, the strength of the approach lies in seamless integration with CMOS technology. While device integration and reliability issues (including high-reliability selective functionalization) should not be trivialized, our approach appears to have potential for extension to a fully integrated system, with wide use as sensors in molecular and cellular arrays.

METHODS

For detailed descriptions of device fabrication, organic synthesis and device functionalization, see the Supplementary Information.

General sensing parameters. In all experiments I_{SD} was measured at 0.25 s intervals. Unfunctionalized sensor measurements used $V_{SD} = -5$ V and $V_{GD} = -33$ V, while for functionalized-sensor measurements, $V_{SD} = -2$ V and $V_{GD} = -20$ V. Mixing was continued after injection of the solution of interest.

Macromolecule sensing. All devices used for functionalized-sensing experiments were nominally similar, with channel thickness $t = 40$ nm and width $w = 50$ –150 nm. Each measurement was produced by a distinct device.

Received 2 August; accepted 30 November 2006.

- Lim, D. V., Simpson, J. M., Kearns, E. A. & Kramer, M. F. Current and developing technologies for monitoring agents of bioterrorism and biowarfare. *Clin. Microbiol. Rev.* **18**, 583–607 (2005).
- Madou, M. J. & Cubicciotti, R. Scaling issues in chemical and biological sensors. *Proc. IEEE* **91**, 830–838 (2003).
- Cui, Y., Wei, Q., Park, H. & Lieber, C. M. Nanowire nanosensors for highly sensitive and selective detection of biological and chemical species. *Science* **293**, 1289–1292 (2001).
- Wang, W. U., Chen, C., Lin, K.-h., Fang, Y. & Lieber, C. M. Label-free detection of small-molecule-protein interactions by using nanowire nanosensors. *Proc. Natl Acad. Sci. USA* **102**, 3208–3212 (2005).
- Tang, T. et al. Complementary response of In_2O_3 nanowires and carbon nanotubes to low-density lipoprotein chemical gating. *Appl. Phys. Lett.* **86**, 103903 (2005).
- Zheng, G., Patolsky, F., Cui, Y., Wang, W. U. & Lieber, C. M. Multiplexed electrical detection of cancer markers with nanowire sensor arrays. *Nature Biotechnol.* **23**, 1294–1301 (2005).
- Hahn, J.-i. & Lieber, C. M. Direct ultrasensitive electrical detection of DNA and DNA sequence variations using nanowire nanosensors. *Nano Lett.* **4**, 51–54 (2004).
- Patolsky, F. et al. Electrical detection of single viruses. *Proc. Natl Acad. Sci. USA* **101**, 14017–14022 (2004).
- Cheng, M. M.-C. et al. Nanotechnologies for biomolecular detection and medical diagnostics. *Curr. Opin. Chem. Biol.* **10**, 11–19 (2006).
- Li, Z. et al. Sequence-specific label-free DNA sensors based on silicon nanowires. *Nano Lett.* **4**, 245–247 (2004).
- Chen, R. J. et al. An investigation of the mechanisms of electronic sensing of protein adsorption on carbon nanotube devices. *J. Am. Chem. Soc.* **126**, 1563–1568 (2004).
- Huang, Y., Duan, X., Wei, Q. & Lieber, C. M. Directed assembly of one-dimensional nanostructures into functional networks. *Science* **291**, 630–633 (2001).
- Evoy, S. et al. Dielectrophoretic assembly and integration of nanowire devices with functional CMOS operating circuitry. *Microelect. Eng.* **75**, 31–42 (2004).
- Englander, O., Christensen, D., Kim, J., Lin, L. & Morris, S. J. S. Electric-field assisted growth and self-assembly of intrinsic silicon nanowires. *Nano Lett.* **5**, 705–708 (2005).
- Elibol, O. H., Morissette, D., Akin, D., Denton, J. P. & Bashir, R. Integrated nanoscale silicon sensors using top-down fabrication. *Appl. Phys. Lett.* **83**, 4613–4615 (2003).
- Clement, N. et al. Electronic transport properties of single-crystal silicon nanowires fabricated using an atomic force microscope. *Physica E* **13**, 999–1002 (2002).
- Wang, D., Sherif, B. A. & Heath, J. R. Silicon p-FETs from ultrahigh density nanowire arrays. *Nano Lett.* **6**, 1096–1100 (2006).
- Liu, Y., Ishii, K., Tsutsumi, T., Masahara, M. & Suzuki, E. Ideal rectangular cross-section Si-fin channel double-gate MOSFETs fabricated using orientation-dependent wet etching. *IEEE Elect. Dev. Lett.* **24**, 484–486 (2003).
- Saitoh, M., Murakami, T. & Hiramoto, T. Large Coulomb blockade oscillations at room temperature in ultranarrow wire channel MOSFETs formed by slight oxidation process. *IEEE Trans. Nanotech.* **2**, 241–245 (2003).
- Tabata, O., Asahi, R., Funabashi, H., Shimaoka, K. & Sugiyama, S. Anisotropic etching of silicon in TMAH solutions. *Sensors Actuators A* **34**, 51–57 (1992).
- Bunimovich, Y. L. et al. Electrochemically programmed, spatially selective biofunctionalization of silicon wires. *Langmuir* **20**, 10630–10638 (2004).
- Sze, S. M. *Physics of Semiconductor Devices* 2nd edn 849 (John Wiley & Sons, New York, 1981).
- Sun, S. C. & Plummer, J. D. Electron mobility in inversion and accumulation layers on thermally oxidized silicon surfaces. *IEEE J. Solid-State Circuits* **15**, 562–573 (1980).
- Sheehan, P. E. & Whitman, L. J. Detection limits for nanoscale biosensors. *Nano Lett.* **5**, 803–807 (2005).
- Laws, G. M. et al. Molecular control of the drain current in a buried channel MOSFET. *Phys. Status Solidi B* **233**, 83–89 (2002).
- Trautmann, A. Microclusters initiate and sustain T cell signaling. *Nature Immunol.* **6**, 1213–1214 (2005).
- Beeson, C. et al. Early biochemical signals arise from low affinity TCR-ligand reaction at the cell-cell interface. *J. Exp. Med.* **184**, 777–782 (1996).
- Strother, T., Hamers, R. J. & Smith, L. M. Covalent attachment of oligodeoxyribonucleotides to amine-modified Si (001) surfaces. *Nucleic Acids Res.* **28**, 3535–3541 (2000).
- Israelachvili, J. N. *Intermolecular and Surface Forces with Applications to Colloidal and Biological Systems* Ch. 12 (Academic Press, New York, 1985).
- Hermanson, G. T. *Bioconjugate Techniques* Ch. 1–3, 5, 7, 8 (Elsevier Science & Technology Books, New York, 1996).

Supplementary Information is linked to the online version of the paper at www.nature.com/nature.

Acknowledgements We thank R. Ilic, D. Westly, M. Metzler and V. Genova (Cornell Nanofabrication Facility) for device processing assistance; T. Ma, R. Sleight, J. Hyland, M. Young and C. Tillinghast for device processing discussions; F. Sigworth and D. Stern for functionalization and sensing discussions and for assistance in manuscript preparation; M. Saltzman, K. Klemic, A. Flyer, J. Bertram and S. Jay for functionalization and sensing discussions; Z. Jiang for scanning electron micrograph imaging assistance; S. R. Lee for Silvaco simulations; and R. Munden for device measurement assistance. This work was partially supported by DARPA through ONR and AFOSR (M.A.R.), NASA (M.A.R.), the NIH (A.D.H.), the Coulter Foundation (T.M.F.), by a Department of Homeland Security graduate fellowship (E.S.), and by a N.S.F. graduate fellowship (E.S., D.A.R.). This work was performed in part at the Cornell Nanoscale Science and Technology Facility, a member of the National Nanotechnology Infrastructure Network that is supported by the NSF.

Author Contributions E.S. performed device fabrication and measurements. J.F.K. assisted in fabrication design, D.A.R. performed device mobility experiments and analysis, and P.N.W. and A.D.H. provided molecules used for device functionalization. D.T.-E. assisted in device characterization. E.S. and T.M.F. performed T-cell isolation and T-cell measurements. D.A.L., T.M.F. and M.A.R. contributed to experimental design, characterization and interpretation. E.S., J.F.K., T.M.F. and M.A.R. analysed the data and wrote the manuscript with contributions from all authors.

Author Information Reprints and permissions information is available at www.nature.com/reprints. The authors declare no competing financial interests. Correspondence and requests for materials should be addressed to M.A.R. (mark.reed@yale.edu) or T.M.F. (tarek.fahmy@yale.edu).

A molecular information ratchet

Viviana Serreli¹, Chin-Fa Lee¹, Euan R. Kay¹ & David A. Leigh¹

Motor proteins and other biological machines are highly efficient at converting energy into directed motion and driving chemical systems away from thermodynamic equilibrium¹. But even though these biological structures have inspired the design of many molecules that mimic aspects of their behaviour^{2–15}, artificial nanomachine systems operate almost exclusively by moving towards thermodynamic equilibrium, not away from it. Here we show that information about the location of a macrocycle in a rotaxane—a molecular ring threaded onto a molecular axle—can be used, on the input of light energy, to alter the kinetics of the shuttling of the macrocycle between two compartments on the axle. For an ensemble of such molecular machines, the macrocycle distribution is directionally driven away from its equilibrium value without ever changing the relative binding affinities of the ring for the different parts of the axle. The selective transport of particles between two compartments by brownian motion in this way bears similarities to the hypothetical task performed without an energy input by a ‘demon’ in Maxwell’s famous thought experiment^{16–19}. Our observations demonstrate that synthetic molecular machines can operate by an information ratchet mechanism^{20–22}, in which knowledge of a particle’s position is used to control its transport away from equilibrium.

Maxwell originally conceived his thought experiment, which leads to a non-equilibrium distribution of thermal energy^{16,17} (temperature demon¹⁹) or brownian particles¹⁸ (pressure demon¹⁹), to illustrate the statistical nature of the second law of thermodynamics. But modern synthetic chemistry allows us to consider his idea from a very different perspective: rather than test the second law by attempting to reduce entropy in an isolated system, how can information transfer between a particle and a ‘gatekeeper’ be accomplished non-adiabatically to form a mechanism for a working brownian motion nanomachine?

This question inspired the design of rotaxane **1** (Fig. 1), which consists of a dibenzo-24-crown-8-based macrocycle mechanically locked onto a linear thread by bulky 3,5-di-*t*-butylphenyl groups situated at either end. (For an outline of the synthesis, with 25 steps in the longest linear sequence, see Supplementary Information.) An α -methyl stilbene unit divides the molecule into two ‘compartments’. When this unit adopts the *E*-stilbene isomeric form, the macrocycle can move randomly along the full length of the thread by brownian motion; in contrast, the *Z*-isomer provides a non-traversable steric barrier²³ that traps the macrocycle in one or other of the two compartments. The α -methyl stilbene ‘gate’ is asymmetrically positioned on the thread between two ammonium groups (monobenzyll ammonium, mba; dibenzyl ammonium, dba) that each bind the crown ether macrocycle non-covalently with rather similar affinities^{24,25} but are distinguishable for the purposes of monitoring the system. Photoinduced switching between the open (*E*-) and closed (*Z*-) forms of the gate can occur either through direct photon absorption by the α -methyl stilbene chromophore, or indirectly via energy transfer from the excited state of a triplet photosensitizer. The former is a minor pathway under our experimental conditions (irradiation at

350 nm wavelength) because the triplet sensitizers employed absorb far more strongly at this wavelength than α -methyl stilbene.

For a change in the distribution of the ring between the two compartments of **1** to be established, the stilbene gate needs to be closed for much of the time. This is accomplished by operating the machine in the presence of benzil (PhCOCOPh); the benzil-sensitized photo-stationary state (PSS) of α -methyl stilbene is typically 82:18 *Z:E* (ref. 26; model compounds used to design **1** all exhibited similar PSS ratios at 350 nm in various solvents, see Supplementary Information). To open the gate preferentially when the macrocycle is in the left-hand (dba) compartment a different photosensitizer, which produces a lower *Z:E* ratio for α -methyl stilbene than benzil, must be associated with the macrocycle to ‘signal’ its position and open the gate. We chose benzophenone (PhCOPh) for this purpose, as it gives a 55:45 *Z:E* PSS ratio²⁶ for α -methyl stilbene and as a substructure it could readily be incorporated into a dibenzo-crown ether (see **1**, Fig. 1). As energy transfer is distance dependent, the rates and efficiencies of the intramolecular photosensitized reaction of dba-*Z*-**1** to *E*-**1** should be very different to that of mba-*Z*-**1** to *E*-**1**, whereas the intermolecular photosensitized isomerization with benzil should be relatively independent of the position of the macrocycle. It may seem counter-intuitive that one can drive the macrocycle distribution away from its equilibrium value without ever changing the binding properties of the ring or either of the two ammonium groups that serve as binding sites. But if conditions are chosen so that the benzil-sensitized reaction dominates (gate closed) when the ring is in the mba compartment (that is, held far from the gate), whereas the benzophenone-sensitized isomerization dominates (gate open) when the ring is in the dba compartment (that is, held near to the gate), then this is precisely what should happen.

The system’s operation is shown in Fig. 1, with the results obtained reported in Fig. 2 and Fig. 3 (see Supplementary Information for additional data). The macrocycle shuttles between the ammonium binding sites of the two co-conformers of *E*-**1** shown in Fig. 1 slowly on the proton nuclear magnetic resonance (¹H NMR) timescale, and so two sets of signals, one for each translational form, are observed in the ¹H NMR spectrum of *E*-**1** (Fig. 2b). The relative integration of these peaks gives the distribution of the macrocycle between the compartments at equilibrium (gate open). The ratio is 65:35 dba:mba in CD₃OD at 298 K, as illustrated by the H_s proton signal (corresponding to the dba binding site occupied) and the H_{s'} proton signal (corresponding to the mba binding site occupied) in the partial spectrum shown in Fig. 3c. Irradiation (350 nm, CD₃OD, 298 K) of the rotaxane isomerizes the α -methyl stilbene unit, giving various amounts of the three diastereomers, dba-*Z*-**1**, mba-*Z*-**1** and *E*-**1**. As with the dba:mba distribution, the *Z:E* ratio can be readily established by the relative integration of various signals (for example, H_{K+K'} and H_{k+k'} or H_{L+L'} and H_{l+l'} shown in Fig. 2b and c, or H_{S+S'} and H_{s+s'} shown at points I–IV in Fig. 3c).

Starting from pristine *E*-**1** and with no benzil present (point I, Fig. 3a), irradiation at 350 nm (CD₃OD, 298 K) interconverts the three diastereomers of **1**, ultimately leading to a 38:21:41

¹School of Chemistry, University of Edinburgh, The King’s Buildings, West Mains Road, Edinburgh EH9 3JJ, UK.

dba-*Z*-1:mba-*Z*-1:*E*-1 photostationary state (that is, point II, Fig. 3a). While the *Z*:*E* ratio of **1** changes from 0:100 to 59:41 during this part of the experiment, the dba:mba ratio remains almost invariant at 65:35 (see below for an explanation of the transient small increase in the population of the dba compartment during the first 5 min of irradiation, Fig. 3b).

After 25 min irradiation of **1** (point II, Fig. 3a), one equivalent of benzil was added and irradiation resumed. The 1:1 combination of the benzil and benzophenone-crown ether photosensitizers produces a higher *Z*:*E* α -methyl stilbene PSS ratio (66:34, point III, Fig. 3a) than the benzophenone-crown ether alone. This modest change is accompanied for the first time, however, by a decrease in the population of the dba-compartment (dba:mba, 58:42). The amount of external sensitizer required for **1** to operate at greatest efficiency is determined by several factors, which include the relative absorptions of the different chromophores, the relative efficiencies of energy transfer from the chromophores to the α -methyl stilbene and between the triplet sensitizers themselves, and the concentration of the external sensitizer. Five equivalents of benzil proved sufficient to increase the *Z*:*E* ratio of **1** at the PSS to 80:20, essentially the same as if no benzophenone was present. Addition of more benzil did not further increase the *Z*:*E* ratio (point IV, Fig. 3a). At this maximum value the dba:mba ratio is 45:55 (dba-*Z*-1:mba-*Z*-1:*E*-1, 32:48:20); nearly one-third of the macrocycles which occupied the more energetically favourable dba compartment at equilibrium (or the PSS

obtained in the absence of benzil) have been pumped into the compartment with the less favourable mba binding site.

To confirm the mechanism by which the macrocycle distribution in **1** is driven away from its equilibrium value, the same photochemical experiment was performed on a rotaxane with a crown ether lacking a photosensitizer unit (Fig. 4). Rotaxane **2** was irradiated (350 nm, CD₃OD, 298 K) in the presence of the unthreaded benzophenone-derivatized crown ether, **3**, both with and without benzil so that isomerization by each photosensitizer could only occur intermolecularly. The results are shown graphically in Fig. 4. Although, like **1**, the *Z*:*E* ratio of **2** changes from 0:100 to 80:20 during the photochemical experiment, the distribution of the macrocycle between the two compartments in rotaxane **2** remains virtually unchanged from its equilibrium value of 52:48 dba:mba. (We note that the underivatized dibenzocrown ether in **2** is slightly less discriminatory for the different ammonium binding sites than the benzophenone-macrocycle in **1**, hence the different dba:mba ratio.)

A small and short-lived increase in the population of macrocycles present in the dba-compartment is observed during the initial irradiation of *E*-**1** in the absence of benzil (Fig. 3b). This occurs because the photosensitized isomerization reaction is a much more frequent occurrence when the photon is absorbed by the macrocycle on the dba binding site of *E*-**1**, which results in dba-*Z*-**1** forming more rapidly from *E*-**1** than mba-*Z*-**1**. Equally, however, dba-*Z*-**1**, in which the photosensitizer is trapped close to the gate, is converted back to

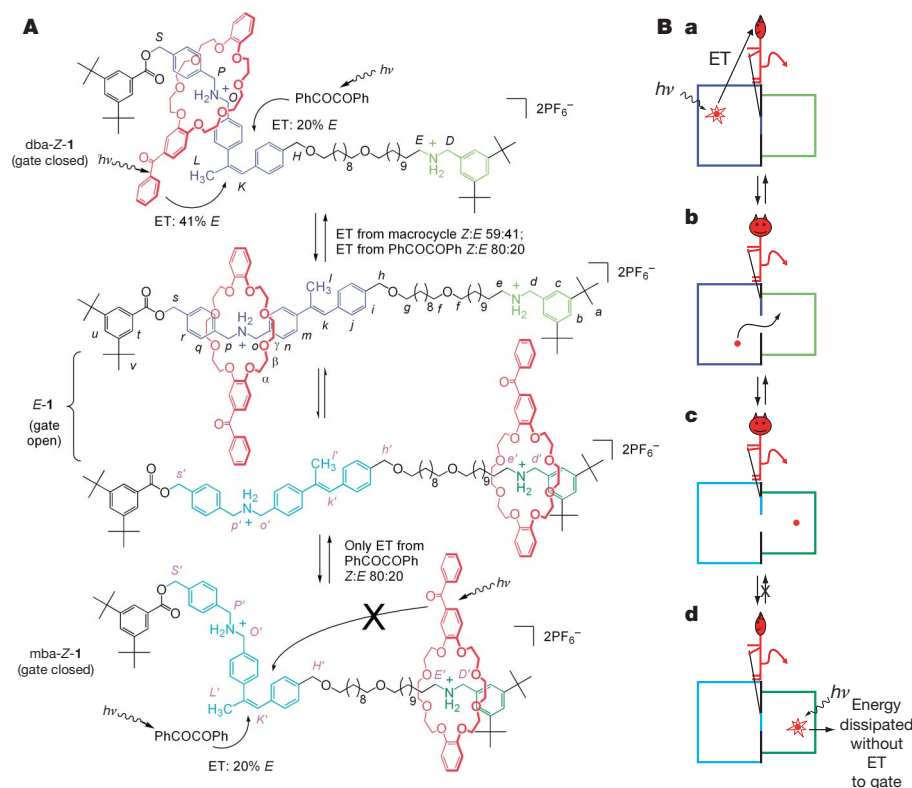


Figure 1 | A photo-operated molecular information ratchet. A, Irradiation of rotaxane **1** (1 mM) at 350 nm in CD₃OD at 298 K interconverts the three diastereomers of **1** and, in the presence of benzil (PhCOCOPh), drives the ring distribution away from the thermodynamic minimum, increasing the free energy of the molecular system without ever changing the binding strengths of the macrocycle or ammonium binding sites. For clarity, the photoinduced energy transfer (ET) pathways are only illustrated for the *Z*- (gate closed) forms of **1** although the same processes occur for the equivalent *E*- (gate open) translational isomers. When the macrocycle is on the mba binding site (green), intramolecular ET from the macrocycle is inefficient and intermolecular ET from benzil dominates (the cross on the intramolecular ET arrow is used to indicate that it is a rare event compared to

other relaxation pathways). When the macrocycle is on the dba binding site (blue), both ET mechanisms can operate efficiently. The amount of benzil present determines the relative contributions of the two ET pathways and thus the nanomachine's effectiveness in pumping the macrocycle distribution away from equilibrium (see Fig. 3). The mechanism requires the shuttling of the ring between the two ammonium groups in *E*-**1** to be slow with respect to the lifetime of the macrocycle-sensitizer triplet excited state. The Greek and italicized lettering are the proton assignments for the ¹H NMR spectra shown in Figs 2 and 3. **B**, Cartoon illustration of the operation of **1** in terms of a non-adiabatic Maxwellian pressure demon^{18,19}. See text for details.

E-1 much faster than is *mba*-*Z*-1, and thus the statistical balance of macrocycles present in the *dba*- and *mba*-compartments is quickly restored as the reaction proceeds. This phenomenon illustrates the fascinating interplay between the statistical balance of the position of the particle (*dba*/*mba* compartment) and the 'statistical balance' of the position of the gate (open *E*-stilbene/closed *Z*-stilbene) in the operation of **1**. Moving either one of these normally orthogonal chemical features away from its 'equilibrium' value moves the other one away too.

By relating the net change of position of the macrocycle between the two compartments in an ensemble of **1** to the sorting of ideal gas particles between two boxes of different volume, it can be shown (see Supplementary Information) that the free-energy change on driving the distribution away from equilibrium is given by equation (1), where *N* is the total number of particles, *x*₁ is the final mole fraction of particles in the *dba* compartment and *y*₁ is the equilibrium mole fraction of particles in *dba*.

$$\Delta G = Nk_B T \left[x_1 \ln \frac{x_1}{y_1} + (1 - x_1) \ln \frac{(1 - x_1)}{(1 - y_1)} \right] \quad (1)$$

Using the experimental values obtained for **1** (Fig. 3a), namely *x*₁ = 0.45 and *y*₁ = 0.65, this gives a free-energy change of $\Delta G = 0.083RT \text{ J mol}^{-1}$.

Note that during the operation of **1** the photons are not raising the energy of a transported component as typically happens in other artificial nanomachines. Instead, the light energy is used to power an information transfer process. As in Maxwell's thought experiment, information about the location of the particle is used to selectively and transiently lower a kinetic barrier and thereby perturb the particle distribution without energetically favouring one compartment over the other at any stage. The effectiveness of the mechanism in **1** depends directly upon the efficiency of the energy transfer to the closed gate from the excited state of a benzophenone-macrocycle that

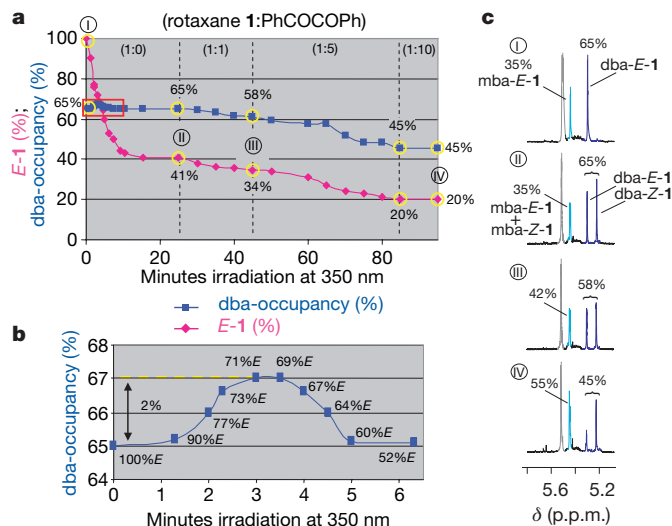


Figure 3 | Operation of a molecular information ratchet. **a**, Change in the *E*:*Z* ratio (*E*-1 (%)), the amount of the 'open gate' form of the sample, shown by purple diamonds) and the *dba*:*mba* ratio (*dba*-occupancy (%), shown by dark blue squares) that occurs during irradiation of **1** at 350 nm in CD₃OD, 298 K: I, pristine *E*-1; II, after 25 min (PSS), no added benzil; III, after a further 20 min (PSS) with 1 equiv. benzil; IV, after a further 40 min with 5 equiv. benzil plus a further 15 min (PSS) with 10 equiv. benzil. A small amount of photodegradation (<2%) occurs over the course of the experiment, and the error in the final *E*:*Z* and *dba*:*mba* ratios is $\pm 2\%$. **b**, Expansion showing the small increase (2–5%, see Supplementary Information) in *dba* compartment occupancy that occurs during the first five minutes of irradiation in the absence of benzil. **c**, ¹H NMR spectral window (*H*_{s'}+*s*, *H*_s and *H*_s, 600 MHz, CD₃OD, 298 K) in which the changes in both the *E*:*Z* and *dba*:*mba* ratios can be seen during the photochemistry experiment.

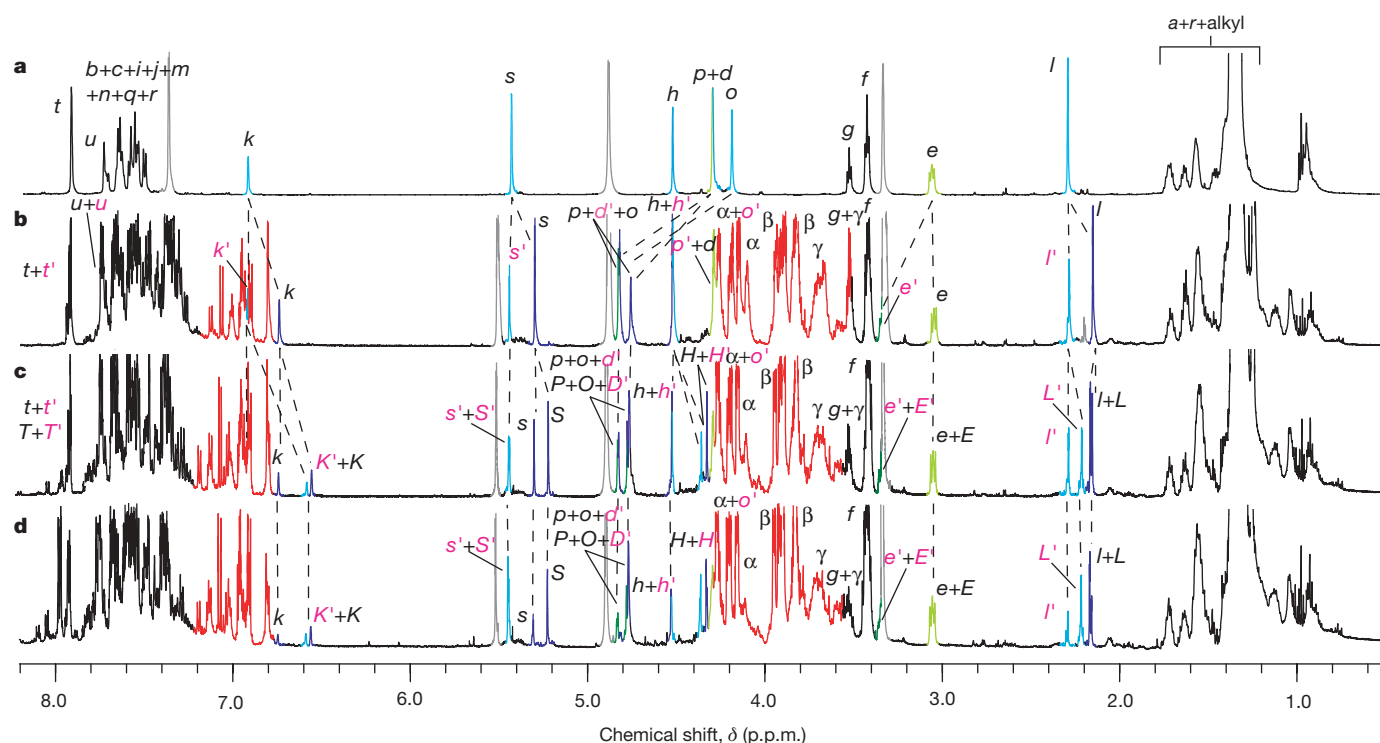


Figure 2 | ¹H NMR spectra (600 MHz, CD₃OD, 298 K) of a working nanomachine. **a**, Thread (*E*-diastereomer); **b**, *E*-1; **c**, **1** at the 350 nm photostationary state (*dba*-*Z*:*mba*-*Z*:*E*-1, 38:21:41); **d**, **1**+benzil (10 equiv.) at the 350 nm photostationary state (*dba*-*Z*:*mba*-*Z*:*E*-1, 32:48:20). Resonances are coloured and the lettering assigned according to Fig. 1: macrocycle, red; occupied *dba* binding site, dark blue;

unoccupied *dba* binding site, light blue; occupied *mba* binding site, dark green; unoccupied *mba* binding site, light green. The overlapping aromatic ring signals above 7.2 p.p.m. are not distinguished in this way. Residual non-deuterated solvents are shown in light grey (the signal at 5.5 p.p.m. is CH₂Cl₂).

is located in the left-hand compartment (dba-Z-1; Fig. 1B, a), compared to that from one in the right-hand compartment (mba-Z-1; Fig. 1B, d).

The second law of thermodynamics demands that an energetic cost be paid for moving a particle distribution away from equilibrium. In both Maxwell's thought experiment and our molecular system, it is the subtle requirement for energy dissipation during the transfer of information that meets this requirement. In practice, the conversion of photonic energy to heat occurs in several places during the photochemical excitation, energy transfer and thermal relaxation processes in the operation of **1**, meaning that the second law is easily satisfied. However, the heat loss in most of these instances could theoretically be eliminated by changing details of the experimental design (for instance, benzil would be unnecessary if **1** could be modified so that the open form of the gate was able to exergonically relax to the closed form). The one part of the mechanism where loss of heat to the environment appears unavoidable is during the isomerization of the gate by the sensitizer attached to the macrocycle. Photochemical excitation is an extremely rapid process and occurs without changes in molecular geometry (the Franck-Condon principle). For olefin photoisomerization to occur, the initial 'vertically' excited state must relax to its preferred geometry (known as the 'perpendicular' state), which is somewhere intermediate between the *Z* and *E* forms. A further rearrangement of this nuclear configuration to the final *Z* or *E* product then occurs following crossing onto the ground-state potential energy surface. Both of these nuclear rearrangements are necessarily energetically downhill processes, requiring dissipation of energy as heat, and cannot be avoided without a concomitant energy cost elsewhere. As the excited state of dba-Z-1 is quenched by energy transfer to open the gate, therefore, the information regarding the macrocycle's (probable) location is erased on decay of the initial, vertically excited state to the perpendicular intermedi-

ate. Thus the part of the mechanism of **1** that intrinsically requires dissipation of energy is equivalent to the erasure of the information known to a gate-operating demon, in agreement with Bennett's resolution²⁷ of the Maxwell demon paradox.

Various methods for the net transport of macrocycles between the binding sites in rotaxanes have previously been demonstrated in the form of stimuli-responsive molecular shuttles^{2,5,8,11,12}. However, these are simple two-state switches^{28,29}, the most basic and functionally limited type of machine mechanism in which the ring distribution is always at, or relaxing towards, equilibrium. In contrast, biological motors and machines use mechanisms that operate far from equilibrium¹. During the past decade, statistical physics has developed a number of theoretical mechanisms that explain how the transport of brownian particles away from equilibrium can occur. These so-called 'brownian ratchet' mechanisms fall into two general classes: energy ratchets³⁰, in which the energy minima and maxima of the potential energy surface are varied irrespective of the particle's location; and information ratchets^{20–22}, where the energy maxima (kinetic barriers to motion) change according to the position of the particle. The energy ratchet concept has recently been used to design some of the first synthetic molecular machines that are more complex than simple switches^{9,28}, but rotaxane **1** is the first example of a synthetic molecular information ratchet. For an information ratchet to function it is unnecessary for the binding affinities of the two compartments to be as similar as they are in **1** (although it affects the efficiency of the mechanism²²); the point is that the particle distribution can be driven away from whatever the equilibrium value is. From the perspective of synthetic molecular machine design, the situation in which the two sites have significantly different binding affinities may prove particularly important because this corresponds to a route by which particles can be pumped energetically uphill against an opposing force.

Received 9 June; accepted 15 November 2006.

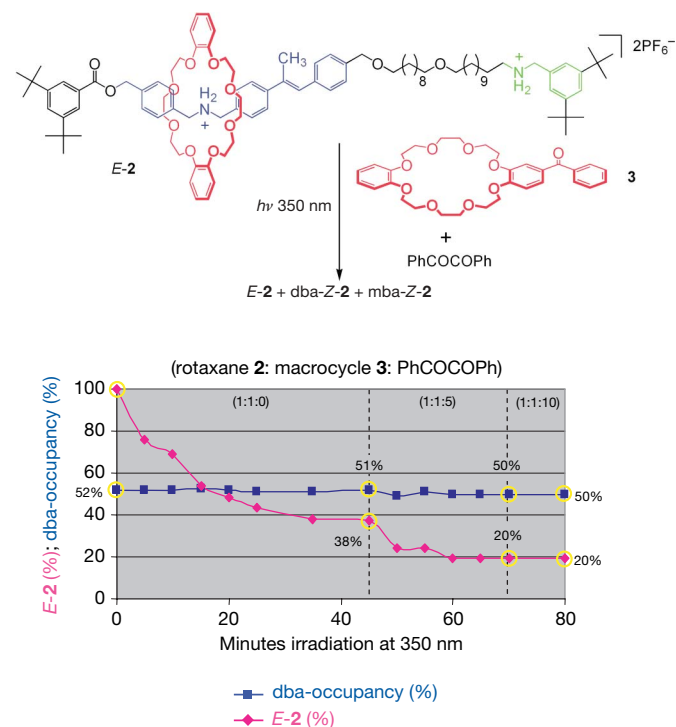


Figure 4 | Operation of rotaxane 2, featuring only intermolecular photosensitization of the α -methyl stilbene gate. The plot shows the change in the *E*:*Z* ratio (*E*-2 (%), shown by purple diamonds) and the dba:mba ratio (dba-occupancy (%), shown by dark blue squares) that occurs during irradiation of **2**+**3** (1:1) at 350 nm in CD₃OD, 298 K in the absence and presence (5 and 10 equiv.) of benzil. There is a small amount (<2%) of photodegradation over the course of the experiment, and the error in the final *E*:*Z* and dba:mba ratios is $\pm 2\%$.

- Schliwa, M. (ed.) *Molecular Motors* (Wiley-VCH, Weinheim, 2003).
- Bissell, R. A., Córdova, E., Kaifer, A. E. & Stoddart, J. F. A chemically and electrochemically switchable molecular shuttle. *Nature* **369**, 133–137 (1994).
- Kelly, T. R., De Silva, H. & Silva, R. A. Unidirectional rotary motion in a molecular system. *Nature* **401**, 150–152 (1999).
- Koumura, N., Zijlstra, R. W. J., van Delden, R. A., Harada, N. & Feringa, B. L. Light-driven monodirectional molecular rotor. *Nature* **401**, 152–155 (1999).
- Brouwer, A. M. et al. Photoinduction of fast, reversible translational motion in a hydrogen-bonded molecular shuttle. *Science* **291**, 2124–2128 (2001).
- Leigh, D. A., Wong, J. K. Y., Dehez, F. & Zerbetto, F. Unidirectional rotation in a mechanically interlocked molecular rotor. *Nature* **424**, 174–179 (2003).
- Thordarson, P., Bijsterveld, E. J. A., Rowan, A. E. & Nolte, R. J. M. Epoxidation of polybutadiene by a topologically linked catalyst. *Nature* **424**, 915–918 (2003).
- Badjić, J. D., Balzani, V., Credi, A., Silvi, S. & Stoddart, J. F. A molecular elevator. *Science* **303**, 1845–1849 (2004).
- Hernández, J. V., Kay, E. R. & Leigh, D. A. A reversible synthetic rotary molecular motor. *Science* **306**, 1532–1537 (2004).
- Fletcher, S. P., Dumur, F., Pollard, M. M. & Feringa, B. L. A reversible, unidirectional molecular rotary motor driven by chemical energy. *Science* **310**, 80–82 (2005).
- Liu, Y. et al. Linear artificial molecular muscles. *J. Am. Chem. Soc.* **127**, 9745–9759 (2005).
- Berná, J. et al. Macroscopic transport by synthetic molecular machines. *Nature Mater.* **4**, 704–710 (2005).
- Shirai, Y., Osgood, A. J., Zhao, Y., Kelly, K. F. & Tour, J. M. Directional control in thermally driven single-molecule nanocars. *Nano Lett.* **5**, 2330–2334 (2005).
- Elkema, R. et al. Molecular machines: Nanomotor rotates microscale objects. *Nature* **440**, 163 (2006).
- Muraoka, T., Kinbara, K. & Aida, T. Mechanical twisting of a guest by a photoresponsive host. *Nature* **440**, 512–515 (2006).
- Maxwell, J. C. Letter to P. G. Tait, 11 December 1867. Reproduced in *The Scientific Letters and Papers of James Clerk Maxwell* Vol. II, 1862–1873 (ed. Harman, P. M.) 331–332 (Cambridge Univ. Press, Cambridge, UK, 1995).
- Maxwell, J. C. *Theory of Heat* Ch. 22 (Longmans, Green and Co., London, 1871).
- Maxwell, J. C. Letter to P. G. Tait, circa. 1875. Reproduced in *The Scientific Letters and Papers of James Clerk Maxwell* Vol. III, 1874–1879 (ed. Harman, P. M.) 185–187 (Cambridge Univ. Press, Cambridge, UK, 2002).
- Leff, H. S. & Rex, A. F. (eds) *Maxwell's Demon 2. Entropy, Classical and Quantum Information, Computing* (Institute of Physics Publishing, Bristol, 2003).
- Astumian, R. D. & Derényi, I. Fluctuation driven transport and models of molecular motors and pumps. *Eur. Biophys. J.* **27**, 474–489 (1998).

21. Parmeggiani, A., Jülicher, F., Ajdari, A. & Prost, J. Energy transduction of isothermal ratchets: Generic aspects and specific examples close to and far from equilibrium. *Phys. Rev. E* **60**, 2127–2140 (1999).
22. Parrondo, J. M. R. & De Cisneros, B. J. Energetics of Brownian motors: A review. *Appl. Phys. A* **75**, 179–191 (2002).
23. Tokunaga, Y., Akasaka, K., Hisada, K., Shimomura, Y. & Kakuchi, S. A rotaxane synthesis based on stilbene photoisomerization. A photoswitchable catch and release process. *Chem. Commun.* 2250–2251 (2003).
24. Kolchinski, A. G., Busch, D. H. & Alcock, N. W. Gaining control over molecular threading: benefits of second coordination sites and aqueous–organic interfaces in rotaxane synthesis. *J. Chem. Soc. Chem. Commun.* 1289–1291 (1995).
25. Ashton, P. R. *et al.* Dialkylammonium ion/crown ether complexes: the forerunners of a new family of interlocked molecules. *Angew. Chem. Int. Edn Engl.* **34**, 1865–1869 (1995).
26. Hammond, G. S. *et al.* Mechanisms of photochemical reactions in solution. XXII. Photochemical *cis–trans* isomerization. *J. Am. Chem. Soc.* **86**, 3197–3217 (1964).
27. Bennett, C. H. The thermodynamics of computation – a review. *Int. J. Theor. Phys.* **21**, 905–940 (1982).
28. Chatterjee, M. N., Kay, E. R. & Leigh, D. A. Beyond switches: ratcheting a particle energetically uphill with a compartmentalized molecular machine. *J. Am. Chem. Soc.* **128**, 4058–4073 (2006).
29. Kay, E. R. & Leigh, D. A. Lighting up nanomachines. *Nature* **440**, 286–287 (2006).
30. Reimann, P. Brownian motors: Noisy transport far from equilibrium. *Phys. Rep.* **361**, 57–265 (2002).

Supplementary Information is linked to the online version of the paper at www.nature.com/nature.

Acknowledgements We thank P. J. Camp and his research group for the free energy calculation, and the EPSRC, the EU project Hy3M and the Carnegie Trust for financial support. D.A.L. is an EPSRC Senior Research Fellow and holds a Royal Society-Wolfson research merit award.

Author Contributions V.S., C.-F.L. and E.R.K. contributed equally to this work.

Author Information Reprints and permissions information is available at www.nature.com/reprints. The authors declare no competing financial interests. Correspondence and requests for materials should be addressed to D.A.L. (David.Leigh@ed.ac.uk).

LETTERS

Importance of rain evaporation and continental convection in the tropical water cycle

John Worden¹, David Noone², Kevin Bowman¹ & the Tropospheric Emission Spectrometer science team and data contributors*

Atmospheric moisture cycling is an important aspect of the Earth's climate system, yet the processes determining atmospheric humidity are poorly understood^{1–4}. For example, direct evaporation of rain contributes significantly to the heat and moisture budgets of clouds⁵, but few observations of these processes are available⁶. Similarly, the relative contributions to atmospheric moisture over land from local evaporation and humidity from oceanic sources are uncertain^{3,7}. Lighter isotopes of water vapour preferentially evaporate whereas heavier isotopes preferentially condense^{8–10} and the isotopic composition of ocean water is known. Here we use this information combined with global measurements of the isotopic composition of tropospheric water vapour from the Tropospheric Emission Spectrometer (TES) aboard the Aura spacecraft^{11,12}, to investigate aspects of the atmospheric hydrological cycle that are not well constrained by observations of precipitation or atmospheric vapour content. Our measurements of the isotopic composition of water vapour near tropical clouds suggest that rainfall evaporation contributes significantly to lower troposphere humidity, with typically 20% and up to 50% of rainfall evaporating near convective clouds. Over the tropical continents the isotopic signature of tropospheric water vapour differs significantly from that of precipitation^{8,10,13}, suggesting that convection of vapour from both oceanic sources and evapotranspiration are the dominant moisture sources. Our measurements allow an assessment of the intensity of the present hydrological cycle and will help identify any future changes as they occur.

Simultaneous profiles of HDO and H₂O are obtained from TES thermal infrared radiances between 1,200 and 1,350 cm^{−1} using maximum a posteriori optimal estimation¹² (Supplementary Information). This approach allows for a precise characterization of the errors in the ratio of singly deuterated water to water (HDO/H₂O) and its vertical resolution (see Supplementary Information). For this analysis, mean values of the isotopic composition (hereafter δD , see Methods) are calculated from averages of HDO and H₂O between 550 and 800 hPa, where the estimated profiles of δD are most sensitive. This average has a typical precision of 10‰ in the tropics and 24‰ at the poles¹². Profiles of atmospheric and surface temperature, surface emissivity, an effective cloud optical depth and cloud top height are also estimated from TES radiances¹⁴ and are used to stratify δD in analysis presented here. Global observations from 50 evenly distributed days between late October 2004 and March 2005 are used. There are 1,150 observations per day, of which typically 400 are found to be of suitable quality for this analysis¹². The horizontal footprint of each observation is 8 km by 5 km.

A bias in the established HDO spectroscopic line strengths requires a correction of 5% in the estimated HDO profiles and is uniform

across all observations. With this correction, the distribution of TES δD measurements is consistent with comparisons to theoretical modelling of infrared spectroscopic HDO line strengths, recent aircraft measurements, values expected near the ocean surface, and general circulation model simulations¹². The bias correction accounts for the a priori constraint and vertical resolution of the HDO and H₂O profile retrieval (see Supplementary Information). Such a bias reduces the confidence one can place on absolute measures of hydrologic cycling derived from the data, but comparisons between different subsets avoid the impact of the bias on findings. For instance, the spatial distribution of observations shows a decrease of both water vapour amount and δD with higher latitudes that is robust irrespective of the bias (Fig. 1). This so-called 'latitude effect' is found also in measurements of δD of precipitation and is due to the preferential removal of heavier nuclides during condensation as vapour is transported poleward⁸ and because rainfall tends to equilibrate isotopically to the background vapour as it falls^{10,15,16}.

TES δD vapour observations are plotted in Fig. 2a as a function of H₂O volume mixing ratio (q_{H_2O}) to distinguish evaporation from condensation processes and infer the water transport characteristics. Theoretical considerations give δD of vapour in equilibrium with ocean water, which is shown in Fig. 2 as the black line which spans sea surface temperatures from 5 to 25 °C. Bulk evaporation describes turbulent mixing of vapour from the saturated layer at the ocean surface into a drier air parcel aloft. The orange curves in Fig. 2 show the evolution of δD under continual evaporation towards isotopic composition of ocean sources of different temperatures. In contrast, a Rayleigh distillation model describes isotopic depletion as vapour is lost to precipitation. The cyan curves show Rayleigh predictions originating from a distribution of saturated oceanic vapour and assume a condensation temperature 15 K colder than the ocean surface (clouds at about 2.5 km). A simple description of the atmospheric water cycle is that any given observation of an air parcel will reflect a history of evaporation and Rayleigh condensation and therefore, as shown in Fig. 2a, lie between the theoretical extremes of the curve for condensation from moisture originating over a warm oceanic source and the curve for evaporation towards equilibrium with a cold oceanic source.

A Rayleigh paradigm posits moist air to be less depleted than dry air. This largely explains the extra-tropical oceanic observations seen in Figs 2b and 3, where moist observations (in which the relative humidity is larger than 80% and the cloud optical depth is larger than 0.3) are partitioned from dry and clear-sky observations (in which the relative humidity is less than 50% and cloud optical depth less than 0.1). Figure 2b shows that the evaporation curves more closely describe the dry air parcels while the Rayleigh condensation

¹Jet Propulsion Laboratory, California Institute of Technology, Pasadena, California, USA. ²Department of Atmospheric and Oceanic Sciences, and Cooperative Institute for Research in Environmental Sciences, University of Colorado, Boulder, Colorado, USA.

*A list of participants and affiliations appears at the end of the paper.

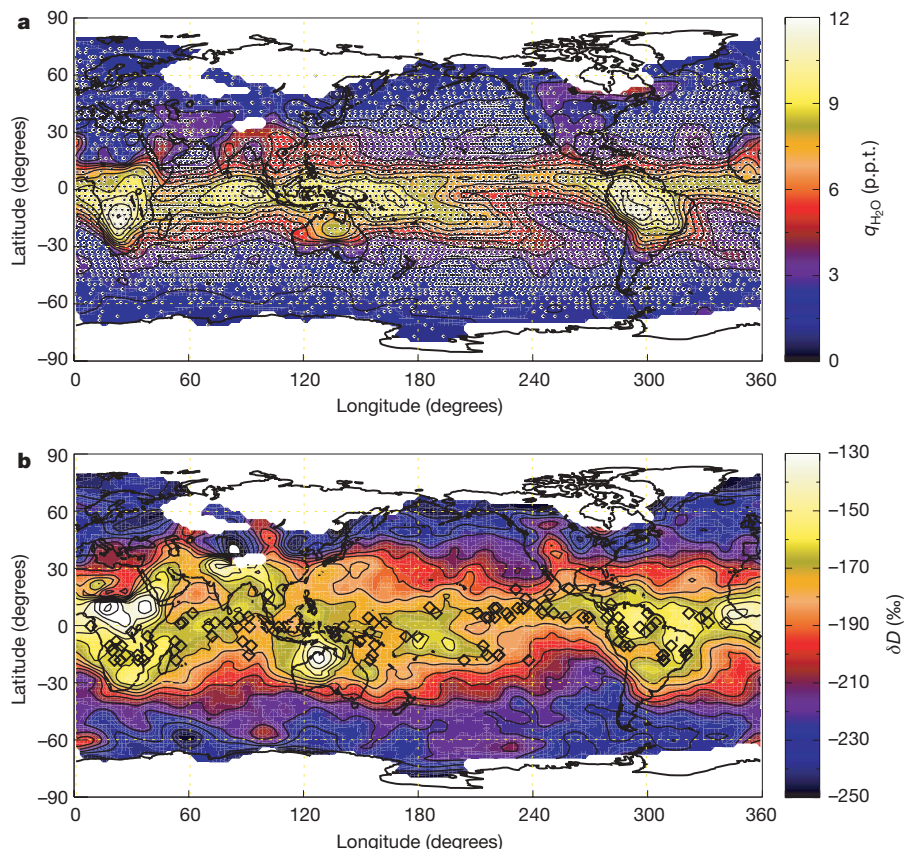


Figure 1 | Global distribution of TES observations averaged vertically between 550 and 800 hPa. a, Water vapour volume mixing ratio $q_{\text{H}_2\text{O}}$ (parts per thousand by volume, p.p.t.). **b**, HDO (δD relative to VSMOW). Observations were made on 50 days between October 2004 and March 2005 at locations shown as dots in **a**. The data are gridded for plotting using a

Cressman scheme with a mean effective radius of 500 km and a maximum radius of 1,200 km. The data are masked where there are less than two observations within 1,200 km. The diamonds in **b** show where the amount effect is evident.

curves more closely describe the moist air parcels. The difference between moist and dry air parcels is shown more clearly in Fig. 3. The extra-tropical dry air parcels are typically 16‰ more depleted than the moist air parcels. The standard error of the mean for the extra-tropics is approximately 2‰. The overlapping distributions are a reminder that any individual air parcel will have a history of both evaporation and condensation.

In sharp contrast to the extra-tropical observations, the tropical observations (Equator-ward of 20° latitude) are not described accurately by the Rayleigh description of evaporation from an oceanic source followed by condensation. Specifically, Fig. 3 shows moist tropical points are more depleted than dry tropical points by 12‰, with the standard error of the mean being 1‰. This excess depletion is also observed in Fig. 2c where individual observations show more depletion than do the set of possible Rayleigh curves. Over 99% of the clear tropical data lie within the two end-member models describing evaporation of a cold oceanic source at 5 °C and condensation from an oceanic source at 25 °C. However, over half of the tropical moist observations are more depleted than the Rayleigh condensation curve. A similar feature, termed the ‘amount effect’, is found statistically in monthly precipitation δD measurements in regions of intense rainfall and is often attributed to the evaporation of falling rain near active convection^{8,17}. The TES vapour results confirm this rehydration mechanism by noting that the location of these anomalous observations corresponds to regions known for active convection (diamonds in Fig. 1b).

The role of rain evaporation can be understood by comparing vapour observations to values predicted by a bulk mass balance isotope model with differing rainfall evaporation fractions. The δD is modelled as an open system in which moisture gain via surface evap-

oration and advection from nearby is balanced by moisture loss via precipitation (Methods and Supplementary Information). In the model, some fraction of the rainfall is evaporated and returned to vapour, thereby producing the amount effect. Such balance is achieved only for adequately large regions in which the mean convective activity is in approximate quasi-equilibrium relative to the slowly evolving large-scale conditions^{5,18,19}. The initial δD will vary with the rain evaporation fraction (that is, the vertical displacement of purple dots in Fig. 2c). Once the flux balance is broken, owing to changes in the advective, precipitation or evaporation rates, the net loss of water is accompanied by an isotopic evolution that follows a Rayleigh-like distillation (purple curves in Fig. 2c), and explains how moist tropical air parcels are more depleted than dry tropical air parcels. The steep slope results from the additional fractionation during rain evaporation and it is this which allows the final depletion to exceed that predicted from a Rayleigh model.

As indicated in Fig. 2c, very few observations require a modelled rain evaporation fraction in excess of 50%, whereas a fraction of around 20% passes through the centre of the distribution of cloudy observations. A mean rain evaporation fraction of 20% is estimated from our simple mass balance model (see Methods) by assuming that no rain evaporation has occurred in the history of the clear-sky observations and that the observed isotopic difference between cloudy and clear-sky observations is 12‰ (Fig. 3). This result is sensitive to the specific assumptions about isotopic exchange and the temperature of the ocean sources (here taken as 25 °C) but because this estimate of 20% is constrained by using the difference between the isotopic composition of the clear sky and cloudy observations (the red and blue curves in Fig. 3), and not their absolute amounts, it is not sensitive to the spectroscopic bias in the measurements. This

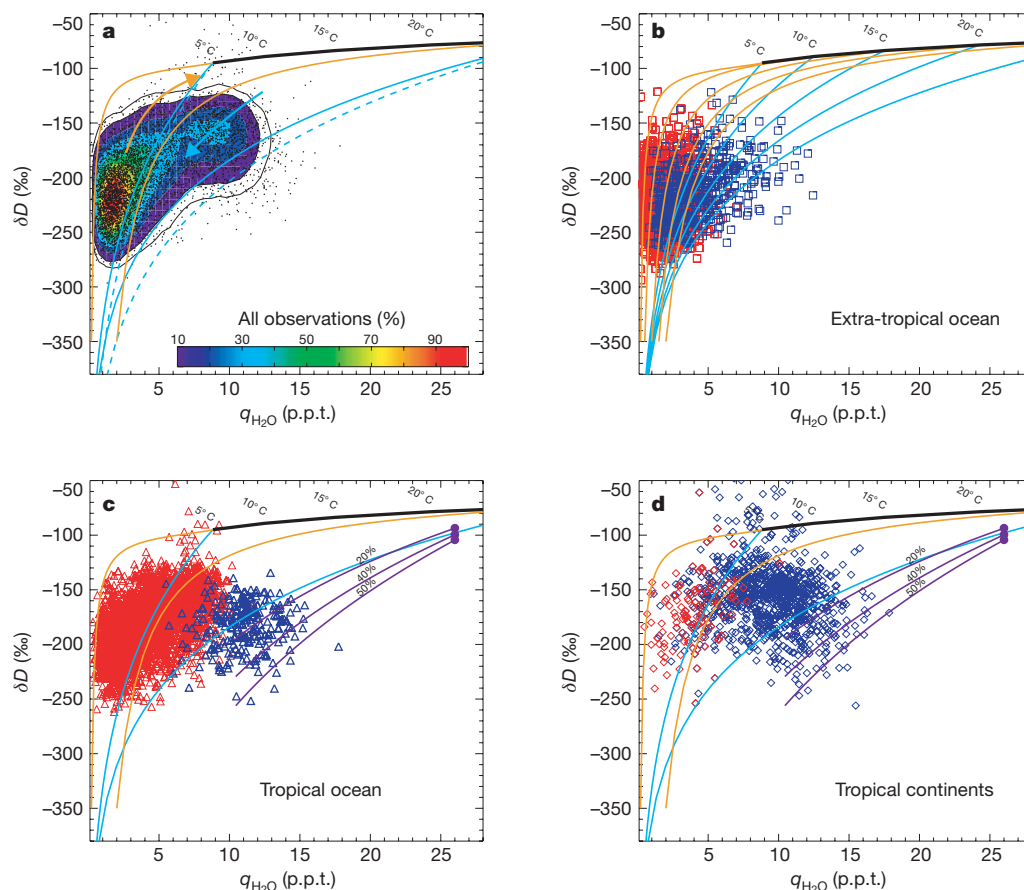


Figure 2 | Scatter plots of δD versus q_{H_2O} reveal underlying hydrologic processes. **a**, Probability distribution of all data (colour shading shows the percentage of the most likely value; the outer black contour envelops 95% of the observations) with dots showing one in three observations. The orange, cyan and purple curves and the purple dots show model predictions as described in the Methods; they are derived in detail in the Supplementary Information. Observations are separated by location as follows: **b**, oceanic

extra-tropics (poleward of 30°); **c**, oceanic tropics (Equatorward of 20°); and **d**, tropical continental areas. Observations are for clear-sky (optical depth < 0.2 and humidity $< 50\%$, red symbols) and cloudy (optical depth > 0.3 and humidity $> 80\%$, blue symbols) conditions. The solid black curve shows the isotopic composition of saturated vapour in equilibrium with the ocean water for a range of surface temperatures as marked in $^\circ C$ along the black line.

evaporation fraction estimate is consistent with the conservative estimate of 30% based on a radar study in a semi-arid environment²⁰ and values from climate model simulations²¹. More importantly, the isotopic distribution of moist and dry vapour as seen in Fig. 2c provides a new climatology with which to assess the cloud hydrology in climate and mesoscale models.

Comparison of the isotopic vapour over continents to that over ocean reveals a more complicated hydrologic cycle than is suggested by a simpler system in which condensation is balanced by evaporation. A conventional view inferred from isotopic measurements of continental precipitation is that an air mass becomes disconnected from the ocean source as it moves inland, and consequently the vapour and precipitation becomes more depleted further inland (the 'continental effect'^{8,22}). In an apparently contradictory way, Fig. 3b shows that continental vapour observations are typically less depleted than the oceanic observations, especially over the Amazon and tropical Africa (Fig. 1b). In addition to these anomalous values, many tropical land observations also show an amount effect, in which the moist air parcels are more depleted than the dry air parcels. Consequently, the TES observations show that the conventional Rayleigh description of a disconnected condensing air mass is inadequate for describing processes controlling free tropospheric water vapour over tropical land.

Two possible sources that can enrich the isotopic composition of free troposphere terrestrial vapour relative to the ocean merit attention—oceanic vapour transported at low altitude inland and vapour from evapotranspiration—both of which are then lofted into the free

troposphere. There is a steep vertical gradient in the isotopic composition of water vapour^{23,24}, which follows the background thermal structure because of the integrated history of condensation. As such, air transported vertically by warm convection will be enriched relative to its surroundings. Vapour from evapotranspiration can be further enriched relative to the oceanic vapour because there is no net fractionation as soil water is extracted from the surface^{13,25}. Evidence for this source is found in those observations that are enriched relative to oceanic vapour (that is, points above the black line in Fig. 2 are almost all cloudy tropical continental points). The amount effect also observed in the tropical land data occurs in regions that are seasonally moist (for example, South America, Southeast Asia). Vertical lofting of less-depleted vapour is found to dominate in arid regions where the convective cloud systems are expected to be characteristically different (for example, northern Australia, east Africa). The widely disparate sources and cloud processes over land highlight the need to account for the regional diversity in the balance of competing processes that affect tropical terrestrial hydrology.

Thus isotopic observations are powerful in diagnosing hydrologic processes that are otherwise not well measured but are central to understanding climate because they reflect exchange between water phases rather than the state measured by conventional (non-isotopic) quantities. Specifically, the isotopic distribution provides a metric for the intensity of the large-scale hydrological cycle through the balances between the rate at which the vapour is restored to known oceanic conditions by evaporation and boundary-layer mixing, and

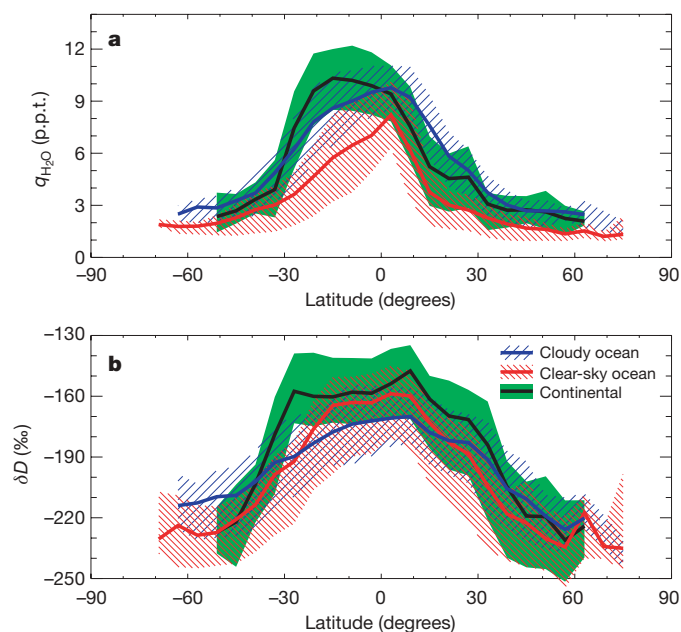


Figure 3 | Contrast between cloudy and clear sky ocean, and continental observations. Zonal mean observed water vapour $q_{\text{H}_2\text{O}}$ (a) and δD binned at 6° latitude (b). The data are stratified (as in Fig. 2) to be clear-sky ocean (red, 53% of observations), and cloudy ocean (blue, 27% of observations). All land observations (black curve, green shading) represent 12% of observations. The red, blue and green shaded areas are bounded by the 25 and 75 percentiles of each subset. Errors on the means in **b** range between 1 to 2‰ for the data Equatorward of 50 degrees.

the rate at which water is removed by intermittent condensation events. Should the intensity of the hydrologic cycle change⁴, isotopic assessment provides a framework for interpreting which processes and water sources are responsible.

METHODS

The isotope ratio is defined as $R = q_{\text{HDO}}/q_{\text{H}_2\text{O}}$, where q is the volume mixing ratio of HDO or H_2O . Isotopic composition is expressed as δD values, where:

$$\delta D = \left(\frac{R}{R_{\text{VSMOW}}} - 1 \right) \times 1,000$$

R_{VSMOW} is the isotope ratio of Vienna Standard Mean Ocean Water reference (3.11×10^{-4}). All mean δD values are mass-weighted (that is, δD refers to mean $q_{\text{H}_2\text{O}}$ and mean q_{HDO}). The foundation of isotopic analysis is that given adequate knowledge of the fractionation processes which accompany water exchange (evaporation, transport and precipitation), the history of the processes that acted on a distribution of observed air parcels can be inferred from δD . Conversely, should the behaviour of the water cycle be assumed, the details of the cloud physics can be deduced from their different effects on δD .

Isotope models shown as curves in Fig. 2 are derived from simple mass balance equations:

$$\frac{\partial q}{\partial t} = E - P + A$$

where A is the advection rate, E is the evaporation rate and P is the precipitation rate. P may be written as the difference between the total condensation rate, C , and the rainfall evaporation rate X (that is, $P = C - X$). Upon inserting expressions for isotopic fractionation during exchange processes, general equations governing the evolution of q_{HDO} and $q_{\text{H}_2\text{O}}$ are written as the sum of three terms (see Supplementary Information for details):

$$\frac{\partial q_{\text{H}_2\text{O}}}{\partial t} = \gamma(q_s - q_{\text{H}_2\text{O}}) - (1-f)C + A$$

$$\frac{\partial q_{\text{HDO}}}{\partial t} = \gamma\eta(R_s q_s - q_{\text{HDO}}) - \alpha_c R C \left(1 - \frac{f}{\alpha_c} \right) + \bar{R} A$$

where γ is a bulk exchange coefficient for evaporation, q_s is the saturation mixing ratio at the ocean surface with isotopic composition in equilibrium with ocean water R_s , f is the fraction of rain evaporated, and \bar{R} is the net isotopic composition

of advection. Isotopic fractionation during condensation is α_c and during rain evaporation is α_e , which accounts for both equilibrium and kinetic effects. During evaporation from the ocean surface the parameter η accounts for kinetic effects.

Although development of this model is straightforward, the simultaneous inclusion of all terms in the hydrologic balances offers deeper insight to the underlying effects of water cycling on the isotopic composition of atmospheric vapour. This development therefore extends more conventional approaches that consider single processes in isolation, which are derived here as simplifications. Four special cases are considered: (1) only condensation is active (A , E and X are zero), which gives the Rayleigh model; (2) some fraction of the rain is evaporated (A and E are zero), which gives a modified Rayleigh model; (3) only evaporation from the surface is allowed (A , C and X are zero), which gives evaporation mixing lines; and (4) all terms are included but assumed to be at steady state (time derivative set equal to zero). The addition of the advection term tends to dilute the isotopic composition towards the assumed isotope ratio of the advected moisture. These different assumptions lead to different curves in δ - q space (as in Fig. 2) owing to the different degrees to which isotopic fractionation is expressed (detailed descriptions of these models are given in the Supplementary Information). In Fig. 2, cyan curves show Rayleigh distillation to liquid ($\alpha_c \approx 1.105$, solid) and ice ($\alpha_c \approx 1.163$, dashed). The orange curves show evaporation mixing lines that originate from vapour in equilibrium with the ocean surface with given temperature (black curve). The purple dots in Fig. 2c show the steady state model with subsequent modified Rayleigh distillation (purple curves) for the given rain evaporation fraction. Fractionation during rain evaporation of condensate is taken as $\alpha_e = 1.098$ and $\eta = 0.995$.

The rain evaporation fraction can be estimated using the mass balance model by assuming steady state, and solving for f based on the mean tropical values for $q_{\text{H}_2\text{O}}$ and δD . Specifically, the mass balance is written for cloudy and clear-sky conditions, and assuming the difference between the distributions is due solely to the rain evaporation. The mass balance shows that the isotopic composition of tropospheric vapour over land cannot exceed the isotopic composition of vapour in equilibrium with ocean water unless there is an enriched water source, such as the supply of soil water by evapotranspiration. In the calculation of f , we take $\gamma = 1.157 \times 10^{-5} \text{ s}^{-1}$ and $C = 8 \text{ mm day}^{-1}$, and A varies from 0 to 8 mm day^{-1} given the observed constraints on $q_{\text{H}_2\text{O}}$ and δ from Fig. 3. For a 12‰ difference between cloudy and clear-sky distributions that share the same isotopic composition near 30°N and 30°S , an f value of 0.2 (20% rain evaporation) is needed to gain balance.

Received 7 February; accepted 30 November 2006.

1. Trenberth, K. E. Changes in tropical clouds and radiation. *Science* **296**, 2095 (2002).
2. Trenberth, K. E., Dai, A. G., Rasmussen, R. M. & Parsons, D. B. The changing character of precipitation. *Bull. Am. Meteorol. Soc.* **84**, 1205–1217 (2003).
3. Roderick, M. L. & Farquhar, G. D. The cause of decreased pan evaporation over the past 50 years. *Science* **298**, 1410–1411 (2002).
4. Bosilovich, M. G., Schubert, S. D. & Walker, G. K. Global changes of the water cycle intensity. *J. Clim.* **18**, 1591–1608 (2005).
5. Emanuel, K. A., Neelin, J. D. & Bretherton, C. S. On large-scale circulations in convecting atmospheres. *Q. J. R. Meteorol. Soc.* **120**, 1111–1143 (1994).
6. Gamache, J. F., Houze, R. A. & Marks, F. D. Dual-aircraft investigation of the inner-core of hurricane Norbert. 3. Water-budget. *J. Atmos. Sci.* **50**, 3221–3243 (1993).
7. Xue, Y. et al. Role of land surface processes in South American monsoon development. *J. Clim.* **19**, 741–762 (2006).
8. Dansgaard, W. Stable isotopes in precipitation. *Tellus* **16**, 436–468 (1964).
9. Gat, J. R. Oxygen and hydrogen isotopes in the hydrologic cycle. *Annu. Rev. Earth Planet. Sci.* **24**, 225–262 (1996).
10. Araguas-Araguas, L., Froehlich, K. & Rozanski, K. Deuterium and oxygen-18 isotope composition of precipitation and atmospheric moisture. *Hydrol. Process.* **14**, 1341–1355 (2000).
11. Beer, R., Glavich, T. A. & Rider, D. M. Tropospheric Emission Spectrometer. *Appl. Opt.* **40**, 2356–2367 (2001).
12. Worden, J., Bowman, K. & Noone, D. TES observations of the tropospheric HDO/ H_2O ratio: retrieval approach and characterization. *J. Geophys. Res.* **111**, D16309, doi:10.1029/2005JD006606 (2006).
13. Gat, J. R. & Matsui, E. Atmospheric water balance in the Amazon basin: an isotopic evapotranspiration model. *J. Geophys. Res.* **96**, 13179–13188 (1991).
14. Worden, J. et al. Predicted errors of tropospheric emission spectrometer nadir retrievals from spectral window selection. *J. Geophys. Res. Atmos.* **109**, D09308, doi:10.1029/2004JD004522 (2004).
15. Hendricks, M. B., DePaolo, D. J. & Cohen, R. C. Space and time variation of $\delta^{18}\text{O}$ and δD in precipitation: Can paleotemperature be estimated from ice cores? *Glob. Biogeochem. Cycles* **14**, 851–861 (2000).
16. Schmidt, G. A., Hoffmann, G., Shindell, D. T. & Hu, Y. Modelling atmospheric stable water isotopes and the potential for constraining cloud processes and

- stratosphere-troposphere water exchange. *J. Geophys. Res.* **110**, D21314, doi:10.1029/2005JD005790 (2005).
17. Lawrence, J. R. *et al.* Stable isotopic composition of water vapor in the tropics. *J. Geophys. Res. Atmos.* **109**, D06115, doi:10.1029/2003JD004046 (2004).
 18. Zhang, G. J. Convective quasi-equilibrium in midlatitude continental environment and its effect on convective parameterization. *J. Geophys. Res. Atmos.* **107**, 4220, doi:10.1029/2001JD001005 (2002).
 19. Arakawa, A. & Schubert, W. H. Interaction of a cumulus cloud ensemble with large-scale environment. 1. *J. Atmos. Sci.* **31**, 674–701 (1974).
 20. Rosenfeld, D. & Mintz, Y. Evaporation of rain falling from convective clouds as derived from radar measurements. *J. Appl. Meteorol.* **27**, 209–215 (1988).
 21. Boville, B. A., Rasch, P. J., Hack, J. J. & McCaa, J. R. Representation of clouds and precipitation processes in the Community Atmosphere Model version 3 (CAM3). *J. Clim.* **19**, 2184–2198 (2006).
 22. Gat, J. R. Atmospheric water balance—the isotopic perspective. *Hydrol. Process.* **14**, 1357–1369 (2000).
 23. Ehrlert, D. H. *Vertical Profiles of HTO, HDO and H₂O in the Troposphere*. NCAR-TN/STR-100 (National Center for Atmospheric Research, Boulder, 1974).
 24. Taylor, A. B. *The Vertical Variations of the Isotopic Concentrations of Tropospheric Water Vapour Over Continental Europe and their Relationship to Tropospheric Structure*. Report INS-R-107 (New Zealand Department of Scientific and Industrial Research, Institute of Nuclear Science, Lower Hutt, 1972).
 25. Flanagan, L. B., Comstock, J. P. & Ehleringer, J. R. Comparison of modeled and observed environmental influences on the stable oxygen and hydrogen isotope composition of leaf water in *Phaseolus vulgaris* L. *Plant Physiol.* **96**, 588–596 (1991).

Supplementary Information is linked to the online version of the paper at www.nature.com/nature.

Acknowledgements We thank W. Read, D. Waliser, H. Su, F. Li, E. Fetzer and B. Kahn for discussions on this work, and C. Still, J. Rial and W. Riley for comments

on earlier versions of this manuscript. The research described in this paper was carried out at the Jet Propulsion Laboratory, California Institute of Technology, under a contract with the National Aeronautics and Space Administration, and at the University of Colorado.

Author Contributions J.W. and K.B. were responsible for the spectroscopic retrievals of the HDO and H₂O profiles and data quality assurance. D.N. developed the isotopic models and led interpretation of the data. The TES team (see below) helped with the development, analysis and validation of the TES data.

Author Information Reprints and permissions information is available at www.nature.com/reprints. The authors declare no competing financial interests. Correspondence and requests for materials should be addressed to D.N. (david.noone@colorado.edu).

The Tropospheric Emission Spectrometer science team and data contributors:

Reinhard Beer³, Annmarie Eldering³, Brendan Fisher³, Michael Gunson³, Aaron Goldman⁴, Robert Herman³, Susan S. Kulawik³, Michael Lampel⁵, Gregory Osterman³, Curtis Rinsland⁶, Clive Rodgers⁷, Stanley Sander³, Mark Shephard⁸, Christopher R. Webster³ & Helen Worden³

Affiliations for participants: ³Earth and Space Sciences Division, Jet Propulsion Laboratory, 4800 Oak Grove Drive, MS 183-301, Pasadena, California 91109, USA.

⁴Department of Physics and Astronomy, University of Denver, Denver, Colorado 80208, USA. ⁵Raytheon Company, 299 N. Euclid Avenue, Suite 500, Pasadena, California 91101, USA. ⁶NASA Langley Research Center, Hampton, Virginia 23681-0001, USA.

⁷Department of Atmospheric Oceanic and Planetary Physics, University of Oxford, Clarendon Laboratory, Parks Road, Oxford OX1 3PU, UK. ⁸Atmospheric and Environmental Research Inc. (AER), 131 Hartwell Avenue, Lexington, Massachusetts 02421, USA.

Evolution of species interactions in a biofilm community

Susse Kirkelund Hansen¹, Paul B. Rainey², Janus A. J. Haagenen¹ & Søren Molin¹

Biofilms are spatially structured communities of microbes whose function is dependent on a complex web of symbiotic interactions^{1,2}. Localized interactions within these assemblages are predicted to affect the coexistence of the component species^{3–5}, community structure⁶ and function^{7–10}, but there have been few explicit empirical analyses of the evolution of interactions¹¹. Here we show, with the use of a two-species community, that selection in a spatially structured environment leads to the evolution of an exploitative interaction. Simple mutations in the genome of one species caused it to adapt to the presence of the other, forming an intimate and specialized association. The derived community was more stable and more productive than the ancestral community. Our results show that evolution in a spatially structured environment can stabilize interactions between species, provoke marked changes in their symbiotic nature and affect community function.

Life is sustained through the activities of microorganisms^{8–10}, most of which function within biofilm communities composed—in some instances—of hundreds of metabolically diverse species^{12–14}. Rules governing biofilm assembly, function and evolution have been largely unexplored^{15,16}, but as with communities of macroorganisms, local interactions between component organisms in spatially structured environments are likely to be of central importance^{11,17–20}. Here we use a community composed of two bacterial species to explore experimentally how spatial structure allows local species interactions to evolve and affect community function.

Acinetobacter sp. (strain C6) and *Pseudomonas putida* (strain KT2440) are two unrelated soil-inhabiting bacteria²¹. When propagated in an environment with benzyl alcohol as the sole carbon source, the persistence of *P. putida* is dependent on the presence of *Acinetobacter*. *Acinetobacter* partitions the primary carbon source into benzoate, a substrate that is partly excreted by *Acinetobacter* and can be metabolized by *P. putida*²². The relationship between *Acinetobacter* and *P. putida* thus approximates that of a host (*Acinetobacter*) and a commensal (*P. putida*) and it is expected to be frequency dependent—although *P. putida* is not expected to persist below a threshold concentration of benzyl alcohol²³. We tested this prediction by determining the ability of each species to invade, when rare, a population dominated by the other species, and did so first in a homogeneous (spatially unstructured) chemostat environment and second in a spatially structured environment: a glass surface within a biofilm flow chamber.

Acinetobacter increased in frequency from rare with a relative fitness significantly greater than zero at all benzyl alcohol concentrations tested (see Supplementary Methods). In the chemostat environment *P. putida* coexisted with *Acinetobacter*, but only at benzyl alcohol concentrations above about 430 μM (Fig. 1). When co-cultivated on a glass surface, *P. putida* and *Acinetobacter* coexisted in

a stable frequency-dependent manner at benzyl alcohol concentrations as low as about 130 μM . Spatial structure thus extended the range of resource concentrations over which the two species coexist. This is most readily explained by higher local concentrations of benzoate in the biofilm flow chambers, but spatial clustering may also facilitate coexistence by minimizing potential competitive interactions, such as those likely to arise from competition for oxygen.

The structure of this two-species community was investigated by examining the glass surface of a 24-h-old biofilm flow chamber by microscopy. This revealed a mutually exclusive association, with

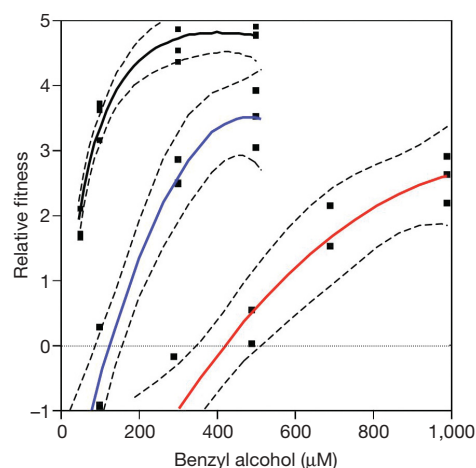


Figure 1 | Coexistence of *P. putida* KT2440 and *Acinetobacter* sp. C6 in structured (biofilm flow chamber) and unstructured (chemostat) environments with benzyl alcohol as the sole carbon source. Fitness measures were determined over 24 h at different concentrations of benzyl alcohol and are the difference between the malthusian parameter of the initially rare species (*P. putida*) and that of the common species (*Acinetobacter*): a fitness of zero indicates equal competitive ability²⁸. Lines are second-order polynomials plus 95% confidence curves fitted to the data (a minimum of three replicate measurements were determined at a minimum of three different concentrations of benzyl alcohol in each experiment). The red line denotes the fitness of ancestral *P. putida* in chemostat culture, the blue line the fitness of *P. putida* in biofilm flow chambers, and the black line the fitness of the derived rough variant of *P. putida* in biofilm flow chambers. The threshold concentration of benzyl alcohol above which *P. putida* and *Acinetobacter* coexist is indicated at the point at which each curve crosses the reference line. A curve for the fitness of the derived rough variant of *P. putida* mutant in chemostat culture is not shown, but in this environment this genotype was unable to increase in frequency against *Acinetobacter* populations at benzyl alcohol concentrations lower than about 950 μM (at 1 mM benzyl alcohol the fitness of derived *P. putida* was 0.69 (95% confidence interval 0.165–1.215)).

¹Infection Microbiology Group, BioCentrum-DTU, The Technical University of Denmark, Building 301, DK-2800 Lyngby, Denmark. ²School of Biological Sciences, University of Auckland, Private Bag 92019, Auckland, New Zealand.

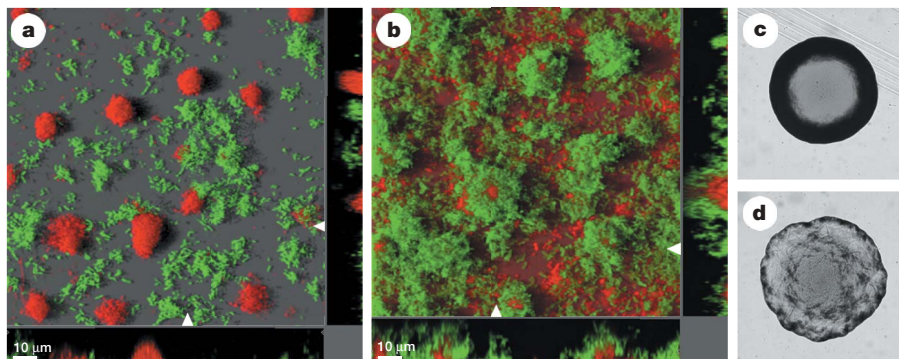


Figure 2 | Characteristic biofilm and colony phenotypes of the ancestral and the derived rough variant of *P. putida*. Flow-chamber biofilms were propagated for 24 h with 500 μM benzyl alcohol as the sole carbon source. **a, b**, Confocal scanning laser microscope (CSLM) micrographs were obtained of mixed biofilms containing *Acinetobacter* sp. C6 (red) and ancestral *P. putida* (green) (**a**) and *Acinetobacter* sp. C6 (red) and a rough variant of *P. putida* (green) (**b**). The main panels show simulated

fluorescence projection images (SFP): the outer horizontal and vertical panels show a cross-section through the x - z dimension at the positions marked by the arrows. The images shown are representative of eight images taken from each of two independent flow chambers. **c**, The smooth colony morphology of the ancestral *P. putida*. **d**, The rough colony morphology of a biofilm-derived genotype.

discrete colonies of *Acinetobacter* surrounded by loose assemblages of *P. putida* (Fig. 2a). After propagation for five days the association changed. At separate focal points across the surface of replicate glass plates, *P. putida* grew in intimate contact with *Acinetobacter*. Within a further five days *Acinetobacter* colonies had been overgrown by a mantle of *P. putida*.

To determine the cause of this altered community structure, cells were harvested from 16 independent ten-day mixed-species flow chambers and spread on agar plates. Careful observation showed that all agar plates harboured a common rough-colony variant of *P. putida* that was phenotypically distinct from the ancestral type (Fig. 2c, d). The phenotype of the variant was heritable, and when inoculated together with ancestral *Acinetobacter* into fresh biofilm flow chambers the structure of the resulting community was radically altered: instead of a mutually exclusive association the two species grew in close contact; *P. putida* formed a mantle over the top of *Acinetobacter* colonies (Fig. 2b). This structure was achieved within 24 h and was fully reminiscent of that observed previously in the five-day flow chambers.

Niche specialist genotypes can evolve when populations experience selection in spatially structured environments¹⁹. The rough variant of *P. putida* might reflect a specific adaptive response to the physical environment afforded by the biofilm flow chamber, to the biological environment afforded by *Acinetobacter*, or to a combination of both of these. To discriminate between these possibilities, we inoculated replicate flow chambers with *P. putida* and maintained them for ten days in the absence of *Acinetobacter*. Bacteria were harvested from the surface of glass plates from biofilm flow chambers and cultured on agar plates. No rough variants of *P. putida* were observed in any of five independent biofilm chambers, and *P. putida* taken from ten-day flow chambers did not grow as a mantle over the top of *Acinetobacter* colonies. Further, no rough variants were detected after propagation of *P. putida* in chemostat culture with *Acinetobacter*.

To examine further the evolutionary significance of the rough *P. putida* variant, its competitive fitness relative to the ancestral genotype was determined in the presence of *Acinetobacter* in both biofilm flow chambers and chemostat culture. The fitness of the rough variant was dependent on environment (by analysis of variance (ANOVA), $F_{1,4} = 1050.94$; $P < 0.0001$) and significantly greater than the wild type in biofilm flow chambers. Enhanced fitness in the biofilm flow chamber was traded against a significantly reduced fitness in chemostat culture (Fig. 3).

In a separate but parallel experiment the fitness of derived *P. putida* was determined relative to the ancestral genotype in the absence of *Acinetobacter* (*P. putida* is unable to grow on benzyl alcohol in the

absence of *Acinetobacter*; benzoate was therefore supplied as the sole carbon source). ANOVA showed that the fitness of the derived rough *P. putida* genotype was not affected by the structure of the environment ($F_{1,4} = 0.03$; $P = 0.87$) and did not differ significantly from the ancestral genotype (Fig. 3).

Together these data indicate that neither spatial structure nor the presence of *Acinetobacter* was sufficient to promote the evolution of the rough variant types: both were necessary, but the adaptive response was specific to *Acinetobacter*.

Suspecting that adaptive evolution on the part of *P. putida* might have stabilized the interaction further, we examined the effect of benzyl alcohol concentration on the coexistence of *Acinetobacter* and the derived rough *P. putida* genotype. In spatially structured flow chambers the two species coexisted stably at the lowest concentration (50 μM) of benzyl alcohol tested (Fig. 1)—a significant improvement in community stability compared with that of the ancestral community. Consistent with the evolution of a more specialized relationship was our observation that coexistence of the derived community was severely compromised in the chemostat environment: the benzyl alcohol concentration required for coexistence exceeded 950 μM (see legend to Fig. 1).

Stabilization of the interaction between *Acinetobacter* and *P. putida* is likely to have implications not only for community structure but also for the symbiotic relationship and function of the community. One way of assessing this impact is by the analysis of productivity (biomass) of the individual species grown alone and in combination (Fig. 4). After three days of propagation in flow chambers with benzyl alcohol as the sole carbon source, the productivity of the derived community was significantly greater than that of both the ancestral community and *Acinetobacter* alone (ANOVA: $F_{2,6} = 106.57$; $P < 0.0001$). This effect was attributable to enhanced productivity of *P. putida* and occurred despite a deleterious effect of *P. putida* on *Acinetobacter*—the species on which *P. putida* is reliant. Selection in a spatially structured environment thus changed the relationship between the two species and tipped the balance towards a more exploitative interaction, but overall community function was enhanced.

Last, in an attempt to understand the genetic and physiological causes of the newly emerged symbiosis, the mutation(s) responsible for the mantle-like growth of *P. putida* were sought (see Supplementary Methods). Two independent mutations were identified in *wapH* (PP4943)—a gene involved in lipopolysaccharide (LPS) biosynthesis (see Supplementary Table 1 and Supplementary Fig. 1). In *P. aeruginosa* the homologous *wapH* gene is necessary for the assembly of outer core LPS²⁴.

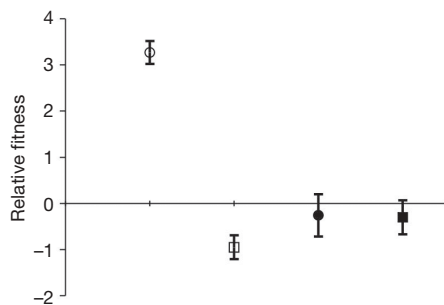


Figure 3 | Competitive fitness of the rough variant of *P. putida*. Fitness was determined relative to ancestral *P. putida* (initial ratio 1:1) in the presence (open symbols) and absence (filled symbols) of *Acinetobacter* in both spatially structured (circles) and unstructured (squares) environments. *P. putida* is unable to grow on benzyl alcohol in the absence of *Acinetobacter*; the fitness of derived *P. putida* in the absence of *Acinetobacter* was therefore determined in environments containing 200 μ M benzoate as the sole carbon source. Data are means and 95% confidence intervals; fitness values with confidence intervals that span zero are not significantly different from that of the ancestral genotype. See the text for ANOVA.

To determine the evolutionary significance of the *wapH* mutation, a non-polar mutation was made in *wapH* from the ancestral strain (see Supplementary Methods). This mutant (SNZ83) was phenotypically indistinguishable from the spontaneously arising rough mutants. The fitness of the mutant was determined by competition with the isogenic wild-type strain (SM1243) in biofilm flow chambers in the presence of *Acinetobacter*. Its fitness relative to the wild type was 3.4 (95% confidence interval 3.214–3.639) and was indistinguishable from that of the spontaneously occurring rough mutant analysed previously (Fig. 3). Mutations within *wapH* are therefore sufficient to generate the rough *P. putida* variant.

The physiological basis of the interaction is complex: *P. putida* is dependent on *Acinetobacter* for benzoate, but the two species also require oxygen. When the concentration of oxygen falls below a threshold, wild-type *P. putida* detaches and leaves the biofilm, resulting in uncolonized zones surrounding each *Acinetobacter* colony (Fig. 2a). Physiological changes in derived *P. putida* (it becomes sticky) cause it to associate with *Acinetobacter* (but not the glass surface), such that the oxygen-dependent detachment programme is overridden. This leads to the intimate association observed in Fig. 2b and is the cause of enhanced fitness in the structured environment in the presence, but not the absence, of *Acinetobacter* (Fig. 3). The close proximity of derived *P. putida* to *Acinetobacter* means that it acquires more benzoate, but this has a detrimental effect on

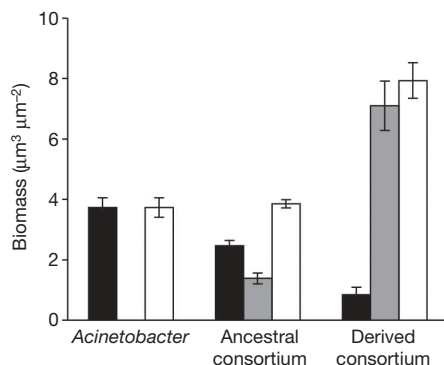


Figure 4 | Productivity of ancestral and derived communities. Biomass was determined after three days by CSLM imaging and COMSTAT analysis. Black bars represent *Acinetobacter*, light grey bars represent *P. putida*, and white bars represent total biomass. Data are means and 95% confidence intervals from three replicate biofilm flow chambers. The negative effect of ancestral *P. putida* on *Acinetobacter* is a consequence of competition for oxygen.

Acinetobacter (Fig. 4), most probably due to intensified competition for oxygen (S.K.H., J.A.J.H., M. Gjermansen, T. Martini Jørgensen, T. Tolker-Nielsen and S.M., unpublished observations).

Biofilm communities might lack the grandeur of a tropical rain-forest, but not their complexity, or their significance in terms of ecosystem function^{8–10}. Central to the structure, composition and function of any community is a complex web of interactions¹¹. Although ecologists often consider such interactions to be hard-wired, they are capable of rapid evolutionary change^{25,26}. Here we have witnessed the first step in the evolution of an interaction between two species with marked effects on community function. The simplicity of our experimental design enables an explicit statement of causality. Spatial structure was the key environmental factor: it allowed the establishment of a structured community (Fig. 2a) and provided the selective conditions necessary for the interaction between *Acinetobacter* and *P. putida* to evolve. Within a short duration the community structure changed: the abundance of each type was altered, and the community became more stable and more productive. Interactions are the key to understanding biological communities: the real challenge is to understand how interactions evolve¹¹.

METHODS

Strains and growth conditions. *Acinetobacter* sp. strain C6 (streptomycin-resistant derivative) was isolated from a toluene gas reactor²¹. The strain was grown at 30 °C in Luria–Bertani (LB) agar with streptomycin (100 μ g ml^{−1}) for plate enumerations. The soil bacterium *Pseudomonas putida* KT2440 (ref. 27) (devoid of plasmid pWW0) and derivatives were grown at 30 °C in minimal AB agar supplemented with 40 mM sodium citrate for plate enumerations. Mixed-species biofilm and chemostat populations were propagated on FAB minimal medium (AB minimal medium with 10 μ M Fe-EDTA replacing FeCl₃) containing benzyl alcohol as specified. Single-species biofilm and chemostat populations of *P. putida* were propagated with FAB medium containing 200 μ M sodium benzoate.

Fitness. Population densities (N_i) were determined at times $t = 0$ and at $t = T$. The malthusian parameter²⁸ (m_i), which is the average rate of increase, was calculated for both competitors: $m_i = \ln[N_i(T)/N_i(0)]/T$. Relative fitness is expressed here as the selection rate constant: $r_{ij} = m_i - m_j$, resulting in a fitness of zero when competing organisms are equally fit.

Biofilm experiments. Biofilms were grown at 24 °C in three-channel flow chambers with individual channel dimensions of 1 × 4 × 40 mm³. The continuous-flow system was assembled and prepared as described²⁹, with an additional overnight wash with sterile milliQ-water. After inoculation the medium flow was stopped for 1 h and resumed at a rate of 3.3 ml h^{−1} (see Supplementary Methods).

Populations were prepared for inoculation into flow chambers by first growing strains overnight in shaken broth culture. The population density of each type was adjusted as necessary and introduced into the chamber. Initial ($t = 0$) and final ($t = 24$ h) population densities were determined either by colony counts on agar plate culture or by measurement of biomass. In chambers containing both *Acinetobacter* and *P. putida*, the density of each type was derived from measures of biomass by fluorescence imaging: 12 images from each biofilm were recorded at random along the flow channel with a Zeiss LSM510 Confocal Scanning Laser Microscope equipped with a 40×/1.3 numerical aperture (n.a.) Plan-Neofluar oil objective plus filter sets for monitoring green fluorescent protein (GFP; green, *P. putida*) and Syto62 (red, *Acinetobacter*) (see Supplementary Methods). Images were analysed by the COMSTAT program³⁰, calculating the biomass volume (μ m³ μ m^{−2}) of each strain. Biofilm images for illustration were recorded with a 63×/1.4 n.a. Plan-APOChromat objective and processed with the IMARIS software package (Bitplane AG). As this is a destructive process, measures at $t = 0$ were obtained from paired control chambers. In chambers without *Acinetobacter*, population densities were obtained by counting colonies arising on agar plates after appropriate dilution. Biofilms were propagated with 500 μ M benzyl alcohol unless otherwise stated. To check for the presence of rough variants of *P. putida* in biofilm flow chambers propagated in the absence of *Acinetobacter*, a minimum of 500 colonies were examined from each of five independent biofilm chambers.

Chemostat experiments. Chemostat vessels (300 ml running volume, dilution rate 0.6 h^{−1}) were operated with a cell density of (1–5) × 10⁷ ml^{−1} depending on the carbon source concentration. Before inoculation, cells from overnight cultures were acclimated for about 6 h in batch culture. Chemostat cultures were grown at 24 °C with aeration. Initial ($t = 0$) and final ($t = 24$ h) population ratios

were determined by plate enumeration. To check for the evolution of the derived rough variant of *P. putida* in chemostat culture a minimum of 1,000 colonies were sampled from each of three replicate chemostats.

Genetic analyses. See Supplementary Methods.

Received 13 September; accepted 8 December 2006.

- Davey, M. E. & O'Toole, G. A. Microbial biofilms: from ecology to molecular genetics. *Microbiol. Mol. Biol. Rev.* **64**, 847–867 (2000).
- Tyson, G. W. *et al.* Community structure and metabolism through reconstruction of microbial genomes from the environment. *Nature* **428**, 37–43 (2004).
- Kerr, B., Riley, M. A., Feldman, M. W. & Bohannan, B. J. M. Local dispersal promotes biodiversity in a real-life game of rock–paper–scissors. *Nature* **418**, 171–174 (2002).
- Hassell, M. P., Comins, H. N. & May, R. M. Species coexistence and self-organizing spatial dynamics. *Nature* **370**, 290–292 (1994).
- Durrett, R. & Levin, S. The importance of being discrete (and spatial). *Theor. Popul. Biol.* **46**, 363–394 (1994).
- Tilman, D. Niche tradeoffs, neutrality, and community structure: a stochastic theory of resource competition, invasion, and community assembly. *Proc. Natl Acad. Sci. USA* **101**, 10854–10861 (2004).
- Loreau, M. *et al.* Ecology—Biodiversity and ecosystem functioning: Current knowledge and future challenges. *Science* **294**, 804–808 (2001).
- Newman, D. K. & Banfield, J. F. Geomicrobiology: how molecular-scale interactions underpin biogeochemical systems. *Science* **296**, 1071–1077 (2002).
- Battin, T. J., Kaplan, L. A., Denis Newbold, J. & Hansen, C. M. Contributions of microbial biofilms to ecosystem processes in stream mesocosms. *Nature* **426**, 439–442 (2003).
- Labrenz, M. *et al.* Formation of sphalerite (ZnS) deposits in natural biofilms of sulfate-reducing bacteria. *Science* **290**, 1744–1747 (2000).
- Thompson, J. N. *The Coevolutionary Process* (Univ. of Chicago Press, Chicago, IL, 1994).
- Ley, R. E. *et al.* Unexpected diversity and complexity of the Guerrero Negro hypersaline microbial mat. *Appl. Environ. Microbiol.* **72**, 3685–3695 (2006).
- Kroes, I., Lepp, P. W. & Relman, D. A. Bacterial diversity within the human subgingival crevice. *Proc. Natl Acad. Sci. USA* **96**, 14547–14552 (1999).
- Ram, R. J. *et al.* Community proteomics of a natural microbial biofilm. *Science* **308**, 1915–1920 (2005).
- Boles, B. R., Thoendel, M. & Singh, P. K. Self-generated diversity produces 'insurance effects' in biofilm communities. *Proc. Natl Acad. Sci. USA* **101**, 16630–16635 (2004).
- An, D., Danhorn, T., Fuqua, C. & Parsek, M. R. Quorum sensing and motility mediate interactions between *Pseudomonas aeruginosa* and *Agrobacterium tumefaciens* in biofilm cocultures. *Proc. Natl Acad. Sci. USA* **103**, 3828–3833 (2006).
- Montoya, J. M., Pimm, S. L. & Sole, R. V. Ecological networks and their fragility. *Nature* **442**, 259–264 (2006).
- Tilman, D. & Kareiva, P. (eds) *Spatial Ecology* (Princeton Univ. Press, Princeton, NJ, 1997).
- Rainey, P. B. & Travisano, M. Adaptive radiation in a heterogeneous environment. *Nature* **394**, 69–72 (1998).
- Forde, S. E., Thompson, J. N. & Bohannan, B. J. Adaptation varies through space and time in a coevolving host–parasitoid interaction. *Nature* **431**, 841–844 (2004).
- Moller, S., Pedersen, A. R., Poulsen, L. K., Arvin, E. & Molin, S. Activity and three-dimensional distribution of toluene-degrading *Pseudomonas putida* in a multispecies biofilm assessed by quantitative in situ hybridization and scanning confocal laser microscopy. *Appl. Environ. Microbiol.* **62**, 4632–4640 (1996).
- Christensen, B. B., Haagensen, J. A., Heydorn, A. & Molin, S. Metabolic commensalism and competition in a two-species microbial consortium. *Appl. Environ. Microbiol.* **68**, 2495–2502 (2002).
- Turner, P. E., Souza, V. & Lenski, R. E. Tests of ecological mechanisms promoting the stable coexistence of two bacterial genotypes. *Ecology* **77**, 2119–2129 (1996).
- Lam, J. S., Matewish, M. & Poon, K. K. H. in *Pseudomonas* Vol. 3 (ed. Ramos, J. I.) 3–53 (Kluwer/Plenum, New York, 2004).
- Urban, M. C. & Skelly, D. K. Evolving metacommunities: toward an evolutionary perspective on metacommunities. *Ecology* **87**, 1616–1626 (2006).
- Thompson, J. N. & Cunningham, B. M. Geographic structure and dynamics of coevolutionary selection. *Nature* **417**, 735–738 (2002).
- Franklin, F. C., Bagdasarian, M., Bagdasarian, M. M. & Timmis, K. N. Molecular and functional analysis of the TOL plasmid pWWO from *Pseudomonas putida* and cloning of genes for the entire regulated aromatic ring meta cleavage pathway. *Proc. Natl Acad. Sci. USA* **78**, 7458–7462 (1981).
- Lenski, R. E., Rose, M. R., Simpson, S. C. & Tadler, S. C. Long-term experimental evolution in *Escherichia coli*. I. Adaptation and divergence during 2,000 generations. *Am. Nat.* **138**, 1315–1341 (1991).
- Christensen, B. B. *et al.* Molecular tools for study of biofilm physiology. *Methods Enzymol.* **310**, 20–42 (1999).
- Heydorn, A. *et al.* Quantification of biofilm structures by the novel computer program COMSTAT. *Microbiology* **146**, 2395–2407 (2000).

Supplementary Information is linked to the online version of the paper at www.nature.com/nature.

Acknowledgements We thank T. Fukami, R. Kassen, D. Refardt, T. Cooper, T. Monds and T. Martini Jørgensen for comment and discussion. Grants from the Danish Research Councils to S.M. supported this work.

Author Contributions S.K.H., S.M. and P.B.R. designed the experiments; S.K.H. and J.A.J.H. conducted the experiments; S.K.H., S.M. and P.B.R. analysed the data and wrote the paper.

Author Information Reprints and permissions information is available at www.nature.com/reprints. The authors declare no competing financial interests. Correspondence and requests for materials should be addressed to P.B.R. (p.rainey@auckland.ac.nz).

Transcription factor control of asymmetric cell divisions that establish the stomatal lineage

Cora A. MacAlister¹, Kyoko Ohashi-Ito¹ & Dominique C. Bergmann¹

The establishment of new cell lineages during development often requires a symmetry-breaking event. An asymmetric division in the epidermis of plants initiates a lineage that ultimately produces stomatal guard cells. Stomata are pores in the epidermis that serve as the main conduits for gas exchange between plants and the atmosphere; they are critical for photosynthesis and exert a major influence on global carbon and water cycles¹. Recent studies implicated intercellular signalling in preventing the inappropriate production of stomatal complexes^{2–4}. Genes required to make stomata, however, remained elusive. Here we report the identification of a gene, *SPEECHLESS* (*SPCH*), encoding a basic helix–loop–helix (bHLH) transcription factor that is necessary and sufficient for the asymmetric divisions that establish the stomatal lineage in *Arabidopsis thaliana*. We demonstrate that *SPCH* and two paralogues are successively required for the initiation, proliferation and terminal differentiation of cells in the stomatal lineage. The stomatal bHLHs define a molecular pathway sufficient to create one of the key cell types in plants. Similar molecules and regulatory mechanisms are used during muscle and neural development^{5,6}, highlighting a conserved use of closely related bHLHs for cell fate specification and differentiation.

Plant–atmosphere gas exchange is modulated by controlling stomatal pore aperture with specialized epidermally derived guard cells. The cell lineage that leads to the production of guard cells is initiated in the postembryonic epidermis when some cells undergo asymmetric ‘entry’ divisions to produce meristemoids (Fig. 1a)^{7,8}. Asymmetric ‘amplifying’ divisions then regenerate the meristemoid and produce another sister cell, thereby increasing the total number of epidermal cells. Sister cells may later undergo their own asymmetric divisions to produce satellite meristemoids. Meristemoids differentiate into guard mother cells (GMCs), which divide symmetrically to create the paired guard cells of typical stomata. The MYB class transcription factors FOUR LIPS and MYB88 and the bHLH domain protein FAMA are required in the transition from division to differentiation in GMCs so that a single pair of functional guard cells is formed^{3,9,10}. The characteristic arrangement of *Arabidopsis* stomata is formed primarily by ‘spacing’ divisions in sister cells that prevent the formation of new meristemoids directly adjacent to existing stomata¹¹. Mutations in the genes encoding the putative receptor *TOO MANY MOUTHS* (*TMM*)⁴, the *ERECTA* (*ER*) family receptor-like kinases² and the MAP-kinase kinase kinase, *YODA*³, affect entry, amplifying and spacing divisions. These stomatal signalling components negatively regulate stomatal initiation.

We created a sensitized genetic background to screen for genes that are required to promote stomatal fate, and identified two allelic mutations, *spch-1* and *spch-2* (Supplementary Methods). No stomata are formed in plants homozygous for *spch-1* (Fig. 1c versus Fig. 1d) or for insertion mutants *spch-3* (SAIL36_B04) or *spch-4* (SALK_078595), and these plants arrest as very small, pale seedlings (Fig. 1b). To

identify the block in stomatal development, the early development of cotyledons was followed in *spch-1*. In these plants, no physically asymmetric entry divisions were visible at 3 days post-germination

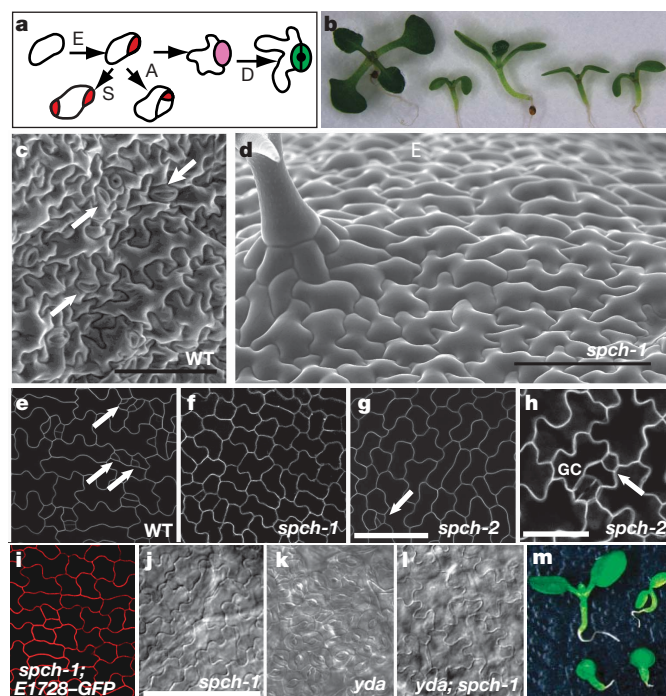


Figure 1 | *SPCH* is required for asymmetric cell division and stomatal formation. **a**, Stages in stomatal development, from left, entry (E) divisions create meristemoids (red) as the smaller daughters of the division. Meristemoids self-renew through an amplifying (A) division, or differentiate into GMCs (pink). GMCs divide once and the daughters differentiate (D) into guard cells (green). Spacing divisions (S) create additional, correctly spaced stomata. **b**, Growth defects of 10-days-post-germination *SPCH* mutant seedlings: from left; wild type (WT), *spch-1*, *spch-2*, *spch-3*, *spch-4* at $\times 4$ magnification. **c**, **d**, Scanning electron microscope images of stomatal distribution in wild type and *spch-1* mutants. Representative stomata indicated by white arrows. **e–g**, Confocal images of 60-hours-old cotyledons of wild type (**e**), *spch-1* (**f**) and *spch-2* (**g**). Entry divisions marked with white arrows. **h**, Confocal image of a 5-days-post-germination *spch-2* cotyledon. GC marks guard cells. White arrow indicates correctly oriented divisions. **i**, Lack of the stomatal marker *E1728::GFP* (green) in 5-days-post-germination *spch-1*. **j–l**, Differential interference contrast (DIC) images of cotyledon epidermis of *spch-1* (**j**), *yodaY295* (**k**) and *spch; yoda* (**l**) note absence of stomata in (**l**). **m**, Overall morphology of *spch; yoda* resembles *yoda*: clockwise from top left; 7-days-post-germination seedlings of wild type, *spch*, *spch; yoda* and *yoda* at $\times 3$ magnification. All scale bars, 100 μm . **e–g**, **i** same magnification. **j–l**, same magnification.

¹Department of Biological Sciences, Stanford University, Stanford, California 94305, USA.

($n = 20$ leaves, ~ 200 cells per leaf), suggesting that *SPCH* is required for the initiation of the stomatal lineage (Fig. 1e versus Fig. 1f).

The mutation *spch-2* significantly reduces the stomatal index (number of stomata per total number of epidermal cells) in all organs compared with the parental line (Supplementary Fig. 1). *spch-2* plants are smaller than wild type (Fig. 1b), but are otherwise healthy and fertile. Fewer cells undergo entry divisions in *spch-2* cotyledons than in wild type (Fig. 1g versus Fig. 1e). Because *spch-2* plants produce some stomata, the role of *SPCH* in later stomatal divisions could be assayed. In *spch-2* pedicels, fewer sister cells were found associated with mature stomata (0.97 ± 0.070 (mean \pm s.e.m.) compared with 1.57 ± 0.062 for wild type), indicating that *SPCH* may have a role in promoting amplifying divisions. Evidence that *SPCH* promotes spacing divisions, but is not required for their orientation, comes from the observation that divisions creating new meristemoids in *spch-2* are oriented relative to existing stomata (Fig. 1h), but that the fraction of stomata found one cell away from another stoma (potentially formed by spacing divisions) is significantly lower in *spch-2* (0.146 ± 0.086 (mean \pm s.e.m.) compared with 0.865 ± 0.029 for wild type; see Supplementary Fig. 1). All stomata in *spch-2* consist of two morphologically normal guard cells ($n = 200$ stomata on 5 leaves), indicating that *SPCH* is not required for the symmetric GMC division. The requirement for *SPCH* in asymmetric divisions seems to be specific to stomatal development. Two important asymmetric cell divisions outside the stomatal lineage—the root cortex/endodermis division and the embryo/suspensor division—

appear normal in *spch-1* roots or in embryos from *spch-1/+* plants, respectively (Supplementary Fig. 2a–f).

The failure of *spch-1* plants to make entry divisions suggests that *spch-1* will be epistatic to any mutations that affect divisions late in the lineage. Consistent with this, double mutants between *spch-1* and *fama-1* exhibit the *spch-1* phenotype (not shown). *YODA*, *TMM* and *ER* encode putative signalling molecules, and mutations in these genes increase entry divisions and can result in the production of excess stomata^{2–4}. *spch-1* is epistatic to all three mutants with respect to the stomatal phenotype, suggesting that *SPCH* acts downstream of or before these genes (Fig. 1j–l and data not shown). *spch-1* plants also fail to express *TMM* and guard cell reporters (Fig. 1i and data not shown). The *spch* epistasis is limited to the stomatal lineage as revealed by *yoda*; *spch-1* double mutants that do not make stomata (Fig. 1l), but exhibit other morphological defects characteristic of *yoda* (Fig. 1m)¹².

SPCH was cloned by mapping the *spch-1* allele to within 37 kb on chromosome 5 and sequencing candidate genes in the region. *spch-1* and *spch-2* harbour mutations in the coding region of At5g53210 (Fig. 2a). *SPCH* encodes a 364 amino acid protein with domains characteristic of bHLH transcription factors including a nuclear localization signal, a putative G-box DNA binding domain and a helix–loop–helix domain (Fig. 2a and Supplementary Fig. 3). There was no *SPCH* transcript detectable in homozygous *spch-3* and *spch-4* by PCR with reverse transcription (RT–PCR) (Fig. 2b), but wild-type transcript levels are present in *spch-1* and *spch-2* (Fig. 2b). *spch-1*

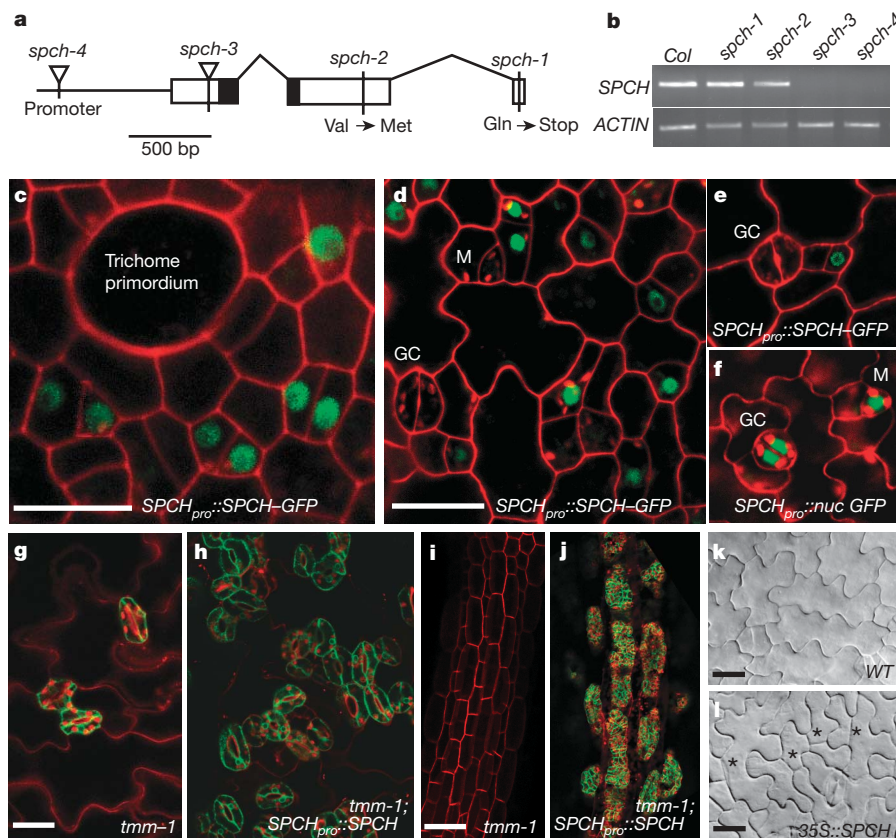


Figure 2 | *SPCH*, a bHLH protein expressed in the epidermis and sufficient for asymmetric cell divisions and stomatal formation. **a**, Hybrid diagram of *SPCH* locus and protein. Coding regions indicated as boxes, bHLH domain shaded. Triangles indicate T-DNA insertion alleles. Location and nature of ethylmethane-sulphonate-induced mutations indicated below the gene. **b**, Expression of *SPCH* in mutants by RT–PCR. A loading control of *ACTIN* is shown below. **c–e**, Confocal images of *SPCH_{pro}::SPCH-GFP* (green) in the epidermis of developing cotyledons and leaves before (c) and during (d) development of the stomatal lineage, and during spacing divisions (e). Cell outlines were counterstained with propidium iodide (red); M

indicates meristemoid, GC marks guard cells. **f**, *SPCH_{pro}::nucGFP* expression continues in the stomatal lineage. **g–j**, Overexpression of *SPCH* induces excess stomatal formation. Confocal image of stomatal marker *E1728::GFP* (green) in a *tmm-1* cotyledon (g), with *SPCH_{pro}::SPCH* in a *tmm-1* cotyledon (h), in a *tmm-1* hypocotyl (i), and with *SPCH_{pro}::SPCH* in a *tmm-1* cotyledon (j). **k–l**, DIC image of cotyledons from wild type (k). *35S::SPCH* (l) induces excessive epidermal divisions, but no extra stomata. * marks ectopic divisions in pavement cells. Scale bars, 15 μ m except in i (50 μ m). **e–f** are at the same magnification as **d**; **h** is the same as **g**, and **j** is the same as **i**.

truncates the last 7 amino acids of the protein (Fig. 2a). The phenotype of *spch-1* is indistinguishable from *spch-3* or *spch-4*, suggesting that this portion of the protein is functionally important. The weak *spch-2* allele is a mis-sense mutation in a moderately conserved region of the carboxy terminus (Fig. 2a and Supplementary Fig. 3).

SPCH is expressed in the developing leaf epidermis. A transcriptional green fluorescent protein (GFP) reporter (*SPCH_{pro}::nucGFP*) and a rescuing translational reporter (*SPCH_{pro}::SPCH-GFP*) are expressed in a subset of epidermal cells that lack overt signs of differentiation (Fig. 2c–e and Supplementary Fig. 4). Expression commences in cotyledons coincident with the onset of postembryonic cell division (Supplementary Fig. 4b), and *SPCH* expression is often found in two neighbouring cells—a pattern consistent with expression in the dividing cell population (Fig. 2c). In older organs, *SPCH_{pro}::SPCH-GFP* expression continues to be restricted to small cells in the epidermis (Fig. 2d), including cells that have recently divided next to stomatal lineage cells (Fig. 2e). Transcriptional and translational SPCH reporters have identical early expression patterns (Supplementary Fig. 4), however *SPCH_{pro}::nucGFP* persists in stomatal lineage cells (Fig. 2f and Supplementary Fig. 4d–e) indicating that SPCH protein may be downregulated post-transcriptionally.

SPCH is necessary for stomatal lineage initiation; to determine whether *SPCH* is also sufficient to create this lineage, *SPCH* was overexpressed. Increasing *SPCH* expression within its native domain (*SPCH_{pro}::SPCH*) in a background wild-type for *SPCH* induces extra asymmetric divisions and the production of excess stomata (Fig. 2g versus h). When expressed in *tmm* (which has clustered stomata on

leaves, but no stomata on stems or hypocotyls)¹³, *SPCH_{pro}::SPCH* induces stomatal formation in all organs indicating that *SPCH* acts downstream of *TMM* (Fig. 2i versus j). *SPCH* expression driven by the *CaMV* 35S promoter induced extra cell divisions in cells that do not normally divide, for example (Fig. 2l versus Fig. 2k) where the straight walls of ectopic divisions are seen within the boundaries of sinuous epidermal pavement cells.

The SPCH protein is very similar to two other bHLHs: FAMA and the protein encoded by At3g06120 (now known as MUTE¹⁴) (>88% similarity in the bHLH domain and 39% over the full length; Fig. 3a and Supplementary Fig. 3). We previously demonstrated that FAMA is expressed in GMCs and is necessary and sufficient to promote guard cell identity¹⁰. We tested whether the third paralogue, *MUTE*, is required for stomatal development. A transcriptional reporter for *MUTE* is expressed strongly in meristemoids and at lower levels in GMCs and guard cells (Fig. 3b). Silencing of *MUTE* leads to the production of cells that do not form pores surrounded by excess stomatal lineage cells: a phenotype consistent with repeated amplifying divisions (Fig. 3c, e versus Fig. 3d, f). Conversely, 35S-driven overexpression of *MUTE* leads to the conversion of the entire leaf epidermis into stomata (Fig. 3g).

SPCH, *MUTE* and *FAMA* have distinct and sequential expression patterns and exhibit loss- and gain-of-function phenotypes consistent with them acting successively during stomatal development. The consecutive use of paralogous bHLHs during development is reminiscent of animal myogenesis and neurogenesis, in which bHLH transcription factors of the *myoD* class and *achaete-scute* complex control

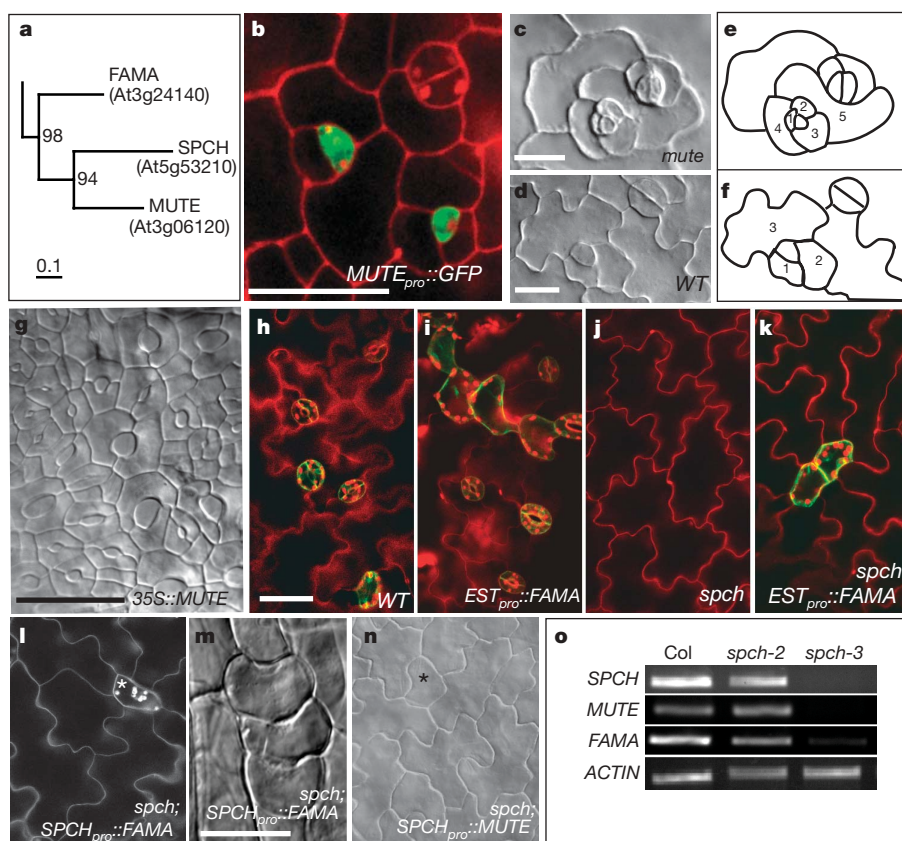


Figure 3 | SPCH-related proteins also control stomatal development.

a, SPCH relatives. Branch lengths are proportional to sequence distance. Bootstrap values (between branches) are based on 1,000 replicates. **b**, Confocal image of *MUTE_{pro}::GFP* (green) expression in meristemoids. **c–f**, DIC images (**c–d**) and cell tracings (**e–f**) of wild-type (**d, f**) and silenced *MUTE* (**c, e**) cotyledon epidermis at 7 days post-germination. Numbering of diagram indicates amplifying divisions. **g**, DIC image of 35S::*MUTE* cotyledon at 7 days post-germination. **h–k**, Confocal images indicating that ectopic *FAMA* expression in the absence of *SPCH* can produce single guard

cells (green) but cannot produce normal stomata: wild type (**h**), induced *EST_{pro}::FAMA* (**i**) *spch-1* (**j**), and *spch-1*; induced *EST_{pro}::FAMA* (**k**). Ectopic *FAMA*-induced guard cells (**i** and **k**) are consistently larger than wild-type (**h**) stomatal guard cells. **l–n**, Single guard cells (*) induced in *spch-3* by *SPCH_{pro}::FAMA* (**l, m**) and *SPCH_{pro}::MUTE* (**n**). **o**, *SPCH*, *MUTE* and *FAMA* expression by RT-PCR in wild-type, *spch-2* (viable) and *spch-3* (null) allele plants. Scale bar, 20 μ m except in **c, d** and **m** (10 μ m). **h–l, n** are at the same magnification.

subsequent stages of cell fate specification and differentiation^{5,6}. We examined whether, in addition to conserved molecules, stomatal development shared regulatory logic with the animal *myoD* and *achaete-scute* systems by testing whether: (1) expression of later genes in the pathway was dependent on the activity of early genes; (2) ectopic expression of late genes could override the requirement for early genes; and (3) the primary difference in the functions of the stomatal bHLHs can be attributed to their unique expression patterns.

Wild-type expression levels of later genes *FAMA* and *MUTE* are dependent on functional *SPCH* (Fig. 3o). Conversely, cells from *spch* mutants are competent to create unpaired guard cells in response to ectopic, oestrogen (EST)-induced, expression of *FAMA* (*EST_{pro}::FAMA*) (Fig. 3j, k). Functional interchangeability of the stomatal bHLHs was tested by promoter swap experiments. Neither the expression of *FAMA* nor the expression of *MUTE* from the *SPCH* promoter (*SPCH_{pro}::FAMA* and *SPCH_{pro}::MUTE*) substituted for *SPCH* function in entry divisions (Fig. 3l–n), although these chimaeric constructs are capable of producing *FAMA* or *MUTE* overexpression phenotypes (Fig. 3m, and Supplementary Fig. 4l).

This work, the accompanying report¹⁴, and our studies of *FAMA*¹⁰ identify genes that control cell fate and cell division at each consecutive step in the stomatal lineage (Supplementary Fig. 5). Together these data represent a major breakthrough in our understanding of how stomata are made. It is striking that stomatal development shares common molecules and some regulatory organization with animal muscle and neural development. The evolutionary history of the bHLH genes, however, suggests that each group independently adopted the use of closely related bHLHs for their cell specification programs¹⁵. *Arabidopsis* stomatal development is valuable as a comparative system to discover both conserved nodes in regulatory networks and novel mechanisms through which bHLH proteins coordinate major developmental decisions. Beyond their usefulness in dissecting fundamental developmental processes, the stomatal bHLHs are tools for manipulating stomatal densities to test plant responses to global climate change and to maximize food or biofuel crop productivity.

METHODS

Detailed methods can be found in Supplementary Information.

Cloning *SPCH*. *SPCH* was cloned using 720 F₂ recombinants to map to 37 kb between cer454361 and cer437355. Candidate genes in the region were PCR amplified and sequenced. *spch-1* and *spch-2* plants exhibited G→A mutations in the coding region of At5g53210. A 6,787 bp genomic fragment from BAC K19E1 was used to rescue *spch-1*. Total RNA from homozygous *spch* mutant plants (four alleles) was collected from whole 2-week-old seedlings. *SPCH* and *ACTIN* complementary DNAs were amplified for 35 and 25 cycles, respectively. **Plant materials and phenotypic analysis.** Markers, mutants and previously published transgenic lines are as follows: enhancer trap line E1728, Poethig lab (<http://enhancertraps.bio.upenn.edu>); plasma membrane marker Q8, ref. 16; *FAMA* T-DNA insertion allele (SALK_100073)¹⁷, ABRC stock centre; *tmm-1*, ref. 18; *yodaY295*, ref. 3; *FAMA EST_{pro}::FAMA*, ref. 10. Plants were grown initially on half strength Murashige and Skoog agar plates in a Percival incubator with 24 h light for 7 days then transferred to soil in a 22 °C growth chamber with 16 h light/8 h dark cycles. When necessary, genotypes were confirmed by PCR using previously described primers or those in Supplementary Methods. Cell outlines were visualized by plasma membrane marker Q8 (ref. 16) or by counterstaining for 1–2 min in 100 µg ml⁻¹ propidium iodide (Molecular Probes). Epidermal phenotypes were also scored on tissue cleared in 70% ethanol and then overnight in Hoyer's solution¹⁹. Quantitative data on stomatal density and index were tested for significance using R statistical computing software (<http://www.R-project.org>; details in Supplementary Information).

DNA manipulations. Plant binary vectors described in ref. 20 and ref. 21 were used to create all stable transgenic lines. Complementary DNA clones of *SPCH*

(pyAt5g53210) and *MUTE* (pyAt3g06120) (ABRC) served as the templates for the creation of rescue and overexpression constructs. Transcriptional reporters for *SPCH* and *MUTE* were made by PCR amplification of 2.5 kb and 1.7 kb of DNA 5' of the translational start sites. Plants were stably transformed using *Agrobacterium*-mediated transformation (strain GV3101) with standard protocols. At least ten T₁ transgenic lines were analysed for each construct.

Received 24 October; accepted 23 November 2006.

Published online 20 December 2006.

- Hetherington, A. M. & Woodward, F. I. The role of stomata in sensing and driving environmental change. *Nature* **424**, 901–908 (2003).
- Shpak, E. D., McAbee, J. M., Pillitteri, L. J. & Torii, K. U. Stomatal patterning and differentiation by synergistic interactions of receptor kinases. *Science* **309**, 290–293 (2005).
- Bergmann, D. C., Lukowitz, W. & Somerville, C. R. Stomatal development and pattern controlled by a MAPKK kinase. *Science* **304**, 1494–1497 (2004).
- Nadeau, J. A. & Sack, F. D. Control of stomatal distribution on the *Arabidopsis* leaf surface. *Science* **296**, 1697–1700 (2002).
- Weintraub, H. *et al.* The *myoD* gene family: nodal point during specification of the muscle cell lineage. *Science* **251**, 761–766 (1991).
- Jan, Y. N. & Jan, L. Y. HLH proteins, fly neurogenesis, and vertebrate myogenesis. *Cell* **75**, 827–830 (1993).
- Nadeau, J. A. & Sack, F. D. Stomatal development in *Arabidopsis*. In *The Arabidopsis Book* (eds Somerville, C. & Meyerowitz, E.) doi:10.1199/tab.0066 (American Society of Plant Biologists, 2002).
- Lucas, J. R., Nadeau, J. A. & Sack, F. D. Microtubule arrays and *Arabidopsis* stomatal development. *J. Exp. Bot.* **57**, 71–79 (2006).
- Lai, L. B. *et al.* The *Arabidopsis* R2R3 MYB proteins FOUR LIPS and MYB88 restrict divisions late in the stomatal cell lineage. *Plant Cell* **17**, 2754–2767 (2005).
- Ohashi-Ito, K. & Bergmann, D. *Arabidopsis* FAMA controls the final proliferation/differentiation switch during stomatal development. *Plant Cell* **18**, 2493–2505 (2006).
- Geisler, M., Nadeau, J. & Sack, F. D. Oriented asymmetric divisions that generate the stomatal spacing pattern in *Arabidopsis* are disrupted by the *too many mouths* mutation. *Plant Cell* **12**, 2075–2086 (2000).
- Lukowitz, W., Roeder, A., Parmenter, D. & Somerville, C. A. MAPKK kinase gene regulates extra-embryonic cell fate in *Arabidopsis*. *Cell* **116**, 109–119 (2004).
- Geisler, M., Yang, M. & Sack, F. D. Divergent regulation of stomatal initiation and patterning in organ and suborgan regions of the *Arabidopsis* mutants *too many mouths* and *four lips*. *Planta* **205**, 522–530 (1998).
- Pillitteri, L. J., Sloan, B. D., Bogenschütz, N. L. & Torii, K. U. Termination of asymmetric cell division and differentiation of stomata. *Nature* doi: 10.1038/nature05467 (this issue).
- Atchley, W. R. & Fitch, W. M. A natural classification of the basic helix-loop-helix class of transcription factors. *Proc. Natl Acad. Sci. USA* **94**, 5172–5176 (1997).
- Cutler, S. R., Ehrhardt, D. W., Griffiths, J. S. & Somerville, C. R. Random GFP::cDNA fusions enable visualization of subcellular structures in cells of *Arabidopsis* at a high frequency. *Proc. Natl Acad. Sci. USA* **97**, 3718–3723 (2000).
- Alonso, J. M. *et al.* Genome-wide insertional mutagenesis of *Arabidopsis thaliana*. *Science* **301**, 653–657 (2003).
- Yang, M. & Sack, F. D. The *too many mouths* and *four lips* mutations affect stomatal production in *Arabidopsis*. *Plant Cell* **7**, 2227–2239 (1995).
- Liu, C. M. & Meinke, D. W. The titan mutants of *Arabidopsis* are disrupted in mitosis and cell cycle control during seed development. *Plant J.* **16**, 21–31 (1998).
- Curtis, M. D. & Grossniklaus, U. A gateway cloning vector set for high-throughput functional analysis of genes in *planta*. *Plant Physiol.* **133**, 462–469 (2003).
- Kubo, M. *et al.* Transcription switches for protoxylem and metaxylem vessel formation. *Genes Dev.* **19**, 1855–1860 (2005).

Supplementary Information is linked to the online version of the paper at www.nature.com/nature.

Acknowledgements We thank members of the lab for discussion and comment on the manuscript and K. Torii for discussions and communication of data before publication. Some stocks were obtained from the *Arabidopsis* Biological Resource Center (ABRC) at Ohio State University. These studies were supported by a US National Science Foundation grant. C.A.M. was supported by an NIH Training grant to Stanford University.

Author Information Sequences have been deposited in Genbank under accession numbers: DQ868373 (*SPCH* messenger RNA); DQ863645 (*MUTE* mRNA) and DQ864972 (*MUTE* genomic). Reprints and permissions information is available at www.nature.com/reprints. The authors declare no competing financial interests. Correspondence and requests for materials should be addressed to D.C.B. (dbergmann@stanford.edu).

Noxious compounds activate TRPA1 ion channels through covalent modification of cysteines

Lindsey J. Macpherson¹, Adrienne E. Dubin^{1,2}, Michael J. Evans¹, Felix Marr^{3†}, Peter G. Schultz^{3,4}, Benjamin F. Cravatt^{1,3} & Ardem Patapoutian^{1,4}

The nervous system senses peripheral damage through nociceptive neurons that transmit a pain signal^{1,2}. TRPA1 is a member of the Transient Receptor Potential (TRP) family of ion channels and is expressed in nociceptive neurons^{3–5}. TRPA1 is activated by a variety of noxious stimuli, including cold temperatures, pungent natural compounds, and environmental irritants^{6–11}. How such diverse stimuli activate TRPA1 is not known. We observed that most compounds known to activate TRPA1 are able to covalently bind cysteine residues. Here we use click chemistry to show that derivatives of two such compounds, mustard oil and cinnamaldehyde, covalently bind mouse TRPA1. Structurally unrelated cysteine-modifying agents such as iodoacetamide (IA) and (2-aminoethyl)methanethiosulphonate (MTSEA) also bind and activate TRPA1. We identified by mass spectrometry fourteen cytosolic TRPA1 cysteines labelled by IA, three of which are required for normal channel function. In excised patches, reactive compounds activated TRPA1 currents that were maintained at least 10 min after washout of the compound in calcium-free solutions. Finally, activation of TRPA1 by disulphide-bond-forming MTSEA is blocked by the reducing agent dithiothreitol (DTT). Collectively, our data indicate that covalent modification of reactive cysteines within TRPA1 can cause channel activation, rapidly signalling potential tissue damage through the pain pathway.

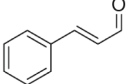
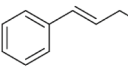
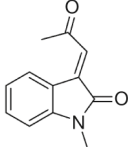
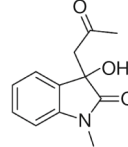
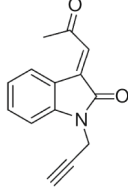
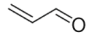
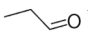
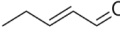
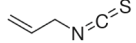
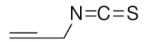
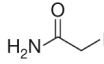
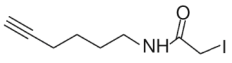
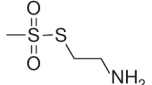
We noted that many TRPA1-activating compounds are electrophiles able to react with cysteines. For example, the nucleophilic mercapto group of cysteines can attack the α,β -unsaturated bond of cinnamaldehyde (CA) via a Michael addition (Table 1). In support of this mechanism, a more reactive cinnamaldehyde-like Michael acceptor with a carbonyl substitution adjacent to the enone¹² (a substituted oxindole, here referred to as super cinnamaldehyde, SC) is also a more potent activator of TRPA1 (Table 1). Interestingly, chemically inert structural analogues of TRPA1 agonists, such as propionaldehyde, cinnamic alcohol and SC alcohol, do not activate TRPA1^{6,9} (Table 1, and not shown). Other activators including isothiocyanates such as mustard oil (MO) could be conjugated with cysteines via an addition to form dithiocarbamates¹³ (Table 1).

We predicted that TRPA1 could be activated by covalent binding of electrophiles to cysteines. We tested if structurally unrelated cysteine-modifying agents could also activate TRPA1. We found TRPA1 was activated by both the commonly used cysteine-modifying alkylating agent iodoacetamide (IA; a standard reagent in mass spectrometry used to bind covalently with free cysteines to avoid protein aggregation) and a reagent that forms disulphide bonds with cysteines, (2-aminoethyl)methanethiosulphonate (MTSEA)^{14,15} (Table 1, and see later). *N*-hydroxyl succinimide (NHS), a lysine modifying agent¹⁶, did not activate TRPA1 in calcium imaging experiments at 100 μ M (not shown). *In vitro*, MO, CA, SC and IA formed adducts with

the cysteine-containing tripeptide glutathione (Glu-Cys-Gly; Supplementary Fig. 1a–e). These data indicate that solvent-accessible cysteine residues in TRPA1 might be covalently modified by these reactive compounds.

Alkyne groups are rarely found *in vivo* and have been used as a tag to monitor covalent modification of proteins via a copper(I)-catalysed

Table 1 | Cysteine-modifying properties of TRPA1 agonists.

TRPA1 agonist	Structure	EC ₅₀	Inactive analogue structure
Cinnamaldehyde (CA)		19.0 μ M	
Super cinnamaldehyde (SC)		0.8 μ M	
SC alkyne (SCA)		0.1 μ M	
Acrolein		5 μ M*	
Pentenal		5 μ M*	
Mustard oil (MO)		33.5 μ M	
Mustard oil alkyne (MOA)		18.4 μ M	
Iodoacetamide (IA)		357 μ M	
Iodoacetamide alkyne (IAA)		134 μ M	
MTSEA		1.58 mM	

* As reported previously⁶. † As reported previously⁹.

¹Department of Cell Biology, ²Department of Molecular Biology, ³Department of Chemistry, The Scripps Research Institute, La Jolla, California 92037, USA. ⁴Genomics Institute of the Novartis Research Foundation, San Diego, California 92121, USA. † Present address: Westfälische Wilhelms-Universität Münster, Schlossplatz 2, D-48149, Münster, Germany.

[3 + 2] cycloaddition reaction between alkyne and azide groups ('click chemistry') (Fig. 1a)^{17–19}. We tested whether alkyne-tagged IA, MO and SC (all three of which retained TRPA1 activity, Table 1) covalently bind to TRPA1 using click chemistry. As expected, a large number of proteins are labelled by the alkyne derivative of IA (IAA; Fig. 1b). Interestingly, alkyne-modified MO (MOA) and SC (SCA) also covalently bound many proteins (Fig. 1b). We next used pull-down experiments and click chemistry to monitor TRPA1 modification directly. All three compounds covalently labelled immunoprecipitated TRPA1 (Fig. 1c). In pulse-chase experiments, covalent modification of TRPA1 by IA or SC derivatives was present 1 h post-wash but returned to background levels by 24 h, possibly owing to protein turnover (Fig. 1d, not shown). These experiments suggest that SC and MO, similar to IA, covalently modify free cysteines within proteins, including TRPA1.

To determine whether TRPA1 agonists label similar sites on the channel, we used the pull-down click labelling method to measure the amount of labelling by IAA after TRPA1-expressing cells were first exposed to IA, SC, MO, CA and icilin. Pre-incubation of cells with untagged IA, SC, CA or MO with subsequent treatment with IAA reduced the rhodamine fluorescence of immunoprecipitated TRPA1

compared with cells treated with IAA alone (Fig. 1e, f). These results indicate that SC, CA and MO covalently label many of the same cysteines that are labelled by IAA. Interestingly, pre-incubation of TRPA1 cells with 100 μ M icilin did not inhibit labelling of the channel by IAA (Fig. 1g). Icilin, an activator of TRPA1 with no obvious reactivity to cysteines, did not react *in vitro* with glutathione as measured by electrospray ionization–mass spectrometry (ESI–MS) (Supplementary Fig. 1f). Therefore, it seems likely that icilin activates TRPA1 through an independent mechanism.

We next employed mass spectrometry to identify the individual modified cysteines within TRPA1 (Fig. 2a)^{14,20,21}. IA application at 100 μ M covalently labelled six cysteines, whereas 400 μ M labelled an additional eight for a total of 14 cysteines (Fig. 2b; Supplementary Fig. 2a, b). These experiments establish that at least 14 residues are reactive and covalently bind IA during a live-cell pulse. It is likely that some of the undetected cysteines could also have been modified by the initial IA pulse. Because the majority of TRPA1 cysteines reside in the intracellular portion of the channel, we used the membrane-impermeable cysteine-disulphide-forming reagent MTSEA-biotin to determine the site of TRPA1 activation. In whole-cell patch clamp electrophysiology experiments, MTSEA-biotin (400 μ M) applied to

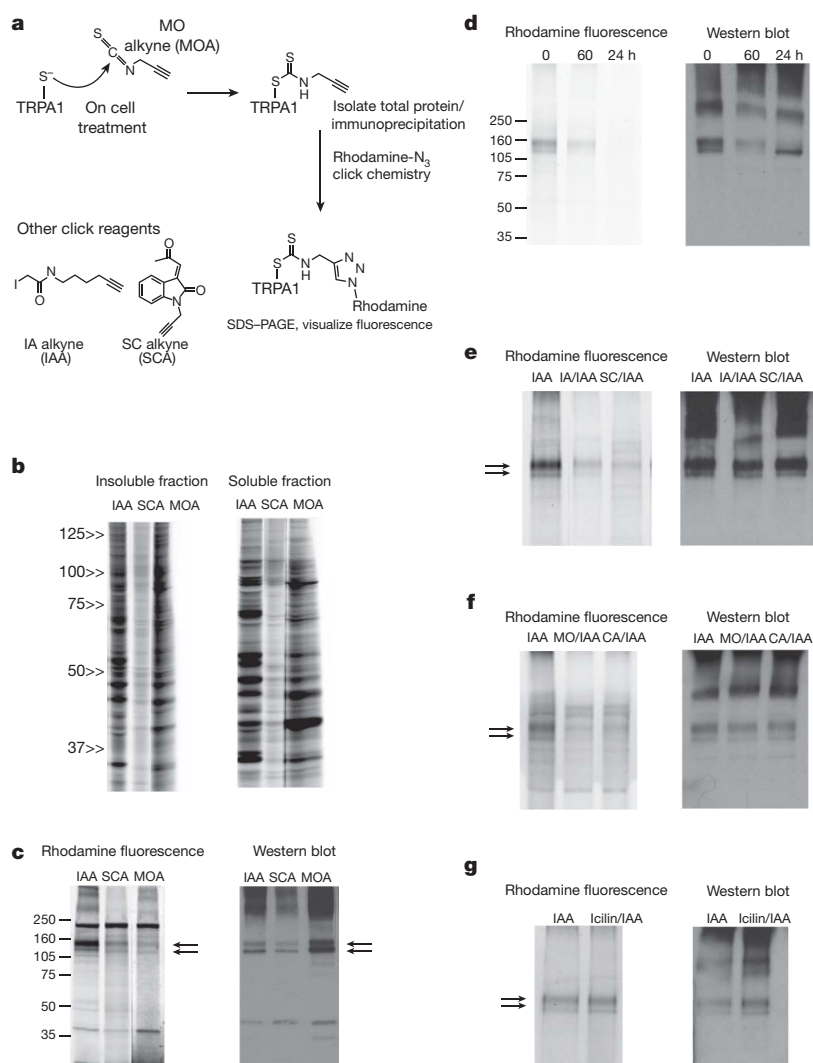


Figure 1 | TRPA1 is covalently modified by reactive compounds.

a, Schematic of the proposed reactions of alkyne reagents with TRPA1, and the click chemistry labelling with rhodamine- N_3 to visualize covalently bound activators on the protein. **b**, **c**, Many cellular proteins (**b**) and immunoprecipitated TRPA1 (**c**) are labelled by rhodamine using the click chemistry method after a 10 min incubation with 100 μ M IAA (left lanes), SCA (middle lanes) or MOA (right lanes). Molecular weight markers are

indicated (kDa). Arrows indicate immunoprecipitated TRPA1 (runs as a doublet). **d**, IAA labelling of immunoprecipitated TRPA1 at 0 min, 60 min and 24 h after initial treatment with 100 μ M IAA. **e–g**, Pre-incubation of TRPA1-expressing cells with untagged compounds followed by labelling of immunoprecipitated TRPA1 with IAA. Left panels, rhodamine fluorescence gel images; right panels, corresponding western blots.

the bath (extracellular) produced no increase in channel activity over a period of 10 min ($n = 2$). When MTSEA-biotin (400 μM) was applied intracellularly through the recording pipette, TRPA1 currents were increased and reversibly blocked by extracellular application of 300 μM menthol, a TRPA1 antagonist²² (Fig. 2c). These results indicate that TRPA1 can be activated by modification of intracellular cysteine residues.

To test whether any single cysteine is required for channel activation, we individually mutated each of the 31 cysteines in mouse TRPA1 to serines and tested the responsiveness of these mutant clones to 100 μM CA and cold using calcium imaging. Of the 31 cysteine mutations, three (C415S, C422S and C622S) revealed no detectable calcium influx in response to either stimulus, whereas the others responded to both stimuli (Fig. 2b; Supplementary Fig. 3a, and not shown). We further characterized these mutations by whole-cell patch clamping. As described for the related TRPM8 and TRPV1 ion channels, TRPA1 is activated by positive voltages

in the absence of agonists (T. Jegla, unpublished observations; Fig. 2d)^{23,24}. Current density amplitudes in response to positive voltage steps were severely reduced for all three mutant clones, although some channel activity above background remained (Fig. 2e; Supplementary Fig. 3e). To assess whether the cysteine mutations caused a selective defect of the channel's ability to be activated by covalently modifying stimuli versus stimuli probably activating TRPA1 via non-covalent mechanisms, we normalized the agonist-evoked responses of the mutants to their own voltage-activated currents. Normalized responses to 30 μM MO were significantly reduced in each of the three mutants compared with wild type (WT), with C622S showing the greatest deficit (Fig. 2f). Interestingly, normalized responses to 100 μM icilin showed no significant difference between wild-type and mutant clones, indicating that the cysteine mutants have a stronger deficit in response to cysteine-reactive MO compared with responses to voltage and icilin (Fig. 2g). These data provide evidence that each of these three cysteines is important for the

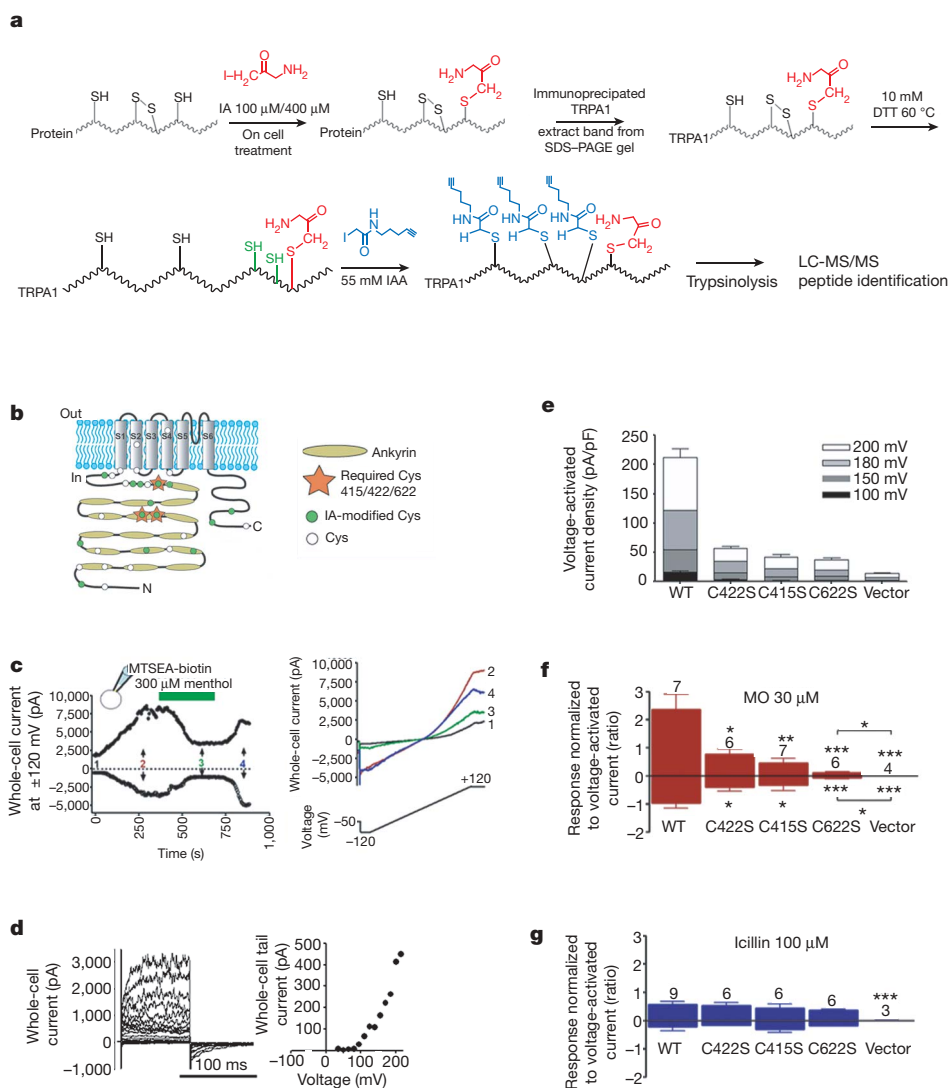


Figure 2 | TRPA1 agonist binds to reactive cysteines, three of which are required for normal channel function. **a**, Schematic of the method used to identify sites covalently bound by IA during on-cell treatment. **b**, Cartoon representation of TRPA1 showing each cysteine residue as a circle. **c**, MTSEA-biotin activates TRPA1 when applied in the intracellular recording solution in whole-cell configuration. Left panel, whole-cell currents at ± 120 mV; right panel, instantaneous TRPA1 current–voltage relationships at points indicated in left panel. **d**, **e**, Voltage-gated whole-cell currents mediated by TRPA1 are significantly attenuated in three cysteine mutants: C415S, C422S and C622S. **d**, Voltage-evoked currents (left) and tail current analysis (right)

of a representative wild-type (WT) TRPA1-expressing cell. **e**, Steady-state current density evoked by voltage steps is shown for the indicated constructs (mean \pm s.e.m., $n = 17$ –23). All values for the cysteine mutants are significantly different from wild type ($P < 0.005$) and all values with the exception of C415S at +100 mV are significantly different from vector controls ($P < 0.05$). **f**, **g**, Whole-cell currents elicited by application of 30 μM MO and 100 μM icilin and normalized to leak-subtracted currents evoked by a step to +180 mV. Plotted is the ratio \pm standard error for the number of individual determinations (cells) shown. * $P < 0.05$; ** $P < 0.01$; *** $P < 0.005$ (Student's t -test).

transduction of reactive compound labelling to channel activation, such that modifications (covalent modification or amino acid substitutions) at these locations can profoundly affect channel gating. However, we cannot rule out the possibility that the three cysteines are also required for appropriate channel conformation. Furthermore, it is likely that other reactive cysteines involved in TRPA1 activation were not highlighted by individual mutation (Fig. 2b).

Michael addition, conjugation, alkylation and disulphide formation of cysteines are relatively stable modifications, and a pulse of an activator could potentially cause prolonged channel activity. Indeed, 2-min pulses of SC, MO, MTSEA and IA caused sustained elevation of intracellular calcium levels over a period of 15–60 min in CHO cells expressing TRPA1 (Fig. 3a; Supplementary Fig. 4a–d). The addition of menthol during the extended period of activation reversibly reduced the elevated calcium levels, arguing that the sustained calcium signal is due to ongoing TRPA1 activity (Fig. 3a, left panel; Supplementary Fig. 4c, d). In contrast, TRPM8 activation by pulses of maximally activating concentrations of menthol shows fast recovery from each pulse, suggesting that prolonged activation is not a general mechanism of all TRP channels (Fig. 3a, right panel). We also investigated the reversibility of TRPA1 activity in isolated patches from TRPA1-expressing HEK cells, in a calcium-free environment to reduce desensitization. TRPA1 single-channel activity (92 pS) was both voltage- and agonist-concentration-dependent (Fig. 3b)²⁵. Similar to results obtained from calcium imaging experiments, a 2-min application of SC (50 μ M) or MO (30 μ M) to an inside-out patch showed continued activity for more than 10 min, which could

be reversibly reduced by menthol, demonstrating that irreversible activation can occur even at moderate concentrations of agonist (Fig. 3c, d). Interestingly, application of 100 μ M icilin to excised inside-out patches enhanced channel activity in a rapidly reversible manner (Fig. 3e), again demonstrating the qualitative differences in mechanism of action of icilin on TRPA1 compared with cysteine-reactive agonists.

Dithiothreitol (DTT) is a cell-permeable reducing agent that can reverse the disulphide modification of cysteines, but not that of the Michael addition or cysteine conjugation reactions (for example, see refs 15, 26). Therefore, DTT should reverse MTSEA-induced, but not SC- or MO-induced activation. This is indeed what we observed in calcium imaging experiments in CHO cells and cultured dorsal root ganglia neurons (Fig. 3f, g; Supplementary Fig. 4i–k, and not shown).

Redox-sensitive cysteine residues have been implicated in modulation of ion channel function, including activation of ryanodine receptors through S-nitrosylation^{27,28}. S-nitrosylation of cysteine residues next to the pore of TRPC5 has also recently been shown to activate the channel²⁹. However, the covalent modification of TRPA1 by pungent compounds is apparently irreversible. How, then, is the channel inactivated? Activated channels still display gating; for instance, inactivation at high voltage (Fig. 3c, left panel; Supplementary Fig. 4h). At a single-channel level, compound-activated channels showed open/closed transitions reflecting open and desensitized states (Fig. 3b). Furthermore, TRPA1 activity can be blocked by intracellular calcium²⁵. Thus, mechanisms exist for inactivating the covalently modified channel.

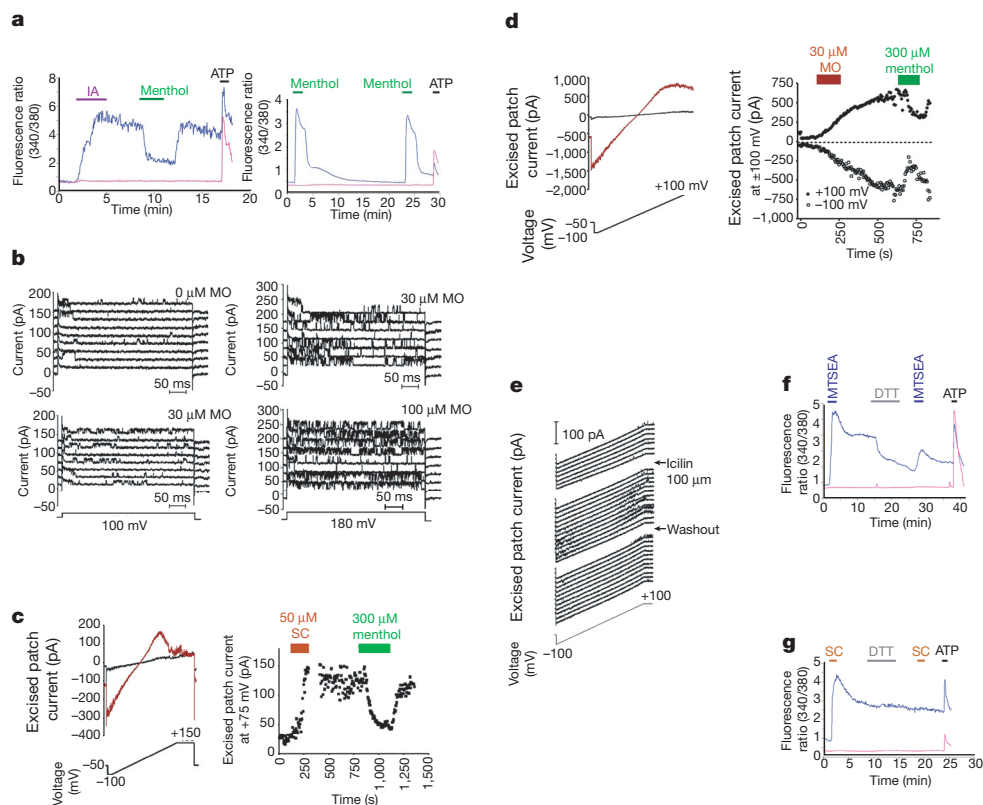


Figure 3 | Reactive compounds can cause sustained activation of TRPA1, and DTT reverses activation of TRPA1 by MTSEA. **a**, Calcium imaging experiments of CHO cells transiently transfected with TRPA1 (left panel) and TRPM8 (right panel). Blue trace indicates the transfected cell average; pink trace, untransfected; average of 15–30 cells. **b**, Single-channel activity evoked by voltage steps to either +100 or +180 mV (from –50 mV) in a single, excised, inside-out wild-type TRPA1 patch, challenged with increasing concentrations of MO. **c**, **d**, SC and MO (50 μ M and 30 μ M, respectively; applied as indicated by the red bars, right panels) activated a non-selective cation conductance in an excised patch from wild-type

TRPA1-expressing HEK cells (left panels). The currents were measured over the entire experiment and plotted versus time (right panels). The currents were reversibly reduced by 300 μ M menthol application (green bars). **e**, Single-channel wild-type TRPA1 activity evoked by voltage ramps recorded every 15 s before, during and after washout of 100 μ M icilin in the bath (arrows). **f**, **g**, DTT (5 mM) reverses TRPA1 activation induced by the disulphide-forming activator MTSEA (400 μ M; **f**), but not the Michael addition activator SC (50 μ M; **g**). TRPA1-expressing cells (blue traces) and untransfected cells (pink traces) were imaged for intracellular calcium levels.

TRPA1 is not unique among proteins to be modified by cysteine reactive agents, but we show it is uniquely activated in response to such stimuli. Interestingly, cytosolic Kelch-like ECH-associated protein 1 (KEAP1) is activated by many of the same compounds that activate TRPA1^{14,15,21,30}. Apparently, reactive compounds can activate at least two pathways through cysteine modification: KEAP1-regulated transcriptional activation of antioxidant enzymes and TRPA1-mediated rapid activation of nociceptors as a warning signal against cell damage. By tuning TRPA1 to respond to covalent modification by reactive compounds, the nervous system can directly assess the noxious environment of sensory neurons.

Note added in proof: Following review of this manuscript, another study reported some of the findings reported here³¹.

METHODS

Protein isolation, click chemistry and fluorescent gel imaging. These were performed essentially as described previously¹⁹. The protocol was modified for TRPA1 immunoprecipitation experiments where cells were treated, lysed and immunoprecipitated with anti-Myc and Protein G agarose beads, and then click-labelled on bead. After SDS–polyacrylamide gel electrophoresis (PAGE), rhodamine fluorescence was visualized in-gel using a Hitachi FMBio IIe flatbed-laser-induced fluorescence scanner (MiraBio, Alameda, California). Gels were reserved for protein transfer to nitrocellulose membranes and western blotting. **Proteomics of IA-labelled TRPA1.** We applied IA (either 100 μ M for 2 min or 400 μ M for 10 min) to living TRPA1-expressing HEK cells. Cells were subsequently lysed, TRPA1 protein immunoprecipitated, and proteins run on SDS–PAGE. Coomassie-stained bands of appropriate TRPA1 mass were excised from the gel, reduced with 10 mM DTT, alkylated with 55 mM IAA (as a substitute for IA in the protocol to differentiate this modification from the IA used in the live-cell treatment), trypsinized and analysed by nano-liquid-chromatography-mass spectrometry/mass spectrometry (LC)–MS/MS on an Agilent ion trap mass spectrometer. A proportion (30–40%) of TRPA1 residues were identified by spectra analysis using the Mascot search engine (Matrix Science).

Electrophysiology. Whole-cell electrophysiological methods were as described previously⁹. Excised patch voltage clamp experiments were performed on the equipment used for whole-cell studies (that is, the Axon Instruments (Molecular Devices Corporation)-based acquisition system). Calcium-free solution contained (in mM): NaCl 124.5, MgCl₂ 2, EGTA 5, HEPES 10, pH 7.4. Cells and excised patches were continuously perfused at 1–2 ml min^{−1} at a constant temperature (>24 °C) to avoid complications of exposing the channels to cool temperatures. Compounds were usually added from 300–1,000-fold stock solutions in ethanol or DMSO. Vehicle control at these concentrations had no effect on TRPA1 activity.

Calcium imaging/ FLIPR. This was performed essentially as described²².

Chemicals. Cinnamaldehyde, mustard oil, iodoacetamide and DTT were purchased from Sigma Aldrich (St Louis, Missouri). MTSEA and MOA (also known as propargyl isothiocyanate) are also commercially available (from Toronto Research Chemicals, North York, Ontario and Oakwood Products, West Columbia, South Carolina, respectively). For synthesis of SC, SCA and IAA see the 'Characterization of Chemical Materials' section in the Supplementary Information.

See Supplementary methods for more detailed information on chemicals.

Received 5 September; accepted 29 December 2006.

Published online 21 January 2007.

- Julius, D. & Basbaum, A. I. Molecular mechanisms of nociception. *Nature* **413**, 203–210 (2001).
- Wood, J. N. & Docherty, R. Chemical activators of sensory neurons. *Annu. Rev. Physiol.* **59**, 457–482 (1997).
- Dhaka, A., Viswanath, V. & Patapoutian, A. TRP ion channels and temperature sensation. *Annu. Rev. Neurosci.* **29**, 135–161 (2006).
- Montell, C. The TRP superfamily of cation channels. *Sci. STKE* **2005**, re3 (2005).
- Clapham, D. E. TRP channels as cellular sensors. *Nature* **426**, 517–524 (2003).
- Bautista, D. M. *et al.* TRPA1 mediates the inflammatory actions of environmental irritants and proalgesic agents. *Cell* **124**, 1269–1282 (2006).
- Macpherson, L. J. *et al.* The pungency of garlic: activation of TRPA1 and TRPV1 in response to allicin. *Curr. Biol.* **15**, 929–934 (2005).
- Jordt, S. E. *et al.* Mustard oils and cannabinoids excite sensory nerve fibres through the TRP channel ANKTM1. *Nature* **427**, 260–265 (2004).

- Bandell, M. *et al.* Noxious cold ion channel TRPA1 is activated by pungent compounds and bradykinin. *Neuron* **41**, 849–857 (2004).
- Story, G. M. *et al.* ANKTM1, a TRP-like channel expressed in nociceptive neurons, is activated by cold temperatures. *Cell* **112**, 819–829 (2003).
- Kwan, K. Y. *et al.* TRPA1 contributes to cold, mechanical, and chemical nociception but is not essential for hair-cell transduction. *Neuron* **50**, 277–289 (2006).
- Dinkova-Kostova, A. T., Massiah, M. A., Bozak, R. E., Hicks, R. J. & Talalay, P. Potency of Michael reaction acceptors as inducers of enzymes that protect against carcinogenesis depends on their reactivity with sulfhydryl groups. *Proc. Natl Acad. Sci. USA* **98**, 3404–3409 (2001).
- Shapiro, T. A., Fahey, J. W., Wade, K. L., Stephenson, K. K. & Talalay, P. Chemoprotective glucosinolates and isothiocyanates of broccoli sprouts: metabolism and excretion in humans. *Cancer Epidemiol. Biomarkers Prev.* **10**, 501–508 (2001).
- Eggler, A. L., Liu, G., Pezzuto, J. M., van Breemen, R. B. & Mesecar, A. D. Modifying specific cysteines of the electrophile-sensing human Keap1 protein is insufficient to disrupt binding to the Nrf2 domain Neh2. *Proc. Natl Acad. Sci. USA* **102**, 10070–10075 (2005).
- Fearon, I. M. *et al.* Modulation of recombinant human cardiac L-type Ca²⁺ channel α_1C subunits by redox agents and hypoxia. *J. Physiol. (Lond.)* **514**, 629–637 (1999).
- Grabarek, Z. & Gergely, J. Zero-length crosslinking procedure with the use of active esters. *Anal. Biochem.* **185**, 131–135 (1990).
- Evans, M. J., Saghatelian, A., Sorensen, E. J. & Cravatt, B. F. Target discovery in small-molecule cell-based screens by *in situ* proteome reactivity profiling. *Nature Biotechnol.* **23**, 1303–1307 (2005).
- Kolb, H. C., Finn, M. G. & Sharpless, K. B. Click chemistry: diverse chemical function from a few good reactions. *Angew. Chem. Int. Edn Engl.* **40**, 2004–2021 (2001).
- Speers, A. E. & Cravatt, B. F. Profiling enzyme activities *in vivo* using click chemistry methods. *Chem. Biol.* **11**, 535–546 (2004).
- Dinkova-Kostova, A. T., Holtzclaw, W. D. & Kensler, T. W. The role of Keap1 in cellular protective responses. *Chem. Res. Toxicol.* **18**, 1779–1791 (2005).
- Hong, F., Freeman, M. L. & Liebler, D. C. Identification of sensor cysteines in human Keap1 modified by the cancer chemopreventive agent sulforaphane. *Chem. Res. Toxicol.* **18**, 1917–1926 (2005).
- Macpherson, L. J. *et al.* More than cool: promiscuous relationships of menthol and other sensory compounds. *Mol. Cell. Neurosci.* **32**, 335–343 (2006).
- Voets, T. *et al.* The principle of temperature-dependent gating in cold- and heat-sensitive TRP channels. *Nature* **430**, 748–754 (2004).
- Brauchi, S., Orio, P. & Latorre, R. Clues to understanding cold sensation: thermodynamics and electrophysiological analysis of the cold receptor TRPM8. *Proc. Natl Acad. Sci. USA* **101**, 15494–15499 (2004).
- Nagata, K., Duggan, A., Kumar, G. & Garcia-Anoveros, J. Nociceptor and hair cell transducer properties of TRPA1, a channel for pain and hearing. *J. Neurosci.* **25**, 4052–4061 (2005).
- Getz, E. B., Xiao, M., Chakrabarty, T., Cooke, R. & Selvin, P. R. A comparison between the sulfhydryl reductants tris(2-carboxyethyl)phosphine and dithiothreitol for use in protein biochemistry. *Anal. Biochem.* **273**, 73–80 (1999).
- Hess, D. T., Matsumoto, A., Kim, S. O., Marshall, H. E. & Stamler, J. S. Protein S-nitrosylation: purview and parameters. *Nature Rev. Mol. Cell Biol.* **6**, 150–166 (2005).
- Matalon, S. *et al.* Regulation of ion channel structure and function by reactive oxygen-nitrogen species. *Am. J. Physiol. Lung Cell. Mol. Physiol.* **285**, L1184–L1189 (2003).
- Yoshida, T. *et al.* Nitric oxide activates TRP channels by cysteine S-nitrosylation. *Nature Chem. Biol.* **2**, 596–607 (2006).
- Wakabayashi, N. *et al.* Protection against electrophile and oxidant stress by induction of the phase 2 response: fate of cysteines of the Keap1 sensor modified by inducers. *Proc. Natl Acad. Sci. USA* **101**, 2040–2045 (2004).
- Hinman, A., Chuang, H. H., Bautista, D. M. & Julius, D. TRP channel activation by reversible covalent modification. *Proc. Natl Acad. Sci. USA* **103**, 19564–19568 (2006).

Supplementary Information is linked to the online version of the paper at www.nature.com/nature.

Acknowledgements We thank T. Earley, M. Garrett, M. Petrus, J. Mathur, K. Spencer and the TSRI Mass Spectrometry Proteomics Core for technical help; and M. Bandell, A. Dhaka, J. Grandl, N. Hong, T. Jegla, L. Stowers and S. Trauger for valuable input. This research was supported by NIH grants and by Novartis Research Foundation. L.J.M. is the recipient of a Ruth Kirschstein Predoctoral Fellowship.

Author Information Reprints and permissions information is available at www.nature.com/reprints. The authors declare no competing financial interests. Correspondence and requests for materials should be addressed to A.P. (ardem@scripps.edu).

LETTERS

The twisted ion-permeation pathway of a resting voltage-sensing domain

Francesco Tombola¹, Medha M. Pathak^{1†}, Pau Gorostiza^{1†} & Ehud Y. Isacoff^{1,2}

Proteins containing voltage-sensing domains (VSDs) translate changes in membrane potential into changes in ion permeability or enzymatic activity^{1–3}. In channels, voltage change triggers a switch in conformation of the VSD, which drives gating in a separate pore domain, or, in channels lacking a pore domain, directly gates an ion pathway within the VSD^{4,5}. Neither mechanism is well understood⁶. In the Shaker potassium channel, mutation of the first arginine residue of the S4 helix to a smaller uncharged residue makes the VSD permeable to ions ('omega current') in the resting conformation ('S4 down')⁷. Here we perform a structure-guided perturbation analysis of the omega conductance to map its VSD permeation pathway. We find that there are four omega pores per channel, which is consistent with one conduction path per VSD. Permeating ions from the extracellular medium enter the VSD at its peripheral junction with the pore domain, and then plunge into the core of the VSD in a curved conduction pathway. Our results provide a model of the resting conformation of the VSD.

In searching for residues that line the omega pathway (Fig. 1), we measured perturbations in the omega current due to 116 alterations of the side chains of 46 residues located in the VSD (S1–S4) and in the pore domain (S5 and S6). Introduced cysteine residues were chemically modified by the thiol-reactive agents ((2-trimethylammonium)ethyl)-methanethiosulphonate (MTSET) or (2-sulphonatoethyl)-methanethiosulphonate (MTSES), which add bulk and either a positive or a negative charge, respectively. The positions modified by MTS reagents were in regions known to be accessible to the external solution⁶. A subset of the positions were identified as facing the omega pathway, either in the vestibule (where the dominant effect was electrostatic) or in the narrow portion of the pathway (where the dominant effect was steric). We mapped the results onto the crystal structure of the VSD of K_v1.2 (ref. 8), believed to be in the activated conformation ('S4 up'), and determined the minimal movement of S4 that would generate a 'down' conformation compatible with a coherent distribution of residues around the omega pore.

In the background of the omega-conducting R362S (R1S) mutant channel (control), we introduced mutations and measured ionic currents in excised inside-out membrane patches from oocytes. Because the omega current (I_{ω}) turns on when the VSD is in the resting state (S4 'down'), whereas the alpha current (I_{α}) from the pore domain turns on when the VSD is activated, the two currents flow over different voltage ranges and can be measured separately within the same patch (Fig. 1). The alpha current was used to normalize for the number of channels, so that the omega currents, (I_{ω})_m from different patches could be compared (Supplementary Information). Figure 1d shows an electrostatic perturbation in which the positively charged MTSET decreases omega current (blue trace), whereas MTSES increases it (red trace). Supplementary Fig. 1 shows the range of perturbations.

To estimate omega pore conductance, open probability and the number of omega pores per channel, we performed a non-stationary fluctuation analysis⁹ (Supplementary Methods). Because the R1S omega conductance was small, we considered 18 manipulations that individually increased omega current by more than 25% and chose a combination of three, which additively increased macroscopic omega current 13-fold (Fig. 2a, b). The single-channel conductance of this BOM (big omega-current mutant) omega pore (3.42 ± 0.12 pS, $n = 8$) was large enough for alpha and omega pores to be counted in the same patch (Fig. 2c). Open probability (at -250 mV) was 0.53 ± 0.02 ($n = 9$). Strikingly, the ratio between the number of

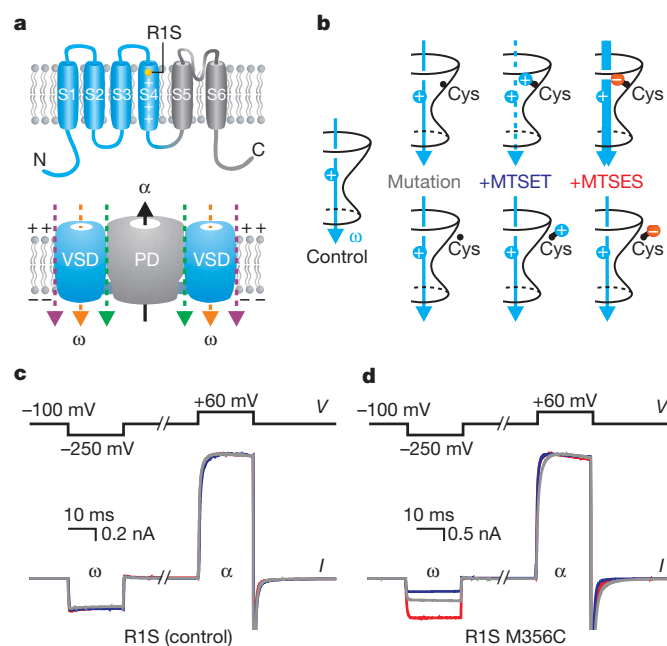


Figure 1 | Perturbation of omega current by mutation and MTS modification. **a**, Top: topology of a K_v channel. Bottom: three possible pathways for the omega current. **b**, Modification of omega current by MTS conjugation to introduced cysteine residue facing the extracellular vestibule of the omega pore (upper row) or located elsewhere in the protein (lower row). Arrows indicate increased (double solid line) or decreased (dotted line) omega current. **c**, Alpha and omega currents elicited by steps to distinct voltages in the control channel (R1S). Normalized traces from three different patches are superimposed. Grey, before treatment with MTS; blue, after MTSET; red, after MTSES. **d**, Alpha and omega currents from channels with a cysteine residue at position 356 (Shaker R1S, M356C). Traces are colour-coded as in **c**.

¹Department of Molecular and Cell Biology, University of California, Berkeley, California 94720, USA. ²Physical Bioscience Division, Lawrence Berkeley National Laboratory, Berkeley, California 94720, USA. †Present addresses: Department of Neurobiology, Harvard Medical School, Boston, Massachusetts 02115, USA (M.M.P.); Center of Bioengineering of Catalonia (CREBEC), 08028 Barcelona, Spain (P.G.).

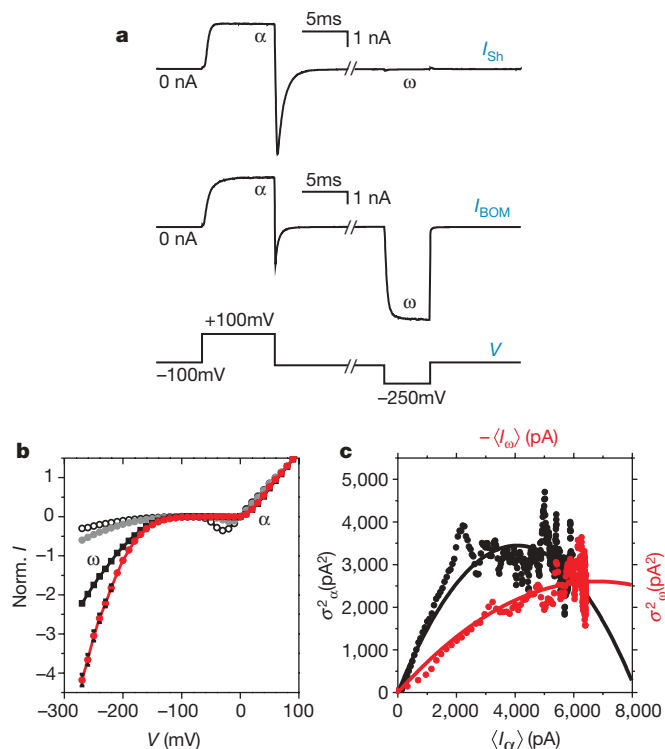


Figure 2 | Alpha and omega pores in the BOM channel. **a**, Current traces from non-omega conducting wild-type channels (I_{sh}) and BOM channels (I_{BOM}). **b**, Normalized $I-V$ plots of channels with the BOM mutations introduced one at a time. Unfilled circles, R1S; grey circles, R1S/S357C; black squares, R1S/S357C/E283D; red circles, R1S/S357C/E283D/M356D (BOM). Each $I-V$ plot is from an average of seven to ten patches. Error bars indicate s.e.m. **c**, Non-stationary fluctuation analysis of BOM channel current. Representative variance-mean plots from the same patch of alpha current for voltage steps from -100 mV to +120 mV (black circles) and omega current for steps from -100 mV to -250 mV (red circles). The scales apply to both graphs. Single channel parameters from the parabolic fit of variance-mean plots are given in Supplementary Methods.

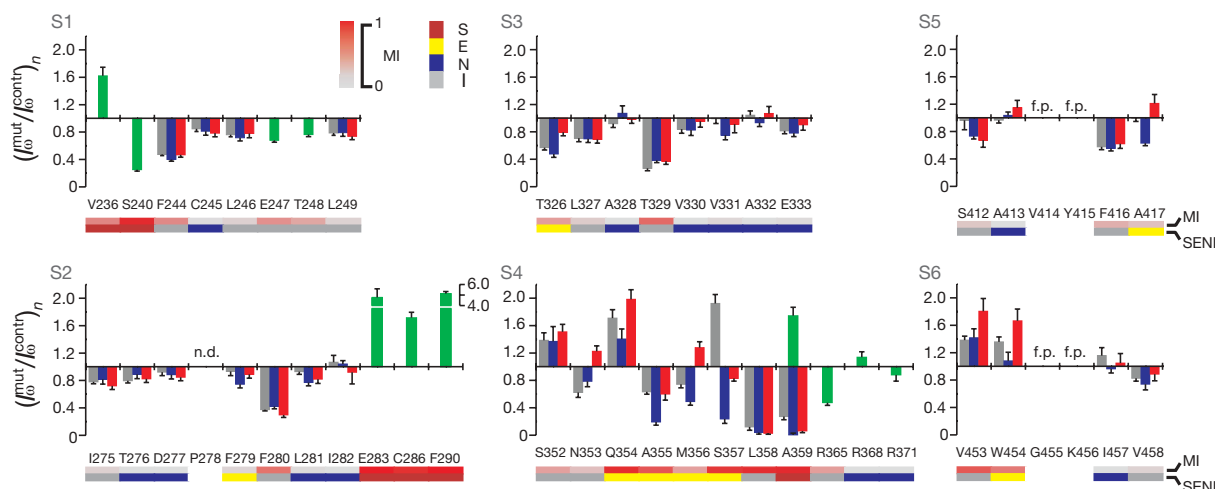


Figure 3 | Impact of side-chain manipulations on omega current amplitude. The magnitude of the perturbation is expressed as a ratio between the normalized omega currents of mutated and control channels at -250 mV (see Supplementary Information). Each column represents one manipulation, following the colour scheme from Supplementary Fig. 1 (grey, cysteine substitution only; blue, with MTSET; red, with MTSES). Green columns are mutants not treated with MTS reagents: V236C, S240T, E247D, T248S, E283D, C286S, F290C, A359G, R365Q, R368Q and R371Q. Each value of $(I_{\omega}^{mut}/I_{\omega}^{contr})_n$ is an average of four to ten measurements. Error bars indicate s.e.m. Each position is associated with two colour labels (horizontal bars below the bar graph): top, MI (maximal impact) scale; bottom, SENI (Steric/Electrostatic/Null/Indirect) classification. Sites in S5 and S6 labelled 'f.p.' face the interior of the pore domain. The cysteine mutant at position 278 (labelled 'n.d.') had no measurable alpha current.

omega and alpha pores (N_{ω}/N_{α}) was 3.7 ± 0.3 ($n = 7$), which is consistent with a channel having four omega pores, one in each VSD.

The impact of side-chain alteration on the omega current was determined as the ratio between the normalized omega current (at -250 mV) of mutant and control channels ($(I_{\omega}^{mut}/I_{\omega}^{contr})_n$) under the same conditions (no MTS treatment, with MTSET, with MTSES). The largest perturbation (maximal impact) at each position was coded on a colour scale from grey (low impact) to red (high impact) (Fig. 3) and mapped onto the crystal structure of $K_V1.2$ (Supplementary Fig. 5a).

Side chains facing the omega pathway should influence the omega current more than side chains facing elsewhere. The nature of the perturbation should depend on where in the pathway the residue is located. Residues in a large vestibule are expected to be dominated by electrostatic interactions with omega cations⁷, and to be increased by the negatively charged MTSES and decreased by the positively charged MTSET, whereas side-chain volume should have little effect (Fig. 1b). Such residues were categorized as 'Electrostatic'. In contrast, side-chain bulk, regardless of charge, should dominate impact at positions that face the narrow portion of the omega pathway. Such positions were categorized as 'Steric'. Positions where the effect could not be consistently attributed to either charge or bulk might lie on the margin of the omega pathway, or else might affect the omega pathway from a distance. These were categorized as 'Indirect'. Residues with little or no impact were categorized as 'Null' and were considered to face away from the omega pathway (Supplementary Fig. 6). In Fig. 3 we label the positions according to these four categories: Steric, Electrostatic, Null and Indirect (SENI). Of the 46 sites that we examined, 6 were Steric and 8 were Electrostatic and were considered likely to lie in the omega ion pathway. As an independent assay of this interpretation, we tested the prediction that alterations at sites that lie in the omega pathway should affect omega pore conductance and blocking. Indeed, we found that selected Steric and Electrostatic positions influence both omega single-channel conductance and pore blocking by large cations (Supplementary Table 1 and Supplementary Fig. 4).

Mapping the SENI classification onto the structure of $K_V1.2$ (ref. 8) (Fig. 4a) leads to two general observations: first, positions in S1, S2 and S3 that lie on the periphery of the VSD tend to be Null or Indirect, whereas Steric and Electrostatic positions face the core of

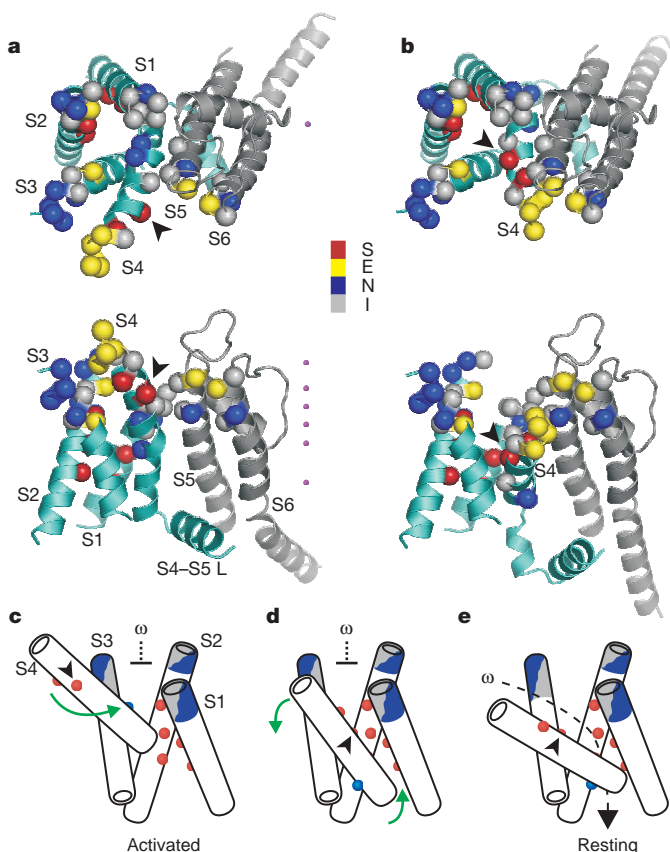


Figure 4 | The omega pathway in the resting VSD. **a**, Assayed positions mapped on the structure of Kv1.2. VSD helices of one subunit (teal), and pore-forming helices of the adjacent subunit (grey) are shown. C α of each position is shown as sphere coloured according to the SENI classification. Potassium ions in the alpha pathway are shown as purple spheres. The black arrowhead indicates the position of R1. **b**, Model of Kv1.2 resting state generated as explained in the text. The colours used are as in **a**. **c**, Diagram of VSD in the activated state as seen from the pore domain. Red spheres represent Steric positions. The blue sphere in S4 is Null position R3. The extracellular ends of S1, S2 and S3 are coloured blue and grey to indicate Null or Indirect, and are seen to face lipid or protein. The green arrow shows the S4 helical screw motion that brings Steric positions of S4 into proximity with Steric positions in S1 and S2, and removes Null positions R3 and R4 from the core of the VSD; see **a** and **b**. **d**, Conformation of VSD resulting from a pure helical screw motion of S4 as shown in **c**. Green arrows indicate a change in tilt of S4 that moves the top of S4 far enough from the other VSD helices to allow ion conduction through the omega pathway. **e**, Conformation of resting VSD resulting from a combined screw motion and the change in tilt of S4 indicated in **c** and **d**. The permeation pathway is shown as a black dashed arrowed line.

the VSD; and second, high-impact positions near external ends of helices tend to be Electrostatic, whereas deeper positions tend to be Steric. This pattern agrees with earlier accessibility analysis^{10–13}, with Electrostatic sites being highly accessible, as would be expected for the vestibule, whereas Steric sites have more limited accessibility, as would be expected for the narrow part of the omega pathway. The cluster of deep Steric positions in S1 and S2 suggests that this is the narrow part of the omega pathway, whereas the Electrostatic positions at the outer ends of S5 and S6 are in a reasonable location for the vestibule (Fig. 4a).

The exception to the coherent shape of the omega pathway is S4. The Steric and Null residues of S4 are out of register with those of S1 and S2: the Steric residues face lipid, and two of the Null residues (R3 and R4) face Steric residues in S1 and S2 (Fig. 4a, c). In addition, the extracellular end of S4 contains high-impact positions, whereas high-impact positions are deeper in other helices. The mismatch between S4 and the other helices suggests that, in the omega ion-conducting

resting state, the position of S4 is different from what is found in the activated state of the Kv1.2 structure. This makes sense, given the known inward motion of S4 at negative voltage and the contrasting lack of inward motion of S1 and S2 (refs 10, 14). Thus, the deactivation rearrangement must place the Steric and Electrostatic positions of S4 in register with those of the other helices.

A helical screw motion of S4 accompanied by an increase in tilt would place S4 in register with the rest of the protein (Fig. 4b). The screw motion moves S4's Steric residues to the same depth as those of S1 and S2, points them towards S1 and S2, and removes S4's Null residues R3 and R4 from that location (Fig. 4c, d). This screw motion consists of an inward movement of 10–13 Å (see Supplementary Information), similar to that estimated from accessibility analysis in Shaker and KvAP^{11,14}, and a rotation of about 180°, consistent with resonance-energy-transfer experiments in Shaker^{15,16} and with modelling studies on Shaker¹⁷ and Kv1.2 (ref. 18). The tilt increases from 39° in the activated ('up') state to about 60° in the resting ('down') state (Fig. 4d, e), similar to that estimated from accessibility analysis in KvAP¹⁴. It places the Electrostatic residues of S4 near those of S5 and S6 and creates space for the vestibule (Supplementary Fig. 7). The screw/tilt motion exposes the outer end of S4 to lipid in a manner that is consistent with hanatoxin's binding to the voltage sensor of Kv2.1 (refs 19, 20). Although moving S4 alone can create a coherent omega pathway, it is also possible that the pathway is formed in the resting state by means of a combined motion with other helices^{14,18,21,22}, even if they do not plunge into the membrane as S4 does.

We propose that, in contrast to the symmetrical alpha pore, ions permeating the VSD do not follow a straight pathway that is perpendicular to the membrane but enter the conduction pathway from the external solution at the interface between S4 and the pore domain (Fig. 4e), where the Electrostatic positions are clustered, and then follow a curved trajectory along the tilted S4 helix until they reach the Steric cluster in the core of the VSD. The ions could then reach the intracellular solution through the deep vestibule that is thought to exist around the internal end of S4 in the resting conformation^{12,23}. The fact that R1 needs to be mutated to a smaller uncharged residue for the omega current to flow suggests that the side chain of R1 acts as a barrier between the deep, narrow portion of the omega pore in the core of the resting VSD and the wide extracellular vestibule at the junction between the VSD and pore domain. This role of R1 is consistent with a focused electric field on the S4 arginine residues^{22,24}.

The structure of the VSD and its voltage-dependent rearrangement have been co-opted in two ways by evolution to control ion flux. In voltage-gated Kv, Nav, Cav, HCN and KAT channels, ion flux is exclusive to a central pore domain controlled by four VSDs, and VSD conduction is prevented by occupancy of the omega pathway by at least one S4 arginine residue in each conformation. In the Hv channel, which contains a VSD but no pore domain, proton flux through the VSD may occur in a conformation in which S4 arginine residues are absent from the narrowest part of an omega-like conduction pathway²⁵. Our results suggest that the key to conformational change in a VSD is a screw motion and a change in tilt of S4, which either control the gate of a separate pore domain or remove a blocking arginine residue from a twisted VSD conduction pathway.

METHODS

Mutations were made in ShH4 $\Delta(6-46)$ as described previously⁷, with the background substitution R1S. The preparation of *Xenopus* oocytes is described in Supplementary Methods. Alpha and omega currents were measured in inside-out excised membrane patches one to two days after injection. Unless otherwise mentioned, intracellular and extracellular solutions contained 100 mM KCl, 10 mM HEPES, 1 mM EDTA, pH 7.1. Modification of introduced cysteine residues with MTSET or MTSES was as described previously⁷. Non-stationary fluctuation analysis⁹ is described in Supplementary Methods. The molecular representation of the Kv1.2 structure and the model of the resting state were made in PyMOL (DeLano Scientific).

Received 28 July; accepted 30 October 2006.

Published online 24 December 2006.

1. Yu, F. H. & Catterall, W. A. The VGL-chanome: a protein superfamily specialized for electrical signaling and ionic homeostasis. *Sci. STKE* **2004**, re15 (2004).
2. Bezanilla, F. The voltage sensor in voltage-dependent ion channels. *Physiol. Rev.* **80**, 555–592 (2000).
3. Murata, Y., Iwasaki, H., Sasaki, M., Inaba, K. & Okamura, Y. Phosphoinositide phosphatase activity coupled to an intrinsic voltage sensor. *Nature* **435**, 1239–1243 (2005).
4. Ramsey, I. S., Moran, M. M., Chong, J. A. & Clapham, D. E. A voltage-gated proton-selective channel lacking the pore domain. *Nature* **440**, 1213–1216 (2006).
5. Sasaki, M., Takagi, M. & Okamura, Y. A voltage sensor-domain protein is a voltage-gated proton channel. *Science* **312**, 589–592 (2006).
6. Tombola, F., Pathak, M. M. & Isacoff, E. Y. How does voltage open an ion channel? *Annu. Rev. Cell Dev. Biol.* **22**, 23–52 (2006).
7. Tombola, F., Pathak, M. M. & Isacoff, E. Y. Voltage-sensing arginines in a potassium channel permeate and occlude cation-selective pores. *Neuron* **45**, 379–388 (2005).
8. Long, S. B., Campbell, E. B. & MacKinnon, R. Crystal structure of a mammalian voltage-dependent Shaker family K⁺ channel. *Science* **309**, 897–903 (2005).
9. Sigworth, F. J. The variance of sodium current fluctuations at the node of Ranvier. *J. Physiol. (Lond.)* **307**, 97–129 (1980).
10. Gandhi, C. S., Clark, E., Loots, E., Pralle, A. & Isacoff, E. Y. The orientation and molecular movement of a K⁺ channel voltage-sensing domain. *Neuron* **40**, 515–525 (2003).
11. Larsson, H. P., Baker, O. S., Dhillon, D. S. & Isacoff, E. Y. Transmembrane movement of the shaker K⁺ channel S4. *Neuron* **16**, 387–397 (1996).
12. Yang, N., George, A. L. Jr & Horn, R. Molecular basis of charge movement in voltage-gated sodium channels. *Neuron* **16**, 113–122 (1996).
13. Yusaf, S. P., Wray, D. & Sivaprasadarao, A. Measurement of the movement of the S4 segment during the activation of a voltage-gated potassium channel. *Pflügers Arch.* **433**, 91–97 (1996).
14. Ruta, V., Chen, J. & MacKinnon, R. Calibrated measurement of gating-charge arginine displacement in the KvAP voltage-dependent K⁺ channel. *Cell* **123**, 463–475 (2005).
15. Cha, A., Snyder, G. E., Selvin, P. R. & Bezanilla, F. Atomic scale movement of the voltage-sensing region in a potassium channel measured via spectroscopy. *Nature* **402**, 809–813 (1999).
16. Glauner, K. S., Mannuzzu, L. M., Gandhi, C. S. & Isacoff, E. Y. Spectroscopic mapping of voltage sensor movement in the Shaker potassium channel. *Nature* **402**, 813–817 (1999).
17. Durell, S. R., Shrivastava, I. H. & Guy, H. R. Models of the structure and voltage-gating mechanism of the shaker K⁺ channel. *Biophys. J.* **87**, 2116–2130 (2004).
18. Yarov-Yarovoy, V., Baker, D. & Catterall, W. A. Voltage sensor conformations in the open and closed states in ROSETTA structural models of K⁺ channels. *Proc. Natl Acad. Sci. USA* **103**, 7292–7297 (2006).
19. Lee, S. Y. & MacKinnon, R. A membrane-access mechanism of ion channel inhibition by voltage sensor toxins from spider venom. *Nature* **430**, 232–235 (2004).
20. Phillips, L. R. *et al.* Voltage-sensor activation with a tarantula toxin as cargo. *Nature* **436**, 857–860 (2005).
21. Chanda, B., Asamoah, O. K., Blunck, R., Roux, B. & Bezanilla, F. Gating charge displacement in voltage-gated ion channels involves limited transmembrane movement. *Nature* **436**, 852–856 (2005).
22. Starace, D. M. & Bezanilla, F. A proton pore in a potassium channel voltage sensor reveals a focused electric field. *Nature* **427**, 548–553 (2004).
23. Islas, L. D. & Sigworth, F. J. Electrostatics and the gating pore of Shaker potassium channels. *J. Gen. Physiol.* **117**, 69–89 (2001).
24. Ahern, C. A. & Horn, R. Focused electric field across the voltage sensor of potassium channels. *Neuron* **48**, 25–29 (2005).
25. Minor, D. L. Jr. A sensitive channel family replete with sense and motion. *Nature Struct. Mol. Biol.* **13**, 388–390 (2006).

Supplementary Information is linked to the online version of the paper at www.nature.com/nature.

Acknowledgements We thank S. Wiese for valuable technical assistance, S. Chakravarthy for help with PyMOL, H. P. Larsson for advice about fluctuation analysis, V. Yarov-Yarovoy for the PDB coordinates of the ROSETTA model of K_v1.2 and for helpful discussion, and S. Kohout and S. Bell for critical comments on the manuscripts. This work was supported by the National Institutes of Health and by a postdoctoral fellowship from the American Heart Association Western States Affiliate (F.T.). P.G. was supported by postdoctoral fellowships from the Generalitat de Catalunya and the Human Frontier Science Program.

Author Information Reprints and permissions information is available at www.nature.com/reprints. The authors declare no competing financial interests. Correspondence and requests for materials should be addressed to E.I. (ehud@berkeley.edu).

LETTERS

Structure prediction for the down state of a potassium channel voltage sensor

Michael Grabe^{1*†}, Helen C. Lai^{1,2*†}, Monika Jain¹, Yuh Nung Jan¹ & Lily Yeh Jan¹

Voltage-gated potassium (Kv) channels, essential for regulating potassium uptake and cell volume in plants and electrical excitability in animals, switch between conducting and non-conducting states as a result of conformational changes in the four voltage-sensing domains (VSDs) that surround the channel pore¹. This process, known as gating, is initiated by a cluster of positively charged residues on the fourth transmembrane segment (S4) of each VSD, which drives the VSD into a 'down state' at negative voltages and an 'up state' at more positive voltages². The crystal structure of Kv1.2 probably corresponds to the up state³, but the local environment of S4 in the down state and its motion in voltage gating remains unresolved^{4–6}. Here we employed several conditional lethal/second-site suppressor yeast screens to determine the transmembrane packing of the VSD in the down state. This screen relies on the ability of KAT1, a eukaryotic Kv channel, to conduct potassium when its VSDs are in the down state, thereby rescuing potassium-transport-deficient yeast⁷. Starting with KAT1 channels bearing conditional lethal mutations, we identified second-site suppressor mutations throughout the VSD that recover yeast growth. We then constructed a down state model of the channel using six pairs of interacting residues as structural constraints and verified this model by engineering suppressor mutations on the basis of spatial considerations. A comparison of this down state model with the up state Kv1.2 structure suggests that the VSDs undergo large rearrangements during gating, whereas the S4 segment remains positioned between the central pore and the remainder of the VSD in both states.

Kv channels such as Shaker move 12–14 gating charges across the membrane on channel opening⁸—a remarkable feat because the primary role of the membrane is to form a low-dielectric barrier preventing the passage of charged species. It has been proposed that the channel accomplishes this in two ways: first, by surrounding the S4 segment, thus shielding its charges from the lipid bilayer; and second, by moving S4 a large distance through the membrane electric field^{9,10}. Recently, both of these assumptions have been called into question. First, whereas mutation-intolerant patches on the periphery of the pore domain¹¹ indicate close apposition between the pore and VSD (as supported by cross-linking studies^{12–15}), gating models developed from the X-ray crystal structures of KvAP suggest only a loose association between these domains¹⁶. Second, major reorientations of the VSD were revealed by cysteine accessibility experiments showing that a span of 12 S4 residues accessible to the cytoplasm in the down state becomes inaccessible in the up state¹⁷. Unfortunately, this result cannot discern between disparate models in which S4 moves a large distance perpendicular to the membrane (more than 15 Å; refs 5,6) or a small distance (1–2 Å; ref. 4). These studies all involve probes and linkers of dimensions comparable to

the distances being measured. It is therefore desirable to develop alternative approaches to resolve these questions.

Voltage-gated ion channels are highly mobile membrane proteins that require a negative membrane potential to stabilize the down state; this poses a difficult problem for structure determination using X-ray crystallography. Here, we probe structural features of the down state using an *in vivo* yeast screen that relies on the ability of KAT1, a Kv channel from *Arabidopsis thaliana*, to rescue potassium-transporter-deficient yeast by facilitating K⁺ entry into the cell. We chose to use KAT1 rather than Shaker because yeast have an extremely negative membrane potential, –100 to –250 mV (ref. 18), which drives VSDs into the down state, a state compatible with K⁺ conduction for KAT1⁷ but not Shaker. We first identified conditional lethal mutations in KAT1's transmembrane region that destroy the VSDs' ability to adopt the correct down state configuration compatible with channel opening, thus compromising yeast growth on low K⁺ media. Next, we screened libraries of mutant VSDs to search for nearby, complementary suppressor mutations that relieve the initial strain, allowing the channel to open and rescue yeast growth. Seminal work in protein biophysics has shown that suppressor mutations most profoundly recover protein function when they lie in close proximity to the site of the original perturbation¹⁹. Therefore, the identified conditional lethal/second-site suppressor residues, which we call pairs, provide structural information by revealing amino acids that are likely to be in close contact in the down state. Previously, this approach was successfully used to determine the transmembrane packing of the Kir 2.1 potassium channel²⁰, which was later verified by the crystal structure of a bacterial homologue²¹.

In an attempt to map out the packing geometry of a Kv channel in the down state, we first identified conditional lethal mutations in S1 and S4 of the VSD and S5 and S6 of the central pore. We then extensively screened these conditional lethals against three mutagenized libraries of S1–S3, S2–S4 or S4, revealing three conditional lethal/second-site suppressor pairs deep within the transmembrane region (Table 1 and Supplementary Table 1). The charge reversal mutation R171E in S4 is conditionally lethal and robustly suppressed by a corresponding charge mutation in S1, C77R (Fig. 1a). Two other pairs were identified from a screen of channels with mutagenized S2–S4, in which we intentionally introduced a conservative I94V mutation into the S1–S2 linker to aid insertion of the mutant library into KAT1 (Supplementary Discussion and Supplementary Table 2). Acidic substitutions of an invariant tryptophan (W75) in S1 compromised channel function in yeast (Fig. 1b). The suppressor M169L in S4 restores the yeast growth prevented by W75D, whereas another screen with the lethal W75E+I94V identified N99D in S2 as a second-site suppressor (Fig. 1b). Our screen also recovered two additional mutations in linker regions, L115P and Y86H + D89G, which

¹Departments of Physiology and Biochemistry, Howard Hughes Medical Institute, and ²Graduate Group in Biophysics, University of California, San Francisco, California 94143, USA.

[†]Present addresses: Department of Biological Sciences, University of Pittsburgh, Pittsburgh, Pennsylvania 15260, USA (M.G.); Center for Basic Neuroscience, University of Texas Southwestern Medical Center, Dallas, Texas 75390, USA (H.C.L.).

*These authors contributed equally to this work.

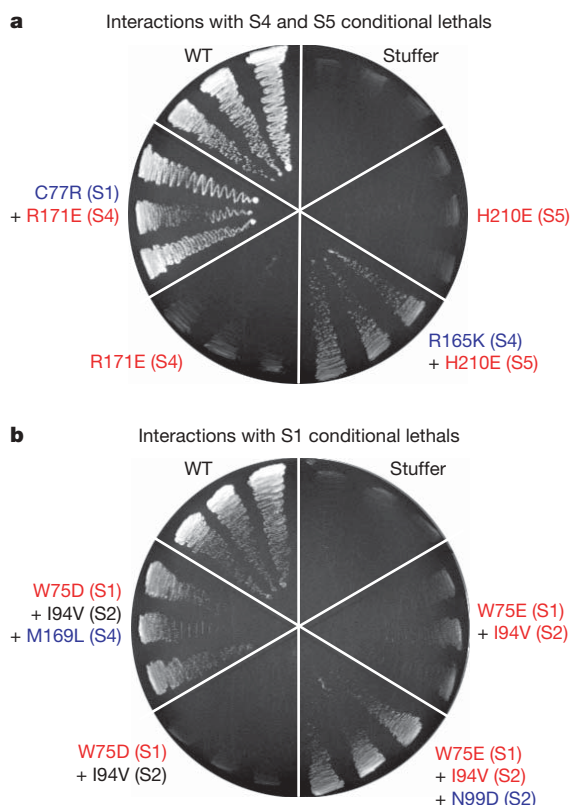
Table 1 | Identified interaction sets and exchange suppressors.

Conditional lethal mutations	Second-site suppressor mutations				
	C77R (S1)	N99D (S2)	R165K (S4)	M169L (S4)	S179N (S4)
W75D (S1)†		+	—	✓	—
W75E + I94V (S1)†		✓	ND	+	ND
R171E (S4)‡	✓	—			
R174E (S4)‡	—	—			
V204E (S5)§	—	—	—	—	✓*
H210E (S5)§	—	—	✓	✓*	—

✓, interacting pair determined from screening; +, growth on low K^+ media; —, no growth; ND, not determined. *, previously identified interactions²; †, ‡ and §, conditional lethal mutations in the same segment. Although M169 in S4 was identified from two different screens, M169L does not suppress V204E, and only leucine at position 169 suppresses H210E or W75D (data not shown). N99D does not suppress the conditional lethal mutations in S4 or S5, thus verifying the specificity of N99D for the W75 site in S1.

suppressed W75E + I94V and R174E, respectively (Supplementary Table 1).

In addition to these three pairs in the transmembrane region, we previously discovered two pairs between S5 and S4 (Table 1)². We carried out directed screens to determine whether the two pairs correspond to one S4 contacting a single S5 segment or two S5 segments of neighbouring subunits. We found that a mutation at the amino-terminal end of S4, R165K, suppresses H210E in S5 (Fig. 1a).

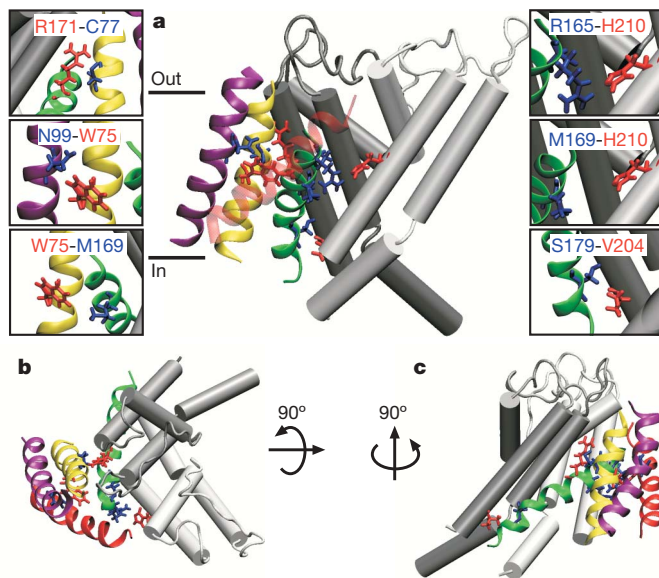
**Figure 1 | Identified conditional lethal and second-site suppressor pairs.**

a, b, Screening revealed three pairs within the transmembrane domain of the channel from random mutagenesis and one from initial directed mutagenesis. Two pairs were identified from KAT1 conditional lethals in S4 and S5 (**a**) and two from conditional lethals in S1 (**b**). Conditional lethals (red throughout) do not support yeast growth on low potassium media (0.4 mM K^+ selective plates), whereas growth is supported by the conditional lethals with their suppressor(s) (blue throughout). The putative transmembrane segment containing the mutation is in parentheses. I94V is black with W75D because it is not required for lethality but is present during screening (see Supplementary Table 2). A KAT1 wild-type positive control and KAT1-stuffer, a non-functional negative control (see Supplementary Methods), are shown.

The physical separation of the S4 suppressors strongly supports the configuration in which S4 makes contact with two S5 segments in the down state (see Supplementary Discussion and Supplementary Fig. 1a). We also conducted control experiments by pairing each suppressor mutation with conditional lethal mutations in neighbouring segments, and we found that suppression was highly specific for the original conditional lethal site (Table 1).

We constructed a down state model of KAT1 using six of our experimentally identified interactions (ticks in Table 1) as structural constraints, in combination with bioinformatic analysis, molecular dynamics and homology modelling as described in the Methods and Supplementary Discussion. This molecular model must obey steric and secondary structural restraints. Moreover, if some of the conditional lethals were to stabilize the up state or intermediate states, rather than destabilizing the down state, it may not be possible to have a model that satisfies our hypothesis—that identified pairs represent residues in close proximity in the down state. Remarkably, a single voltage sensor resulting from this analysis accommodates the close proximity for each conditional lethal/suppressor pair (Fig. 2a). The N-terminal end of S4 contacts S5 (white), presumably of its own subunit, whereas the carboxy-terminal end contacts the S5 (grey) of the neighbouring subunit (Fig. 2). C77–R171, N99–W75, and R165–H210 are all in contact, and the distances between side chains are fairly small: M169–W75, ~2.0 Å; S179–V204, ~1.0 Å; and M169–H210, ~3.5 Å. Thus, although it is possible that the conditional lethal/second-site suppressor interactions occur in more than one state, our model is consistent with the assumption that our experiments are probing a single state of the voltage sensor.

Using the model, we computed the average distance between either of two known conditional lethals in S5—V204E and F207D—and all residues along S4 (Fig. 3a) in an attempt to engineer suppressor mutations. Two residues, S179 and F182, presented themselves as likely suppressor sites for F207D. Screening with random codons at both positions revealed that mutating S179 to histidine suppresses F207D (Fig. 3b), whereas no suppressor mutations were found for

**Figure 2 | A single model is consistent with the experimental data.** **a**, A single VSD is pictured against two central pore subunits (white, same subunit; grey, neighbour). This is one of the top 10% of the 200 models generated as judged by the proximity of the six highlighted conditional lethal/second-site suppressor pairs. All residues are in van der Waals contact or within 1–2 Å, except M169–H210, which fall on opposing helical faces and are 3.5 Å apart. Helices are coloured: S1, yellow; S2, purple; S3, red; and S4, green. Visualization of the helical placement is aided by an extracellular view (**b**) and a rotated side view (**c**).

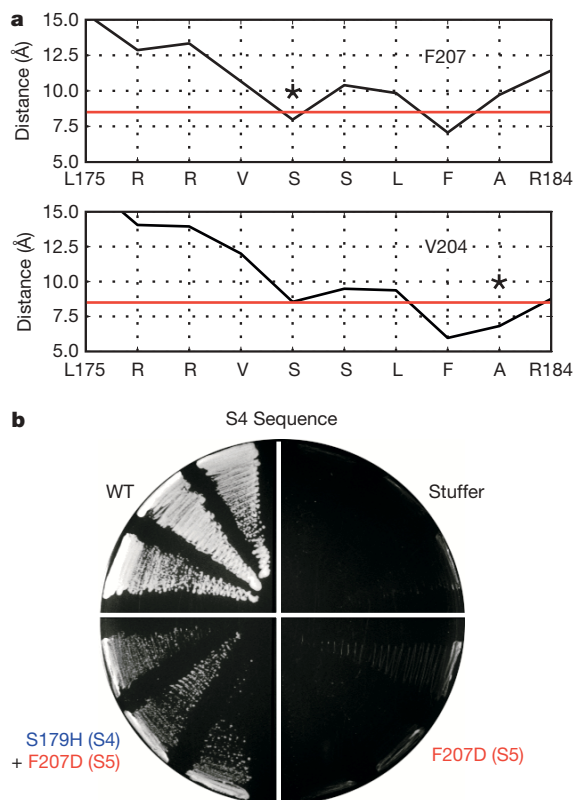


Figure 3 | Verification of the model. **a**, The average $C\alpha$ to $C\alpha$ distances between F207 or V204, both sites of conditional lethals, and all S4 positions were calculated for the top 10% of the models. Residues closer than 8 Å (red line) were screened against the conditional lethal mutations, V204E and F207D, to verify the model. Asterisks indicate sites of suppression. **b**, S179H, identified in **a**, rescues the conditional lethality of F207D on selective K^+ plates. Wild-type and stuffer controls are shown.

F182. Similarly, our model predicts F182 and A183 to be in close proximity to V204, and we found that polar or positively charged mutations (Ser, Asn, Lys or His) at A183 suppress V204E, whereas no suppressor at position F182 was found (data not shown). Therefore, using directed screening that was based on our model, we were able to identify suppressors with a 50% success rate compared with our initial yield of roughly one suppressor for every 10,000 attempts using random mutagenesis. Thus, these experiments provide strong evidence for the soundness of our methodology and reliability of our model.

The model reveals that S4 contacts S5 along one helical face and S1 on the N-terminal half of the opposite face, contrary to models based on KvAP, which propose that S4 has minimal contact with the rest of the channel⁶. Close proximity between S1 and S2 as well as S4 and S2 can be inferred from the shared conditional lethal mutation in S1 (W75) with suppressors in both S2 (N99D) and S4 (M169L). This positioning of S4 between the central pore and the rest of the voltage sensor may reflect energetic considerations of shielding charged residues on S4 from the bilayer²². Although S4 has contact with S1 and S2, the C-terminal end of the S4 helix most probably has significant lipid contact (Fig. 2c). The voltage-sensor segments (S1–S4) form a parallel bundle in the Kv1.2 structure, leaving little room for water to significantly solvate the S4 helix owing to the close, perpendicular packing. In contrast, S4 makes a 57° crossing angle with respect to S1, S2 and the pore axis in our down state model, which reduces the helix–helix packing and leaves portions of S4 exposed to the cytoplasm and extracellular space (Fig. 2 and Supplementary Fig. 2a). It is likely that water penetrates these regions, consistent with increased cysteine accessibility^{17,23} and the ability of mutant VSDs to permeate ions in the down state^{24,25}.

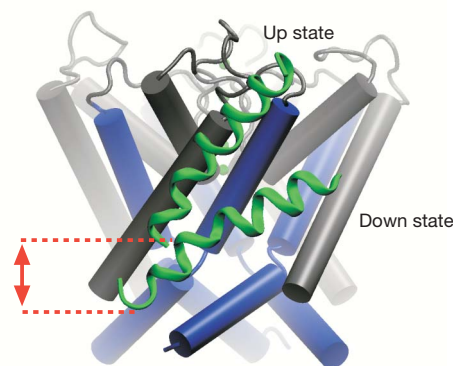


Figure 4 | The extent of S4 movement during voltage gating. The S4 segment is pictured in the down state with the up state (based on the Kv1.2 structure) superimposed. Dashed lines indicate the extent of the movement of the C-terminal end. The inner helices (S6) of the central pore are blue, and the S5 segments are grey.

Comparing our down state model with the Kv1.2 structure reveals that the N-terminal end of S4 moves 12–15 Å perpendicular to the membrane, which is in agreement with recent biotin–avidin experiments⁵ (see Supplementary Movie). Electrostatic calculations using the Shaker sequence predict that this motion transfers 10–12 charges, similar to experimental measurements⁸ (see Supplementary Discussion and Supplementary Fig. 2b). How does this movement gate the channel? As S4 transits to the down state, its C-terminal end descends vertically (Fig. 4), forcing the S4–S5 linker (not shown) down to a position where its interaction with the inner pore helix (S6) closes the Kv1.2 channel²⁶. How can similar motions of the voltage sensors bring about the opposite gating of KAT1 (a hyperpolarization-activated channel) and Shaker (a depolarization-activated channel)? The Kv1.2 structure reveals several hydrophobic interactions between the S4–S5 linker and the S6 segment²⁶; however, KAT1 is highly polar in this region, suggesting that coupling may be electrostatic (see Supplementary Discussion and Supplementary Figs 3 and 4). The voltage sensor movements suggested here should help in understanding how such fundamental differences in coupling might account for the opposite gating of hyperpolarization- and depolarization-activated channels.

METHODS

Molecular biology and library construction. Yeast screens and selection were carried out as previously described². Detailed methods are described in Supplementary Information.

Model construction. We used Modeller8v0 (ref. 27) to construct an open state model of the KAT1 pore region using the Kv1.2 crystal structure. We repeated this process for the four transmembrane segments S1–S4 without the loop regions. Initial structures were generated by randomly positioning S1–S4 away from the central pore with the helices ordered as in the Kv1.2 structure. Several sets of force restraints were then placed on the initial, randomized structure, including restraints between identified pairs from our screens. Molecular dynamics simulations using NAMD 2.5 (ref. 28) were performed, allowing the protein complex to pack together. This was followed by minimization of the entire system. We repeated this process 200 times, and the model presented in the text is one of the top 10% of models ranked according to the spatial satisfaction of the experimental constraints. The orientation of S4 is very similar among the models in the top 10%.

Received 29 September; accepted 29 November 2006.
Published online 24 December 2006.

1. Hille, B. *Ion channels of excitable membranes*, 3rd edn (Sinauer, Sunderland, Massachusetts, 2001).
2. Lai, H. C., Grabe, M., Jan, Y. N. & Jan, L. Y. The S4 voltage sensor packs against the pore domain in the KAT1 voltage-gated potassium channel. *Neuron* **47**, 395–406 (2005).
3. Long, S. B., Campbell, E. B. & Mackinnon, R. Crystal structure of a mammalian voltage-dependent Shaker family K^+ channel. *Science* **309**, 897–903 (2005).

4. Posson, D. J., Ge, P., Miller, C., Bezanilla, F. & Selvin, P. R. Small vertical movement of a K⁺ channel voltage sensor measured with luminescence energy transfer. *Nature* **436**, 848–851 (2005).
5. Ruta, V., Chen, J. & Mackinnon, R. Calibrated measurement of gating-charge arginine displacement in the KvAP voltage-dependent K⁺ channel. *Cell* **123**, 463–475 (2005).
6. Jiang, Y., Ruta, V., Chen, J., Lee, A. & MacKinnon, R. The principle of gating charge movement in a voltage-dependent K⁺ channel. *Nature* **423**, 42–48 (2003).
7. Anderson, J. A., Huprikar, S. S., Kochian, L. V., Lucas, W. J. & Gaber, R. F. Functional expression of a probable *Arabidopsis thaliana* potassium channel in *Saccharomyces cerevisiae*. *Proc. Natl Acad. Sci. USA* **89**, 3736–3740 (1992).
8. Schoppa, N. E., McCormack, K., Tanouye, M. A. & Sigworth, F. J. The size of gating charge in wild-type and mutant Shaker potassium channels. *Science* **255**, 1712–1715 (1992).
9. Catterall, W. A. Molecular properties of voltage-sensitive sodium channels. *Annu. Rev. Biochem.* **55**, 953–985 (1986).
10. Guy, H. R. & Seetharamulu, P. Molecular model of the action potential sodium channel. *Proc. Natl Acad. Sci. USA* **83**, 508–512 (1986).
11. Li-Smerin, Y., Hackos, D. H. & Swartz, K. J. A localized interaction surface for voltage-sensing domains on the pore domain of a K⁺ channel. *Neuron* **25**, 411–423 (2000).
12. Gandhi, C. S., Clark, E., Loots, E., Pralle, A. & Isacoff, E. Y. The orientation and molecular movement of a K⁺ channel voltage-sensing domain. *Neuron* **40**, 515–525 (2003).
13. Laine, M. *et al.* Atomic proximity between S4 segment and pore domain in Shaker potassium channels. *Neuron* **39**, 467–481 (2003).
14. Neale, E. J., Elliott, D. J., Hunter, M. & Sivaprasadarao, A. Evidence for intersubunit interactions between S4 and S5 transmembrane segments of the Shaker potassium channel. *J. Biol. Chem.* **278**, 29079–29085 (2003).
15. Broomand, A., Mannikko, R., Larsson, H. P. & Elinder, F. Molecular movement of the voltage sensor in a K channel. *J. Gen. Physiol.* **122**, 741–748 (2003).
16. Jiang, Y. *et al.* X-ray structure of a voltage-dependent K⁺ channel. *Nature* **423**, 33–41 (2003).
17. Baker, O. S., Larsson, H. P., Mannuzzu, L. M. & Isacoff, E. Y. Three transmembrane conformations and sequence-dependent displacement of the S4 domain in Shaker K⁺ channel gating. *Neuron* **20**, 1283–1294 (1998).
18. Serrano, R. & Rodriguez-Navarro, A. Ion homeostasis during salt stress in plants. *Curr. Opin. Cell Biol.* **13**, 399–404 (2001).
19. Schreiber, G. & Fersht, A. R. Energetics of protein–protein interactions: analysis of the Barnase–Barstar interface by single mutations and double mutant cycles. *J. Mol. Biol.* **248**, 478–486 (1995).
20. Minor, D. L. Jr, Masseling, S. J., Jan, Y. N. & Jan, L. Y. Transmembrane structure of an inwardly rectifying potassium channel. *Cell* **96**, 879–891 (1999).
21. Kuo, A. *et al.* Crystal structure of the potassium channel KirBac1.1 in the closed state. *Science* **300**, 1922–1926 (2003).
22. Grabe, M., Lecar, H., Jan, Y. N. & Jan, L. Y. A quantitative assessment of models for voltage-dependent gating of ion channels. *Proc. Natl Acad. Sci. USA* **101**, 17640–17645 (2004).
23. Latorre, R. *et al.* Molecular coupling between voltage sensor and pore opening in the *Arabidopsis* inward rectifier K⁺ channel KAT1. *J. Gen. Physiol.* **122**, 459–469 (2003).
24. Starace, D. M. & Bezanilla, F. A proton pore in a potassium channel voltage sensor reveals a focused electric field. *Nature* **427**, 548–553 (2004).
25. Tombola, F., Pathak, M. M. & Isacoff, E. Y. Voltage-sensing arginines in a potassium channel permeate and occlude cation-selective pores. *Neuron* **45**, 379–388 (2005).
26. Long, S. B., Campbell, E. B. & MacKinnon, R. Voltage sensor of Kv1.2: structural basis of electromechanical coupling. *Science* **309**, 903–908 (2005).
27. Sali, A. & Blundell, T. L. Comparative protein modelling by satisfaction of spatial restraints. *J. Mol. Biol.* **234**, 779–815 (1993).
28. Kale, L. *et al.* NAMD2: greater scalability for parallel molecular dynamics. *J. Comput. Phys.* **151**, 283–312 (1999).

Supplementary Information is linked to the online version of the paper at www.nature.com/nature.

Acknowledgements We thank J. Schroeder for the KAT1 construct; S. Kurtz for providing the yeast strain; D. Minor for experimental guidance; W. Zhou for experimental assistance; A. Fay, F. Haass and S. Nayak for critically reading the manuscript; and members of the Jan Laboratory and B. Tu for their support, advice and input at all stages of this project. This work was supported by a National Science Foundation Interdisciplinary Informatics Fellowship (M.G.), an American Heart Association Pre-doctoral Fellowship (H.C.L.), an NIH Structural Biology Training grant (H.C.L.), and an R01 grant from the NIMH. Y.N.J. and L.Y.J. are HHMI investigators.

Author Contributions M.G. carried out all the computational aspects of this project and H.C.L. performed the yeast screens assisted by M.J. The project was a collaborative effort through iterative cycles of experiment and computational model building. All authors discussed the results and commented on the manuscript.

Author Information Reprints and permissions information is available at www.nature.com/reprints. The authors declare no competing financial interests. Correspondence and requests for materials should be addressed to L.Y.J. (lily.jan@ucsf.edu).

LETTERS

***bicoid* RNA localization requires specific binding of an endosomal sorting complex**Uwe Irion^{1†} & Daniel St Johnston¹

bicoid messenger RNA localizes to the anterior of the *Drosophila* egg, where it is translated to form a morphogen gradient of Bicoid protein that patterns the head and thorax of the embryo. Although *bicoid* was the first localized cytoplasmic determinant to be identified^{1–4}, little is known about how the mRNA is coupled to the microtubule-dependent transport pathway that targets it to the anterior, and it has been proposed that the mRNA is recognized by a complex of many redundant proteins, each of which binds to the localization element in the 3' untranslated region (UTR) with little or no specificity⁵. Indeed, the only known RNA-binding protein that co-localizes with *bicoid* mRNA is Staufen, which binds non-specifically to double-stranded RNA *in vitro*^{6,7}. Here we show that mutants in all subunits of the ESCRT-II complex (VPS22, VPS25 and VPS36) abolish the final Staufen-dependent step in *bicoid* mRNA localization. ESCRT-II is a highly conserved component of the pathway that sorts ubiquitinated endosomal proteins into internal vesicles^{8,9}, and functions as a tumour-suppressor by removing activated receptors from the cytoplasm^{10,11}. However, the role of ESCRT-II in *bicoid* localization seems to be independent of endosomal sorting, because mutations in ESCRT-I and III components do not affect the targeting of *bicoid* mRNA. Instead, VPS36 functions by binding directly and specifically to stem-loop V of the *bicoid* 3' UTR through its amino-terminal GLUE domain¹², making it the first example of a sequence-specific RNA-binding protein that recognizes the *bicoid* localization signal. Furthermore, VPS36 localizes to the anterior of the oocyte in a *bicoid*-mRNA-dependent manner, and is required for the subsequent recruitment of Staufen to the *bicoid* complex. This function of ESCRT-II as an RNA-binding complex is conserved in vertebrates and may clarify some of its roles that are independent of endosomal sorting.

Genetic screens for mutations that disrupt anterior–posterior patterning of the *Drosophila melanogaster* embryo have identified a few genes that are required at different stages for the anterior localization of *bicoid* mRNA, but most of these seem to have an indirect role in the process. Mutations in *exuperantia* (*exu*) abolish all stages of *bicoid* mRNA localization^{13,14}, but the function is unclear, because Exu protein is a component of a translational repression complex that co-purifies with *oskar* mRNA, but not with *bicoid* itself⁵. Swallow, γ -Tubulin37C, Dgrip75, Dgrip128 and Minispindles are necessary for the localization of *bicoid* mRNA from stage 10B of oogenesis onwards, and function to nucleate anterior microtubules that direct localization at this stage^{16–18}. Finally, Staufen is required for *bicoid* mRNA localization at the end of oogenesis and in the early embryo^{19,20}. Unlike the other *trans*-acting factors, Staufen is a dsRNA-binding protein, and associates with *bicoid* mRNA at the oocyte anterior from stage 10B onwards⁶.

bicoid mRNA is localized by distinct and partially redundant mechanisms at different stages of oogenesis, which may explain

why genetic screens have missed many of the essential *trans*-acting factors. In mutants that disrupt only early localization, the localization of the mRNA in late oocytes can rescue anterior development, whereas mutants that disrupt only late localization result in a gradient of mRNA that induces some anterior patterning, unless *bicoid* translation is also impaired^{21–23}. To circumvent this problem, we performed a direct visual screen in germline clones for mutants that alter the localization of *bicoid* mRNA in living oocytes using GFP–Staufen as a marker²⁴. This screen identified one complementation group, called *larsen*, that is required for the anterior localization of *bicoid* mRNA. GFP–Staufen fails to localize to the anterior cortex of the oocyte in homozygous germline clones of both *larsen* alleles (Fig. 1a, b, d, e), whereas its posterior localization with *oskar* mRNA is unaffected. The stronger allele, *lsn*^{5F3–8}, is homozygous lethal, and females with a homozygous mutant germ line do not lay eggs. However, the weaker allele, *lsn*^{2B6–3}, is only semi-lethal, and mutant germline clones result in eggs in which *bicoid* mRNA forms a gradient across the anterior half of the embryo (Fig. 1f)—a phenotype very similar to that seen for *staufen* mutants⁶.

Both *larsen* alleles correspond to mutations in the highly conserved protein, VPS22 (Supplementary Fig. 1). VPS22, together with VPS25 and VPS36, forms ESCRT-II (endosomal sorting complex required for transport), one of four complexes (the VPS27/HRS complex, ESCRT-I, -II and -III) that act in a linear pathway to sort mono-ubiquitinated transmembrane proteins within the endosomal compartment into internal vesicles, leading to the formation of multivesicular bodies^{9,25}. Mutants in *Drosophila* ESCRT-I and ESCRT-II components have been shown to cause a tumorous phenotype, because activated receptors accumulate on endosomes, rather than being removed from the cytoplasm and degraded^{10,11,26}. Mammalian ESCRT-II was independently identified as a complex that binds to the RNA polymerase II elongation factor, ELL^{27,28}, whereas the fission yeast VPS22/Larsen homologue regulates the expression of centriolar proteins during meiosis²⁹. However, the relationship between these functions and endosomal protein sorting remains unclear.

To test whether the role in *bicoid* mRNA localization is specific for Larsen/VPS22 or whether the whole ESCRT-II is involved in the process, we examined mutants in the other two components of this complex, *vps25* and *vps36*. Homozygous germline clones of *vps25*^{Pb2931} and *vps36*^{L5212} show an identical phenotype to *lsn*^{5F3–8}: GFP–Stau does not localize to the anterior of the oocyte (Fig. 1g–j), and the flies do not lay eggs. We therefore tested whether other multivesicular-body-sorting mutants also disrupt *bicoid* mRNA localization. However, *bicoid* mRNA localizes normally in germline clones that are mutant for *hrs* (*vps27*), the ESCRT-I components *vps28* and *erupted* (*ept*), and the ESCRT-III component *vps32* (Fig. 2c–f). Thus, the ESCRT pathway seems to be dispensable for *bicoid* mRNA localization, indicating that ESCRT-II has another

¹Wellcome Trust/Cancer Research UK Gurdon Institute and Department of Genetics, University of Cambridge, Tennis Court Road, Cambridge CB2 1QN, UK. †Present address: Max-Planck-Institut für Entwicklungsbiologie, Spemannstraße 35, 72076 Tübingen, Germany.

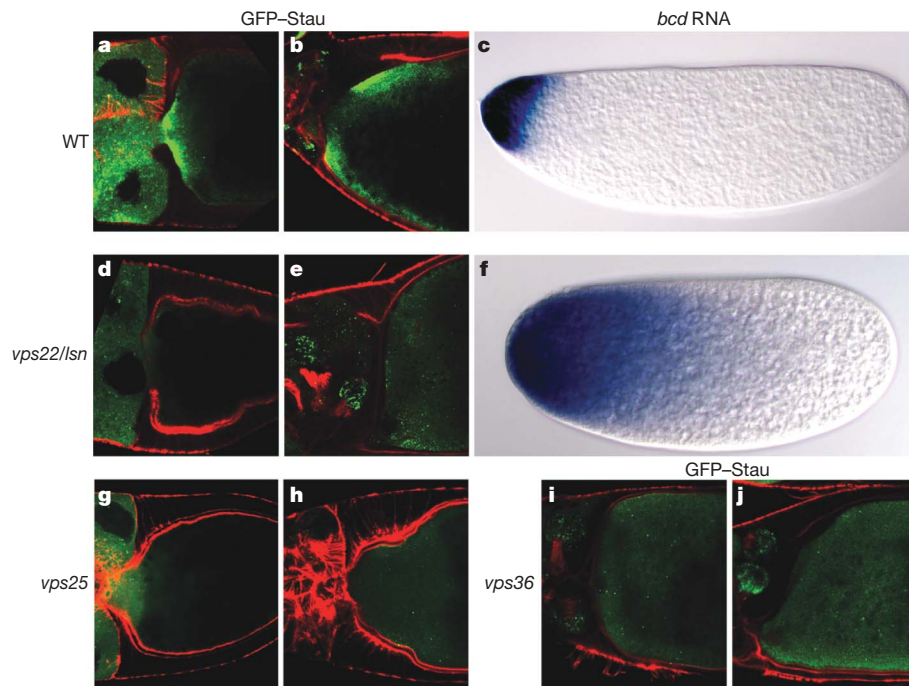


Figure 1 | Mutations in *lsn* and *vps36* disrupt the anterior localization of GFP-Staufen and *bicoid* mRNA. **a, b**, GFP-Staufen (Stau) (green) localization to the anterior cortex of wild-type stage 11 (**a**) or stage 13 (**b**) oocytes. The actin cortex is labelled with rhodamine-phalloidin (red). **c**, *bicoid* (*bcd*) mRNA localization in a freshly laid wild-type egg. **d, e**, Homozygous *vps22/lsn* germline clones, showing the absence of GFP-Stau at the anterior pole of the oocyte at stage 10B (**d**) or stage 13

(**e**). **f, g**, *bcd* mRNA localization in an embryo derived from a *vps22/lsn* germline clone. **g, h**, Homozygous *vps25*^{Pb2931} germline clones, showing the absence of GFP-Stau at the anterior pole of the oocyte at stage 10B (**g**) or stage 13 (**h**). **i, j**, Homozygous *vps36* (*l(3)l5212*) germline clones, showing the absence of GFP-Stau at the anterior pole of the oocyte at stage 11 (**i**) or stage 13 (**j**).

function in addition to the sorting of ubiquitinated proteins into multivesicular bodies.

Given the role of ESCRT-II in *bicoid* mRNA localization, we tested whether any of the proteins of the complex interact with the *bicoid* localization signal, using a yeast three-hybrid assay³⁰. Both Staufen and VPS36, but not VPS22 or VPS25, interact with the *bicoid* 3' UTR

in this assay, resulting in growth of the yeast cells on plates lacking histidine and in the expression of α -galactosidase (Fig. 3a). To determine whether VPS36 protein binds directly to *bicoid* RNA, we performed an ultraviolet (UV) radiation cross-linking assay with purified recombinant VPS36 and *in vitro* transcribed *bicoid* 3' UTR. VPS36 cross-links efficiently to the *bicoid* 3' UTR in this assay,

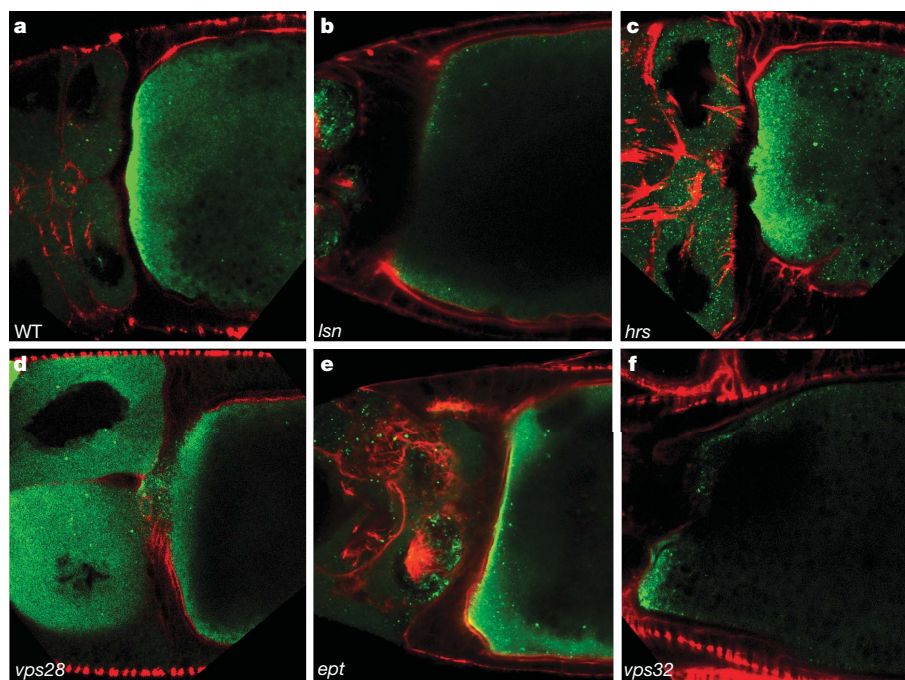
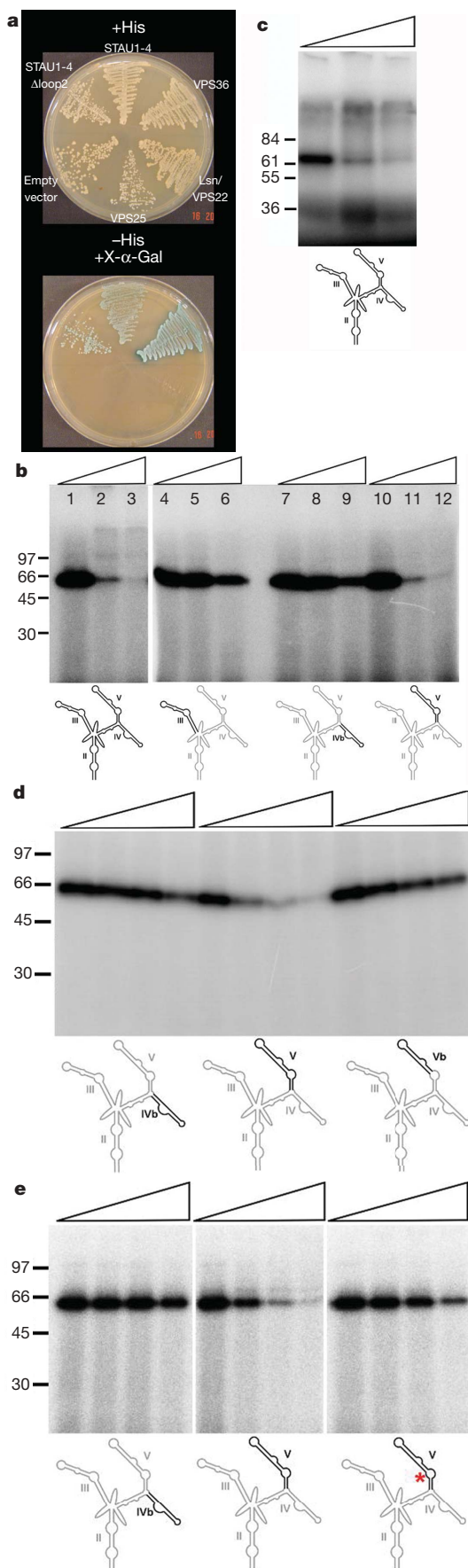


Figure 2 | Localization of GFP-Staufen in oocytes mutant for different ESCRT components. **a**, The anterior localization of GFP-Stau in a wild-type stage

11 oocyte. **b–f**, GFP-Stau localization in *lsn*^{2B6-3} (**b**), *hrs*^{D28} (**c**), *vps28* (*l(2)k16503*) (**d**), *ept*^{P26} (**e**) and *vps32* (*KG01481*) (**f**) germline clones.



indicating that it contacts single-stranded regions of the RNA directly (Fig. 3b). Furthermore, this interaction is specific, because the binding is competed by excess unlabelled *bicoid* 3' UTR, but not by control RNAs (Fig. 3b, d, e and data not shown). Given the high degree of conservation of ESCRT-II, we tested whether *Xenopus laevis* VPS36 also interacts with the mRNA, and found that its N-terminal GLUE domain¹² binds specifically to the *bicoid* 3' UTR, indicating that the RNA-binding activity of VPS36 is conserved in vertebrates (Fig. 3c).

To map the binding site within the mRNA more precisely, we tested the ability of single stem-loops of the *bicoid* 3' UTR to compete for binding to VPS36. Stem-loop V competed as well as the full-length 3' UTR, whereas stem-loops III, IVb and the distal part of stem-loop V did not compete (Fig. 3b, d). We then performed a random mutagenesis to map the VPS36 binding site within stem-loop V, and found that none of the distal mutations affects the interaction, whereas three base changes in the proximal stem and the central loop-region strongly reduce VPS36 binding (Fig. 3e and Supplementary Fig. 2). Thus, VPS36 binds specifically to the proximal part of stem-loop V, and recognizes specific bases, most probably in the context of the RNA structure of this region.

We next examined whether VPS36 associates with *bicoid* mRNA *in vivo* by generating transgenic flies expressing YFP-VPS36 under the control of its endogenous promoter. YFP-VPS36 is ubiquitously expressed in the ovary, and shows a general cytoplasmic localization with some clouds in the nurse cells (Fig. 4a). From stage 10B/11 of oogenesis, the protein localizes to the anterior cortex of the oocyte in the same region as *bicoid* mRNA (Fig. 4b, c). This anterior accumulation is abolished in *exu* mutants, which block *bicoid* mRNA localization at an earlier stage (Fig. 4d), and in *sryδ* mutants, in which *bicoid* RNA is not transcribed (Fig. 4e). Thus, VPS36 co-localizes with *bicoid* mRNA at the anterior, and this localization is *bicoid* mRNA-dependent, indicating that the protein binds directly to the RNA *in vivo*, as it does *in vitro*.

Both ESCRT-II and Staufin are recruited to *bicoid* mRNA at stage 10B, and are then required for its localization during the final stages of oogenesis. *staufer* mutants have no effect on the anterior recruitment of VPS36 (Fig. 4f), whereas mutants in *larsen/vps22* and *vps36* abolish the anterior recruitment of Staufin protein at this stage (Figs 1 and 2). ESCRT-II therefore binds to *bicoid* mRNA independently of Staufin, and is required for the subsequent recruitment of the latter to form a functional *bicoid* mRNA localization complex.

Figure 3 | VPS36 binds specifically to stem-loop V of the *bicoid* 3' UTR.

a, Three-hybrid assay using the full-length *bcd* 3' UTR as an RNA bait. Growth on media lacking histidine and α -galactosidase activity (blue staining) indicates an interaction between the protein and the RNA. VPS36 interacts with *bcd* RNA in this assay, as does the region of Staufin containing the first four dsRNA-binding domains with or without the insert in dsRBD2 (Δ loop2). In contrast, Lsn/VPS22 and VPS25 show no interaction. **b–e**, UV cross-linking assay using purified recombinant *Drosophila* VPS36 protein or the purified GST-GLUE domain from *Xenopus* VPS36 (**c**) and full-length ³²P-labelled *bcd* 3' UTR as a probe. **b**, VPS36 binding to the full-length 3' UTR in the presence of increasing amounts of competitor RNA (first lane, no competitor; second lane, 10-fold excess; third lane, 100-fold excess). The binding of VPS36 is inhibited by an excess of the full-length 3' UTR (lanes 1–3) and stem-loop V (lanes 10–12), but not by stem-loops III or IVb (lanes 4–9). **c**, The *Xenopus* GLUE domain can be cross-linked to the *bcd* 3' UTR (first lane, no competitor; second lane, 10-fold excess; third lane, 100-fold excess). **d**, The distal region of stem-loop V does not compete for VPS36 binding (lanes 9–12), indicating that the binding site must include part of the proximal region (lanes 1, 5 and 9, no competitor; lanes 2, 6 and 10, equal amount; lanes 3, 7 and 11, 5-fold excess; lanes 4, 8 and 12, 25-fold excess). **e**, Stem-loop V carrying three base changes in the central loop region shows an impaired ability to compete for VPS 36 binding. The probe is stem-loop V, and the competitors are stem-loop IVb, stem-loop V, and stem-loop V with the following three mutations: 419 A→G, 427 A→C, 428 C→A (numbering starts with the first nucleotide after the Stop codon, see Supplementary Fig. 2).

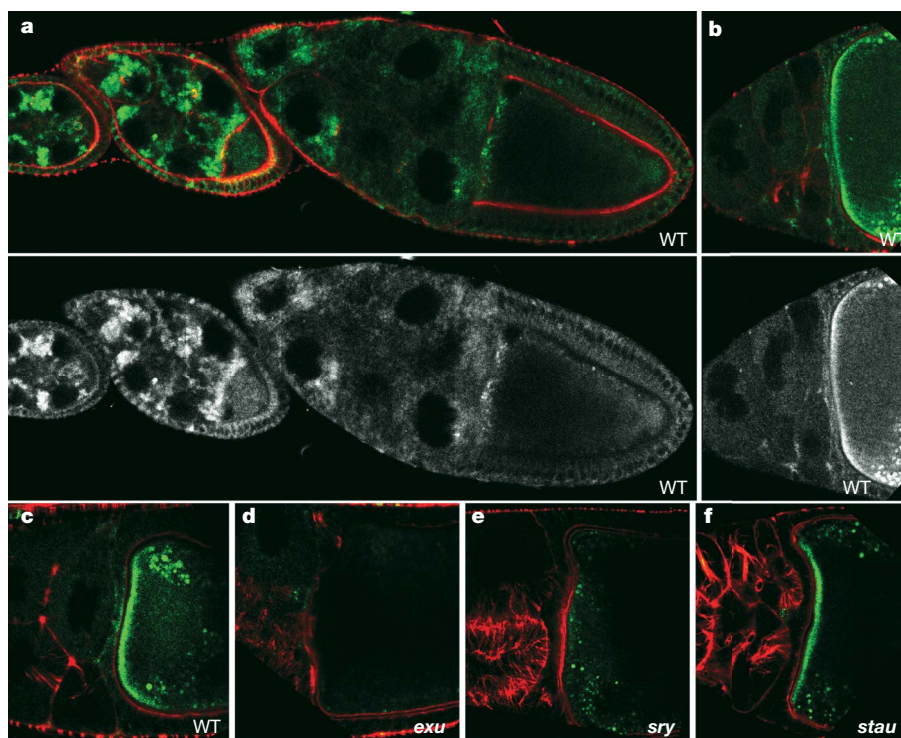


Figure 4 | VPS36 is recruited to the anterior of the oocyte by *bicoid* mRNA.

a–f, Expression of a YFP–VPS36 fusion protein (green) under the control of the endogenous *vps36* promoter. **a**, VPS36 is expressed in both the germ line and the somatic follicle cells of the ovary. The actin cytoskeleton has been counter-stained in red with rhodamine–phalloidin (the bottom panel shows the YFP channel alone). The protein shows a uniform distribution in the cytoplasm of the oocyte and the follicle cells, with a patchy distribution in the nurse cells, which becomes more dispersed as oogenesis progresses. At stage 10B, VPS36 begins to accumulate at the anterior pole of the oocyte. **b**, Close-

up of the anterior of a stage 11 egg chamber, showing the strong enrichment of VPS36 at the anterior cortex. The green spheres in the oocyte cytoplasm here and in **d** and **e** are not due to YFP–VPS36, but the background autofluorescence of yolk granules at late stages. **c–f**, Localization of YFP–VPS36 at stage 11 in wild type (**c**), *exu*^{VL}/*exu*^{SC} (**d**), *sry*- δ^{14} /*Df*(3R)X3F,P[ry⁺,*sry*DB56] (**e**), and homozygous *stau*^{D3} (**f**) oocytes. The fusion protein does not localize to the anterior cortex in *exu* mutants, which disrupt all stages of *bicoid* mRNA localization, or in *sry* mutants, which prevent *bicoid* transcription, but localizes normally in *stau* mutants.

Our results demonstrate that ESCRT-II is required for the anterior localization of *bicoid* mRNA, and is a sequence-specific RNA-binding complex that recognizes the *bicoid* localization signal. This activity of ESCRT-II seems to be independent of its well-characterized role in endosomal protein sorting, and is conserved (*Xenopus* VPS36 also interacts specifically with the *bicoid* 3' UTR), indicating that ESCRT-II may have a role in mRNA localization in vertebrates. In future, it will be important to determine whether this conserved RNA-binding activity of ESCRT-II plays any part in endosomal trafficking, or in the other proposed functions of the complex in transcription elongation and the regulation of centriole assembly.

METHODS

A more detailed description of the materials and methods used can be found in Supplementary Information.

Drosophila genetics. Flies were grown under standard conditions on corn-meal medium. Germline clones were induced using the autosomal Dominant Female Sterile technique. For detailed information and the genotypes of the flies used see Supplementary Information.

Yeast three-hybrid assay. For the yeast three-hybrid assay we used the system that is based on the transcription factor GAL 4 and the RNA binding protein RevM10 from HIV-1, as well as its binding element (Rev responsive element, RRE)³⁰.

UV cross-linking. The purified proteins were pre-incubated with the competitor RNAs for 20 min at room temperature in cross-linking buffer (PBS + 5% glycerol, 2 mM DTT, 0.2% NP-40, 100 μ g ml⁻¹ heparin and 100 μ g ml⁻¹ tRNA). After addition of the probe and a further 20 min of incubation the cross-linking was performed using a 'Stratalinker 1800' at maximum power for 5 min. The samples were treated with RNaseA (0.5 μ g ml⁻¹) for 1 h at 37 °C and after SDS–polyacrylamide gel electrophoresis the radioactivity was visualized using a phosphorimager.

Staining and microscopy. Staining was performed as described²⁴. Pictures were taken using a BioRad 1024 Confocal Microscope and processed with Adobe Photoshop.

Received 20 October; accepted 1 December 2006.

1. Frohnhofer, H. G. & Nüsslein-Volhard, C. Organization of anterior pattern in the *Drosophila* embryo by the maternal gene *bicoid*. *Nature* **324**, 120–125 (1986).
2. Berleth, T. *et al.* The role of localization of *bicoid* RNA in organizing the anterior pattern of the *Drosophila* embryo. *EMBO J.* **7**, 1749–1756 (1988).
3. Driever, W. & Nüsslein-Volhard, C. A gradient of Bicoid protein in *Drosophila* embryos. *Cell* **54**, 83–93 (1988).
4. Driever, W. & Nüsslein-Volhard, C. The Bicoid protein determines position in the *Drosophila* embryo in a concentration-dependent manner. *Cell* **54**, 95–104 (1988).
5. Arn, E. A., Cha, B. J., Theurkauf, W. E. & Macdonald, P. M. Recognition of a *bicoid* mRNA localization signal by a protein complex containing Swallow, Nod, and RNA binding proteins. *Dev. Cell* **4**, 41–51 (2003).
6. St Johnston, D., Beuchle, D. & Nüsslein-Volhard, C. *staufer*, a gene required to localize maternal RNAs in the *Drosophila* egg. *Cell* **66**, 51–63 (1991).
7. Ramos, A. *et al.* RNA recognition by a Staufen double-stranded RNA-binding domain. *EMBO J.* **19**, 997–1009 (2000).
8. Babst, M. A protein's final ESCRT. *Traffic* **6**, 2–9 (2005).
9. Babst, M., Katzmam, D. J., Snyder, W. B., Wendland, B. & Emr, S. D. Endosome-associated complex, ESCRT-II, recruits transport machinery for protein sorting at the multivesicular body. *Dev. Cell* **3**, 283–289 (2002).
10. Vaccari, T. & Bilder, D. The *Drosophila* tumor suppressor *vps25* prevents nonautonomous overproliferation by regulating Notch trafficking. *Dev. Cell* **9**, 687–698 (2005).
11. Thompson, B. J. *et al.* Tumor suppressor properties of the ESCRT-II complex component Vps25 in *Drosophila*. *Dev. Cell* **9**, 711–720 (2005).
12. Teo, H. *et al.* ESCRT-I core and ESCRT-II GLUE domain structures reveal role for GLUE in linking to ESCRT-I and membranes. *Cell* **125**, 99–111 (2006).
13. Frohnhofer, H. G. & Nüsslein-Volhard, C. Maternal genes required for the anterior localization of *bicoid* activity in the embryo of *Drosophila*. *Genes Dev.* **1**, 880–890 (1987).

14. Macdonald, P. M., Luk, S. K. & Kilpatrick, M. Protein encoded by the *exuperantia* gene is concentrated at sites of *bicoid* mRNA accumulation in *Drosophila* nurse cells but not in oocytes or embryos. *Genes Dev.* **5**, 2455–2466 (1991).
15. Wilhelm, J. E. et al. Isolation of a ribonucleoprotein complex involved in mRNA localization in *Drosophila* oocytes. *J. Cell Biol.* **148**, 427–440 (2000).
16. Theurkauf, W. E. & Hazelrigg, T. I. *In vivo* analyses of cytoplasmic transport and cytoskeletal organization during *Drosophila* oogenesis: characterization of a multi-step anterior localization pathway. *Development* **125**, 3655–3666 (1998).
17. Moon, W. & Hazelrigg, T. The *Drosophila* microtubule-associated protein Mini spindles is required for cytoplasmic microtubules in oogenesis. *Curr. Biol.* **14**, 1957–1961 (2004).
18. Vogt, N., Koch, I., Schwarz, H., Schnorrer, F. & Nüsslein-Volhard, C. The γ TuRC components Grip75 and Grip128 have an essential microtubule-anchoring function in the *Drosophila* germline. *Development* **133**, 3963–3972 (2006).
19. Ferrandon, D., Elphick, L., Nüsslein-Volhard, C. & St Johnston, D. Staufén protein associates with the 3'UTR of *bicoid* mRNA to form particles that move in a microtubule-dependent manner. *Cell* **79**, 1221–1232 (1994).
20. Weil, T. T., Forrest, K. M. & Gavis, E. R. Localization of *bicoid* mRNA in late oocytes is maintained by continual active transport. *Dev. Cell* **11**, 251–262 (2006).
21. St Johnston, D., Driever, W., Berleth, T., Richstein, S. & Nüsslein-Volhard, C. Multiple steps in the localization of *bicoid* RNA to the anterior pole of the *Drosophila* oocyte. *Development* **107** (Suppl.), 13–19 (1989).
22. Macdonald, P. M., Kerr, K., Smith, J. L. & Leask, A. RNA regulatory element BLE1 directs the early steps of *bicoid* mRNA localization. *Development* **118**, 1233–1243 (1993).
23. Micklem, D. R., Adams, J., Grunert, S. & St Johnston, D. Distinct roles of two conserved Staufén domains in *oskar* mRNA localization and translation. *EMBO J.* **19**, 1366–1377 (2000).
24. Martin, S. G., Leclerc, V., Smith-Litière, K. & St Johnston, D. The identification of novel genes required for *Drosophila* anteroposterior axis formation in a germline clone screen using GFP-Staufén. *Development* **130**, 4201–4215 (2003).
25. Teo, H., Perisic, O., Gonzalez, B. & Williams, R. L. ESCRT-II, an endosome-associated complex required for protein sorting: crystal structure and interactions with ESCRT-III and membranes. *Dev. Cell* **7**, 559–569 (2004).
26. Moberg, K. H., Schelble, S., Burdick, S. K. & Hariharan, I. K. Mutations in *erupted*, the *Drosophila* ortholog of mammalian Tumor Susceptibility Gene 101, elicit non-cell-autonomous overgrowth. *Dev. Cell* **9**, 699–710 (2005).
27. Kamura, T. et al. Cloning and characterization of ELL-associated proteins EAP45 and EAP20. A role for yeast EAP-like proteins in regulation of gene expression by glucose. *J. Biol. Chem.* **276**, 16528–16533 (2001).
28. Schmidt, A. E., Miller, T., Schmidt, S. L., Shiekhatair, R. & Shilatifard, A. Cloning and characterization of the EAP30 subunit of the ELL complex that confers derepression of transcription by RNA polymerase II. *J. Biol. Chem.* **274**, 21981–21985 (1999).
29. Jin, Y., Mancuso, J. J., Uzawa, S., Cronembold, D. & Cande, W. Z. The fission yeast homolog of the human transcription factor EAP30 blocks meiotic spindle pole body amplification. *Dev. Cell* **9**, 63–73 (2005).
30. Putz, U., Skehel, P. & Kuhl, D. A tri-hybrid system for the analysis and detection of RNA–protein interactions. *Nucleic Acids Res.* **24**, 4838–4840 (1996).

Supplementary Information is linked to the online version of the paper at www.nature.com/nature.

Acknowledgements We are very grateful to R. Williams, O. Perisic and H. Teo for giving us the purified recombinant *Xenopus laevis* VPS36 GLUE domain, and for their helpful advice on ESCRT-II. We thank J. Oberdick and Z. Zhang for sharing their unpublished results on rat VPS36. This work was supported by a Wellcome Trust Principal Research Fellowship to D.St J. and by the Max-Planck-Gesellschaft (U.I.).

Author Information GenBank accession numbers for the VPS36 genomic rescue construct and the Venus–VPS36 construct (see Supplementary Information) are EF152770 and EF152771, respectively. Reprints and permissions information is available at www.nature.com/reprints. The authors declare no competing financial interests. Correspondence and requests for materials should be addressed to D.St J. (ds139@mole.bio.cam.ac.uk).

TPP1 is a homologue of ciliate TEBP- β and interacts with POT1 to recruit telomerase

Huawei Xin¹, Dan Liu¹, Ma Wan¹, Amin Safari¹, Hyeung Kim¹, Wen Sun¹, Matthew S. O'Connor¹ & Zhou Songyang¹

Telomere dysfunction may result in chromosomal abnormalities, DNA damage responses, and even cancer¹. Early studies in lower organisms have helped to establish the crucial role of telomerase and telomeric proteins in maintaining telomere length and protecting telomere ends^{2–7}. In *Oxytricha nova*, telomere G-overhangs are protected by the TEBP- α/β heterodimer^{3,4}. Human telomeres contain duplex telomeric repeats with 3' single-stranded G-overhangs, and may fold into a t-loop structure that helps to shield them from being recognized as DNA breaks^{8,9}. Additionally, the TEBP- α homologue, POT1, which binds telomeric single-stranded DNA (ssDNA)¹⁰, associates with multiple telomeric proteins (for example, TPP1, TIN2, TRF1, TRF2 and RAP1) to form the six-protein telosome/shelterin^{11,12} and other subcomplexes. These telomeric protein complexes in turn interact with diverse pathways to form the telomere interactome¹³ for telomere maintenance. However, the mechanisms by which the POT1-containing telosome communicates with telomerase to regulate telomeres remain to be elucidated. Here we demonstrate that TPP1 is a putative mammalian homologue of TEBP- β and contains a predicted amino-terminal oligonucleotide/oligosaccharide binding (OB) fold. TPP1–POT1 association enhanced POT1 affinity for telomeric ssDNA. In addition, the TPP1 OB fold, as well as POT1–TPP1 binding, seemed critical for POT1-mediated telomere-length control and telomere-end protection in human cells. Disruption of POT1–TPP1 interaction by dominant negative TPP1 expression or RNA interference (RNAi) resulted in telomere-length alteration and DNA damage responses. Furthermore, we offer evidence that TPP1 associates with the telomerase in a TPP1–OB-fold-dependent manner, providing a physical link between telomerase and the telosome/shelterin complex. Our findings highlight the critical role of TPP1 in telomere maintenance, and support a yin–yang model in which TPP1 and POT1 function as a unit to protect human telomeres, by both positively and negatively regulating telomerase access to telomere DNA.

It is unknown whether heterodimers that are similar to ciliate TEBP- α/β are used in other species for telomere-end maintenance. TEBP- α homologues include mammalian POT1 and *Saccharomyces cerevisiae* Cdc13, which contain OB folds and function in telomere-capping control by directly binding to telomeric ssDNA^{4,10,14}. However, no mammalian TEBP- β homologues have been identified. We recently cloned the human telomeric protein TPP1 and showed direct interactions between human TPP1 and human POT1 (refs 15, 16). Given that POT1 is a TEBP- α homologue, we predicted that TPP1 might function as the mammalian homologue of TEBP- β . Secondary-structure analyses suggest the presence of a potential OB fold within TPP1 (residues 87–240; Fig. 1a; Supplementary Fig. 2a). In addition, three-dimensional position-specific scoring matrix threading analysis predicted that the TPP1 N terminus (residues 87–316) is most similar to the N-terminal core domain of TEBP- β

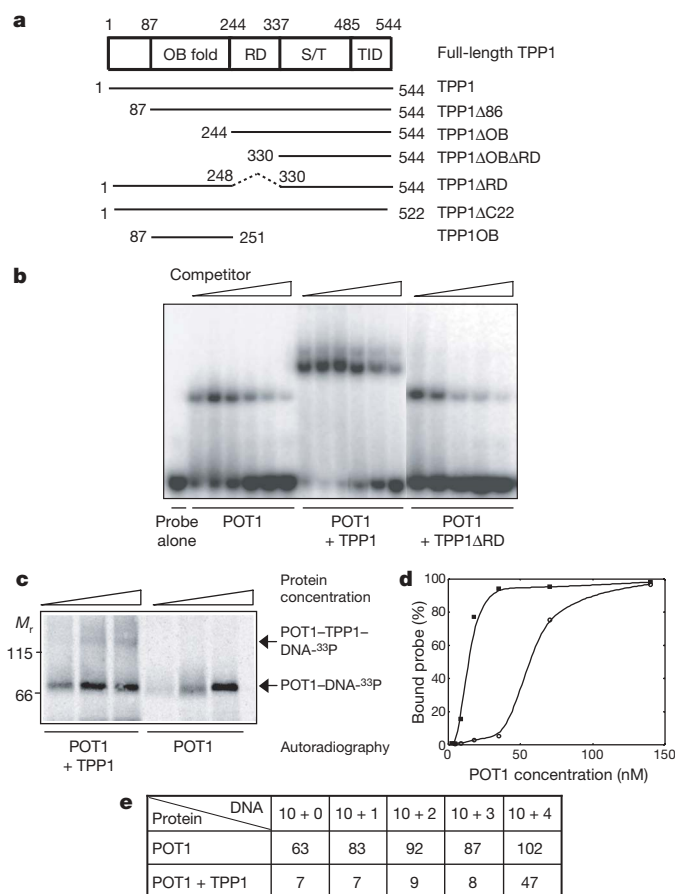


Figure 1 | TPP1 is a homologue of ciliate TEBP- β that interacts with POT1 to bind ssDNA. **a**, TPP1 domain organization and TPP1-deletion mutants. RD, POT1-recruitment domain. S/T, Ser-rich region. TID, TIN2-interacting domain. **b**, Flag-tagged POT1 alone, or co-purified with wild-type TPP1 or TPP1ΔRD from 293T cells, were tested for their binding to the radiolabelled probe 49T3. Increasing amounts of non-radiolabelled 49T3 competitors (0, 30, 60, 120, 240 and 480 nM) were also added. **c**, POT1, TPP1 and telomeric DNA form a ternary complex. Increasing amounts of insect-cell-purified POT1 (35, 70 and 140 nM), or TPP1 plus POT1 (17.5, 35 and 70 nM) were incubated with the ³³P-labelled oligonucleotide 10 + 0 (TTACGGTTAGGGTTAG). The reactions were then treated with UV and glutaraldehyde to cross-link DNA to proteins, followed by SDS-PAGE and autoradiography. **d**, TPP1 enhances POT1 DNA-binding affinity. EMSA was performed using the radiolabelled oligonucleotide 10 + 0 (15 nM) and 2-fold dilutions (from 140 nM) of POT1 (open circles) or POT1 plus TPP1 (filled squares). **e**, Estimated K_d (nM) of POT1 and POT1–TPP1 to G-strand oligonucleotides with different 3'-end nucleotides.

¹Verna and Marrs McLean Department of Biochemistry and Molecular Biology, Baylor College of Medicine, One Baylor Plaza, Houston, Texas 77030, USA.

(ref. 17; Supplementary Fig. 2b). TEBP- α contains three OB folds, the first two are involved in ssDNA recognition whereas the third one interacts with TEBP- β (ref. 17). Interestingly, we found that POT1 probably harbours a third OB fold as well (in its PTP/TPP1-binding region—PBR—domain, which associates with TPP1; data not shown). These observations suggest evolutionarily conserved interaction motifs between TEBP- α/β and POT1–TPP1, and that TPP1 is a putative homologue of TEBP- β .

Next, we tested whether TPP1, similar to TEBP- β (ref. 4), could cooperate with POT1 in recognizing telomeric ssDNA. Although TPP1 exhibited little or no telomere ssDNA-binding activities in gel-shift experiments (Supplementary Fig. 2c) as was reported for TEBP- β (ref. 4), the addition of TPP1 to POT1 oligonucleotide-binding reactions resulted in super-shifted probes compared with POT1 alone, implying the formation of a POT1–TPP1–DNA complex (Fig. 1b). Deletion of the POT1-binding recruitment domain (RD) of TPP1 (TPP1 Δ RD) abolished the super-shift, suggesting that direct POT1–TPP1 interaction is required for POT1–TPP1–DNA complex formation. Further support for the ternary complex came from antibody super-shift experiments (Supplementary Fig. 2c), and from cross-linking experiments in which radio-labelled telomere ssDNA could be cross-linked with insect-cell-purified POT1 and TPP1 (Fig. 1c).

Compared with POT1 alone, POT1–TPP1 together exhibited a ~ 9 -fold increase in affinity (7 nM versus 63 nM) for the oligonucleotide that contains the decamer core recognized by POT1 (TTACGGTTAGGGTTAG, 10 + 0) (Fig. 1d, e; Supplementary Fig. 2d, e). Notably, POT1–TPP1 also had much higher affinity (compared with POT1 alone) towards core telomere repeats containing 3' nucleotide extensions (for example, TTAGGGTTAGGG, 10 + 2) (Fig. 1e)¹⁸. In fact, TPP1 enhanced the affinity of POT1 to a number of the telomere oligonucleotides tested (Fig. 1e), emphasizing the biochemical

and structural similarities between TEBP- α/β and POT1–TPP1, and indicating that TPP1 is indeed a TEBP- β homologue.

TPP1 binds and targets POT1 to telomeres through the TPP1 RD domain and the POT1 PBR domain¹⁵. POT1 may also be recruited to telomeres through its interaction with TRF2 (ref. 19), or through its two N-terminal OB folds¹⁸. To examine the role of POT1 N-terminal

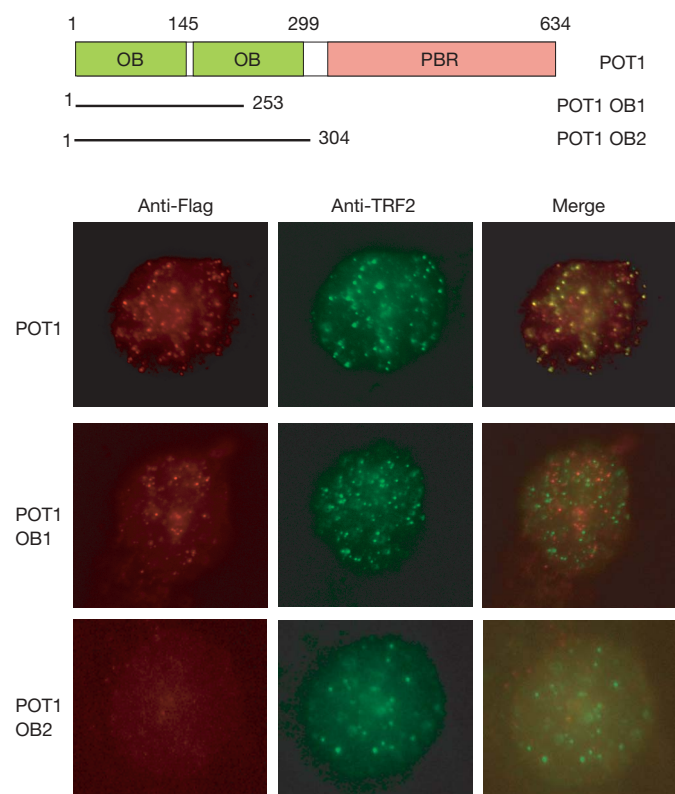


Figure 2 | POT1 telomeric targeting depends on POT1–TPP1 interaction. Immunostaining analysis of Flag-tagged POT1, POT1 OB1, or POT1 OB2 using polyclonal anti-Flag (red) and anti-TRF2 antibodies (green). PBR, TPP1-binding region.

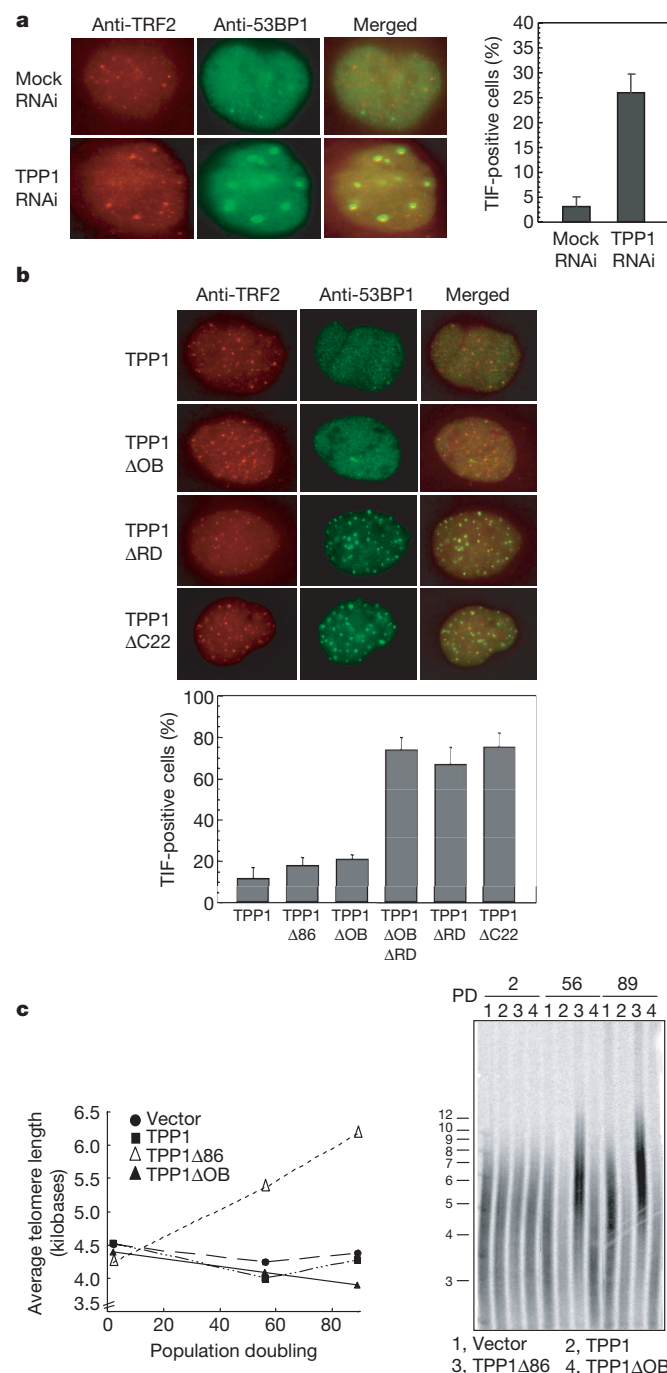


Figure 3 | The TPP1 OB fold and TPP1–POT1 interaction are important for telomere-end protection and -length control. **a**, TPP1 knockdown results in TIF. HTC75 cells stably expressing TPP1 shRNA sequences were immunostained (left panel) with anti-53BP1 (green) and TRF2 (red) antibodies and quantified (right panel). Error bars indicate s.e.m. ($n > 4$). **b**, TIF analysis of HTC75 cells expressing full-length or truncated TPP1 (top panel) and quantification (bottom panel). Error bars indicate s.e.m. ($n \geq 4$). **c**, HTC75 cells expressing full-length or N-terminally truncated TPP1 were subjected to Telomere Restriction Fragment analysis as previously described¹⁵ (left panel). Right panel, Southern hybridization blot showing telomere length. PD, population doubling.

OB folds in telomere targeting, we analysed the localization of POT1 PBR-deletion mutants that contained only the first (POT1 OB1) or both (POT1 OB2) OB folds. Both POT1 mutants were defective in telomere localization as determined by indirect immunofluorescence (Fig. 2), and the ability of POT1 OB2 to chromatin-immunoprecipitate telomeric DNA was greatly reduced (>10 -fold; Supplementary Fig. 3a), supporting the notion that the OB folds alone are insufficient for POT1 telomeric targeting. Furthermore, RNAi knock-down of TPP1 led to reduced telomere localization of endogenous POT1 (Supplementary Fig. 3c). Taken together, these data indicate that POT1 telomere targeting depends largely on its interaction with TPP1, and underlines the critical role of the POT1–TPP1 complex in telomere maintenance.

Disruption of the POT1–TPP1 interaction may lead to de-protected telomere ends and Telomere Dysfunction Induced Foci (TIF; for example, 53BP1 telomeric foci)^{20–23}. Indeed, RNAi knock-down of TPP1 resulted in a $\sim 20\%$ increase in TIF-positive cells (Fig. 3a). Furthermore, in cells expressing TPP1 Δ RD or TPP1 Δ C22 (a TIN2-interacting domain (TID) mutant that should compromise the telomeric association of endogenous POT1–TPP1)²⁴, TIFs were readily detectable in $>70\%$ of the cells (Fig. 3b), whereas TPP1 Δ 86 and TPP1 Δ OB expressing cells were similar to TPP1 cells (Fig. 3b; Supplementary Fig. 4). Given that both TPP1 Δ 86 and TPP1 Δ OB

contain intact RD and TID domains (Fig. 1a), these observations imply that the TPP1 RD domain may be more critical than the OB fold in POT1 telomere targeting and POT1-mediated end protection *in vivo*. For POT1-mediated length control, we have shown previously that the PBR-only mutant of POT1 (POT1 PBR) can act as a dominant negative form to elongate telomeres¹⁵. The interaction of POT1 PBR with TPP1 seems necessary for its telomere elongation phenotype, because mutations in the PBR region that disrupted the TPP1–POT1 PBR interaction¹⁵ resulted in a failure of these mutants to extend telomeres (Supplementary Fig. 5). These results reaffirm the notion that TPP1 binding is required for POT1-mediated telomere-length control. Taken together, our data establish that the interaction between POT1 and TPP1 serves to modulate POT1 function at the telomeres, and that POT1 and TPP1 together function as a unit in end protection and length control of telomeres.

How does the POT1–TPP1 complex regulate telomere length? Both the RD and TID domains of TPP1 (Fig. 1a) are probably critical for this function because they are required for TPP1 and POT1 targeting^{15,24,25}. Indeed, overexpression of the dominant negative mutant TPP1 Δ RD led to dramatically extended telomeres (data not shown), as is the case for TPP1 Δ C22 (ref. 24). These observations are consistent with the model where the six-protein complex may negatively regulate telomerase access by sequestering telomere ends^{11,12}. Consequently, displacement of POT1 from telomeric ssDNA makes telomeres more accessible to the telomerase²⁶. To determine whether the TPP1 OB fold has any role in telomere-length control, we examined HTC75 cells expressing TPP1 mutants with N-terminal deletions. All the TPP1 mutants examined in this study (except for TPP1 Δ C22) were targeted to the telomeres (data not shown). As previously reported^{15,16,25}, full-length TPP1 expression had little effect on telomere length (Fig. 3c). Deletion of the first 86 amino acids (TPP1 Δ 86 with an intact OB fold) resulted in telomere lengthening, indicating a possible regulatory role for the first 86 amino acids (Fig. 3c). Interestingly, further deletion into the OB fold (TPP1 Δ OB) abrogated the telomere elongation effect, indicating that the TPP1 OB fold may positively regulate telomere length by directly participating in telomerase recruitment.

We went on to test this hypothesis by investigating whether TPP1 could interact with the telomerase. In precipitation experiments using extracts from human cells expressing tandem affinity purification tag (TAP)–human Telomerase Reverse Transcriptase (TERT) and glutathione *S*-transferase (GST)–TPP1, we found TAP–TERT associated with GST–TPP1 (Fig. 4a). In addition, both TAP–TERT and endogenous TPP1 were eluted as a ~ 2 MDa complex by gel filtration (Fig. 4b). Furthermore, both full-length TPP1 and TPP1 OB fold (Fig. 1a), but not TPP1 Δ OB Δ RD, were able to pull down *in vitro* translated haemagglutinin (HA)–TERT proteins as well as telomerase activity (Fig. 4c). These observations indicate that the putative TPP1 OB fold may be required for regulating telomerase recruitment. Consistent with this idea, whereas robust telomerase activity was detected in Flag–TPP1 immunoprecipitates from HT1080 cells, deletion of the putative TPP1 OB fold (TPP1 Δ OB and TPP1 Δ OB Δ RD) led to a reduction (>5 -fold) in associated telomerase activity (Fig. 4d). In contrast, the POT1-binding mutant TPP1 Δ RD still retained the ability to associate with telomerase activity (Fig. 4d), suggesting that the TPP1 OB fold, but not POT1, participates in recruiting telomerase. Because TPP1 alone does not bind ssDNA, POT1 and TPP1 (as integral components of the telosome/shelterin) probably function together to positively recruit telomerase to telomeric ssDNA through the TPP1 OB fold, in addition to protecting telomere ends and negatively regulating telomerase access.

Our results underlined the evolutionarily conserved mechanism in telomere-end capping, where OB-fold-containing TEBP homologues work in concert to protect telomere overhangs. This mode of end protection is probably more widely used than previously thought, because TPP1 homologues are found in many of the vertebrate species examined. It is interesting to note that, unlike

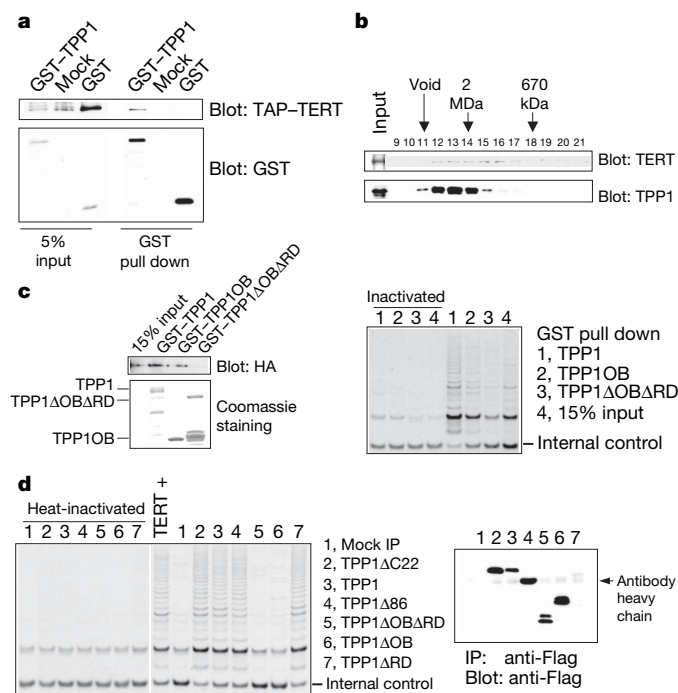


Figure 4 | The TPP1 OB fold is important for recruitment of telomerase activity. **a**, 293T cells transiently expressing TAP–TERT alone (mock), with GST, or with GST–TPP1 were harvested, lysed and incubated with glutathione beads. The precipitates were resolved by SDS–PAGE and blotted with peroxidase-anti-peroxidase (PAP; for protein A on the TAP-tag) or anti-GST–HRP. **b**, Nuclear extracts from HeLa cells expressing TAP–TERT were fractionated, resolved by SDS–PAGE and probed with PAP and anti-TPP1 antibody¹⁵. **c**, TPP1 interacts with telomerase *in vitro*. *In vitro*-translated HA–TERT/TR was immunoprecipitated with anti-HA agarose beads and eluted with HA peptides (Sigma)³⁰. GST-tagged TPP1, TPP1OB and TPP1 Δ OB Δ RD, were then used to pull down HA–TERT/TR, followed by SDS–PAGE and blotting with anti-HA antibodies (left panel) or TRAP assays (right panel). Samples were also heat-inactivated for negative controls. **d**, Anti-Flag immunoprecipitates from HTC75 cells expressing Flag-tagged TPP1 mutants were eluted with Flag peptides for TRAP assays (left panel), or probed with anti-Flag antibodies (right panel). Samples were also heat-inactivated for negative controls. On the basis of serial dilutions and comparisons with the positive control (TERT +; ≈ 500 cells), we estimated TPP1 to bring down $\sim 20\%$ telomerase activity.

TEBP- β (ref. 27), TPP1 does not seem to promote G-quadruplex formation *in vitro* (data not shown), suggesting a functional divergence in this respect. Most importantly, our findings suggest dual roles of the POT1–TPP1 complex in regulating telomerase access. The binding of the POT1–TPP1 complex to telomeric ssDNA serves to cap telomere ends and prevent telomerase access to the ssDNA template. Indeed, previous studies have demonstrated that expression of POT1-OB-fold-deletion mutants or the TPP1 RD domain alone extends telomeres^{15,26}. However, POT1–TPP1 can also physically recruit the telomerase complex, perhaps to facilitate rapid telomere repair/extension during the cell cycle or in response to local telomere damage on POT1 disassociation (Supplementary Fig. 1)²⁸. Notably, the TPP1 OB fold is at the centre of both processes. The yin–yang model of POT1–TPP1 function highlights the dynamic nature of telomere regulation, and the complexity of telomere maintenance pathways mediated by the telomerase together with telomere protein complexes within the telomere interactome.

METHODS

Oligonucleotides and vectors. Oligonucleotides used were: 49T3, AAGGATA ATGCCACGGTGCAGGACGGCACTG(TTAGGG)₃; 10 + 0, TTACGGTTAGG GTTAG; and 10 + 1 through 10 + 4 with increasing 3' extensions of 10 + 0 (G, GG, GGT and GGGT).

Various TPP1, POT1, and TAP–TERT constructs were cloned into pcDNA3 or a Flag-tagged pBabe-based vector for transient or stable expression. POT1, TPP1 and TPP1 mutants were cloned into pGEX or the pFAST baculovirus vector system (Invitrogen) for insect cell or *Escherichia coli* expression. HA–TERT and TR plasmids are gifts from J. L. Chen (Arizona State University). For RNAi, a pRetro-dual vector or a retroviral shRNA vector expressing sequences from TPP1 siRNA Oligo 1 was used²⁴.

Protein expression and purification. Flag-tagged TPP1, POT1, TPP1 or TPP1 Δ RD were expressed alone or together in 293T cells and purified using anti-Flag agarose beads (Sigma). GST–TPP1, GST–POT1, Flag–POT1 or GST–TPP1 Δ OB were expressed alone or together in a baculovirus insect cell system (Invitrogen), purified using glutathione beads, and eluted with glutathione or cleaved from the N-terminal GST tag by the ProScission Protease (Amersham).

Electrophoretic Mobility Shift Assay (EMSA), antibody supershift and cross-linking. EMSA was performed as described previously¹⁸. For antibody supershift, the purified proteins were incubated first with either anti-GST or anti-Flag M2 antibodies followed by addition of radiolabelled DNA probes. For cross-linking, radiolabelled DNA and protein mixtures were cross-linked by ultraviolet (UV) radiation and then incubated with 0.004% glutaraldehyde for 60 min at room temperature²⁹.

Telomere Repeat Amplification Protocol (TRAP). Anti-Flag immunoprecipitates from wild-type- and mutant-TPP1-expressing HTC75 cells were eluted with Flag peptides (Sigma), diluted, and used for TRAP assays using a telomerase detection kit (Chemicon). *In vitro*, TPP1-associated telomerase activities were similarly assayed.

Chromatographic fractionation of telomere-associated complexes. Gel filtration experiments were performed as previously described¹¹ using nuclear extracts from TAP–TERT expressing HeLa cells, followed by SDS–polyacrylamide gel electrophoresis and western blotting. More detailed methodology and reagent information can be found in Supplementary Methods.

Received 24 August; accepted 20 November 2006.

Published online 21 January 2007.

1. Chadwick, D. J. & Cardew, G. (eds) *Telomeres and Telomerase* (John Wiley & Sons, Chichester, UK, 1997).
2. Gottschling, D. E. & Zakian, V. A. Telomere proteins: specific recognition and protection of the natural termini of *Oxytricha* macronuclear DNA. *Cell* **47**, 195–205 (1986).
3. Greider, C. W. & Blackburn, E. H. The telomere terminal transferase of *Tetrahymena* is a ribonucleoprotein enzyme with two kinds of primer specificity. *Cell* **51**, 887–898 (1987).
4. Gray, J. T., Celandier, D. W., Price, C. M. & Cech, T. R. Cloning and expression of genes for the *Oxytricha* telomere-binding protein: specific subunit interactions in the telomeric complex. *Cell* **67**, 807–814 (1991).
5. Lingner, J. & Cech, T. R. Telomerase and chromosome end maintenance. *Curr. Opin. Genet. Dev.* **8**, 226–232 (1998).

6. Shore, D. Telomere length regulation: getting the measure of chromosome ends. *Biol. Chem.* **378**, 591–597 (1997).
7. Bertuch, A. A. & Lundblad, V. The maintenance and masking of chromosome termini. *Curr. Opin. Cell Biol.* **18**, 247–253 (2006).
8. Henderson, E., Hardin, C. C., Walk, S. K., Tinoco, I. Jr & Blackburn, E. H. Telomeric DNA oligonucleotides form novel intramolecular structures containing guanine–guanine base pairs. *Cell* **51**, 899–908 (1987).
9. Griffith, J. D. *et al.* Mammalian telomeres end in a large duplex loop. *Cell* **97**, 503–514 (1999).
10. Baumann, P. & Cech, T. R. Pot1, the putative telomere end-binding protein in fission yeast and humans. *Science* **292**, 1171–1175 (2001).
11. Liu, D., O'Connor, M. S., Qin, J. & Songyang, Z. Telosome, a mammalian telomere-associated complex formed by multiple telomeric proteins. *J. Biol. Chem.* **279**, 51338–51342 (2004); published online 20 September 2004.
12. de Lange, T. Shelterin: the protein complex that shapes and safeguards human telomeres. *Genes Dev.* **19**, 2100–2110 (2005).
13. Songyang, Z. & Liu, D. Inside the mammalian telomere interactome: regulation and regulatory activities of telomeres. *Crit. Rev. Eukaryot. Gene Expr.* **16**, 103–118 (2006).
14. Nugent, C. I., Hughes, T. R., Lue, N. F. & Lundblad, V. Cdc13p: a single-strand telomeric DNA-binding protein with a dual role in yeast telomere maintenance. *Science* **274**, 249–252 (1996).
15. Liu, D. *et al.* PTP interacts with POT1 and regulates its localization to telomeres. *Nature Cell Biol.* **6**, 673–680 (2004); published online 6 June 2004.
16. Ye, J. Z. *et al.* POT1-interacting protein PIP1: a telomere length regulator that recruits POT1 to the TIN2/TRF1 complex. *Genes Dev.* **18**, 1649–1654 (2004); published online 1 July 2004.
17. Horvath, M. P., Schweiker, V. L., Bevilacqua, J. M., Ruggles, J. A. & Schultz, S. C. Crystal structure of the *Oxytricha nova* telomere end binding protein complexed with single strand DNA. *Cell* **95**, 963–974 (1998).
18. Lei, M., Podell, E. R. & Cech, T. R. Structure of human POT1 bound to telomeric single-stranded DNA provides a model for chromosome end-protection. *Nature Struct. Mol. Biol.* **11**, 1223–1229 (2004); published online 21 November 2004.
19. Yang, Q., Zheng, Y. L. & Harris, C. C. POT1 and TRF2 cooperate to maintain telomeric integrity. *Mol. Cell. Biol.* **25**, 1070–1080 (2005).
20. Takai, H., Smogorzewska, A. & de Lange, T. DNA damage foci at dysfunctional telomeres. *Curr. Biol.* **13**, 1549–1556 (2003).
21. d'Adda di Fagagna, F. *et al.* A DNA damage checkpoint response in telomere-initiated senescence. *Nature* **426**, 194–198 (2003); published online 13 November 2005.
22. Wu, L. *et al.* Pot1 deficiency initiates DNA damage checkpoint activation and aberrant homologous recombination at telomeres. *Cell* **126**, 49–62 (2006).
23. Hockemeyer, D., Daniels, J. P., Takai, H. & de Lange, T. Recent expansion of the telomeric complex in rodents: Two distinct POT1 proteins protect mouse telomeres. *Cell* **126**, 63–77 (2006).
24. O'Connor, M. S., Safari, A., Xin, H., Liu, D. & Songyang, Z. A critical role for TPP1 and TIN2 interaction in high-order telomeric complex assembly. *Proc. Natl Acad. Sci. USA* **103**, 11874–11879 (2006).
25. Houghtaling, B. R., Cuttonaro, L., Chang, W. & Smith, S. A dynamic molecular link between the telomere length regulator TRF1 and the chromosome end protector TRF2. *Curr. Biol.* **14**, 1621–1631 (2004).
26. Loayza, D. & de Lange, T. POT1 as a terminal transducer of TRF1 telomere length control. *Nature* **424**, 1013–1018 (2003).
27. Fang, G. & Cech, T. R. The β subunit of *Oxytricha* telomere-binding protein promotes G-quartet formation by telomeric DNA. *Cell* **74**, 875–885 (1993).
28. Verdun, R. E., Crabbe, L., Haggblom, C. & Karlseder, J. Functional human telomeres are recognized as DNA damage in G2 of the cell cycle. *Mol. Cell* **20**, 551–561 (2005).
29. Fang, G. & Cech, T. R. *Oxytricha* telomere-binding protein: DNA-dependent dimerization of the alpha and beta subunits. *Proc. Natl Acad. Sci. USA* **90**, 6056–6060 (1993).
30. Chen, J. L. & Greider, C. W. Determinants in mammalian telomerase RNA that mediate enzyme processivity and cross-species incompatibility. *EMBO J.* **22**, 304–314 (2003).

Supplementary Information is linked to the online version of the paper at www.nature.com/nature.

Acknowledgements We thank J. L. Chen for kindly providing the HA–TERT and hTR plasmids and we thank A. Laegerle, K. Huang and L.-Y. Chen for help. This work was supported by awards to Z.S. and D.L. from NIH, the Department of Defense, the American Cancer Society, and the American Heart Association. Z.S. is a Leukaemia and Lymphoma Society Scholar.

Author Information Reprints and permissions information is available at www.nature.com/reprints. The authors declare no competing financial interests. Correspondence and requests for materials should be addressed to Z.S. (songyang@bcm.tmc.edu).

naturejobs

**THE CAREERS
MAGAZINE FOR
SCIENTISTS**

The global plight of postdocs was highlighted by the recent *Naturejobs* contest to select four fellows to write monthly journal entries on our Career View page. We received a host of entries from a number of countries running the gamut of the physical and life sciences. But despite the volume and diversity, the sample entries revealed some interesting similarities.

The word 'crossroads' kept cropping up to describe the fellows' situation. Even though nearly all of the entries came from academic postdocs, many expressed uncertainty about whether university research would be their ultimate destination. Such doubts are worrying and encouraging in almost equal measure. They are unnerving because they underline the number of hurdles that must be negotiated if you want to get established in science — from picking a country and a lab, to work in to worrying about publishing pressures. But they are encouraging because they reveal that the postdocs are still open to alternative career paths, such as publishing, law and policy.

Although all of the entries we received described compelling situations, after several rounds of judging we picked four writers who best seemed to articulate these issues. Maria Ocampo-Hafalla wrote about the pressures she felt as she chose a new position and adviser that meant her switching research focus and crossing the Atlantic (page 564). Unabashed idealist Peter Jordan from Australia hopes his training in mathematical modelling at the US National Institutes of Health will help "make a difference" by somehow improving human health. Christopher Rowan expressed a mixture of excitement and trepidation about his impending move from Britain to South Africa, where he will study rocks. And Moira Sheehan, a plant-biology postdoc at Cornell University in Ithaca, New York, is looking to balance lab work and family life as she awaits her second child.

We would like to thank all of the applicants who shared their stories, and congratulate the four who made the final cut. We look forward to hearing what decisions they make at this crucial crossroads in their career.

Paul Smaglik, *Naturejobs* editor

CONTACTS

Editor: Paul Smaglik

Assistant Editor: Gene Russo

European Head Office, London

The Macmillan Building,
4 Crinan Street,
London N1 9XW, UK
Tel: +44 (0) 20 7843 4961
Fax: +44 (0) 20 7843 4996
e-mail: naturejobs@nature.com

European Sales Manager:

Andy Douglas (4975)
e-mail: a.douglas@nature.com

Business Development Manager:

Amelie Pequignot (4974)
e-mail: a.pequignot@nature.com

Natureevents:

Claudia Paulsen Young
(+44 (0) 20 7014 4015)
e-mail: c.paulsenyoung@nature.com

France/Switzerland/Belgium:

Muriel Lestringuez (4994)

UK/Ireland/Italy/RoW:

Nils Moeller (4953)

Scandinavia/Spain/Portugal:

Evelina Rubio-Morgan (4973)

Germany/Austria/The Netherlands:

Reya Silao (4970)

Online Job Postings:

Matthew Ward (+44 (0) 20 7014 4059)

Advertising Production Manager:

Stephen Russell
To send materials use London
address above.

Tel: +44 (0) 20 7843 4816

Fax: +44 (0) 20 7843 4996

e-mail: naturejobs@nature.com

Naturejobs web development:

Tom Hancock

Naturejobs online production:

Catherine Alexander

US Head Office, New York

75 Varick Street,

9th Floor,

New York,

NY 10013-1917

Tel: +1 800 989 7718

Fax: +1 800 989 7103

e-mail: naturejobs@natureny.com

US Sales Manager:

Peter Bless

Japan Head Office, Tokyo

Chiyoda Building,

2-37 Ichigayatamachi,

Shinjuku-ku,

Tokyo 162-0843

Tel: +81 3 3267 8751

Fax: +81 3 3267 8746

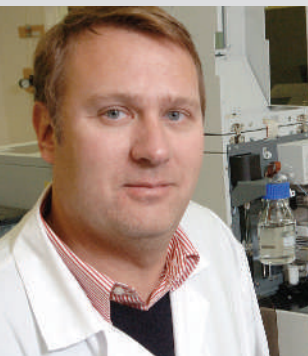
Asia-Pacific Sales Manager:

Ayako Watanabe

e-mail: a.watanabe@natureasia.com

MOVERS

**Christoph Borchers, director,
University of Victoria–Genome BC Proteomics
Centre, Victoria, British Columbia, Canada**



2004–06: Director, Biomarkers Facility Core, Center of Environmental Health Susceptibility, University of North Carolina, Chapel Hill, North Carolina
2001–06: Faculty director, UNC–Duke Michael Hooker Proteomics Center, Chapel Hill, North Carolina

Christoph Borchers has spent his entire career fascinated by the prospect of solving biomedical problems using mass spectrometry analyses of biomolecules. Only recently has this become a reality.

When Borchers began his undergraduate chemistry degree at the University of Konstanz in his native Germany, it was impossible to analyse macromolecules such as proteins without destroying their structure. By the time Borchers completed his PhD there in 1996, new ionization techniques not only allowed him to analyse intact molecular ions formed from peptides and proteins, but also to determine the amino-acid sequence as well as the primary protein structure. He used these tools to identify the binding site of a protein known for pumping drugs out of cells. "Colleagues still laughed at the thought of analysing proteins with mass spectrometry," says Borchers.

With no jobs in Germany in this emerging field, Borchers jumped at an offer from the US National Institute of Environmental Health Sciences in North Carolina's Research Triangle Park. During his five years there he went from visiting fellow to staff scientist. His chairman suggested he give a seminar at the University of North Carolina; Borchers didn't realize that it was an interview as well. He accepted a position as assistant professor and also became founding faculty director of the university's Michael Hooker Proteomics Core Center.

When he arrived, the entire proteomics facility consisted of one mass spectrometer. With help from an anonymous donor and grants from the National Center for Research Resources, he amassed more advanced equipment. Nearby Duke University joined as the centre grew. Then his success convinced a search committee to hire him as director of the University of Victoria–Genome BC Proteomics Centre.

"He's demonstrated the ability to bring together top-class researchers and industry collaborators around the health applications of proteomics — major areas we want to concentrate on at BC," says Martin Taylor, the University of Victoria's vice-president of research.

It was a tough decision, says Borchers, but a thriving Canadian proteomics community convinced him to move. Genome Canada and Genome BC fund large-scale research, and Genome BC has a network of interested clinicians. He now wants to expand research capabilities by developing diagnostic tools for early disease detection, and developing mass spectrometry-based structural proteomics. ■

Virginia Gewin

NETWORKS & SUPPORT

Better offices, better postdocs

Postdocs often exist in no-man's land. No longer students in the care of the research institution, they are left without guidance about benefits, training or professional development. University offices dedicated to their needs can help. Yet of 135 academic institutions tracked by the US National Postdoctoral Association (NPA), 34 have no postdoc office and 61 have no postdoc association. Some 14 have no postdoc infrastructure at all.

Creating the infrastructure is a time-consuming and often frustrating endeavour. In response, the Alfred P. Sloan Foundation, which funded the formation of the NPA in 2003, recently awarded funding to create a postdoc leadership mentoring project. It will pair mentors who have set up postdoc associations or offices with protégés who seek to do so.

The project offers up to 45 travel awards for mentors and protégés to go to the NPA annual meeting in Berkeley, California, from 30 March to 1 April. It will be an important venue for founders to pass on experience to the next generation of postdocs — a history that is too easily lost after people move on, says Chris Blagden, a founder of the postdoc association at New York University's School of Medicine.

According to a recent survey by the researchers' society Sigma Xi, 82% of

postdocs represented by an office or association were satisfied with their experience; 9% reported conflicts. But only 59% of unrepresented postdocs were satisfied and 22% reported conflicts. "We've been able to make the case that postdoc offices and associations are critical elements for postdoc training," says Alyson Reed, the NPA's executive director.

Virginia Cox of the Sloan Foundation hopes the project will lead to the formation of at least ten associations or offices. Allison De Marco, a postdoc at Pennsylvania State University, who is applying to be a protégé, says her big challenge is learning how to keep fellow postdocs interested while keeping up her own research.

Time constraints, money and institutional resistance can also be formidable challenges, says Reed. Many institutions worry that a postdoc organization will lead to a labour union demanding better pay and benefits. She says leaders need to learn how to communicate effectively with the administration.

"The best success stories come from postdoc associations working with faculty members to champion policies that improve housing subsidies, childcare and career development plans," says Reed. ■

Virginia Gewin

POSTDOC JOURNAL

Happily ever after?

He was a smart and successful scientist whose profile I had read on the Internet. We exchanged a few e-mails, and before I knew it, I was on a plane to meet him. I was so nervous I could hardly sleep. I saw where he worked, met his colleagues and was interviewed by his friends. After I flew home, I waited anxiously until he contacted me again.

Then we decided to move forward. Within weeks of finishing my doctorate, I left my family, my friends and my home in the United States to join him in London. I have been with him for one year now, for better or for worse, in good times and in bad... And he's not even my husband.

Choosing a postdoctoral mentor is like deciding on a life partner. You consider your similarities and differences, you decide what you bring to and want from the relationship, and you plan a future together. I changed my field from DNA repair to chromosome segregation, my model organism from mouse to yeast, and my country of residence from the United States to the United Kingdom.

After all, every good relationship entails hard work and sacrifice, as my husband (the real one) and I experienced when we both had to find postdocs in London. But how do you cope when it feels like the honeymoon is ending? One year into my postdoc, I am still striving for happily ever after. ■

Maria Ocampo-Hafalla is a research fellow at Cancer Research UK's London Research Institute.

Bias cut

Women, it seems, often get a raw deal in science — so how can discrimination be tackled?



Lutz Bornmann

When it comes to applying for grants, women seem to be at a disadvantage — they are potentially less likely to succeed than their male counterparts. So suggests a meta-analysis of 21 studies conducted by my colleagues Rüdiger Mutz and Hans-Dieter Daniel and I (see <http://arxiv.org/abs/math.ST/0701537>). The cause of this discrepancy is unknown. It could be that fewer women principal investigators apply for grants. Gender bias — whether implicit or explicit — could come into play. Or the explanation could be institutional; there are more men than women in high-ranking positions, meaning fewer women have a chance to make decisions.

There has been widespread acknowledgement of how gender affects scientific careers.

A comprehensive review of the literature on gender differences in the careers of academic scientists by the US National Science Foundation (NSF),

concludes: “Taken as a whole, the body of literature we reviewed provides evidence that women in academic careers are disadvantaged compared with men in similar careers. Women faculty earn less, are promoted less

frequently to senior academic ranks, and publish less frequently than their male counterparts.”

But the NSF doesn't address peer review as a component of this discrepancy. Conventionally, peer review is regarded as a sure guarantee of good science. It reassures us about the quality of scientific work and that taxpayers' money is well spent. Our meta-analysis suggests that there are robust gender differences in grant peer-review procedures, and our results line up with the NSF's broader conclusion on gender differences in the careers of academic scientists.

Whatever the cause, our paper

also reports some ways to rule out gender bias — whether intentional or unintentional. One possible way to avoid bias in the grant peer-review process is to mask applicants' gender. In journal peer review, masking authors' gender has proved to be a satisfactory precaution against bias. But masking is not equally suitable for all types of submission. It is impossible to pass valid judgment on a short-communication manuscript without some personal knowledge of the author.

It is questionable, as well, whether the gender of the applicant in grant peer review should be masked. Apart from assessment of the proposed research, decisions are also based on the applicant's track record. The European Molecular Biology Organization (EMBO) in Heidelberg, Germany, is planning an experiment in which the committee in the research-fellowship selection process will be totally gender-blinded, according to EMBO's programme manager, Gerlind Wallon.

The first step to identify bias and tackle its potential sources is a continuous, professional evaluation of the selection process and its outcomes. A few years ago, our team analysed the peer-review selection process for the Boehringer Ingelheim Fund (BIF) fellowships (see *Nature* **430**, 591; 2004). Although the selection process proved highly valid in identifying the most promising junior scientists, and there was no gender difference at postdoctoral level, we did find a slight gender bias in the selection of PhD students. The results were thoroughly discussed by the review committee and the foundation continued to monitor its selection process closely. This allowed the BIF to see a considerable increase in female applicants and scholars in the next few years, with nearly 50% of the 2006 PhD scholarships awarded to women. But according to

Hermann Fröhlich, managing director of the BIF, the growing number of young women participating and succeeding in one of the most competitive selection processes for scholarships may be due to social change. And as the BIF evaluates young researchers and their projects at the earliest possible phase in the scientific career, its figures may indicate that large numbers of women have started to reach for the top in science.

The Pioneer Award for innovative research given by the US National Institutes of Health (NIH) shows that there are other effective measures against gender bias. In 2004 there were no women among the 9 scientists chosen, but in 2005, 6 of the 13 winners were women, and in 2006, 4 of 13. After the first round, the NIH specifically encouraged women to apply, accepted only self-nominations rather than institutional submissions and spent more time training its reviewers.

Changes such as widening submission policies, ‘masking’ fellowship applicants and regularly evaluating the peer-review process have started closing the gender gap in grant success. Other moves will help women rise to higher levels of leadership in science and erase unintentional gender bias. The Committee on Science, Engineering, and Public Policy of the US National Academies proposes setting up programmes to provide women with mentoring and support. It also aims to restructure hiring and promotion procedures to reduce bias and encourage diversity. This will include training search committees and heads of department to recognize bias, and to reduce it. ■

Lutz Bornmann is a researcher at the Professorship for Social Psychology and Research on Higher Education at the Swiss Federal Institute of Technology, Zurich.

“Women did very much better when only self-nominations were accepted, not institutional submissions.”



THE NATIONAL INSTITUTES OF HEALTH

OPPORTUNITIES @ NIH



Staff Scientist in Protein Biochemistry Research Triangle Park, North Carolina

The Laboratory of Signal Transduction at the National Institute of Environmental Health Sciences is recruiting a staff scientist in support of the Transmembrane Signaling Group headed by Dr. Lutz Birnbaumer. The incumbent will oversee group efforts in studying molecular mechanisms involved in the activation of G proteins by guanine nucleotide exchange factors, including the interaction of genetically engineered rhodopsins with transducin extracted and purified from mammalian retinas. The selectee will be expected to personally execute experiments, oversee up to three technical support personnel and train and supervise group graduate students and postdoctoral fellows in the conduct of this area of research. The successful candidate is expected to work with minimal guidance, carry the research to publishable stages and work on these and other projects as defined by the group leader.

Minimum qualifications include a doctoral degree, successful completion of postdoctoral training, record of publications and strong background in protein purification techniques and analysis of enzymatic and physicochemical properties of mammalian and recombinant proteins.

For additional information, contact Dr. Lutz Birnbaumer at birnbau1@niehs.nih.gov. For additional information concerning the research projects and publications, visit the following website: <http://dir.niehs.nih.gov/dirlst/groups/birnbaumer.htm>. Applications from women and minorities are particularly encouraged. To apply, submit a curriculum vitae, bibliography, brief statement of research interests and arrange for three letters of recommendation to be sent by **March 16, 2007**, to the address indicated below. Applications received after that date will be considered as needed:

Mr. Will Williams (DIR-07-02)
National Institutes of Health
National Institute of Environmental Health Sciences
P.O. Box 12233, Maildrop A2-06
111 Alexander Drive, Room A202
Research Triangle Park, NC 27709
e-mail: dir-apps@niehs.nih.gov

DHHS and NIH are Equal Opportunity Employers



Functions of Sir2 and Nuclear Receptors Research Triangle Park, North Carolina

Postdoctoral positions are available immediately in the Laboratory of Signal Transduction at the National Institute of Environmental Health Sciences (NIEHS), a major research institute of the NIH located in Research Triangle Park, North Carolina. NIEHS offers an outstanding research environment and has been constantly rated by The Scientist as one of the best places for post-docs to work.

Our research is focused on the roles of NAD⁺-dependent protein deacetylase Sir2 and corresponding post-translational modification of nuclear receptors in aging and age-associated diseases. We have shown that SIRT1, the mammalian orthology of Sir2, physically interacts and deacetylates Liver X Receptors (LXRs), thus regulates their transcriptional activity and cholesterol homeostasis. Current research areas include nuclear receptor signaling pathways regulated by SIRT1 and their roles in metabolism, aging, and metabolic diseases such as atherosclerosis and obesity.

We seek highly self-motivated individuals who have a strong background in signaling and transcriptional/translational regulation, and are interested in aging research. Experience with mouse models is a plus.

To apply, please send a cover letter, CV and list of three references to Dr. Xiaoling Li at email: lix3@niehs.nih.gov.



DHHS and NIH are Equal Opportunity Employers



Tenure/Tenure-Track Position Laboratory of Persistent Viral Diseases Rocky Mountain Laboratories, Hamilton, Montana

National Institute of Allergy and Infectious Diseases (NIAID)
National Institutes of Health

The Laboratory of Persistent Viral Diseases (LPVD), Rocky Mountain Laboratories, NIAID, NIH, DHHS, in Hamilton, Montana, seeks applicants for a tenured or tenure-track position (full to assistant professor equivalent) to conduct independent research on host immune or inflammatory responses in neuropathogenic viral diseases. Candidates with a background in adaptive or innate immunity, including neuroinflammation and gliosis are preferred; those interested in neurobiology, biochemistry or pathogenesis of CNS infections are also encouraged to apply. Candidates must hold a Ph.D., D.V.M., or M.D. degree and have a minimum of 3 years of relevant postdoctoral experience. Candidates must be able to develop an independent research program, supervise staff and fellows, and collaborate with other LPVD researchers working on CNS viral or prion diseases.

Rocky Mountain Laboratories' state-of-the-art facilities include an operational BSL-3 facility, a BSL-4 lab and animal facility nearing completion, and in-house core facilities for genomics, electron microscopy, and flow cytometry. Research programs focus on prions, murine retroviruses, HIV, flaviviruses, and numerous pathogenic prokaryotic organisms. The lab is located in the scenic Bitterroot Valley of western Montana with easy access to some of the finest outdoor recreational opportunities in North America. Additional information on the position may be obtained by contacting Dr. Bruce Chesebro at bchesebro@niaid.nih.gov.

Application Process: Salary depends on degree and qualifications. To apply, submit a curriculum vitae and bibliography, including a list of your five most significant papers, and a 2-3-page description of a proposed research program, via e-mail to **Ms. Felicia Braunstein** at braunsteinf@niaid.nih.gov. In addition, three letters of recommendation must be sent directly from the referees to **Ms. Felicia Braunstein, Committee Manager, NIAID/NIH; 10 Center Drive, Bldg. 10, Rm. 4A31, MSC-1356; Bethesda, MD 20892-1356**. Applications must reference **AD #010** and must be received by **March 9, 2007**. Applicants will be notified when their applications are received and then complete. All information provided by applicants will remain confidential.



TENURE TRACK POSITION

The Laboratory of Cellular and Molecular Biology (LCMB), Center for Cancer Research, of the National Cancer Institute, National Institutes of Health (<http://ccr.cancer.gov/labs/lab.asp?labid=64>) has a long tradition of excellence in the investigation of signal transduction pathways involved in both normal cellular function and malignant transformation. The Laboratory now invites applications for a tenure track investigator to develop an independent basic research program in cellular and molecular biology with emphasis on understanding basic signal transduction processes. Areas of potential interest include but are not restricted to the role of signaling pathways in stem cell biology, inflammation and cancer, or malignant transformation. The applicant should hold a Ph.D, M.D., or M.D., Ph.D. degrees. Salary is commensurate with education and experience. This position is supported by the intramural Center for Cancer Research of the National Cancer Institute. A two-page statement of research interests and goals should be submitted in addition to three letters of recommendation and a curriculum vitae by March 9, 2007 to: Mrs. Erin M. Breedlove, Executive Secretary, Laboratory of Cellular and Molecular Biology, CCR, NCI, Building 37, Room 2066, Bethesda, MD 20892-4256; phone: 301-496-9683. Fax: 301-496-8479, email: breedlove@mail.nih.gov. Candidates must be U.S. citizens or permanent residents. NIH Tenure track investigators with educational debts may be eligible for the NIH Loan Repayment Program. The NCI is an Equal Opportunity Employer.



Tenure Track/Tenure Investigator Positions in Systems Immunology and Infectious Disease Modeling



The National Institute of Allergy and Infectious Diseases (NIAID), Division of Intramural Research (DIR) is seeking several outstanding individuals for its new Program in Systems Immunology and Infectious Disease Modeling (PSIIM).

Modern technology allows the analysis of immune responses and host-pathogen interactions at multiple levels - from intracellular signaling networks, to individual cell behavior, to the functioning of a tissue, organ, and even the whole organism. The challenge is not only to collect large amounts of data, but also to organize it in a manner that enhances our understanding of *how* the immune system operates or *how* pathogens affect their hosts. To do this, we need to develop detailed quantitative models that can be used to predict the behavior of a complex biological system. These models can help to explain the mechanisms underlying physiological and pathological responses to infection or vaccination, which can then be exploited to design better therapies or vaccines.

Achieving this goal requires an interdisciplinary effort and to this end the PSIIM will be organized as an integrated team of scientists and support staff with expertise in computational biology, bioinformatics, proteomics, cell biology, immunology, and infectious diseases, rather than as a group of independent laboratories. These teams will have access to the latest technology for gene-expression profiling, high-content screening of RNAi libraries for the discovery of pathway components, imaging tools, cores for the genetic manipulation of animals and for proteomic analysis, and a substantial computer infrastructure. BSL-3 facilities for working with high priority pathogens will also be available.

The PSIIM is now recruiting for tenure-track or tenure level team leader appointments in three key areas:

Computational Biology: The incumbent will lead a group focused on the development and improvement of software tools for multiscale modeling and simulation that can be used by the PSIIM as well as by biologists interested in subjects other than immunity or infectious diseases. The ideal candidate will have a strong background in mathematics, physics, and computer programming, and a clear desire and ability to interact with and support the efforts of biologists. A demonstrated ability to generate computer software tools for biological modeling will be a strong plus.

Molecular/Cell Biology: The incumbent will lead a group involved in the design, implementation, and interpretation of screening efforts to identify and determine the interactions among the components in signaling networks that could then be modeled using the software generated by the computational biology team or obtained from other sources. Discovery tools such as gene arrays, high content image-based screens using RNAi methods, various protein-protein hybrid screening methodologies, and optical imaging are expected to be key elements in the efforts of this group. A strong background in basic cell biology and molecular biology with experience in analysis of protein-protein interactions, signaling, and/or gene regulation is required. Expertise in large-scale screening is highly desirable.

Infectious Diseases: The incumbent will be responsible for developing novel approaches to systems-wide analysis of the interaction of infectious agents and their hosts. These may include the use of gene expression signatures, the production of gene modified animals, the development of methods for *in vivo* testing of the predictions of models, and the use of sophisticated imaging and other tools for probing the interaction of pathogens and host cells *in vitro*. A strong background in viral and/or bacterial infectious diseases and cell and molecular biology are necessary; training in the immunology of infectious diseases and substantial bioinformatics experience are highly desirable.

These positions and the research activities they conduct are fully funded by the intramural research program of NIH. Each team leader is expected to build a working group consisting of postdoctoral fellows, staff scientists, technicians, and students. The team leaders will work with the program director to help set the goals for the PSIIM and to determine how best to reach these goals as an integrated group. To ensure appropriate career trajectories for those joining the PSIIM team, the NIH has modified its tenure policies to encourage and account for contributions made in such a team science setting. Applicants should be seeking a difficult challenge in which creativity, technical expertise, and a strong desire to achieve in a team environment are critical for success.

Interested candidates may contact **Dr. Ronald Germain, Program Director, PSIIM, DIR, NIAID at 301/496-1904 or email (rgermain@niaid.nih.gov)** for additional information about these positions.

To apply, submit your curriculum vitae, bibliography, and detailed statement of how you can contribute to the success of the PSIIM program to: **Felicia Braunstein at braunsteinf@niaid.nih.gov**. In addition, three letters of reference must be sent directly from the referee to **Dr. Robert Hohman, Chair, NIAID Search Committee, c/o Ms. Felicia Braunstein, DIR Committee Management Team Lead, 10 Center Drive, MSC 1356, Building 10, Room 4A31, Bethesda, Maryland 20892-1356**. Completed applications **MUST** be received by **February 16, 2007 for computational biology, March 16, 2007 for molecular/cell biology, as well as for infectious diseases**. Please refer to ad #012 for computational biology, #013 for Molecular/Cell Biology and #014 for infectious disease on all correspondence. Further information on these positions and guidance on submitting your application are available at: <http://healthresearch.niaid.nih.gov>. For more information about NIAID systems biology program, please visit <http://www.nih.gov/catalyst/2006/06.09.01/page1.html>

NW95632R

THE NIH IS DEDICATED TO BUILDING A DIVERSE COMMUNITY IN ITS TRAINING AND EMPLOYMENT PROGRAMS

OPPORTUNITIES @ NIH THE NATIONAL INSTITUTES OF HEALTH